A Measurement of the Proton's Weak Charge Using an Integration Čerenkov Detector System

by

Peiqing Wang

A Thesis submitted to the Faculty of Graduate Studies of

The University of Manitoba

in partial fulfillment of the requirements of the degree of

DOCTOR OF PHILOSOPHY

Department of Physics and Astronomy

University of Manitoba

Winnipeg

Copyright © 2011 by Peiqing Wang

This work is dedicated

to my family.

Acknowledgments

I would like to thank these people who have provided support, encouragement, guidance and assistance in the preparation of this dissertation.

First and foremost, my extra special thanks goes to my supervisor, Prof. Michael Gericke, who has offered insight and guidance for my work in experimental physics. My extra special thanks also goes to Dr. David Mack, who has been abundantly instructive and helpful, and has passed on numerous hand-on experiences to me and assisted me in the details of my research.

Then, I would like to greatly thank Prof. Shelley Page for firstly leading me into the world of subatomic physics, Dr. Willie Falk and Dr. Lawrence Lee for being my research mentors, Prof. Jeffrey Martin, Prof. James Birchall, Dr. Desmond Ramsay, Prof. Willem van Oers, Prof. David Armstrong, Dr. Gregory Smith, Dr. David Gaskell, Dr. Dipangkar Dutta, Dr. Paul King, Dr. Klaus Grimm, Prof. Garth Huber, Prof. Gerald Gwinner and Prof. Douglas Goltz for giving me many advices. Without the generous help of these individuals, this dissertation would not have been possible. I would also like to extend my extra special thanks to my family and friends for the support over the years.

I am indebted to my many colleagues for providing a stimulating and fun environment. I am especially grateful to Anna Micherdzinska, Vladas Tvaskis, Wouter Deconinck, Rob Mahurin, Scott MacEwan, Mark McCrea, David Harrison, Alexandre Coppens, Amrendra Narayan, Siyuan Yang, Josh Hoskins, Nuruzzaman, Jiawei Mei, Jeong Han Lee, John Leacock, Donald Jones, John Leckey, Katherine Myers, Juliette Mammei, Russell Mammei, Rakitha Beminiwattha and Buddhini Waidyawansa.

Finally, NSERC (Natural Sciences and Engineering Research Council of Canada), CFI (Canada Foundation for Innovation), DOE (US Department of Energy) and NSF (National Science Foundation of USA) are gratefully acknowledged for funding the experiment.

Abstract

The Q-weak experiment at Thomas Jefferson National Accelerator Facility (USA) will make a precision determination of the proton weak charge $Q_W^P = 1 - 4\sin^2\theta_W$ with approximately 4% combined statistical and systematic uncertainties via a measurement of the parity violating asymmetry in elastic electron-proton scattering at very low momentum transfer and forward angle. This will allow an extraction of the weak mixing angle $\sin^2\theta_W$ at $Q^2 = 0.026$ (GeV/c)^2 to approximately 0.3%. The weak mixing angle is a fundamental parameter in the Standard Model of electroweak interactions. At the proposed accuracy, a measured deviation of this parameter from the predicted value would indicate new physics beyond what is currently described in the Standard Model. Without deviation from the predicted value, this measurement would place stringent limits on possible extensions to the Standard Model and constitute the most precise measurement of the proton's weak charge to date. The key experimental apparatus include a liquid hydrogen target, a toroidal magnetic spectrometer and a set of eight Čerenkov detectors. The Čerenkov detectors form the main detector system for the Q-weak experiment and are used to measure the parity violating asymmetry during the primary Q-weak production runs.

The Čerenkov detectors form the main subject of this thesis. Following a brief introduction to the experiment, the design, development, construction, installation, and testing of this detector system will be discussed in detail. This is followed by a detailed discussion of detector diagnostic data analysis and the corresponding detector performance. The experiment has been successfully constructed and commissioned, and is currently taking data. The thesis will conclude with a discussion of the preliminary analysis of a small portion of the liquid hydrogen data.

Table of Contents

1 Introduction **1**

2 Theory and Experimental Observables **5**

2.1 Brief Overview of the Standard Model and New Physics 5
2.2 The Electro-weak Theory and the Weak Mixing Angle 10
2.3 Weak Charges in the Standard Model 19
2.4 Weak Charges of the Proton and Neutron in the SU(3) Quark Model 22
2.5 The Parity Violating Asymmetry in Electron-Proton Scattering 24
2.6 Electro-Weak Radiative Corrections and the Running of the Weak Mixing Angle . 34
2.7 Q-weak and New Physics beyond the Standard Model 40
2.8 Summary 46

3 The Experiment **47**

3.1 Overview 47
3.2 Continuous Polarized Electron Beam 54
3.3 Beam Property Monitor and Feedback Control 57
3.4 Precision Beam Polarimetry 62
3.4.1 Møller Polarimeter 62
3.4.2 Compton Polarimeter 65
3.5 Liquid Hydrogen Cryotarget System 67
3.6 Q-weak Spectrometer 71
3.6.1 Collimator and Shield Wall 71
3.6.2 Toroidal Magnet 73
3.6.3 Tracking Detectors 74
3.7 Main Detector 84
3.8 Luminosity Monitor 85

4 Main Detector System **89**
4.1 Overview . . . 89
4.2 Design Criteria . . . 100
4.3 Simulations and Detector Design . . . 107
4.4 Detector Construction . . . 116
4.4.1 Radiator and Light Guide . . . 116
4.4.2 Preradiator . . . 119
4.4.3 Photomultiplier Tubes . . . 121
4.4.4 PMT Bases . . . 127
4.4.5 Main Detector Mounting and Support Structure . . . 131
4.4.6 Diagnostic System . . . 139
4.5 Electronics and Data Readout (DAQ) . . . 141
4.5.1 Electronics . . . 142
4.5.2 Data Acquisition . . . 151
4.6 Bench/Beam Testing and Detector Diagnostics . . . 153
4.6.1 Radiation Hardness . . . 154
4.6.2 PMT-Base Linearity . . . 156
4.6.3 Detector Performance . . . 158
4.7 Auxiliary and Background Detectors . . . 168
4.8 Summary . . . 169

5 Analysis **171**
5.1 Overview . . . 171
5.2 Data Quality . . . 173
5.3 Raw Asymmetries . . . 175
5.4 Blind Analysis . . . 179
5.5 Corrections for Helicity-Correlated Beam Properties . . . 179
5.6 Background Corrections . . . 184
5.7 Physics Asymmetry . . . 186
5.8 Hadronic Structure Contributions . . . 190
5.9 The Proton's Weak Charge and Weak Mixing Angle . . . 192

6 Conclusion and Outlook **195**

Appendices **197**

A Miscellaneous Details of the Main Detector **197**
A.1 Detector Parameters 197
A.1.1 Detector and PMT serial number 197
A.1.2 Transmission spectrum and refractive index of fused silica 198
A.1.3 PMT quantum efficiency 199
A.1.4 PMT saturation voltage and current 200
A.1.5 Gain tests for current mode PMT bases 201
A.1.6 Single photo-electron calibration 202
A.1.7 Typical current mode yield 203
A.1.8 High voltage and pre-amplifier settings 204
A.2 Gluing Procedure 205
A.3 Detector Installation 208
A.4 Detector Survey Results 211
A.5 CAD Drawings of Preradiator, Radiator Box and Exoskeleton 212

B My Contributions to the Q-weak Experiment **227**

C The Q-weak Collaboration **229**

Bibliography **235**

Index **247**

List of Figures

2.1 Mexican hat potential 12
2.2 The neutral current (NC) and electromagnetic current (EM) interaction vertices. . . 19
2.3 The two possible tree-level amplitudes contributing to the e-q interaction 21
2.4 Process of an electron–nucleon scattering 25
2.5 Typical reduced QED corrections to Z exchange 36
2.6 Typical one-loop self-energy diagrams 36
2.7 Electroweak vertex and box diagrams 36
2.8 Running of weak mixing angle 38
2.9 Model independent mass limit 44
2.10 Knowledge of the neutral weak effective couplings 45

3.1 CAD layout of the Q-weak apparatus 50
3.2 Elastic event distribution 52
3.3 The CEBAF accelerator at Jefferson Lab 55
3.4 Pillbox cavity beam current monitor 58
3.5 Schematics of a 4-wire stripline beam position monitor 59
3.6 Locations of Q-weak halo monitors 60
3.7 Layout of the Hall C Møller polarimeter 63
3.8 Top view of the Hall C Møller polarimeter 63
3.9 Preliminary Møller beam polarization measurements 64
3.10 Schematic diagram of the Compton polarimeter layout. 65
3.11 Compton region during installation 66
3.12 Preliminary beam polarization result 67
3.13 Schematic of the transverse flow target 68
3.14 Photons of target scattering chamber and target cell 69
3.15 Noise frequency spectrum measured for liquid hydrogen target 70
3.16 Shielding wall and detector shielding hut 72

3.17 Q-weak toroidal magnetic field spectrometer 73
3.18 Side view of GEM preamps and readout board 76
3.19 Photo of the Region 1 GEM 77
3.20 Photo of the region 2 HDC's 79
3.21 Photo of the region 3 VDC's 81
3.22 Photo of the trigger scintillator 82
3.23 Focal plane scanner and the flux distribution 84
3.24 Photos of luminosity monitors 86

4.1 Electron flux profile on the focal plane 90
4.2 Concept diagram of Q-weak Čerenkov detector 91
4.3 Q-weak coordinate systems and main detector arrangement 92
4.4 Main detector geometry and the average incident electron trajectory 93
4.5 Momentum threshold of Čerenkov radiation 94
4.6 Čerenkov light wavelength distribution 95
4.7 Čerenkov angle and TIR critical angle versus the refractive index 96
4.8 Čerenkov lights escape from quartz bar 96
4.9 Simulated shower activities in the lead pre-radiator 98
4.10 Visualization of Q-weak Geant4 simulation 108
4.11 Visualization of the main detector implementation in the simulation 110
4.12 Preradiator shower noise 111
4.13 Main detector tilt angle simulation 112
4.14 Total light yield and light yield correlation between two PMTs 113
4.15 Position dependent light yield on the Čerenkov bar 113
4.16 Simulated variation of light yield as a function of electron hit position 114
4.17 Simulated variation of the light yield at normal incidence 114
4.18 Elastic event distribution by Q^2 115
4.19 Momentum transfer determined from simulation 116
4.20 The optical assembly of main detector 119
4.21 Shower profile in lead 120
4.22 Dimensions of the 130 mm 9312WKB photomultiplier tube 122
4.23 Čerenkov light collections by PMT with different PMT window 123
4.24 Quantum efficiency for the S20 photocathode 124
4.25 Schematic diagram for the low gain current mode PMT base 129
4.26 Schematic diagram for the high gain pulsed mode PMT base 130
4.27 Exploded view of the radiator box 132
4.28 PMT housing portion cut along the bar 133

4.29 Quartz holding bracket 134
4.30 Photos of assembled main detectors 135
4.31 Exoskeleton of the radiator module 136
4.32 Schematic view of the main detector array mechanical support structure 137
4.33 Schematic view of the radial adjustment 138
4.34 Schematic disgram of LED power distribution panel 140
4.35 Schematic of the current mode signal chain. 143
4.36 Photo of the low-noise preamplifier 145
4.37 Schematic diagram of low noise preamplifier 146
4.38 TRIUMF electronics block diagram 148
4.39 Photo of the TRIUMF VME digital integrator 149
4.40 Setup for radiation damage measurement 155
4.41 Light transmission after irradiation 156
4.42 Linearity measurement of the low gain PMT-Base combination 157
4.43 PMT-Base linearity versus anode current 158
4.44 Main detector pedestal vs. run number 159
4.45 Main detector pedestal variance 160
4.46 Representive pulse height distribution 161
4.47 Light yield distribution on the Čerenkov detector 1 161
4.48 Hit position dependent photo-electron yield 162
4.49 Accepted Q^2 distribution and main detector light yield weighting 163
4.50 Simulated total light yield on the main detector 164
4.51 Main detector ADC spectrum 165
4.52 Beam time evaluation 168
4.53 Photos of auxiliary detectors 169

5.1 Array of measured asymmetries from the main detectors 178
5.2 Distributions of helicity-correlated beam property corrections 182
5.3 Sensitivities to x, y, x', y', energy and charge asymmetry 183
5.4 Corrections to the combined detector asymmetry 183
5.5 Corrections to the combination of all main detectors asymmetry 184
5.6 Asymmetry versus Wien setting and IHWP status 189

A.1 Main detector geometry and the average incident electron trajectory 198
A.2 PMT saturation voltage and current 200
A.3 Saturation as a function of wavelength 200
A.4 Photo of the main detector optical assembly 207

A.5 Main detector installation photos 210
A.6 Main detector survey result 211
A.7 CAD drawing of preradiator end piece 212
A.8 CAD drawing of preradiator T-bar piece 212
A.9 Radiator box CAD drawing 1 of 10 213
A.10 Radiator box CAD drawing 2 of 10 214
A.11 Radiator box CAD drawing 3 of 10 215
A.12 Radiator box CAD drawing 4 of 10 216
A.13 Radiator box CAD drawing 5 of 10 217
A.14 Radiator box CAD drawing 6 of 10 218
A.15 Radiator box CAD drawing 7 of 10 219
A.16 Radiator box CAD drawing 8 of 10 220
A.17 Radiator box CAD drawing 9 of 10 221
A.18 Radiator box CAD drawing 10 of 10 222
A.19 Exoskeleton CAD drawing 1 of 4 223
A.20 Exoskeleton CAD drawing 1 of 4 224
A.21 Exoskeleton CAD drawing 2 of 4 225
A.22 Exoskeleton CAD drawing 3 of 4 226

C.1 Q-weak Collaboration Picture 234

List of Tables

2.1 The generations of matter 6
2.2 $SU(2) \times U(1)$ electroweak unification particles and charges 18
2.3 The tree level electromagnetic and weak couplings 20
2.4 The weak couplings 21
2.5 Theoretical uncertainties 39

3.1 The anticipated experimental uncertainties 53
3.2 Basic parameters of the Q-weak experiment 54
3.3 Beam parameters 57
3.4 Partial list of Q-weak beam specifications 61
3.5 Luminosity monitor parameters compared to main detector 87

4.1 Alignment tolerances of Čerenkov angle w.r.t TIR critical angle 95
4.2 Čerenkov radiator and light guide parameters 117
4.3 Material properties of Spectrosil® 2000 synthetic fused silica 118
4.4 Comparisons of noise contributions from different sources 145
4.5 Main registers of the TRIUMF VME integrator 149
4.6 High voltage channel arrangement of the main detector system 150

5.1 Q-weak Run-I asymmetry data 190
5.2 Comparison between theoretical prediction and Q-weak measurement 193

A.1 Main detector serial number 197
A.2 PMT serial number for each detector 197
A.3 Refractive index of Spectrosil® 2000 synthetic fused silica 198
A.4 Quantum efficiency of 9312WKB PMT with S20 photocathode 199
A.5 Gain measurements for the current mode low gain PMT bases 201
A.6 Bias voltages at a PMT gain of 1000 201

A.7 Single photo-electron calibration I 202
A.8 Single photo-electron calibration II 202
A.9 Single photo-electron calibration III 202
A.10 Typical current mode yields of main detectors 203
A.11 High voltages and currents of event mode high gain bases 204
A.12 Pre-amplifier offset settings 204
A.13 Current mode PMT high voltage and gain settings 204
A.14 Current mode parameters and settings for the Q-weak Run-I 204
A.15 Parameters for preparing optical glue 206

Chapter 1

Introduction

One of the greatest achievements of physics in the twentieth century is the development of the Standard Model; a theory which describes the fundamental particles of nature and their interactions. The Standard Model asserts that the fundamental particles that make up all matter are quarks and leptons, and that they interact through the strong, weak, and electromagnetic fundamental interactions by exchanging force carrier particles. The Standard Model makes many predictions and many of them have been verified by experimental tests.

Despite the fact that the Standard Model has had enormous success, there are many indications that the Standard Model is not a complete theory of fundamental particles and interactions; it does not predict and explain everything. For instance, it cannot predict particle masses without experimental data; a large number of parameters need to be measured and inserted into the theory, and so on. To discover a more complete theory beyond the Standard Model, we need to measure the unknown parameters, test predictions and look for new phenomena not predicted in the current model. The only way to settle these questions is by performing very precise experiments.

The Q-weak collaboration[1] at the Thomas Jefferson National Accelerator Facility, USA, (TJNAF, also referred to as Jefferson Laboratory or JLab) is conducting an experiment which will make a precision determination of a fundamental parameter of the Standard Model – the proton's weak

[1] See Appendix C for a collaboration list.

charge (the proton's vector neutral current coupling). The proton's weak charge sets the strength with which it couples to other particles via the weak interaction, much like the proton's electric charge sets the strength with which it couples to other particles via the electromagnetic interaction. It is a very sensitive parameter of the Standard Model and can be used as a probe to search for possible new physics beyond the Standard Model – a precise measurement of the proton's weak charge will enable us to test whether the Standard Model in fact provides an exact description of the weak interaction or whether an important new physics process remains to be accounted for.

The Q-weak experiment aims to measure the proton's weak charge (Q_W^P) with approximately 4% combined statistical and systematic uncertainties through a measurement of the parity violating asymmetry in elastic electron-proton scattering at very low momentum transfer, and at forward angles. This will enable an extraction of $\sin^2\theta_W$ ($Q_W^P = 1 - 4\sin^2\theta_W$ at the tree level, where θ_W is the weak mixing angle) at a momentum transfer of $Q^2 = 0.026$ (GeV/c)^2 to an accuracy of approximately 0.3%. It tests the Standard Model predicted "running" of $\sin^2\theta_W$ (variation of $\sin^2\theta_W$ with Q^2) off the Z^0 pole, at lower energies.

The experiment employs JLab's high luminosity polarized electron beam. The electrons are scattered from a liquid hydrogen target and harvested by a toroidal magnetic spectrometer to focus the electrons onto a set of Čerenkov detectors (the Q-weak main detectors). The experimental observable – the parity violating asymmetry in elastic electron-proton scattering is measured by these detectors.

Main detector performance directly affects the success of the experiment, particularly the experimental precision to be reached. Therefore, the detectors have to be carefully designed and constructed. The main focus of this thesis is the design, construction and testing of the main detectors.

The remainder of this dissertation is organized as follows:

- Chapter 2: a brief discussion of the background, motivation and theory of the experiment,
- Chapter 3: an outline of the experimental apparatus and setup,

- Chapter 4: a detailed explanation of the design and construction of the detector system,
- Chapter 5: a brief description of the analysis of the experimental data,
- Chapter 6: a summary of the emphasized work and experiment status.

Chapter 2

Theory and Experimental Observables

2.1 Brief Overview of the Standard Model and New Physics

Our current understanding of physical phenomena is based on four fundamental interactions: gravitation, the electromagnetic interaction, the strong interaction, and the weak interaction. According to the Standard Model, interactions are mediated between particles by the exchange of intermediate virtual vector bosons (see Table 2.1). These are spin 1 particles and include: eight types of gluons, mediating the strong interactions; the photon as the mediator of the electromagnetic interaction; and the W^+, W^-, and Z^0 bosons as mediators of the weak interaction.

The weak interaction takes a special role among the four known forces, because it is the only one known to violate parity. A parity transformation is defined as a mirror reflection of a physical process, followed by a 180 degree rotation about the axis normal to the reflection plane. Historically, fundamental physical processes are expected to be invariant with respect to such transformations. However, it was discovered in 1957 by C.S. Wu and co-workers [Wu et al., 1957] that parity was violated in the beta-decay of Cobalt-60, by measuring the number of electrons emitted in a particular direction with respect to an applied magnetic field. In this case, the parity transformation could be performed by simply counting the number of electron emissions in opposite directions, while keeping the magnetic field and therefore the polarization of the nucleus constant. This property of

Fermions	Generation I	Generation II	Generation III	bosons	
Quarks	up **u** 0.003 GeV/c^2 +2/3	charm **c** 1.3 GeV/c^2 +2/3	top **t** 175 GeV/c^2 +2/3	photon γ 0 0	Force Carriers (spin=1)
(spin=1/2)	down **d** 0.006 GeV/c^2 -1/3	strange **s** 0.1 GeV/c^2 -1/3	bottom **b** 4.3 GeV/c^2 -1/3	gluon **g** 0 0	
Leptons	electron neutrino ν_e $< 1\times10^{-8}$ GeV/c^2 0	muon neutrino ν_μ < 0.0002 GeV/c^2 0	tau neutrino ν_τ < 0.02 GeV/c^2 0	Z boson Z^0 91.187 GeV/c^2 0	
(spin=1/2)	electron **e** 0.00051 GeV/c^2 -1	muon μ 0.106 GeV/c^2 -1	tau τ 1.7771 GeV/c^2 -1	W boson $W^\pm$ 80.4 GeV/c^2 ±1	

Table 2.1: The generations of matter are organized by increasing mass (values are given at bottom-left corner for each flavor, in units of GeV/c^2) and decreasing electric charges: +2/3, -1/3 and 0, -1 (values are given at bottom-right corner for each flavor, in units of electron charge) [Nakamura et al., 2010].

the weak interaction had been proposed shortly before this by Lee and Yang [Lee and Yang, 1956].

The Standard Model of electro-weak interactions was developed during the late 60's and early 70's primarily to explain the observed properties of the weak interaction at higher energies and the observed particles and their interactions in this context. The theory predicted the existence of three heavy exchange particles, the W^+, W^- and the Z^0, as mediators of the weak interaction [Weinberg, 1967] [Weinberg, 1971]. The theory gave rise to the necessity of mixing between the electromagnetic force (mediated by the photon) and the weak force, to preserve $SU(2)\times U(1)$ gauge invariance in a unified model [Weinberg, 1974]. The degree of mixing between the two forces is fixed by the so-called weak (or Weinberg) mixing angle, at the Z-pole and at lowest order in perturbation, but obtains an energy dependence from higher order processes, resulting in the "running" of the weak mixing angle (see Fig. 2.8 for reference). This is further explained in section 2.6.

The predicted heavy gauge bosons were detected during experiments at CERN, in the early 1980's [Rubbia, 1985] and also later [Arnaudon et al., 1993] and their measured masses (M_W =

80.403 ± 0.029 GeV, M_Z = 91.188 ± 0.002 GeV) correspond exactly (to within the small experimental uncertainty) to the values predicted by the Standard Model. In general, the Standard Model correctly predicts most current experimental results. This is considered to be one of the great scientific achievements of the late 20th century.

In its current form, the Standard Model combines the electromagnetic interaction, the weak interaction, and the strong interactions. Quarks interact via all three forces contained in the Standard Model (the force of gravity on fundamental particles is being omitted here, due its very small size $\sim 10^{-35}$ relative to the weak interaction). Leptons interact via the electromagnetic and weak interactions, but not via the strong interaction, with the exception of neutrinos, which interact via the weak interaction only. The interactions are mediated by various exchange particles, such as the W^+, W^- and the Z^0 bosons mentioned above. A more detailed description of the Standard Model and the particles it describes is given in the following sections.

According to the Standard Model, matter is comprised of six different "flavors" of quarks, which include the up quark (u), the down quark (d), the charm quark (c), the strange quark (s), the top quark (t), and the bottom quark (b), six types of leptons, which include the electron (e) the electron neutrino (ν_e), the muon (μ), the muon neutrino (ν_μ), the tau (τ), and the tau neutrino (ν_τ), as well as their respective anti-particles.

These particles all carry an intrinsic spin of 1/2 and therefore belong to the group of particles known as fermions, obeying Fermi-Dirac statistics and the Pauli exclusion principle. As far as is presently known, these are all point-like particles and are considered fundamental in the sense that none of them has been observed to possess intrinsic excited states (as opposed to excited states relative to each other). Thus, they are considered to be the most elementary particles of matter, and are grouped into so-called "generations" according to increasing mass (see Table 2.1).

Quarks are confined in hadrons and cannot appear in isolation. Hadrons include mesons and baryons and are the bound state configurations of quarks – a meson consists of a quark and an anti-quark – a baryon consists of three valance quarks and a so-called quark sea. Ordinary matter consists of electrons and two kinds of hadrons: proton (a *u*-*u*-*d* quark triplet in the constituent quark

model), and neutron (a *u*-*d*-*d* quark triplet in the constituent quark model). These are the lightest hadrons we know and all heavier hadrons decay into these within a 10^{-20} to 10^{-10} second range [Nakamura et al., 2010]. Since the neutron is slightly heavier than the proton, a free neutron will decay into a proton with a mean lifetime of 885.7(8) seconds [Nakamura et al., 2010]. The neutron is stable only in its bound state, inside nuclei. Many heavier hadrons (also known as hyperons) are known to have existed for a brief period in the early stages of the universe. Today, these are routinely created in high energy accelerator collisions or they occur naturally in high energy cosmic ray interactions.

Among these basic interactions, electromagnetic interactions are experienced by particles that possess electric charge and electromagnetic bound states exist at the atomic level. The strong interaction acts between quarks and anti-quarks and binds them into baryons (hadrons and mesons) and is also responsible for binding hadrons into nuclei. The weak interaction gives rise to decays (massive hadrons and leptons decay into lighter hadrons and leptons, for instance). There are no weak bound states.

Each of these three interactions is associated with a charge, the size of which sets the strength of the interaction. The electric charge for the electromagnetic interaction, the "color" charge for the strong interaction, and the weak charge for the weak interaction. A given interaction between particles occurs only if the interacting particles possess the corresponding charge. For example, quarks carry color, electric and weak charge, but leptons only carry weak and electric charge (except for neutrinos, which only have weak charge). Thus, there is no strong interaction between quarks and leptons.

The probabilities and rates at which a certain interaction take place can be calculated by following the theory of the Standard Model. We can then test the Standard Model by comparing the measured results with the theory. As of today, the Standard Model has been tested and confirmed at the 0.1% level in processes for which perturbation theory is applicable. The success of this effort was recognized by several Nobel Prizes in Physics for theorists and experimentalists. For instance, the 1979 Nobel prize was awarded to theorists Sheldon Glashow, Abdus Salam and Steven Wein-

berg for proposing the theory of electromagnetic and weak interactions, the 1999 prize was awarded to theorists Gerardus ′tHooft and Martinus Veltman for elucidating the mathematical theory that underlies the model. On the other hand, the 1984 Nobel prize was awarded to experimentalists Carlo Rubbia and Simon van der Meer for the detection of the $W^{\pm}$ and Z^0 particles predicted by the model, the 1976, 1988, 1990 and 1995 Nobel Prizes were given for other experiments that corroborated aspects of the Standard Model.

Despite the fact that the Standard Model has had enormous success, there are many reasons that lead us to believe that the Standard Model is not a fundamental theory, as there are many parameters in the model which have to be fixed by experimental input, rather than emerging as a result of the theory itself. For instance, neither the size of any of the coupling constants for the strong, electromagnetic, or weak interactions, nor any of the quark or leptons masses are predicted by the model. Other questions include why there are generations (three) of quarks and leptons which is usually a sign of some higher symmetry, whether there is a relationship between the electro-weak and the strong interactions, whether there is a relationship between leptons and quarks (e.g. why do the proton and the electron have exactly opposite electric charges, but are so different in their other properties), what is the origin of CP violation, and finally, the obvious omission of gravity.

It is widely expected that there is a more fundamental theory beyond the Standard Model, and there are many candidates (such as string theory based super-symmetry, for example). In order to find a successful theory, we need to test parameters within the Standard Model that are sensitive to new physics phenomena not predicted in the current model. The weak charge of the proton is such a parameter and the Q-weak experiment currently underway at Jefferson Laboratory is one such important experimental test. As stated in the introductory chapter, the goal of the experiment is to measure the proton's weak charge with approximately 4% combined statistical and systematic uncertainties and to extract the weak mixing angle at a momentum transfer of $Q^2 = 0.026$ (GeV/c)^2 to an accuracy of approximately 0.3%. This measurement will impact our knowledge about the quark couplings, provide a sensitive test of the Standard Model up to the TeV scale and search possible new physics beyond the Standard Model.

2.2 The Electro-weak Theory and the Weak Mixing Angle

The main goal of this section is to provide enough detail, such that a clear definition of the weak mixing angle is obtained, in the context of the electro-weak theory. Wherever possible and available, references are used to refer the reader to common theoretical treatments and calculations, since a complete theoretical treatment is beyond the scope of this dissertation (see for example, reference [Commins and Bucksbaum, 1983]). In-depth calculations are shown only in cases where a proper reference cannot be found. The following discussion uses notation and concepts from standard text book references such as [Martin and Shaw, 2008].

As mentioned above, the electroweak theory combines the electromagnetic and weak interactions. This is done in the framework of gauge field theories and means that the fields that describe the particles interacting in this way satisfy both $U(1)$ (E&M) and $SU(2)$ (weak isospin) gauge transformations. Under this combined gauge transformation four gauge fields emerge from the requirement to keep the free matter field Lagrangian (the Dirac equation) invariant under these transformations. A direct consequence of this is the introduction of new terms into the Lagrangian, which involve interactions between the gauge fields and the matter fields:

$$ig\overline{\psi}_L\gamma^\mu\vec{T}\cdot\vec{W}_\mu\psi_L\ , \tag{2.1}$$

$$ig'\overline{\psi}\gamma^\mu YB_\mu\psi\ , \tag{2.2}$$

where Y and T are the generators of the $U(1)$ and $SU(2)$ gauge transformations,

$$e^{ig'YP(x)} \qquad \text{and} \qquad e^{ig\vec{T}\cdot\vec{f}(x)}, \tag{2.3}$$

respectively. Y is called the weak hypercharge and is defined as

$$Y = \frac{Q}{|e|} - I_W^3 \tag{2.4}$$

with Q being the electric charge of a given particle in units of e and I_W^3 being the weak isospin. All matter fields (except neutrinos) transform under $U(1)$ but only left handed matter fields transform under $SU(2)$. The fundamental coupling constants g and g' set the strength of the interactions between the matter fields and the gauge fields and must be determined by experiment. What is missing from the Lagrangian (due to requiring gauge invariance) are any mass terms (terms proportional to m^2). Neither the matter fields nor the gauge fields have mass and therefore (as is) do not correspond to fields that describe the real particles that are observed.

Mass terms are introduced into the Standard Model Lagrangian via the mechanism of spontaneous symmetry breaking, also referred to as the Higgs mechanism (a detailed discussion of this is beyond the scope of this thesis, but see for example references [Halzen and Martin, 1984] or [Griffiths, 2008]). The point of spontaneous symmetry breaking is that while the Lagrangian itself is required to be invariant (e.g. symmetric) with respect to $SU(2)$ isospin transformations, the lowest energy state does not have to be; and it is the lowest energy state around which we do perturbative expansions to calculate observables, etc. This concept is used in the Klein-Gordon equation (which is valid for a spin-0 boson like the proposed Higgs) to produce the mass terms of the four gauge bosons. The Klein-Gordon Lagrangian can be written as:

$$\mathcal{L} = (D^\mu \Phi)^\dagger \left(D_\mu \Phi\right) + \mu^2 |\Phi|^2 - \lambda |\Phi|^4 \equiv \mathcal{T} + \mathcal{V} \tag{2.5}$$

with a potential given by (an example of a potential is illustrated in Fig. 2.1)

$$\mathcal{V} = -\mu^2 |\Phi|^2 + \lambda |\Phi|^4 \tag{2.6}$$

and with a kinetic term given in terms of covariant derivatives that leave the Lagrangian invariant under $SU(2) \times U(1)$ transformations

$$D_\mu \Phi = \partial_\mu \Phi + i\frac{g}{2}\left(\vec{W}_\mu \cdot \vec{\tau}\right)\Phi + \frac{1}{2} i g' B_\mu \Phi \,. \tag{2.7}$$

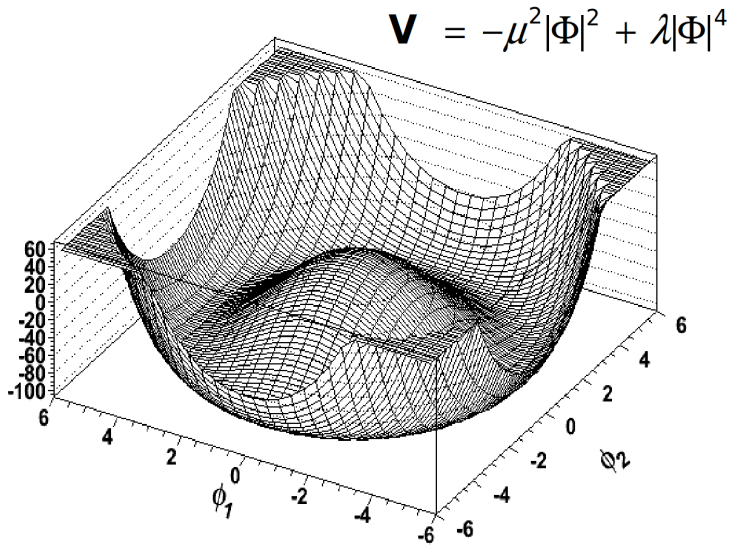

Figure 2.1: Mexican hat potential – the potential graph of the function $\mathcal{V} = -\mu^2\,|\Phi|^2 + \lambda\,|\Phi|^4$.

The solutions to Eqn. 2.5 are complex isospin doublets

$$\Phi(x) = \begin{pmatrix} \phi_1(x) \\ \phi_2(x) \end{pmatrix} . \tag{2.8}$$

For the chosen potential, the energy is minimized if

$$|\Phi|^2 = |\phi_1|^2 + |\phi_2|^2 = \frac{\mu^2}{2\lambda} . \tag{2.9}$$

There are an infinite number of minimum energy states, but one only needs to choose one and in doing so the chosen vacuum state breaks the isospin symmetry:

$$\Phi(x) = \begin{pmatrix} 0 \\ \phi_2(x) \end{pmatrix} \quad \longrightarrow \quad |\Phi| = |\phi_2| = \frac{\mu}{\sqrt{2\lambda}} \equiv \frac{1}{2}\nu . \tag{2.10}$$

This is the Higgs vacuum expectation value and the corresponding state is

$$\Phi = \frac{1}{2}\begin{pmatrix} 0 \\ v \end{pmatrix} . \tag{2.11}$$

If this state is used in the kinetic term of the Lagrangian :

$$(D^{\mu}\Phi)^{\dagger}\left(D_{\mu}\Phi\right) \tag{2.12}$$

with the definition of the covariant derivative above, then one obtains

$$(D^{\mu}\Phi)^{\dagger}\left(D_{\mu}\Phi\right) = \frac{1}{8}v^2\left[g^2\left(W_{\mu}^{1}W_{1}^{\mu} + W_{\mu}^{2}W_{2}^{\mu}\right) + g^2\left(W_{\mu}^{3} - \frac{g'}{g}B_{\mu}\right)^2\right] \tag{2.13}$$

and with the definitions:

$$W_{\mu}^{-} = \frac{1}{\sqrt{2}}\left(W_{\mu}^{1} + iW_{\mu}^{2}\right) , \tag{2.14}$$

$$W_{\mu}^{+} = \frac{1}{\sqrt{2}}\left(W_{\mu}^{1} - iW_{\mu}^{2}\right) . \tag{2.15}$$

This turns into

$$(D^{\mu}\Phi)^{\dagger}\left(D_{\mu}\Phi\right) = \frac{1}{4}v^2g^2W_{\mu}^{+}W^{\mu-} + \frac{1}{8}v^2\left(W_{\mu}^{3}, B_{\mu}\right)\begin{pmatrix} g^2 & -gg' \\ -gg' & g'^2 \end{pmatrix}\begin{pmatrix} W_{\mu}^{3} \\ B_{\mu} \end{pmatrix}. \tag{2.16}$$

The first term is the sought mass term for the $W^{\pm}$ bosons, with a definition of the mass as

$$M_W \equiv \frac{1}{2}vg . \tag{2.17}$$

The second term is expressed in terms of the electro-weak mixing matrix. This matrix has the two eigenvalues 0 and $g'^2 + g^2$ with corresponding eigenvectors (g', g) and $(g, -g')$ respectively. The

diagonal form of this matrix is therefore

$$\begin{pmatrix} 0 & 0 \\ 0 & g^2 + g'^2 \end{pmatrix}, \tag{2.18}$$

and the unitary matrix that does the transformation into the space where the matrix is diagonal is

$$S = \frac{1}{\sqrt{g'^2 + g^2}} \begin{pmatrix} g' & g \\ g & -g' \end{pmatrix} = S^\dagger . \tag{2.19}$$

When this matrix is applied to the second term, one finds

$$\begin{aligned} &\left(W_\mu^3, B_\mu\right) S S^\dagger \begin{pmatrix} g^2 & -gg' \\ -gg' & g'^2 \end{pmatrix} S S^\dagger \begin{pmatrix} W_\mu^3 \\ B_\mu \end{pmatrix} \\ &= \frac{1}{\sqrt{g'^2 + g^2}} \left(g' W_\mu^3 + g B_\mu \,,\, g W_\mu^3 - g' B_\mu\right) \begin{pmatrix} 0 & 0 \\ 0 & g'^2 + g^2 \end{pmatrix} \frac{1}{\sqrt{g'^2 + g^2}} \begin{pmatrix} g' W_\mu^3 + g B_\mu \\ g W_\mu^3 - g' B_\mu \end{pmatrix} . \end{aligned} \tag{2.20}$$

It is common to refer to the diagonal matrix that is obtained as the mass matrix for the neutral bosons and the newly obtained linear combinations

$$A_\mu = \frac{g' W_\mu^3 + g B_\mu}{\sqrt{g'^2 + g^2}} \qquad \text{photon,} \tag{2.21}$$

$$Z_\mu = \frac{g W_\mu^3 - g' B_\mu}{\sqrt{g'^2 + g^2}} \qquad \text{Z boson} \tag{2.22}$$

are the mass eigenstates with masses $M_A = 0$ and $M_Z = \frac{1}{2} v \sqrt{g^2 + g'^2}$ respectively. With this, one gets the kinetic term in the vacuum Lagrangian:

$$\begin{aligned} (D^\mu \Phi)^\dagger \left(D_\mu \Phi\right) &= \frac{1}{4} v^2 g^2 W_\mu^+ W^{\mu -} + \frac{1}{8} v^2 \left(g'^2 + g^2\right) Z_\mu Z^\mu + 0 A_\mu A^\mu \\ &= M_W W_\mu^+ W^{\mu -} + \frac{1}{2} M_Z Z_\mu Z^\mu + \frac{1}{2} M_A A_\mu A^\mu . \end{aligned} \tag{2.23}$$

In the Standard Model, the weak mixing angle is then defined as:

$$\frac{g'}{g} = \tan\theta_W \ . \tag{2.24}$$

It unifies the electromagnetic and weak interactions by relating the respective coupling strengths so that $\sqrt{g'^2 + g^2} = 1$ and

$$Z_\mu = W^3_\mu \cos\theta_W - B_\mu \sin\theta_W, \tag{2.25}$$

$$A_\mu = W^3_\mu \sin\theta_W + B_\mu \cos\theta_W. \tag{2.26}$$

The weak mixing angle is the central parameter of the electroweak theory, as it is directly related to the coupling constants in the gauge theory (the parameters of the gauge transformation that directly define the strength of the resulting interactions g and g') and therefore defines the weak charge of the various particles described in the Standard Model. The numerical value of the weak mixing angle is 0.23154 ± 0.00016 at the energy corresponding to the Z mass [Abbiendi et al., 2001].

Note that the Higgs in the above Lagrangian would be obtained by exciting it out of the vacuum, via a perturbation on the vacuum state:

$$\Phi = \frac{1}{\sqrt{2}}\begin{pmatrix} 0 \\ v \end{pmatrix} \qquad \longrightarrow \qquad \begin{pmatrix} 0 \\ \frac{1}{\sqrt{2}}v + h(x) \end{pmatrix}. \tag{2.27}$$

Therefore the above mass matrix not only defines the mass terms for the intermediate vector bosons, but also defines the strength with which these bosons couple to the Higgs.

We may rewrite Eqns. 2.14, 2.15, 2.25, and 2.26 and obtain the gauge fields in terms of the now

defined intermediate vector bosons:

$$W^1_\mu = \frac{1}{\sqrt{2}}\left(W^-_\mu + W^+_\mu\right) , \tag{2.28}$$

$$W^2_\mu = \frac{i}{\sqrt{2}}\left(W^-_\mu - W^+_\mu\right) , \tag{2.29}$$

$$W^3_\mu = A_\mu \sin(\theta_W) + Z_\mu \cos(\theta_W) , \tag{2.30}$$

$$B_\mu = A_\mu \cos(\theta_W) - Z_\mu \sin(\theta_W) . \tag{2.31}$$

Eqns. 2.1 and 2.2 then tell us that the interaction part of the matter field Standard Model Lagrangian can be rewritten in terms of the weak mixing angle. For the neutral current interactions (the ones involving the neutral vector bosons), which are the dominant terms in the determination of the proton weak charge, one finds

$$\begin{aligned}\mathcal{L} =& g\overline{\psi}_L\gamma^\mu \begin{pmatrix} \left(Y+\frac{1}{2}\right)A_\mu \sin\theta_W & 0 \\ +\frac{1}{2\cos\theta_W}\left[1-(2Y+1)\sin^2\theta_W\right]Z_\mu & \\ & \left(Y-\frac{1}{2}\right)A_\mu \sin\theta_W \\ 0 & -\frac{1}{2\cos\theta_W}\left[1+(2Y-1)\sin^2\theta_W\right]Z_\mu \end{pmatrix}\psi_L \\ &+ gY\sin\theta_W\overline{\psi}_R\gamma^\mu\psi_R A_\mu - gY\frac{\sin^2\theta_W}{\cos\theta_W}\overline{\psi}_R\gamma^\mu\psi_R Z_\mu .\end{aligned} \tag{2.32}$$

The central concept in all field theories is Lorentz invariance and this severely restricts the kind of particle currents one is allowed to construct. The allowed currents are categorized according to how they transform under Lorentz boosts: scalar, vector, and tensor. Additionally, these may also be parity odd (switching sign under a parity transformation) and then perform differently under Lorentz transformations . These are referred to as pseudo-scalars, pseudo-vectors and pseudo-tensors. Since the intermediate vector bosons are Lorentz vectors they have to couple to vector currents (to produce Lorentz scalar amplitudes). Thus, we are left with two possible bilinear currents: vector ($\overline{\psi}\gamma^\mu\psi$) and pseudo-vector ($\overline{\psi}\gamma^\mu\gamma_5\psi$). The general interaction Lagrangian consists of a linear superposition of these, with arbitrary signs: $\overline{\psi}\gamma^\mu(1 \pm \gamma_5)\psi$. Both of these combinations are observed for neutral

currents, but currently only one combination is observed experimentally: $\overline{\psi}\gamma^{\mu}(1-\gamma_5)\psi$ for weak charged currents. This is referred to as the $\mathcal{V}-\mathcal{A}$ (for vector minus axial vector) structure of the electro-weak interaction and is one of the observed properties of nature for which the Standard Model provides no theoretical explanation.

The presence of the pseudo-vector provides for parity violation in the electro-weak interaction but the $\mathcal{V}-\mathcal{A}$ structure is purely based on observation and is "forced" into the theory by separating the fields into left-handed and right-handed components:

$$\psi_L = \frac{1}{2}(1-\gamma_5)\psi \ , \tag{2.33}$$

$$\psi_R = \frac{1}{2}(1+\gamma_5)\psi \ , \tag{2.34}$$

and only allowing for left-handed particles or right-handed antiparticles. Since the charged interactions are purely iso-vector and have only left-handed particle currents, the three lepton and quark generations transform as isospinors (indicated by the upper case Ψ_L) :

$$\Psi_{L,\ell} \equiv \begin{pmatrix} \psi_{L,\nu_\ell} \\ \psi_{L,\ell} \end{pmatrix}, \qquad \Psi_{L,q} \equiv \begin{pmatrix} \psi_{L,u} \\ \psi_{L,d_c} \end{pmatrix}, \begin{pmatrix} \psi_{L,c} \\ \psi_{L,s_c} \end{pmatrix}, \begin{pmatrix} \psi_{L,t} \\ \psi_{L,b_c} \end{pmatrix}. \tag{2.35}$$

In addition, the neutral weak interaction allows all particles to form right-handed currents. However, right-handed neutrinos are not observed. The hypercharge for all Standard Model particles is given in Table 2.2.

Restricting the remainder of this discussion to those particles that are of relevance to the discussion of the weak charge of the proton (e^-, u, d, s) and using Eqns. 2.33 and 2.34 in Eqn. 2.32,

$SU(2)\times U(1)$ unification	electroweak particles	Weak isotopic charge	Weak hypercharge	Electric charge
Quark doublet	u_L	+1/2	+1/3	+2/3
	d_L	-1/2	+1/3	-1/3
Quark singlets	u_R	0	+4/3	+2/3
	d_R	0	+2/3	-1/3
Lepton doublet	$(\nu_e)_L$	+1/2	-1	0
	e_L	-1/2	-1	-1
Lepton singlet	e_R	0	-2	-1
Boson triplet	W^+	+1	0	+1
	W^0/Z^0	0	0	0
	W^-	-1	0	-1
Boson singlet	B	0	0	0
Speculative Higgs boson doublet	ϕ^+	+1/2	+1	+1
	ϕ^0	-1/2	+1	0

Table 2.2: $SU(2)\times U(1)$ electroweak unification particles and charges

together with the respective hypercharge, one gets the following expressions:

$$\mathcal{L}_e = -\frac{g}{4\cos\theta_W}\overline{\psi}_e\gamma^\mu\left(1-4\sin^2\theta_W-\gamma_5\right)\psi_e Z_\mu - g\sin\theta_W\overline{\psi}_e\gamma^\mu\psi_e A_\mu\ , \tag{2.36}$$

$$\mathcal{L}_u = -\frac{g}{4\cos\theta_W}\overline{\psi}_u\gamma^\mu\left(-1+\frac{8}{3}\sin^2\theta_W+\gamma_5\right)\psi_u Z_\mu + g\frac{2}{3}\sin\theta_W\overline{\psi}_u\gamma^\mu\psi_u A_\mu\ , \tag{2.37}$$

$$\mathcal{L}_{d,s} = -\frac{g}{4\cos\theta_W}\overline{\psi}_{d_c,s_c}\gamma^\mu\left(1-\frac{4}{3}\sin^2\theta_W-\gamma_5\right)\psi_{d_c,s_c} Z_\mu - g\frac{1}{3}\sin\theta_W\overline{\psi}_{d_c,s_c}\gamma^\mu\psi_{d_c,s_c} A_\mu\ . \tag{2.38}$$

These are the dominant terms of the Standard Model Lagrangian which enter into the calculation of the proton weak charge and the experimental observable – the parity violating asymmetry in electron-proton scattering. At the tree level (lowest order in perturbation), it is the interference between the amplitudes formed from the photon exchange portion and the Z-boson exchange portion of the Lagrangian that gives rise to the observed asymmetry. However, small higher order corrections to this also include amplitudes involving $W^\pm$ exchange.

Using Eqns. 2.1, 2.14, and 2.15, it is easy to show that

$$\mathcal{L}^{\pm}_{u,d} = -\frac{g}{2\sqrt{2}}\overline{\psi}_u\gamma^\mu(1-\gamma_5)\psi_d W^-_\mu - \frac{g}{2\sqrt{2}}\overline{\psi}_d\gamma^\mu(1-\gamma_5)\psi_u W^+_\mu \ , \tag{2.39}$$

$$\mathcal{L}^{\pm}_{u,s} = -\frac{g}{2\sqrt{2}}\overline{\psi}_u\gamma^\mu(1-\gamma_5)\psi_s W^-_\mu - \frac{g}{2\sqrt{2}}\overline{\psi}_s\gamma^\mu(1-\gamma_5)\psi_u W^+_\mu \ . \tag{2.40}$$

The lepton sector of the charged interaction couples neutrinos and charged leptons and is not included in the current discussion.

2.3 Weak Charges in the Standard Model

The general neutral interactions are usually written down in terms the vector and axial vector coupling constant g_V and g_A, as well as the electromagnetic charge (see Fig. 2.2 for reference):

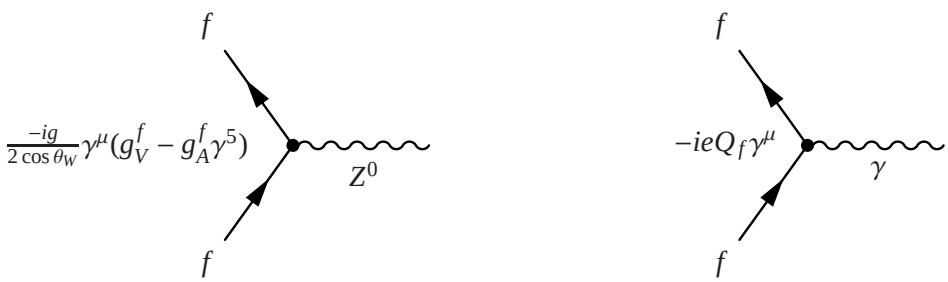

Figure 2.2: The neutral current (NC) and electromagnetic current (EM) interaction vertices.

$$\mathcal{L}_i = \frac{g}{4\cos\theta_W} J^\mu_{Z,i} Z_\mu + J^\mu_{\gamma,i} A_\mu \ , \tag{2.41}$$

where

$$J^\mu_{Z,i} \equiv \overline{\psi}_i\gamma^\mu(g_{V_i} + g_{A_i}\gamma_5)\psi_i \ , \tag{2.42}$$

$$J^\mu_{\gamma,i} \equiv Q_i\overline{\psi}_i\gamma^\mu\psi_i \ . \tag{2.43}$$

The vector and axial vector coupling constant g_V and g_A, along with the electric charge and weak isospin are listed in Table 2.3. To lowest order, the weak charges for the particles in the Standard

	g_V	g_A	Q	I_W^3
e^-	$-1+4\sin^2\theta_W$	1	-1	$-\frac{1}{2}$
u	$1-\frac{8}{3}\sin^2\theta_W$	-1	$\frac{2}{3}$	$\frac{1}{2}$
d, s	$-1+\frac{4}{3}\sin^2\theta_W$	1	$-\frac{1}{3}$	$-\frac{1}{2}$

Table 2.3: The tree level electromagnetic and weak couplings

Model are defined as [Nakamura et al., 2010]

$$C_{1i} = -\frac{1}{2}g_{V,i}\ , \tag{2.44}$$

$$C_{2i} = \frac{1}{2}g_{A,i}\left(1-4\sin^2\theta_W\right)\ . \tag{2.45}$$

The weak charges are listed in Table 2.4, together with the expressions obtained after all radiative corrections are applied (see section 2.6 on radiative corrections). For the purpose of theoretical predictions of the weak charge of the proton, the first three parameters in Table 2.4 dominate. The remaining three parameters are related to the axial vector coupling which is also measured in charged interactions. In terms of the parity violating asymmetry that is being measured, the connection with theory is again the combination of these two types of couplings.

There are two possible combinations including the axial coupling at either vertex (the electron vertex or the quark vertex). As mentioned above, the Q-weak experiment elastically scatters electrons from protons ($e^-p \rightarrow e^-p$). This process is mediated either by the exchange of a virtual Z boson or by photon-exchange as in Fig. 2.3. At low energies (and at tree level) the heavy intermediate vector boson dynamics can be largely ignored, producing an effective four-fermion contact interaction between the electron and a given quark (similar to the four fermion contact interaction for beta decay – the Fermi theory).

Parameter	Tree Level	With Radiative Corrections
C_{1u}	$-\frac{1}{2}(1-\frac{8}{3}\sin^2\theta_W)$	$-\frac{1}{2}\rho'(1-\frac{8}{3}\kappa'\sin^2\theta_W)+\lambda_{1u}$
C_{1d}	$-\frac{1}{2}(-1+\frac{4}{3}\sin^2\theta_W)$	$-\frac{1}{2}\rho'(-1+\frac{4}{3}\kappa'\sin^2\theta_W)+\lambda_{1d}$
C_{1s}	$-\frac{1}{2}(-1+\frac{4}{3}\sin^2\theta_W)$	$-\frac{1}{2}\rho'(-1+\frac{4}{3}\kappa'\sin^2\theta_W)+\lambda_{1s}$
C_{2u}	$-\frac{1}{2}(1-4\sin^2\theta_W)$	$-\frac{1}{2}\rho(1-4\kappa\sin^2\theta_W)+\lambda_{2u}$
C_{2d}	$\frac{1}{2}(1-4\sin^2\theta_W)$	$\frac{1}{2}\rho(1-4\kappa\sin^2\theta_W)+\lambda_{2d}$
C_{2s}	$\frac{1}{2}(1-4\sin^2\theta_W)$	$\frac{1}{2}\rho(1-4\kappa\sin^2\theta_W)+\lambda_{2s}$

Table 2.4: The weak couplings at tree level and with higher order corrections.

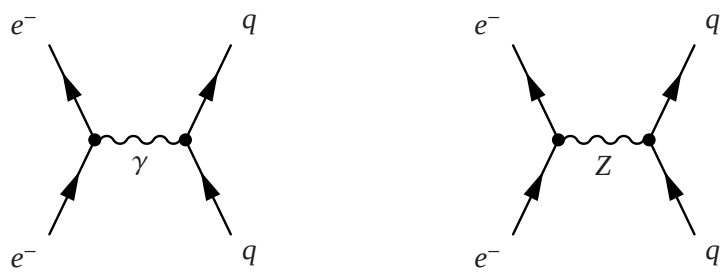

Figure 2.3: The two possible tree-level amplitudes (lowest order in perturbation) contributing to the interaction between an electron and a quark.

In general, the amplitude of Z boson exchange with an individual quark is:

$$M \sim \frac{(i\mathcal{L}_Z)^2}{2} = \left(\frac{-ig}{2\cos\theta_W}\right)^2 J_Z^\nu \left(g_{\nu\mu} - \frac{q_\nu q_\mu}{M_Z^2}\right)\left(\frac{-i}{q^2 - M_Z^2}\right) J_Z^\mu \,. \tag{2.46}$$

In the limit that the four-momentum transfer is small compared to M_Z, i.e., $\mid q^\mu \mid \ll M_Z$, one can neglect the q-dependent terms in the propagator, and the interaction reduces to a four-fermion contact interaction, leading to the effective Hamiltonian density

$$\mathcal{H}_{eff}^{NC} = iM = \frac{g^2}{8M_Z^2\cos\theta_W} J_{Z\mu} J_Z^\mu = \frac{G_F}{\sqrt{2}} J_{Z\mu} J_Z^\mu \tag{2.47}$$

with the Fermi constant defined as

$$\frac{G_F}{\sqrt{2}} = \frac{g^2}{8M_W^2} = \frac{g^2 + g'^2}{8M_Z^2} \,. \tag{2.48}$$

Therefore, the effective neutral current four-fermion operator is

$$\mathcal{L}_{eff}^{NC} = -\mathcal{H}_{eff}^{NC} = -\frac{G_F}{\sqrt{2}} J_{Z\mu} J_Z^{\mu} \,. \tag{2.49}$$

Using Eqn. 2.42, Eqn. 2.49 can be decomposed into Lorentz vector components: $\mathcal{V}(q) \times \mathcal{V}(e)$ and $\mathcal{A}(q) \times \mathcal{A}(e)$, and axial vector components: $\mathcal{V}(q) \times \mathcal{A}(e)$ and $\mathcal{A}(q) \times \mathcal{V}(e)$. A Lorentz vector conserves parity and an axial vector violates parity. Neglecting the parity conserving terms which have no contribution to the parity violating interaction amplitude, and replacing the g_V and g_A couplings with the weak charges, one is left with [Nakamura et al., 2010]:

$$\mathcal{L}_{eq}^{PV} = -\frac{G_F}{\sqrt{2}} \sum_{q=u,d,s} \left[C_{1q}\, \bar{e}\gamma_\mu\gamma_5 e \bar{q}\gamma^\mu q + C_{2q}\, \bar{e}\gamma^\mu e \bar{q}\gamma^\mu\gamma^5 q \right] \,. \tag{2.50}$$

For the purposes of a proton weak charge measurement the axial coupling at the quark vertex needs to be suppressed. This is done in the Q-weak experiment by a particular choice of kinematics including energy and scattering angle (see section 2.5 and section 3.1 on the electron scattering and experimental setup).

2.4 Weak Charges of the Proton and Neutron in the SU(3) Quark Model

As mentioned above, the Q-weak experiment elastically scatters polarized electrons from unpolarized protons. This process is mediated either by exchange of a virtual Z^0 boson or by photon exchange as in Fig. 2.3.

The lowest order effective weak Lagrangian for the parity violation part of an electron-nucleon

interactions is given by

$$\mathcal{L}_{ef}^{PV} = -\frac{G_F}{\sqrt{2}} g_A^e Q_w^f \bar{e}\gamma_\mu\gamma_5 e \bar{f}\gamma^\mu f, \tag{2.51}$$

or in terms of quarks as:

$$\mathcal{L}_{eq}^{PV} = -\frac{G_F}{\sqrt{2}} \bar{e}\gamma_\mu\gamma_5 e \sum_q C_{1q}\, \bar{q}\gamma^\mu q, \tag{2.52}$$

which is Eqn. 2.50, after neglecting the contributions of $\mathcal{A}(q) \times \mathcal{V}(e)$ terms. The coupling in Eqn. 2.51 is the weak charge of the nucleon. In the SU(3) quark model, the nucleon can be decomposed into quarks of the three lightest flavors and the current can be separated into isoscalar, isovector and strange quark current parts. Thus the relation between the weak charge of the nucleon and the quark weak couplings can be obtained through this flavor decomposition. This is discussed in more detail in the references [Musolf et al., 1994], [Commins and Bucksbaum, 1983] and [Greiner and Müller, 2001]. In general, the weak charge of a fermion is then given by

$$Q_W^f = 2g_V^f = 2I_3^f - 4Q_f \sin^2\theta_W, \tag{2.53}$$

where I_3^f is the 3rd component of weak isospin and Q_f is the hypercharge. At tree level, for instance, the neutron has weak charge -1 and the proton's weak charge is

$$Q_W^p = 1 - 4\sin^2\theta_W\ , \tag{2.54}$$

which can be written as a linear combination of the quark couplings introduced above:

$$Q_W^p(\mathrm{SM}) = -2(2C_{1u} + C_{1d})\ . \tag{2.55}$$

The Standard Model coefficients take the values [Nakamura et al., 2010]

$$C_{1u}/2 = -0.09425 \pm 0.00010, \tag{2.56}$$

$$C_{1d}/2 = +0.17070 \pm 0.00008,$$

for up and down quarks, respectively, so that $Q_w^p \approx 0.0712$.

2.5 The Parity Violating Asymmetry in Electron-Proton Scattering

At low energies particles undergo weak interactions much less frequently than they do electromagnetic interactions, because the interaction rates depend on the mass of the exchanged particle – the $W^{\pm}$ and Z^0 bosons are very heavy and this mass effect makes the interaction at low energies weak and short-ranged. It is this short range behavior that makes the weak interaction appear so weak at lower energies. Note however that, at higher energies, or when shorter distances are probed, the weak interaction is stronger than the electromagnetic interaction and a "probing" particle is much more likely to interact weakly than electromagnetically.

The small size of the weak interaction makes precision measurements of electro-weak observables challenging. However, discussed in the previous sections and as outlined in section 2.7, such measurements can provide important insight into new physics or serve as a precise confirmation of the Standard Model.

Jefferson National Laboratory in Newport News, Virginia, USA is the world's premier electron scattering facility. The high beam luminosity and polarization and high (parity) quality electron beam make Jefferson National Laboratory the facility of choice to perform high precision parity experiments with high energy electron beams.

The following sections contain a review of the parity violating electron scattering (PVES) methodology and provides a derivation of the connection between the measurement observable, the parity violating asymmetry, and the weak charge of the proton.

The basic electron-nucleon elastic scattering process is shown in Fig. 2.4. For a relativistic electron, the total energy is $E \simeq p$. So for elastic scattering, by energy and momentum conservation, we have

$$p_3 = \frac{p_1}{1 + \frac{p_1}{M}(1 - \cos\theta)}. \tag{2.57}$$

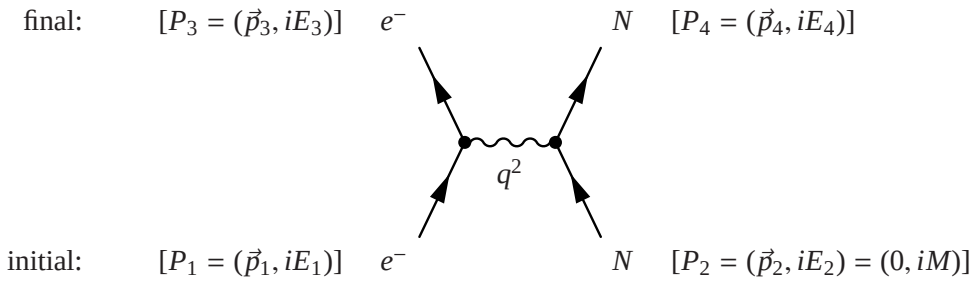

Figure 2.4: Process of an electron e^- elastically scattered from a nucleon N. The kinematic information for the electron and the nucleon is specified by their 4-momenta (a 4-momentum is defined as $P = (iE, \vec{p})$, where $\vec{p}$ is the 3-momentum of the particle and E is its total energy). We define the initial e^- and N 4-momenta as P_1 and P_2, and the final e^- and N 4-momenta as P_3 and P_4. The rest masses for the electron and the nucleon are m and M ($m << M$), respectively. A scattering angle θ (not shown) is defined as the angle between $\vec{p}_3$ and $\vec{p}_1$ in the laboratory frame.

The 4-momentum transfer Q between the incoming and outgoing electron is defined as

$$Q \equiv P_1 - P_3 = \left[i(E_1 - E_3), (\vec{p_1} - \vec{p_3})\right] \ . \tag{2.58}$$

we have

$$Q^2 = -(E_1 - E_3)^2 + (\vec{p_1} - \vec{p_3})^2 \simeq 2E_1E_3(1 - \cos\theta). \tag{2.59}$$

or (in terms of 3-momentum)

$$Q^2 \equiv -q^2 = 4p_1p_3 \sin^2\frac{\theta}{2} \ . \tag{2.60}$$

As mentioned above, the process of an electron scattering from a nucleon is a parity violating process. The parity violation arises through the interference between the weak neutral-current (Z^0 exchange) and the purely electromagnetic contributions to the transition amplitude (i.e., there is an interference term between parity-conserving (PC) and parity-violating (PV) amplitudes due to γ and Z^0 exchange. See the discussion about combinations of the vector and axial vector couplings in section 2.3).

In the Born approximation (tree level), the amplitudes for the electromagnetic and weak neutral

currents are given by:

$$\mathcal{M}_\gamma = -\frac{e^2}{q^2} j^\mu_\gamma J_{\gamma\mu} \,, \tag{2.61}$$

$$\mathcal{M}_Z = -\frac{G_F}{2\sqrt{2}} j^\mu_Z J_{Z\mu} \,. \tag{2.62}$$

From section 2.3 we know that the matrix elements of the electroweak and weak leptonic currents are given by

$$j^\mu_\gamma = \bar{u}_e(p_3)\gamma^\mu u_e(p_1) \,, \tag{2.63}$$

$$j^\mu_Z = \bar{u}_e(p_3)(g^e_V\gamma^\mu + g^e_A\gamma^\mu\gamma_5)u_e(p_1) \,, \tag{2.64}$$

$$J^\mu_\gamma = \bar{u}_N(p_4)\Gamma^\mu_\gamma u_N(p_2) \,, \tag{2.65}$$

$$J^\mu_Z = \bar{u}_N(p_4)\Gamma^\mu_Z u_N(p_2) \,. \tag{2.66}$$

where

$$\Gamma^\mu_\gamma = \gamma^\mu F_1^{\gamma N}(Q^2) + \frac{i\sigma^{\mu\nu}q_\nu}{2M} F_2^{\gamma N}(Q^2) \,, \tag{2.67}$$

$$\Gamma^\mu_Z = \gamma^\mu F_1^{ZN}(Q^2) + \frac{i\sigma^{\mu\nu}q_\nu}{2M} F_2^{ZN}(Q^2) + \gamma^\mu\gamma_5 G_A^{ZN}(Q^2) \,. \tag{2.68}$$

F_1 is the Dirac form factor and F_2 is the Pauli form factor. G_A is the axial form factor. The form factors are introduced to encapsulate the internal structure of the nucleon. The weak couplings in the hadronic current have been absorbed into the form factors. F_1 and F_2 can be related to Sachs Form Factors [Sachs, 1964]:

$$G_E(Q^2) = F_1(Q^2) - \tau F_2(Q^2) \,, \tag{2.69}$$

$$G_M(Q^2) = F_1(Q^2) - F_2(Q^2) \,, \tag{2.70}$$

which are the Fourier transforms of the charge and magnetization of the nucleon. The nucleon form

factors play an important role in the PVES asymmetry expressions. Therefore, it is instructive to give some details here.

In the Standard Model, the nucleons are comprised of quarks and gluons, as well as virtual quark anti-quark pairs. The electromagnetic and weak form factors contain contributions from the various quark flavors in the nucleon. Neglecting heavy quark contributions to the nucleon EM structure[1], the proton and neutron are comprised of (uud) and (udd) and a small fraction of $\overline{u}u$, $\overline{d}d$ and $\overline{s}s$ configurations (u, d and s are the up, down and strange quarks). The form factors can be flavor-decomposed as a sum of flavor form factors weighted by their EM and weak charges respectively as

$$F_{1,2}^{\gamma N} = \sum_j Q_j F_{1,2}^{\gamma j}, \qquad F_{1,2}^{ZN} = \sum_j g_V^j F_{1,2}^{Zj}, \qquad G_A^Z = \sum_j g_A^j G_A^{Zj}, \tag{2.71}$$

where Q^j, g_V^j and g_A^j are the electric, weak vector and axial vector charges for quark flavor j, respectively. $F_{1,2}^{\gamma j}$, $F_{1,2}^{Zj}$ and G_A^{Zj} are the Dirac, Pauli and axial form factors for quark flavor j. The vector currents for individual quark flavors can be made identical in the EM and neutral currents by factoring out the charges. Therefore one can use F_1^j, F_2^j which are common to $J_\gamma^{\mu,N}$ and $J_Z^{\mu,N}$. Eqns. 2.65 and 2.66 can then be rewritten as a sum of the underlying quarks currents as

$$J_\gamma^\mu = \overline{u}_N(p_4) \sum_j Q_j \left[\gamma^\mu F_1^j + \frac{i\sigma^{\mu\nu} q_\nu}{2M} F_2^j \right] u_N(p_2), \tag{2.72}$$

$$J_Z^\mu = \overline{u}_N(p_4) \sum_j \left[g_V^j \left(\gamma^\mu F_1^j + \frac{i\sigma^{\mu\nu} q_\nu}{2M} F_2^j \right) + g_A^j G_A^j \gamma^\mu \gamma_5 \right] u_N(p_2), \tag{2.73}$$

Using the Table 2.3, the vector form factors in Eqn. 2.71 can be written out explicitly as

$$F_{1,2}^\gamma = \frac{2}{3} F_{1,2}^u - \frac{1}{3} \left(F_{1,2}^d + F_{1,2}^s \right), \tag{2.74}$$

$$F_{1,2}^Z = \left(1 - \frac{8}{3} \sin^2 \theta_W \right) F_{1,2}^u - \left(1 - \frac{4}{3} \sin^2 \theta_W \right) \left(F_{1,2}^d + F_{1,2}^s \right), \tag{2.75}$$

[1]The contributions of heavier quarks are negligible as the energy scale of Quantum Chromodynamics (QCD), Λ_{QCD} is 200 MeV, and the next lightest quark after the strange quark (with a mass of 95 MeV/c^2) on the mass scale is the charm with a mass of 1.25 GeV/c^2.

or equivalently,

$$G_{E,M}^{\gamma,N} = \frac{2}{3}G_{E,M}^{u} - \frac{1}{3}\left(G_{E,M}^{d} + G_{E,M}^{s}\right) , \tag{2.76}$$

$$G_{E,M}^{Z,N} = \left[1 - \frac{8}{3}\sin^2\theta_W\right]G_{E,M}^{u} - \left[1 - \frac{4}{3}\sin^2\theta_W\right]\left(G_{E,M}^{d} + G_{E,M}^{s}\right), \tag{2.77}$$

where $G_{E,M}^{u}$, $G_{E,M}^{d}$ and $G_{E,M}^{s}$ are the electromagnetic form factors corresponding to the u, d and s quarks in the nucleon. And the axial form factor in Eqn. 2.71 can be written out explicitly as

$$G_A^Z = -G_A^u + G_A^d + G_A^s. \tag{2.78}$$

Eqns. 2.76 – 2.77 are generic for the nucleons. To apply them to the proton or neutron, one can add nucleon species superscripts (p or n) on the form factors. Similar to the nucleon Sachs form factors, the form factors for a given quark flavor, multiplied by the quark's electric charge, correspond to the Fourier transforms for the charge and magnetization densities (in the Breit frame – center of mass frame) of this quark flavor inside the nucleon. One should note that each flavor form factor includes both the quark and anti-quark contributions. For nucleons the u and d flavor form factors contain contributions from both the valence and sea quarks, whereas the s flavor form factors arise purely from the $s\bar{s}$ sea.

Charge symmetry of the strong interaction [2] implies that:

$$G_{E,M}^{u,p} = G_{E,M}^{d,n} , \qquad G_{E,M}^{d,p} = G_{E,M}^{u,n} , \qquad G_{E,M}^{s,p} = G_{E,M}^{s,n} . \tag{2.79}$$

where the s flavor form factor is the same for both neutron and proton. The breaking of these equalities is generally at the level of 1% or less [Miller, 1998]. Given the experimental precision, charge symmetry violation can be generally neglected. So neglecting charge symmetry violation,

[2] A good symmetry of the strong interactions is charge symmetry, which states that in exchanging the $u(\bar{u})$ and $d(\bar{d})$ quarks, a proton becomes a neutron, and vice versa. In other words, the (u, d) quarks in the proton are in the same wave function as (d, u) quarks in the neutron, and the strange quark wave functions of the proton and neutron are identical.

Eqns. 2.76 - 2.77 can be rewritten for the proton and the neutron as:

$$G_{E,M}^{\gamma,p} = \frac{2}{3}G_{E,M}^{u} - \frac{1}{3}\left(G_{E,M}^{d} + G_{E,M}^{s}\right) , \tag{2.80}$$

$$G_{E,M}^{\gamma,n} = \frac{2}{3}G_{E,M}^{d} - \frac{1}{3}\left(G_{E,M}^{u} + G_{E,M}^{s}\right) , \tag{2.81}$$

$$G_{E,M}^{Z,p} = \left[1 - \frac{8}{3}\sin^2\theta_W\right]G_{E,M}^{u} - \left[1 - \frac{4}{3}\sin^2\theta_W\right]\left(G_{E,M}^{d} + G_{E,M}^{s}\right) , \tag{2.82}$$

$$G_{E,M}^{Z,n} = \left[1 - \frac{8}{3}\sin^2\theta_W\right]G_{E,M}^{d} - \left[1 - \frac{4}{3}\sin^2\theta_W\right]\left(G_{E,M}^{u} + G_{E,M}^{s}\right) . \tag{2.83}$$

The flavor form factors are normalized at $Q^2 = 0$. The charges of the quarks are factored out, the electric flavor form factors represent the net numbers of the quarks. Therefore we have

$$G_E^u(0) = 2, \quad G_E^d(0) = 1, \quad G_E^s(0) = 0. \tag{2.84}$$

These lead to the weak charge of the proton and neutron:

$$Q_W^p = G_E^{Z,p}(0) = 1 - 4\sin^2\theta_W, \tag{2.85}$$

$$Q_W^n = G_E^{Z,n}(0) = -1. \tag{2.86}$$

The electron scattering cross-section is given by [Martin and Shaw, 2008]

$$\frac{d\sigma}{d\Omega} = \left(\frac{\alpha}{4MQ^2}\frac{E_3}{E_1}\right)^2 |\mathcal{M}|^2 , \tag{2.87}$$

where the square of the scattering amplitude is given by

$$|\mathcal{M}|^2 = |\mathcal{M}_\gamma + \mathcal{M}_Z|^2 = |\mathcal{M}_\gamma|^2 + 2\Re(\mathcal{M}_\gamma^*\mathcal{M}_Z) + |\mathcal{M}_Z|^2 . \tag{2.88}$$

$|\mathcal{M}_\gamma|^2$ is the electromagnetic scattering probability, resulting only from photon exchange. $|\mathcal{M}_Z|^2$ is the weak scattering probability resulting only from Z-boson exchange. Due to the large mass of the Z-boson, this term is very small compared to the other terms and can be neglected. $\mathcal{M}_\gamma^*\mathcal{M}_Z$ and

$\mathcal{M}_\gamma \mathcal{M}_Z^*$ are the interference terms and give rise to the parity violating signal, due to the presence of the axial vector coupling in the $\mathcal{M}_Z$ amplitudes.

The cross-section for electromagnetic elastic scattering of relativistic electrons from a nucleon (accounting only for one photon exchange, but see reference [Blunden et al., 2005] for the discussion about two photon exchanges) is given by

$$\frac{d\sigma}{d\Omega} = \left(\frac{\alpha}{4MQ^2}\frac{E_3}{E_1}\right)^2 |\mathcal{M}_\gamma|^2 \,. \tag{2.89}$$

which, in terms of the electric and magnetic form factors of the nucleon, is given by

$$\frac{d\sigma}{d\Omega} = \left(\frac{d\sigma}{d\Omega}\right)_{Mott}\left[\left(\frac{G_E^2 + \tau G_M^2}{1+\tau}\right) + 2\tau G_M^2 \tan^2\frac{\theta}{2}\right], \tag{2.90}$$

where

$$\tau \equiv \frac{Q^2}{4M^2} \tag{2.91}$$

and

$$\left.\frac{d\sigma}{d\Omega}\right|_{Mott} = \frac{(\hbar c\alpha)^2}{4E_0^2\sin^4(\theta/2)}\left(\frac{E'}{E_0}\right)\cos^2(\theta/2) = \frac{(\hbar c\alpha)^2\cos^2(\theta/2)}{4E_0^2\sin^4(\theta/2)[1+2\frac{E_0}{M}\sin^2(\theta/2)]} \tag{2.92}$$

(α is the fine-structure constant).

The differential cross-section $\left.\frac{d\sigma}{d\Omega}\right|_{Mott}$ describes the cross-section for electrons scattering from a point-like spin-0 target with recoil correction. The Sach form factors G_E and G_M are functions of momentum transfer and are very well determined by experiment [Qattan et al., 2005]. They describe the static distribution and motion of electric charge inside the nucleon, i.e., they provide a description of the electromagnetic structure of the nucleon. In the limit as $Q^2 \to 0$ (low energy limit), G_E is equal to the normalized electric charge and G_M coincides with the magnetic moment. The differential cross-section $\frac{d\sigma}{d\Omega}$ depends on the fourth power of the electric charge since it is proportional to α^2, and the electromagnetic coupling constant α is proportional to e^2. The form factors G_E and G_M determined from "ordinary" (parity-conserving) electron scattering should really

be denoted as G_E^γ and G_M^γ to emphasize that they are electromagnetic structure functions probed by photon exchange.

The interference term in Eqn. 2.88 can be isolated by measuring the PV cross-section asymmetry in elastic scattering. For a parity violation experiment, the initial beam is defined by two properties: the particle momentum and the angular momentum. Both relative (or orbital) angular momentum with respect to the target particle as well as intrinsic angular momentum are important. However, while every effort is made in the experiment to reduce the former to as close to zero as possible, the latter is maximized in a controlled way. The intrinsic angular momentum, or spin, refers to the magnetic moment of the particle and is mostly longitudinal for relativistic particles; meaning that it is oriented either along the direction of particle momentum (right-handed helicity) or against the direction of particle momentum (left-handed helicity). Helicity does not change sign under a parity transformation, while momentum does. So a straightforward way to "prepare" a parity transformation is to reverse the helicity of a particle while keeping its momentum constant. For this to be efficient, a goal of the experimental setup is to have the beam of electrons maximally polarized (prepared in states of well defined helicity at any given point in time), while the target particles are prepared with zero average polarization.

The parity-violating asymmetry A_{PV} is defined as the difference between the number of scattered electrons for one helicity state and the number of electrons scattered for the opposite helicity state, divided by the sum of the two contributions:

$$A_{PV} = \frac{\left(\frac{d\sigma}{d\Omega}\right)_R - \left(\frac{d\sigma}{d\Omega}\right)_L}{\left(\frac{d\sigma}{d\Omega}\right)_R + \left(\frac{d\sigma}{d\Omega}\right)_L} , \tag{2.93}$$

where the subscript "L" and "R" refer to the electron beam helicity.

The weak neutral amplitude $\mathcal{M}_Z$ can be decomposed into a parity violating part and a parity

conserving part, i.e., $\mathcal{M} = \mathcal{M}_Z^{PC} + \mathcal{M}_Z^{PV}$, thus

$$A_{PV} = \frac{2\mathcal{M}_\gamma^* \mathcal{M}_Z^{PV}}{|\mathcal{M}_\gamma|^2 + 2\mathcal{M}_\gamma^* \mathcal{M}_Z^{PV} + |\mathcal{M}_Z^{PV}|^2} \sim \frac{2\mathcal{M}_\gamma^* \mathcal{M}_Z^{PV}}{|\mathcal{M}_\gamma|^2} , \tag{2.94}$$

where the parity conserving part is canceled out in the amplitude difference. This leads to

$$A_{PV} = -\left(\frac{G_F Q^2}{4\sqrt{2}\pi\alpha}\right) \frac{g_A^e \left(\varepsilon G_E^{\gamma N} G_E^{ZN} + \tau G_M^{\gamma N} G_M^{ZN}\right) + g_V^e \varepsilon\prime G_M^{\gamma N} G_A^{ZN}}{\varepsilon \left(G_E^{\gamma N}\right)^2 + \tau \left(G_M^{\gamma N}\right)^2} , \tag{2.95}$$

where

$$\epsilon = [1 + 2(1+\tau)\tan^2(\theta/2)]^{-1}, \qquad \epsilon' = [\tau(1+\tau)(1-\epsilon^2)]^{1/2} \tag{2.96}$$

are kinematical quantities with θ the electron scattering angle in the target rest frame. The quantity A_{PV} is the asymmetry in the cross section for elastic scattering of longitudinally polarized electrons with positive and negative helicities, from an unpolarized nucleon target.

Eqn. 2.95 is valid for all nucleons. For a proton target [3], this in turn can be expressed, by using the tree level electron vector and axial couplings ($g_V = -1 + 4\sin^2\theta_W$, and $g_A = 1$), as:

$$A_{PV} = -\left(\frac{G_F Q^2}{4\sqrt{2}\pi\alpha}\right) \frac{\epsilon G_E^{\gamma p} G_E^{Zp} + \tau G_M^{\gamma p} G_M^{Zp} - (1 - 4\sin^2\theta_W)\epsilon' G_M^{\gamma p} G_A^{Zp}}{\epsilon (G_E^{\gamma p})^2 + \tau (G_M^{\gamma p})^2} . \tag{2.97}$$

The Sachs weak neutral form factors $G_E^{Zp}(Q^2)$ and $G_M^{Zp}(Q^2)$ are introduced here to describe the proton's electric and magnetic structure as probed by the Z boson. The $Q^2 \to 0$ limit of $G_E^Z(Q^2)$ gives the proton's weak charge.

Eqn. 2.97 can be expressed in terms of the electric and magnetic form factors of the proton ($G_E^{\gamma p}$ and $G_M^{\gamma p}$), the electric and magnetic form factors of the neutron ($G_E^{\gamma n}$ and $G_M^{\gamma n}$), the strange electric and magnetic form factors (G_E^s and G_M^s), the neutral weak axial form factor of the proton (G_A^{Zp}) by

[3] Use of a proton target offers the simplest possible system on which to perform a low-energy search for new neutral current physics in the semileptonic sector. As in the case of neutron β-decay, a combination of measurements (lifetime and asymmetry parameter) allow one to perform an extraction of the charged current vector coupling constant with minimal hadronic complications.

using the relations obtained from Eqns. 2.80 – 2.83:

$$G_E^{Zp} = (1 - 4\sin^2\theta_W)G_E^{\gamma p} - G_E^{\gamma n} - G_E^s \,, \tag{2.98}$$

$$G_M^{Zp} = (1 - 4\sin^2\theta_W)G_M^{\gamma p} - G_M^{\gamma n} - G_M^s \,, \tag{2.99}$$

$$G_A^{Zp} = -G_A^p + G_A^s \,. \tag{2.100}$$

One can then recast the asymmetry in the form

$$A_{PV}(\vec{e}, p) = -\frac{G_F Q^2}{4\sqrt{2}\pi\alpha}\left(A_p + A_n + A_s + A_e\right) \tag{2.101}$$

with

$$A_p = 1 - 4\sin_W^\theta = Q_W^p \,, \tag{2.102}$$

$$A_n = Q_W^n \frac{\epsilon G_E^{\gamma p} G_E^{\gamma m} + \tau G_M^{\gamma p} G_M^{\gamma n}}{\epsilon (G_E^{\gamma p})^2 + \tau (G_M^{\gamma n})^2} \,, \tag{2.103}$$

$$A_s = Q_W^s \frac{\epsilon G_E^{\gamma p} G_E^s + \tau G_M^{\gamma n} G_M^s}{\epsilon (G_E^{\gamma p})^2 + \tau (G_M^{\gamma p})^2} \,, \tag{2.104}$$

$$A_e = Q_W^e \frac{\epsilon' G_A^{Zp} G_M^{\gamma p}}{\epsilon (G_E^{\gamma p})^2 + \tau (G_M^{\gamma p})^2} \,, \tag{2.105}$$

where Q_W^p, Q_W^n, Q_W^s, and Q_W^e are the proton weak charge, neutron weak charge, strange weak charge and electron weak charge, respectively.

The asymmetry (Eqn. 2.97) can therefore be rewritten as:

$$A_{PV} = \frac{-G_F}{4\pi\alpha\sqrt{2}}[Q^2 Q_W^p + F^p(Q^2, \theta)] \,. \tag{2.106}$$

where F^p is a Q^2- and θ-dependent form factor, combining all hadronic contributions to the asymmetry [Musolf et al., 1994] [Erler et al., 2003]. At low momentum transfer (forward-angle scattering

where $\theta \to 0$, $\epsilon \to 1$ and $\tau \ll 1$), the above asymmetry equation can be rewritten as:

$$A_{PV}(\vec{e}, p) = \frac{-G_F}{4\pi\alpha\sqrt{2}}\left[Q^2 Q_W^p + Q^4 B(Q^2)\right]. \tag{2.107}$$

$B(Q^2)$ is a hadronic form factor term that contains the form factors G_E^γ, G_M^γ and G_E^Z, G_M^Z. Note that, at low momentum transfer, the Q_W^p term dominates and that under these kinematic conditions, the asymmetry A_{PV} is proportional to $Q^2 Q_W^p$. Therefore, neglecting radiative corrections, the leading term in the equation is simply $Q_W^p = 1 - 4\sin^2\theta_W$. Thus, if the parity-violating asymmetry A_{PV} and momentum transfer Q^2 are measured very precisely, and the hadronic form factors are extrapolated from other experimental results (for details, see reference [Young et al., 2007]), the proton's weak charge and hence the weak mixing angle can be determined.

2.6 Electro-Weak Radiative Corrections and the Running of the Weak Mixing Angle

As shown in the previous sections, the value of the weak mixing angle ultimately determines the strength of the weak interaction. However, as mentioned above and shown in Fig. 2.8, this value is not constant. To gain an understanding of why the value of the weak mixing angle (and therefore the strength of the weak interaction) varies with energy, it is instructive to first consider the analogous effect in the electromagnetic interaction.

The strength of the electromagnetic interaction is parameterized in terms of the fine structure constant α, since it is directly related to the electron charge – the coupling constant in the quantum electrodynamics (QED) context, and $\alpha = e^2/4\pi$. At low energy, corresponding to atomic distance scales and above, the strength of the fine structure constant is measured to be $1/\alpha = 137.035999084(51)$ [Hanneke et al., 2008]. However, it has been experimentally verified that the value of α changes as the electromagnetic interaction is probed at increasingly higher energies (e.g. $1/\alpha = 127.4 \pm 2.1$ at 193 GeV) [Abbiendi et al., 2004]. This variation is consistent with

theory and is explained in terms of radiative corrections in QED. In QED, the interaction between particles is described in terms of virtual photon exchange. Quantum mechanically, the amplitude for observed interactions is a sum of all amplitudes for indistinguishable (not directly observable) processes, which includes all possible combinations of electron-positron pair loops as a result of virtual pair creation and annihilation. Each additional loop corresponds to a higher order in perturbation and is referred to as the next order in radiative correction. The combination to all orders in perturbation gives the interaction strength an energy dependence and produces the theoretical prediction for the "running" of the fine structure constant (see references [Mandl and Shaw, 1984] [Bjorken and Drell, 1998]). Conceptually, this process may be envisioned as virtual photons forming a photon cloud around the particle since they are continually emitted and reabsorbed. These are then envisioned to temporarily transform into virtual electron-positron pairs that will be polarized in the field between the interacting charged particles (the so-called "vacuum polarization" effect).

The polarized electrons and positrons behave like a dielectric and produce a screening effect on the bare particle charge. The screening effect is probed to a different extent at different distances from the bare particle and thus leads to an energy dependent interaction strength. Radiative corrections would account for the variation of the effective QED coupling $\alpha(\mu^2)$ with energy scale μ, to high precision, using perturbation theory techniques.

The same property is observed for the strong interaction, where the coupling strength varies with energy due to gluons and quark anti-quark pair creation and annihilation. However, contrary to the photon, the gluon field is a Yang-Mills field (meaning gluons carry a charge and can therefore interact with each other) and the radiative corrections now also include gluon loops in addition to fermion (quark) loops. Together with the fact that gluons, as described in the Standard Model, are massless (like the photon) this leads to asymptotic freedom, which means that, at very high energies, or small probed distance, quarks are quasi-free and perturbation theory can be used at high energies only (see a discussion in reference [Gross and Wilczek, 1973]).

In the weak interaction the intermediate vector bosons are described by Yang-Mills fields as well and the radiative corrections here also include boson loops, as well as fermion loops. However,

in this case the bosons are massive and perturbation theory can be used to all orders. In addition one now also has diagrams, in which both one or more photons and one or more heavy W or Z bosons are exchanged in the same amplitude. One such example is the so-called γZ-box diagram as shown in Fig. 2.5. Several classes of radiative corrections to electroweak quantities are summarized by Langacker in reference [Langacker, 2009] where typical diagrams are given, as shown in Fig. 2.5, 2.6 and 2.7.

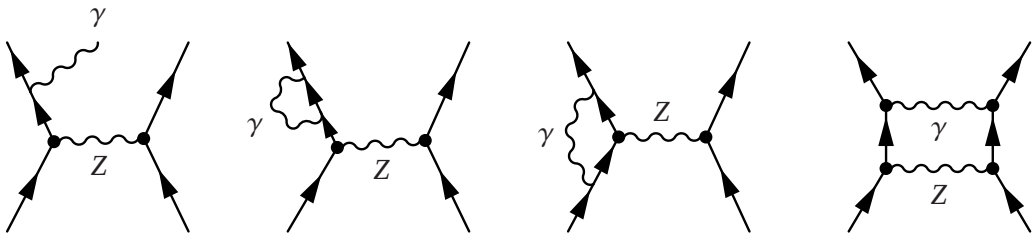

Figure 2.5: Typical reduced QED corrections to Z exchange. Vacuum polarization diagrams are not included.

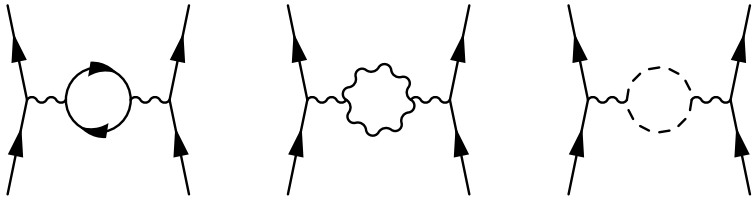

Figure 2.6: Typical one-loop self-energy diagrams, also known as vacuum polarization or oblique diagrams.

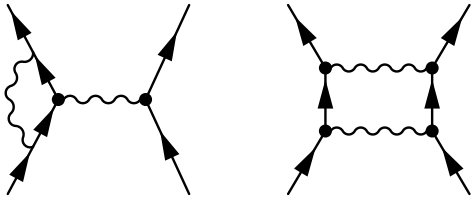

Figure 2.7: Electroweak vertex and box diagrams, involving W and Z bosons.

The weak mixing angle is uniquely related to neutral (Z^0) boson currents and the radiative corrections related to γ-Z amplitudes in particular cause the change of the weak mixing angle with respect to energy (see reference [Erler and Ramsey-Musolf, 2005b]). This phenomenon is known as the "running of the weak mixing angle", which is a prediction made by the electroweak theory of the Standard Model.

The curve in Fig. 2.8 shows the variation of the weak mixing angle with energy scale μ, together with the existing world data, verifying the running and some of the proposed future measurements. High energy measurements in electron-positron collider experiments at the Z-pole fix the value of the weak mixing angle at the energy corresponding to the mass of the Z boson. The deviation of the weak mixing angle from this value with energy is a result of the radiative corrections discussed above. The turning point of the curve corresponds to the momentum transfer $Q = M_W$. The Standard Model predicts a shift of +0.007 of $\sin^2\theta_W$ at low momentum transfer with respect to the Z-pole best fit value of 0.23119 ± 0.00014.

Accurate measurements of the weak mixing angle at various energies therefore provide a stringent test of the Standard Model. Electro-weak radiative corrections are calculated to high precision and the line thickness in Fig. 2.8 represents the uncertainty of the theoretical calculations. There continues to be significant effort in further improving the uncertainty on these calculations (see references [Sibirtsev et al., 2010] and [Gorchtein and Horowitz, 2009]). Therefore, if the precision in a weak charge measurement is high enough and theoretical uncertainties do not pose a barrier to interpretability, a statistically significant deviation between the prediction and experimental value will indicate possible "new physics" that is not included in the current model.

There are several ways in which the Standard Model parameters can be represented in the presence of higher-order radiative corrections. The authors of the references [Marciano and Sirlin, 1983] [Marciano and Sirlin, 1984] who computed the $\gamma(Z\gamma)$ contributions at $Q^2 = 0$ parameterize the electroweak radiative effects in terms of parameters ρ, κ and λ such that the couplings of fermions in the

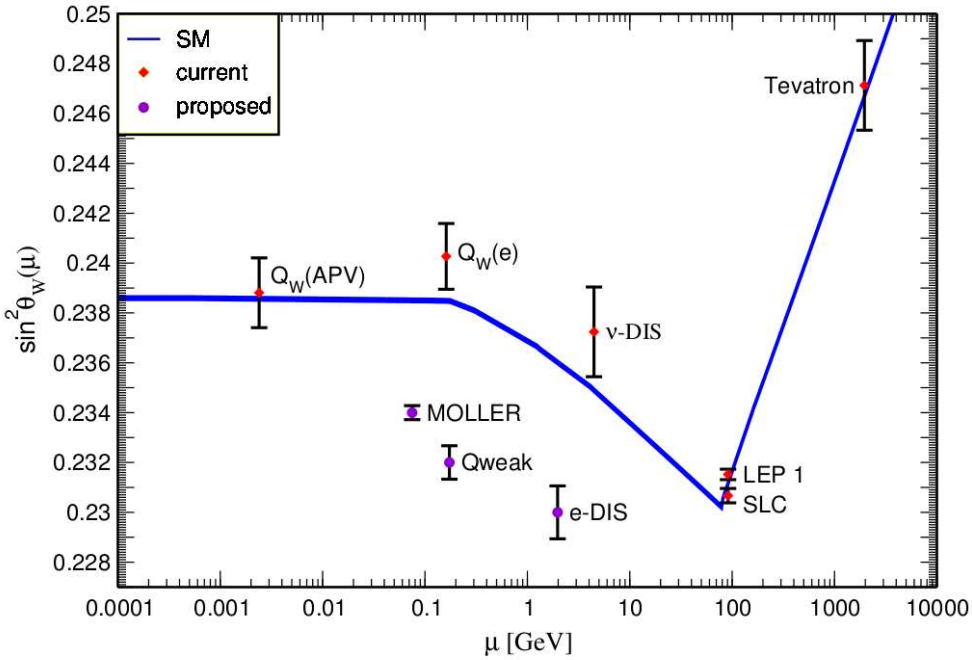

Figure 2.8: Energy scale dependence of the weak mixing angle $\sin^2\theta_W$ defined in the modified minimal subtraction ($\overline{\text{MS}}$) scheme [Erler and Ramsey-Musolf, 2005b], showing the current situation and ongoing Q-weak experiment and other proposed experiments.

presence of higher order corrections can be redefined as:

$$Q_W^f = \rho(2I_3^f - 4Q_f\kappa\sin^2\theta_W) + \lambda_f \ . \tag{2.108}$$

At the tree level, one has $\rho = 1 = \kappa$ and $\lambda_f = 0$. Including the radiative corrections, the proton's weak charge takes the form [Erler et al., 2003]:

$$Q_W^p = [\rho_{NC} + \Delta_e][1 - 4\sin^2\hat{\theta}_W + \Delta_e'] + \Box_{WW} + \Box_{ZZ} + \Box_{\gamma Z}. \tag{2.109}$$

The theoretical uncertainties of the proton's weak charge (Q_W^p) determination from different

source	$\Delta Q_W^p / Q_W^p$	reference
uncertainty of $\sin^2\theta_W$ determined from experiments at the Z-pole ($\Delta \sin^2\theta_W(M_Z)$)	$\pm 0.8\%$	[Erler et al., 2003]
hadronic contributions to the running of $\sin^2\theta_W$ ($\Delta \sin^2\theta_W(Q)_{\text{hardonic}}$)	$\pm 0.4\%$	[Erler et al., 2003]
charge symmetry	0	[Erler et al., 2003]
strong corrections to γZ-box graphs	$\pm 0.7\%$	[Erler et al., 2003]
	$\sim 7\%$	[Gorchtein and Horowitz, 2009]
	$6.6^{+1.5}_{-0.6}\%$	[Sibirtsev et al., 2010]
	$8.0 \pm 1.3\%$	[Rislow and Carlson, 2010]
	$7.6 \pm 2.8\%$	[Gorchtein et al., 2011]
strong corrections to WW-box graphs	$\pm 0.1\%$	[Erler et al., 2003]
strong corrections to ZZ-box graphs	$\pm 0.01\%$	[Erler et al., 2003]

Table 2.5: Theoretical uncertainties for the determination of the proton's weak charge in the kinematics of the Q-weak experiment. The radiative corrections and the corresponding calculation uncertainties of radiative corrections are compared to the value of the proton's weak charge of $Q_W^p = 0.0713 \pm 0.0008$ that includes Standard Model contributions at tree level and one-loop radiative corrections.

source are summarized in Table 2.5. As mentioned before, Q_W^p will be determined by measuring the PV asymmetry and beyond the tree level, the PV asymmetry too receives corrections from higher order radiative effects, such as vertex corrections, wave function renormalization, vacuum polarization, and inelastic bremsstrahlung, which are well known and included in standard data analyses [Tjon et al., 2009]. The calculation in reference [Erler et al., 2003] showed that the effects of strong interaction corrections to the WW and ZZ box graphs are well below the one percent level. Less well determined are radiative corrections arising from the interference of Born and TBE (two boson exchange) diagrams, both electromagnetic ($\gamma\gamma$) and electroweak (γZ) [Tjon et al., 2009]. There are large discrepancies of current calculations for the γZ-box graphs (as seen in the Table

2.5). For example, the most recent calculation by [Gorchtein et al., 2011] gave a correction to the asymmetry equivalent to a shift in the proton weak charge of (0.0054 ± 0.0020) at the kinematics of the Q-weak experiment. The shift changes the Q_W^p value by 7.6%; the latter uncertainty leads to a relative uncertainty of 2.8% in the determination of the proton's weak charge. They obtain a new Standard Model prediction for the Q_W^p in the kinematics of the Q-weak experiment of $(0.0767 \pm 0.0008 \pm 0.0020_{\gamma Z})$.

2.7 Q-weak and New Physics beyond the Standard Model

Precise measurements of the running of the weak mixing angle at various energies constitute tests for physics beyond the Standard Model, as far as the current theory makes precise predictions of the measured observable. To test the running of the weak mixing angle, one can conduct measurements of observables which are related and sensitive to changes in the weak mixing angle. To date, the running of the weak mixing angle, as predicted by the Standard Model, has been confirmed, but not at high precision. Compared to theoretical predictions, the running is not particularly well constrained experimentally, as seen in Fig. 2.8.

The measurements performed at LEP [4] [Abreu, 1993] [Ackerstaff, 1997] [Abbiendi et al., 2006] and SLC [5] [Abe et al., 2000a] [Abe et al., 2000b] [Abe et al., 2001] near the Z-pole are the most precise measurements of the weak mixing angle. The other three measurements at lower energy, APV (atomic parity violation), Q_W^e (SLAC E-158) Møller (electron-electron) scattering, and ν-DIS (NuTeV, deep inelastic neutrino-nucleus scattering), test the "running" with roughly the same large uncertainties on the extracted value of $\sin^2\theta_W$. The APV experiment [Bennett and Wieman, 1999] measured the weak charge of the Cesium nucleus ($Q_W(Cs)$) by exploiting parity-violating effects in atomic Cesium, then extracting the weak mixing angle at very low Q^2. However, the reliability of the result for $\sin^2\theta_W$ is subject to theoretical atomic structure uncertainties [Ramsey-Musolf, 1999]. A recent high-precision calculation of parity violation in a cesium atom was carried out by Porsev

[4] The Large Electron-Positron Collider at CERN (European Laboratory for Particle Physics at Geneva, Switzerland).
[5] The Stanford Linear Collider.

et. al. [Porsev et al., 2009], who combine previous measurements with calculations and extract the weak charge of the 133-Cs nucleus, $Q_W(Cs) = -73.16(29)_{\text{expt}}(20)_{\text{theor}}$, reducing theoretical uncertainty by a factor of 2 compared to previous evaluations. The NuTeV experiment [Zeller et al., 2002] (done at Fermilab) extracts the value of $\sin^2\theta_W$ at $\mu \sim 3$ GeV from deep inelastic scattering of neutrinos from a BeO target. The result has a slightly greater precision than the one from atomic parity violation, but the contributions and uncertainties from the radiative corrections, and possible isospin symmetry violation can not be clearly interpreted yet [Londergan and Thomas, 2005]. The E-158 experiment at SLAC [Anthony et al., 2004] [Anthony et al., 2005], which reports a measurement of the weak charge of the electron (Q_W^e), is a parity violating Møller scattering (electron-electron) experiment at low momentum transfer ($Q^2 = 0.026$ GeV^2). The extracted value of $\sin^2\theta_W$, within statistical and systematic uncertainties, is consistent with the Standard Model expectation. Due to this being a pure leptonic measurement, it has a very clean interpretation, since hadronic uncertainties are largely absent. However, the experimental uncertainty is still too large to signal new physics or put significant constraints on the current model by itself (the implications of this measurement are discussed in reference [Czarnecki and Marciano, 2000]).

The current situation motivates the preparation of new higher precision experiments to determine $\sin^2\theta_W$ at low energy to complement the Z-pole measurements. The Q-weak collaboration at Thomas Jefferson National Accelerator Facility is currently running an experiment which will precisely measure the parity violating asymmetry in elastic electron-proton scattering to infer the proton's weak charge and hence the weak mixing angle [Nakamura et al., 2010] [Page et al., 2006] [Qweak-Collaboration, 2004]. As a fundamental property of the Standard Model, the proton's weak charge has never been precisely measured. The Q-weak experiment will provide the first precise measurement of the proton's weak charge.

To lowest order in perturbation theory, protons and electrons have equal and opposite weak charges: $Q_W^{p,e} = \pm(1 - 4\sin^2\theta_W)$. This implies, for the extraction of $\sin^2\theta_W$ from the weak charge

measurements, that the uncertainty in the weak mixing angle is:

$$\Delta\left(\sin^2\theta_W\right) = \frac{1}{4}\Delta Q_W^{p,e} = \frac{1}{4}\left(\frac{\Delta Q_W^{p,e}}{Q_W^{p,e}}\right)Q_W^{p,e} = \frac{1}{4}\left(\frac{\Delta Q_W^{p,e}}{Q_W^{p,e}}\right)\left(1-4\sin^2\theta_W\right). \tag{2.110}$$

The value of the weak mixing angle, $\sin^2\theta_W$, is numerically close to 0.23, which means that $\Delta(\sin^2\theta_W)/\sin^2\theta_W \simeq 0.087(\Delta Q_W^{p,e}/Q_W^{p,e})$ and small changes in $\sin^2\theta_W$ make a big difference on Q_W^p. Consequently, the factor 1/4 makes a weak charge measurement on the proton or electron particularly sensitive to deviations arising from new physics[6]. In contrast, the APV experiment measures $Q_W(Z,N)$ for a heavy atom; due to the dominant neutron contributions to the atom's weak charge, the observable Q_W^p is suppressed; the required experimental precision for the APV is about an order of magnitude larger than needed for directly measuring the weak charge of proton or electron to extract $\sin^2\theta_W$ to comparable accuracy. Moreover, the theoretical uncertainties in the interpretation of parity violating elastic scattering at low Q^2 are small, which makes the parity violating elastic scattering asymmetry interpretable as a new physics probe.

Comparing with the SLAC E-158 "e-e" scattering experiment, the proposed Q_{Weak}^p "e-p" scattering experiment will be performed at similar momentum transfer, but with higher precision, and significantly smaller statistical and systematic uncertainties. The Q-weak experiment aims to reach a 4% measurement of Q_W^p, which corresponds to an uncertainty of $\sim$ 0.0008 in $\sin^2\theta_W$ ($\Delta(\sin^2\theta_W)/\sin^2\theta_W \sim 0.35\%$); the E-158 experiment has a combined statistical and systematic uncertainty of $\sim$ 9%, which corresponds to an uncertainty of $\sim$0.0018 in $\sin^2\theta_W$ ($\Delta(\sin^2\theta_W)/\sin^2\theta_W \sim$ 0.79%) [Anthony et al., 2005].

The sensitivity to new physics in terms of mass/coupling ratios can be estimated by adding a new contact term to the electron quark Lagrangian (Eqn. 2.52). New physics is then incorporated by adding to the Standard Model Lagrangian a term of the form [Erler et al., 2003]:

$$\mathcal{L}_{NEW}^{PV} = \frac{g^2}{4\Lambda^2}\bar{e}\gamma_\mu\gamma_5 e\sum_f h_V^q\,\bar{q}\gamma^\mu q, \tag{2.111}$$

[6]It should be noted, however, that there are different radiative corrections to Q_W^p and Q_W^e. As a result, the measured values are quite different at low Q^2 ($Q_W^p = 0.0713 \pm 0.0008$ and $Q_W^e = -0.0403 \pm 0.0053$ [Nakamura et al., 2010].

where g is a new coupling constant, which sets the strength of the coupling between quarks, leptons, and possible new gauge particles with masses up to Λ. The quark-specific coefficients h_V^q are proportional to the weak charges associated with possible new weak physics. So the full Lagrangian including the Standard Model and new physics can be written as:

$$\mathcal{L}^{\mathrm{PV}} = \mathcal{L}^{\mathrm{PV}}_{\mathrm{SM}} + \mathcal{L}^{\mathrm{PV}}_{\mathrm{NEW}} \,. \tag{2.112}$$

Including new physics, the measured weak charge is related to the theory prediction according to

$$Q_W^{New} \equiv Q_W^{Exp} - Q_W^{SM} \,, \tag{2.113}$$

thus,

$$\Delta Q_W^{New} \simeq \Delta Q_W^{Exp} \tag{2.114}$$

since the SM errors are relatively small. Using the above Lagrangian expression for new physics in Eqn. 2.111, the statistical significance (S) associated with the observation of a deviation from the Standard Model prediction is

$$S = \frac{\frac{g^2}{4\Lambda^2} Q^p_{SW}}{\frac{G_F}{\sqrt{2}} \Delta Q_W^{Exp}} \,, \tag{2.115}$$

where $Q^p_{SW} = 2(2h_1^u + h_1^d)$. On rearranging terms this yields

$$\Lambda^2 \cdot \frac{1}{g^2 Q^p_{SW}} = -\frac{1}{2\sqrt{2}G_F} \frac{1}{S\,\Delta Q_W^{Exp}} \,. \tag{2.116}$$

The theoretical prediction is that the interaction strength is largely determined by Λ and that the couplings are of order 1. So taking Eqn. 2.116 and setting $g^2 Q^p_{SW} \to 1$, we find

$$\Lambda = \frac{1}{\sqrt{2\sqrt{2}G_F}} \frac{1}{\sqrt{2\Delta Q_W^{Exp}}} = 2.3 \quad \mathrm{TeV} \tag{2.117}$$

for a 4% measurement of Q_W^p at 95% confidence level (CL). This result should be interpreted as of order a few TeV. Fig. 2.9 shows a model independent mass limit with respect to the flavor dependence of the relevant potential new physics. Therefore, a 4% Q-weak measurement could, for example, see new physics processes mediated by new gauge particles, with masses of up to a few TeV.

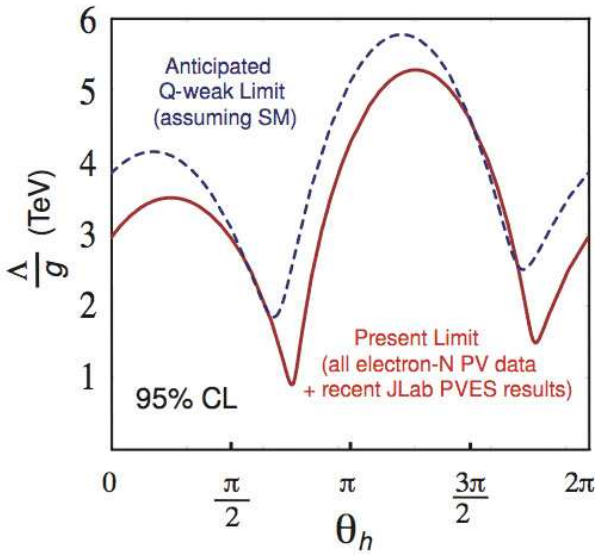

Figure 2.9: Model independent mass limit [Young et al., 2007] – the bounds on the size of the interaction represented by Eqn. 2.111. New physics is ruled out at the 95% confidence level below the curve, whereas previous data constrained a lower bound on relevant new physics $\Lambda/g > 0.4$ TeV. θ_h is the flavor mixing angle of potential new physics, which sets the isospin dependence by $h_V^u = \cos\theta_h$ and $h_V^d = \sin\theta_h$.

There are many models which have long been considered as the best motivated extensions to the Standard Model, such as: SUSY Loops, E_6 Z', RPV SUSY, Leptoquarks. The mass limits for a particular model may vary from the above value (for a discussion of various models and the sensitivity of a 4% Q_W^p measurement, see reference [Ramsey-Musolf, 1999], [Erler et al., 2003] and references within). However, the model dependent analysis illustrates the decisive role a Q-weak measurement could play as discussed in reference [Qweak-Collaboration, 2004]. For example, a particularly well-motivated class of new physics models predict the existence of extra TeV scale Z'

bosons. In the simplest models based on Grand Unified Theories (GUT), one expects $g \sim 0.45$, so that one can study Z' bosons (with unit charges) up to $M_{Z'} \approx 2.1$ TeV. Z' bosons are predicted in many extensions to the SM, ranging from the more classical GUT and technicolor models to supersymmetry and string theories. The sensitivity to non-perturbative theories (such as technicolor and other strong coupling dynamics) with $g \sim 2\pi$ could even reach $\Lambda \approx 14.5$ TeV. The latter observation would tightly constrain the *sign* of the new couplings of any new particles discovered at the LHC, which might be sufficient information to choose between possible models (see [Erler et al., 2003] [Qweak-Collaboration, 2004] and references within).

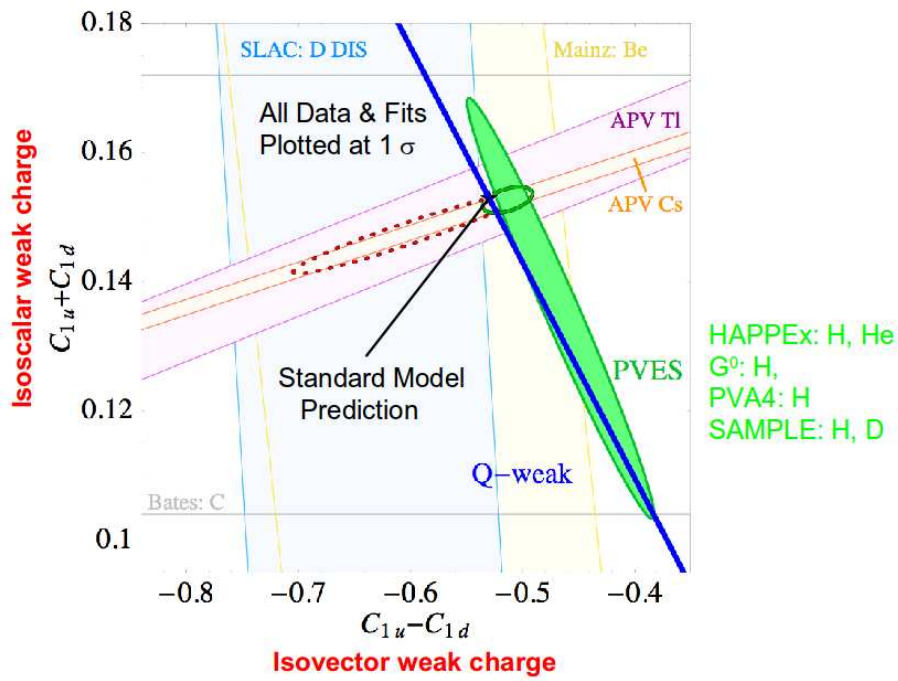

Figure 2.10: The anticipated knowledge of the neutral weak effective couplings after the Q-weak measurement of the weak charges [Young et al., 2007]. The dotted contour displays the previous experimental limits (95% confidence level) [Erler and Ramsey-Musolf, 2005a] [Nakamura et al., 2010] together with the prediction of the Standard Model (black star). The filled ellipse denotes the new constraint provided by recent high precision PVES scattering measurements on hydrogen, deuterium and helium targets (at 1 standard deviation), while the solid contour (95% confidence level) indicates the full constraint obtained by combining all results. All other experimental limits shown are displayed at 1 standard deviation.

The weak charge measurements are somewhat more restrictive than the collider measurements in that they are only sensitive to new neutral-current physics which is parity violating. The various weak charge experiments actually probe different combinations of new electron, up quark, and down quark couplings. Fig. 2.10 shows the present experimental constraints on the couplings to light quarks (the weak charges of u-, d-quarks) derived from the Cesium weak charge results [Bennett and Wieman, 1999] and MIT-Bates ^{12}C [Souder et al., 1990] and SLAC Deuterium [Prescott et al., 1979] parity violation measurements, as well as the anticipated knowledge after the Q-weak measurement of the weak charges associated with an axial coupling to the electron and a vector coupling to the up and down quarks. The phase space plot indicates a dramatic improvement on the constraints (the narrow blue band). This impact of the Q-weak measurement arises from its high precision and complementarity to existing data.

2.8 Summary

In summary, the proton's weak charge is suppressed in the SM and thus sensitive to physics beyond the SM. The aim of the Q-weak experiment is to make a precise measurement of the proton weak charge and provide constraints on possible new physics beyond the Standard Model. The following chapter will introduce the experiment and its major components.

Chapter 3

The Experiment

The three main parameters needed for a successful measurement of the proton weak charge include the parity violating asymmetry, the momentum transfer, and the beam polarization. Many systematic effects must be studied and suppressed by experimental methods. To do this, a variety of experimental equipment and methodologies must be used. This chapter describes the Q-weak experimental apparatus needed to perform the measurement. An overview is given of all major or crucial pieces of equipment used in the experiment. This includes the source, as part of the continuous electron beam facility, the beam monitors, the precision beam polarimetry, the liquid hydrogen cryotarget, spectrometer system, and various detector systems. A detailed discussion about the main Čerenkov detectors and their performance, will follow in the next chapter. The main Čerenkov detectors are used to measure the parity violating asymmetry.

3.1 Overview

The Q-weak experiment will extract the proton's weak charge from a precision measurement of the parity violating asymmetry A_{PV} in elastic e-p scattering. Neglecting the contribution of the hadronic structure function $B(Q^2)$, the expected asymmetry can be estimated according to Eqn. 2.106 as:

$$A_{PV} \sim \left[\frac{-G_F}{4\pi\alpha\sqrt{2}}\right] Q^2 Q_W^p \sim -2\times 10^{-7}\ , \tag{3.1}$$

where $G_F = 1.17\times 10^{-5}$ GeV^{-2}, $\alpha^{-1} = 137$, $Q^2 = 0.026$ GeV^2, $Q_W^p = 1 - 4\sin^2\theta_W \sim 0.08$.

In order to determine Q_W^p to an uncertainty of ±4%, the uncertainty in the asymmetry (ΔA_{PV}) should be no greater than 1×10^{-8}. There are many sources that can lead to a significant false asymmetry, since A_{PV} itself is very small[1]. Therefore, the e-p scattering experiment has to be carried out with a high statistical precision and excellent control of systematic effects, which in turn requires:

- a highly polarized, high current electron beam with a measured polarization accuracy of 1% or better[2];
- a reliable liquid hydrogen target with minimal density fluctuations while being operated at high beam current;
- a high power magnetic spectrometer with the capability to focus the elastically scattered electrons onto the main detectors, while separating the elastic and inelastic events; the spectrometer also needs to be highly symmetric, to reduce systematic uncertainty sensitivities.
- a low noise, stable integrating detector system with large solid angle acceptance and uniform response, which can efficiently measure the high rate of elastically scattered electrons in a high radiation environment.

Eqn. 2.106 shows that the asymmetry is essentially proportional to Q^2, so the measured Q^2 uncertainty will to a large extent determine the accuracy to which we can extract the physics asymmetry. Therefore, a good Q^2 determination is important. From Eqns. 2.57 and 2.59, we see that the value of Q^2 can be determined by measuring the energy of the incident electrons (or the energy of the scattered electrons) and the corresponding scattering angles. In the experiment, the elastically

[1]Another important term entering the asymmetry Eqn. 2.106 is the hadronic structure function $B(Q^2)$, which depends on the results of other experiments. In fact, $B(Q^2)$ contributes -1×10^{-7} to the asymmetry; hence, $A_{PV} \sim -0.3$ ppm.

[2]Note that the experimental asymmetry is $A_{exp} = PA_{PV}$; thus, it is important to accurately measure the polarization P.

scattered electrons will be distributed across the main detector angular acceptance. In addition, there will be a small dilution from inelastic events which arise from the target windows (mostly), the detector wall and the general background in the experimental hall. In practice, the Q^2 for the elastic events needs to be measured, averaged over the detector acceptance and weighted by the detector response to obtain the average momentum transfer $\langle Q^2 \rangle$ and $\langle Q^4 \rangle$. This requires:

- measuring the beam energy, determining the scattering angle and the energy of the elastically scattered electrons;
- finding the scattering vertex to determine the radiation energy loss of the incident electron;
- accurate measurements of the elastic electron and the inelastic electron contributions to the detector signal;
- suppressing background contributions.

To accomplish the $\langle Q^2 \rangle$ and $\langle Q^4 \rangle$ determination, a set of accurate tracking detectors is employed in the experimental setup. However, due to the statistical uncertainty requirement for measuring A_{PV}, the rate in the main experiment will be very high (about 800 MHz within each main detector acceptance at the planned beam current of 180 μA). The tracking detectors cannot operate at such a rate. To solve this problem, the experiment was designed to do dedicated tracking mode measurements, using low beam current (less than 1 nA calibration mode) and then extrapolate the results to high beam current operation (180 μA production mode).

As the asymmetry (A_{PV}) and the momentum transfer (Q^2) are determined, the proton's weak charge (Q_W^p) can be extracted from Eqn. 2.107. The weak mixing angle can be obtained from Eqn. 2.54 by taking into account high order radiative corrections (see section 2.6). The estimated value for Q_W^p is about 0.0721 at $Q^2 = 0.026$ (GeV/c)^2.

The overall layout of the experiment is shown schematically in Fig. 3.1. The key elements of the experimental apparatus include a longitudinally polarized electron beam, a liquid hydrogen target, a room temperature 8-fold symmetric toroidal magnetic spectrometer, 8 Čerenkov detectors for the

measurement of scattered electrons at forward angles, and a set of tracking devices. The experiment has two operating modes: one is a low-current calibration mode for the Q^2 acceptance mapping; the other is a high-current production mode for the asymmetry determination. The tracking detectors cannot be used in high current production mode.

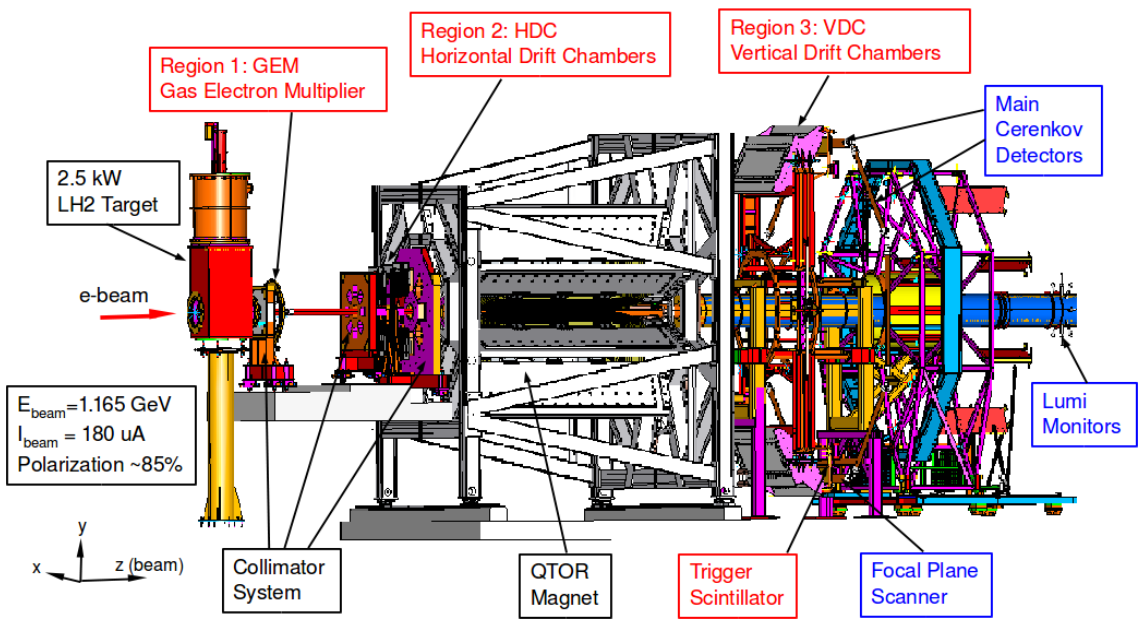

Figure 3.1: The Q-weak experimental apparatus. The scattered electrons are selected by a collimator system and are steered by the QTOR magnet onto the quartz Čerenkov detector bars. The tracking detectors (shown in red) will be used during low current running (to be retracted during high current running), to determine the momentum transfer and backgrounds, and to help characterize the properties of the main detector system. Luminosity monitors are used to monitor target density fluctuations and provide a sensitive null asymmetry test.

In the experiment, the ~ 85% [3] longitudinally polarized electron beam is incident on a 35 cm long liquid hydrogen target. The scattered electrons are selected to the angle range of interest (5 - 12 degrees) by three collimators. The selected electrons pass through the toroidal magnetic field of

[3]This is the design value, but the actual experimental value is higher.

the Q-weak spectrometer with a field integral of about 0.67 T·m along the envelope of the elastic electron trajectories. The magnetic field deflects the elastic electrons by about 10° and provides a clean separation between the elastically scattered electrons and inelastically scattered electrons. The elastic electrons are focused onto a set of eight, 200 cm $\times$ 18 cm rectangular quartz bars. The electrons then produce Čerenkov light as they pass through the bars. The Čerenkov photons are detected by photo-multiplier tubes (PMTs). The Čerenkov signal is read out either in current mode to achieve the high statistical precision required for the asymmetry measurement or in counting mode for accurate Q^2 determination. The inelastically scattered electrons are bent out of the detector acceptance by the spectrometer, so they only make a small contribution to the Čerenkov signal. A typical distribution of elastic events at a Čerenkov detector is shown in Fig. 3.2.

The tracking system can precisely determine the 4-momentum transfer Q^2 and the contribution of inelastic scattering events to the Čerenkov detector signal. The system includes three regions of tracking chambers, a focal plane electron flux scanner (not shown in Fig. 3.1), trigger scintillators and associated shielding. The regions are defined according to the locations of different tracking detectors.

The Region-I tracking chamber at the first collimator is a gas electron multiplier (GEM) used to locate the scattering vertex; the Region-II horizontal drift chambers (HDCs), which are surrounded by the second two-stage collimator, combined with the Region-I GEM can determine the scattering angle of elastic electrons. The Region-III system is located in front of main Čerenkov detectors. It has two vertical drift chambers (VDCs), which are used to measure the momentum of electrons, and define particle trajectories incident on the Čerenkov bars.

The focal plane electron flux scanner consists of a small active area quartz Čerenkov detector and a pair of air-core light guide pipes. The scanning Čerenkov signal is read out by PMTs in counting mode for all beam currents. It can map the rate distribution of the main Čerenkov bars at both low beam current and high beam current so that the Q^2 mapping at low beam current can be extrapolated to high beam current with confidence. The trigger scintillators are mounted immediately downstream of the Region-III VDCs and will provide the trigger and timing for the other tracking

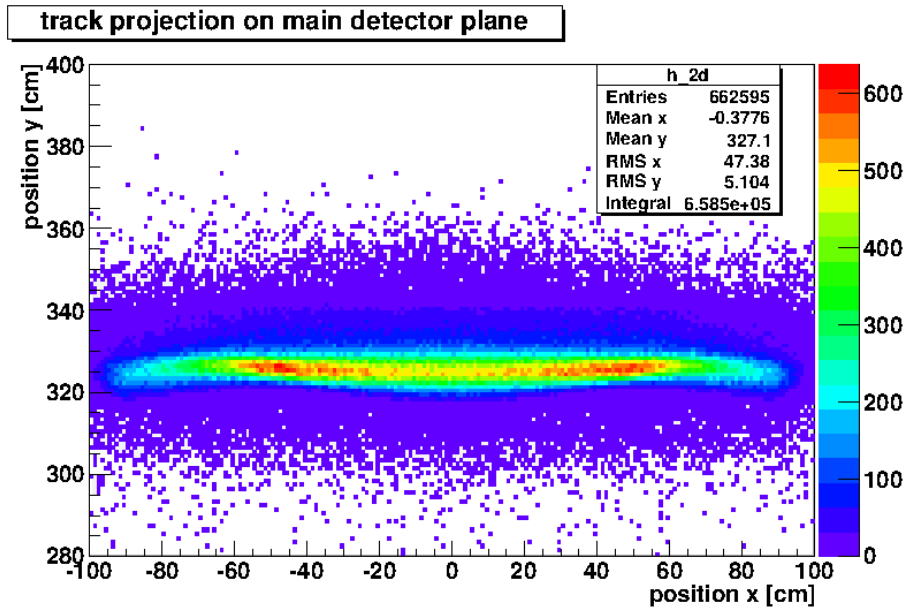

Figure 3.2: A measured distribution of elastic events at a Čerenkov detector. The center of the target is 650 cm upstream from the center of the magnetic spectrometer, and the detector bar is in the focal plane, located 578 cm downstream from the center of the magnetic spectrometer. The Y-coordinates run across the width of the detector bar. The X-coordinates run along the detector bar and are measured with respect to the detector center. Note that the X and Y axes are not to scale. The Y direction corresponds to the scattering angle θ, while the X direction corresponds to the azimuthal angle ϕ. The color coded axis on the right indicates the relative event rate (in arbitrary units).

detectors.

The uncertainty in the Q-weak measurement is the combination of statistical and systematic uncertainties. Any of the remaining systematic uncertainties must be theoretically calculable with uncertainties well below that of the combined statistical and systematic measurement uncertainty. Table 3.1 shows the anticipated experimental uncertainties [Qweak-Collaboration, 2007] in the Q-weak experiment.

The ultimate goal of the experiment is to determine Q_W^p with 4% combined statistical and systematic uncertainties. From Eqn. 2.110, we know this uncertainty corresponds to $\sim 0.3\%$ precision for a determination of $\sin^2\theta_W$ at $Q^2 \sim 0.026$ (GeV)^2.

Source	$\Delta A/A$	$\Delta Q_W^p/Q_W^p$
Statistical	2.1%	3.2%
Systematic:		2.6%
Hadronic structure corrections	–	1.5%
Beam polarization	1.0%	1.5%
Average Q^2 determination	0.5%	1.0%
Helicity-correlated beam properties	0.5%	0.7%
Background	0.5%	0.7%
Total	2.5%	4.1%

Table 3.1: The anticipated experimental uncertainties in the Q-weak experiment

Hadronic corrections enter at order Q^4 in the parity-violating asymmetry, whereas the value of Q_W^p enters at order Q^2. Therefore, decreasing the value of Q^2 reduces the uncertainties on Q_W^p. However, this also decreases the size of the asymmetry, making longer counting times necessary to achieve a given statistical uncertainty. The optimized value for Q^2 is about 0.026 (GeV)^2 based on Monte Carlo simulation. This small momentum transfer requires low beam energy ($\sim$ 1.165 GeV) and small scattering angle (5° - 12°) for the elastic electrons.

Note that the nucleon structure contributions $B(Q^2)$ can be determined experimentally by extrapolation from the other forward angle parity-violating experiments at higher Q^2 than will be employed for Q-weak (Q^2 ~0.026 GeV^2). However, the extrapolation from these higher values of Q^2 to 0.026 GeV^2 introduces some uncertainty into the extraction of Q_W^p from the measured asymmetry. From the program of PV measurements (SAMPLE, HAPPEx I, HAPPEx II, G0, PVA4, see references [Young et al., 2006] [Acha et al., 2007] [Armstrong et al., 2005] [Maas et al., 2005a] [Maas et al., 2004]), the uncertainty in Q_W^p due to these Q^2-dependent effects can be calculated (see reference [Qweak-Collaboration, 2007] for a detailed discussion).

The basic (as designed) parameters of the experiment are presented in Table 3.2. A 2500 hour production measurement will determine the proton's weak charge to $\sim$ 4% combined statistical and systematic uncertainty. The experiment has completed its first data phase and acquisition of production data is expected to be completed in May 2012.

Parameter	Value
Incident Beam Energy	1.165 GeV
Beam Polarization	85%
Beam Current	180 μA
LH_2 Target Thickness	35 cm (0.04 X_0)
Production Running Time	2544 hours
Nominal Scattering Angle	7.9°
Scattering Angle Acceptance	±3°
Acceptance	49% of 2π
Solid Angle	$\Delta\Omega$ = 37 msr
Acceptance Averaged Q^2	$\langle Q^2 \rangle = 0.026$ (GeV/c)^2
Acceptance Averaged Physics Asymmetry	$\langle A \rangle = -0.234$ ppm
Acceptance Averaged Experimental Asymmetry	$\langle A \rangle = -0.200$ ppm
Integrated Cross section	4.0 μb
Integrated Rate (all sectors)	6.5 GHz (0.81 GHz per sector)

Table 3.2: Basic parameters of the Q-weak experiment [Qweak-Collaboration, 2007]

3.2 Continuous Polarized Electron Beam

The high current, polarized electron beam for the Q-weak experiment is produced by the continuous electron beam accelerator facility (CEBAF) at the Thomas Jefferson National Accelerator Facility (TJNAF). The CEBAF accelerator consists of a polarized electron source and injector and a set of superconducting RF linear accelerators connected to each other by two arc sections which contain steering magnets (a schematic diagram of the racetrack-shaped accelerator layout is shown in Fig. 3.3). It is a continuous-wave [4], superconducting radio-frequency (SFR) accelerator operating at a fundamental frequency of 1497 MHz.

Three interlaced 499 MHz polarized electron beams separated by 120° RF phase are produced at the polarized source and accelerated to an energy, 67.5 MeV for example, in the injector. The electrons are then directed to the north linac, a nominal 600 MeV superconducting RF (radio-frequency) linear accelerator (made from superconducting niobium RF cavities which are cooled to approximately 4 K by liquid helium, to remove electrical resistance and allowing the most efficient transfer

[4] A distinguishing feature of CEBAF is the continuous nature of the electron beam. Strictly, there is some beam structure, but the pulses are very much shorter and closer together with a bunch length of less than 1 picosecond.

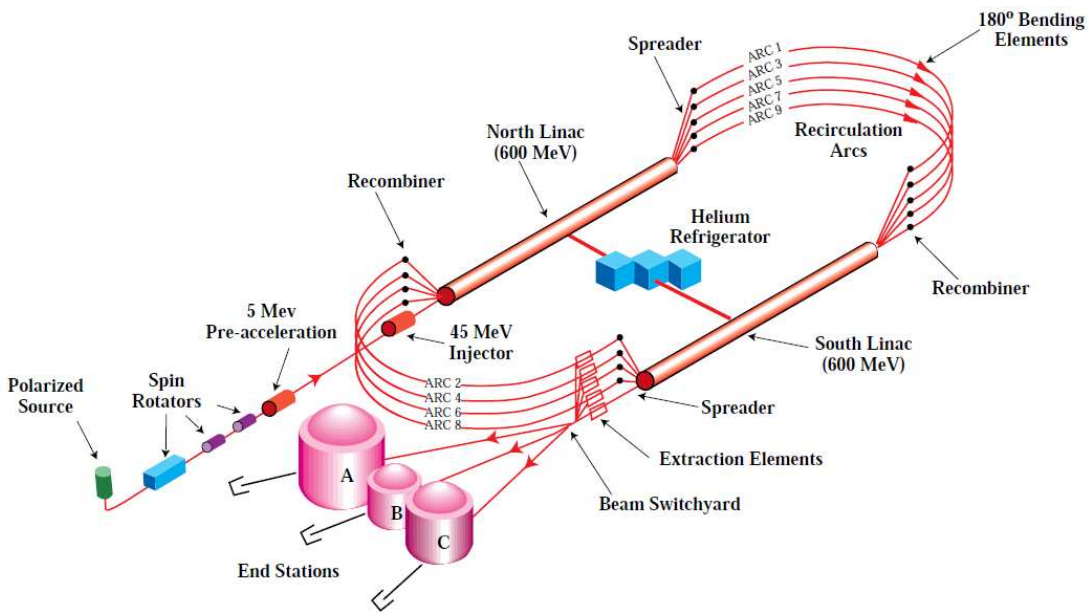

Figure 3.3: The continuous electron beam accelerator facility (CEBAF) at Jefferson Lab.

of energy to an electron), where they are accelerated to an energy of 667.5 MeV. After traversing the north linac, the electrons are steered by magnets through a 180° turn in the east recirculation arc and then enter the south linac, identical to the north linac. At the end of south linac, the one-pass nominal 1267.5 MeV beam can be either extracted and transported at the beam switch-yard for redirection to the experimental end stations, labeled Hall A, Hall B, and Hall C, or steered through a second turn in the west recirculation arc for further acceleration. As the electron beam makes up to five successive orbits, its energy is increased up to a maximum of ~6 GeV. The electron beams can be delivered (with some restrictions) simultaneously to three experimental halls with different beam currents and energies in each hall. When a polarized beam is required in one (or all) of the halls, those restrictions increase. To obtain the Q-weak energies of 1165 MeV, the accelerated energies and the injector energy are scaled down. The beam is diverted into the hall before going through the second pass.

The polarized electron beam is produced by the CEBAF polarized electron source. The polarized electrons can be generated by optical illumination of a strained crystal of gallium arsenide

(GaAs) with circularly polarized light [Pierce et al., 1980] [Prepost and Maruyama, 1995]. The circularly polarized laser light is produced using a Pockels cell to reverse helicity with a fixed frequency in a pseudo random way over several states (even number of helicity states to form a "pair","quartet", "octet"). The Q-weak experiment requires the long-term delivery of high current beam with high polarization (one year of beam at 180 μA and polarization greater than 80%). This in turn requires good photocathode material, a reliable Ti-Sapphire laser and long photogun operating lifetime. A new type of photocathode material has been adopted by the Q-weak experiment – strained-superlattice GaAs. This material provides a polarization $\sim$ 90% with five times greater quantum efficiency than standard strained layer GaAs [Maruyama et al., 1992]. For the Q-weak experiment the helicity will be changed every 1/960 s, referred to as a macropulse (MPS), in a random way over a set of four helicity states (a quartet). The asymmetry is formed by taking the difference of the charge normalized detector yields between the two states with positive helicity and the two states with negative helicity over the total yield in the quartet. In addition to the rapid helicity reversal, an insertable half wave plate (IHWP) in the laser line was used to change the helicity every day or so in an independent, mechanical way in order to check for false asymmetries in the electronics and accelerator.

The electron's polarization vector precesses relative to its' velocity due to Larmor precession when it passes through bending magnets in the accelerator. Wien filters are used to compensate for the precession of the electron's spin in the arcs between the north and south linacs and the arc going into Hall C. A Wien filter has homogenous magnetic and electric fields ($\vec{E}$ and $\vec{B}$) which are perpendicular to each other and transverse to the velocity of the electrons ($\vec{v}$). If the Lorentz force equilibrium condition ($\vec{E} = -\vec{v} \times \vec{B}$) is fulfilled, the electrons velocity will be unperturbed as they travel through the crossed fields [Steiner et al., 2007].

3.3 Beam Property Monitor and Feedback Control

Fluctuations in beam properties introduce additional statistical uncertainty as well as systematic uncertainties in the form of false asymmetries (for example). The former is associated with random fluctuations, while the latter is associated with helicity correlated fluctuations. The beam condition is specified by the beam current, the beam energy, the beam position and angle at the target, and the beam size at the target. To control uncertainties due to fluctuations in these parameters, the following sets of observables are measured continuously:

beam charge and the charge difference	Q	ΔQ		
beam energy and the energy difference	E	ΔE		
beam position and the position change at the target	X	ΔX	Y	ΔY
beam angle and the angle change at the target	X'	$\Delta X'$	Y'	$\Delta Y'$

Table 3.3: Beam parameters

To remove helicity correlated beam charge fluctuations, the main detector yield needs to be normalized to the beam charge for the asymmetry measurements, so a linear, low noise beam charge monitor (BCM) is essential (knowledge of absolute charge is only needed to determine the luminosity). Q-weak makes use of non-invasive beam current measurement with a radiation-hard resonant cylindrical "pillbox" RF cavity monitor (see Fig. 3.4). The electron beam passing through the cavity will excite the resonant transverse electromagnetic wave (TM010 mode) at 1.497 GHz (the beam acceleration frequency). An antenna (probe loop) reads out the resonant energy (the power induced by the beam inside the cavity) and outputs a signal proportional to the current, thus providing a measurement of the beam current.

The BCM output RF signals are down-converted to lower frequencies, filtered to improve signal-to-noise ratio, and converted to DC signals for digitization. The cavity BCM is very stable and linear[5] and has large dynamic range. However, since it collects a signal which is proportional to

[5]Due to non-linearities in the signal chain, the RF beam monitors must be used at currents above 100 nA. But this only has relevance for tracking mode running.

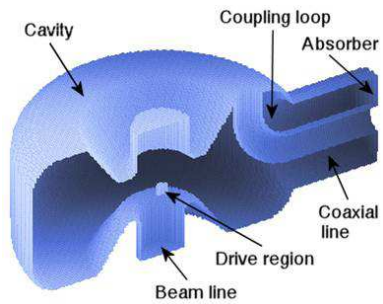

Figure 3.4: Pillbox cavity beam current monitor (BCM). Beam electrons entering the cavity encounter an electric field which slows them down infinitesimally, extracting power from the beam and storing it temporarily in the cavity. While half the RF power goes into heating the cavity walls, the other half is extracted magnetically by a loop antenna and sent to the processing electronics by RF cable.

the beam intensity, it can only provide a relative measurement of the beam current. Therefore, the BCM's were calibrated absolutely with respect to the Unser monitor[6].

Beam position is measured with stripline beam position monitors (BPMs), which consist of four 1/4-wavelength antenna wires (X^+, X^-, Y^+, Y^-) oriented parallel to the beam axis and positioned as shown in Fig. 3.5). The beam power couples into the antenna at 1.497 GHz and the signal amplitude on each wire depends on the distance between the antenna and the beam. Neglecting the finite length and radii of the antennae, as well as the finite size of the beam, to first order the coupling of the beam to each antenna is $V \propto$ (constant + r), where r is the distance of the beam from the BPM center [Barry, 1991]. Thus signals from the four antennae can be combined to determine the position of the beam. Assuming the beam is at $Y = 0$, then r is simply X, and the beam position is therefore

$$X \propto \frac{V^+ - V^-}{V^+ + V^-} \ . \tag{3.2}$$

BPM's are instrumented with Switched Electrode Electronics (SEE) — a sample-and-hold module with which a single electronics chain is rapidly switched between the antennas [Powers, 1998].

[6] An Unser monitor [Kazimi et al., 1995] can be self-cross-calibrated to an absolute current source.

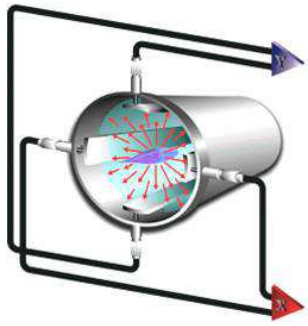

(a) 4-wire stripline BPM

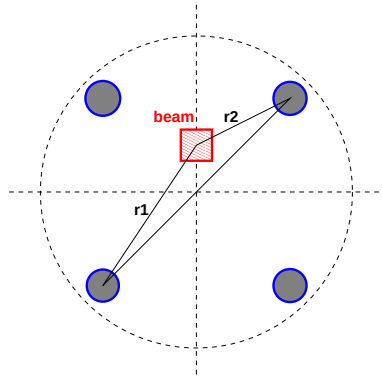

(b) A large, square-rastered beam is shown off the central axis of the BPM.

Figure 3.5: Schematics of a 4-wire stripline beam position monitor

So the gain drifts are canceled out exactly and offset drifts and nonlinearities in the electronics are approximately canceled if the beam is roughly centered in the BPM so that the V^+ and V^- signals are of comparable magnitude. The 1.497 GHz signal is converted to a lower frequency by a RF down-converter, then filtered and converted to a DC voltage for digitizing.

These BPM's are stable, linear over large current ranges, have good signal to noise ratio, and have useful bandwidths well into the 10's of kHz range. They also can be used to make relative energy measurements by using the known dispersion of the beam in the Hall C arc and measuring the position in a BPM in the arc (absolute energy measurements are made in dedicated runs using the superharp [Yan et al., 1995] where the beam is set up in a dispersive tune). In addition to the 4-wire BPM's, several sensitive cavity-type position monitors are also available for the beam position measurements.

The beam halo is monitored by using Lucite detector and scintillation counters to determine whether the beam is interacting somewhere in the accelerator. There is a 2 mm thick aluminum halo target with two apertures in the beamline. The apertures can be moved in and out of the beam as necessary. If the halo is small enough then there will be minimal interaction with the halo target as the beam passes through the hole in the target. One aperture on the halo target is an 8 mm square opening, to be used to test the limit of the halo; the other aperture is a 13 mm diameter

hole, to be used as continuous halo monitor during production running. The Q-weak halo monitors (numbered from 3 to 8) are located immediately downstream of the halo targets and upstream of the Q-weak liquid hydrogen target (the locations of Q-weak halo monitors are approximately indicated by arrows on a part of Hall C beamline CAD layout in Fig. 3.6. A complete beamline layout can be found in reference [Benesch, 2009]). The beam halo can also be estimated using the main detectors (or luminosity monitors) while employing hole targets of varying diameters as well as a solid target for normalization.

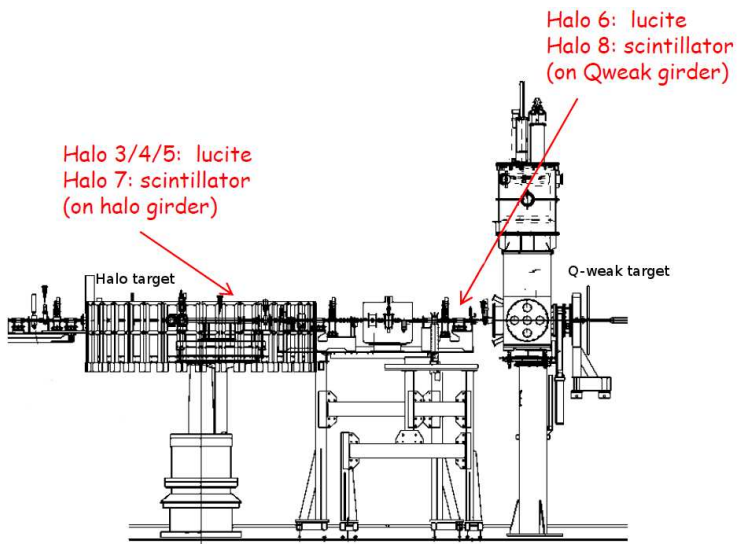

Figure 3.6: Locations of Q-weak halo monitors

The Q-weak experiment has helicity correlated beam requirements (the Q-weak helicity correlated beam specifications are summarized in Table 3.4). In order to minimize helicity-correlated beam property fluctuations (intensity, energy, angle, and beam position), a set of feedback control systems is being commissioned.

An “IA” (Intensity Attenuator) feedback system is used to reduce helicity-correlated beam intensity asymmetries and a “PZT” (Piezo-electric transducer) feedback system is used to control helicity-correlated beam position changes. The IA system consists of a Pockels cell sandwiched between linear polarizers and a wave-plate. Application of relatively small voltages (<10 V) can be

Beam Parameter	Q-weak Specification
Maximum run-averaged helicity correlated charge asymmetry	0.1 ppm
Maximum run-averaged helicity correlated position difference	40 nm
Maximum run-averaged helicity correlated angle difference	100 nrad
Maximum run-averaged helicity correlated energy difference	10 ppb
Maximum beam Current	180 μA
Polarization	~85% (with superlattice GaAs)

Table 3.4: Partial list of Q-weak beam specifications [Qweak-Collaboration, 2004]

used to control the intensity of the laser beam. The intensity asymmetry is measured continuously using beam charge monitors in the hall. The measured asymmetries (obtained from a real-time analyzer) are used to determine the needed control voltage to be applied to the IA to decrease the intensity asymmetry. Without a feedback system, the smallest intensity asymmetries that can be achieved with careful setup are ~20-30 ppm. With the system on, asymmetries can be suppressed down to about 0.2 ppm. The PZT system consists of a mirror in the laser beam path, mounted on a Piezo-electric transducer. The angle of the mirror can be changed by application of a voltage on the Piezo-electric transducer. The laser position could be adjusted in a helicity-correlated way to compensate for helicity-correlated beam position change measured in the experimental hall. However, the PZT system only allows adjustment of helicity-correlated position differences, based on position measurements close to the experimental target. The beam position also changes due to tuning of the accelerator, therefore the system requires frequent re-calibration. In order to control both the position and angle of the beam, a system based on correction coils is implemented. The coils are used to move the beam in the horizontal or vertical directions in a helicity-correlated manner, to decrease both helicity-correlated position and angle differences at the target. In addition, there is a significant coupling between helicity-correlated position differences and intensity asymmetries due to beam scraping on apertures in the injector. The coils also eliminate the problem of the coupling between helicity-correlated position differences and intensity asymmetries.

3.4 Precision Beam Polarimetry

The Q-weak design beam polarization (P_e) is $\geq 85\%$, and the measured asymmetry is $A_{exp} = P_e A_{PV}$. The electron beam polarization must be measured with an absolute uncertainty at the 1% level in order to extract the physics asymmetry from the measured asymmetries and determine the proton's weak charge with the proposed overall uncertainty. The polarimetry in Q-weak is performed using the existing Hall C Møller polarimeter [Hauger et al., 2001] in combination with the new Hall C Compton polarimeter. The Møller polarimeter is capable of better than 1% measurements at low currents ($< 10\ \mu$A). The measurements using the Møller polarimeter must be made in dedicated runs. Each measurement will interrupt beam delivery to the main experiment, and must be done periodically (every 3 to 4 days, for example). Each measurement takes 6-8 hours. In order to extend the operating current range, a Compton polarimeter was installed in Hall C beam tunnel, upstream of the existing Møller polarimeter (see the beam-line layout in reference [Benesch, 2009]).

3.4.1 Møller Polarimeter

The Møller polarimeter (see the schematic drawing in Fig. 3.7 and a top view photo in Fig. 3.8) measures the electron beam polarization by using the electron-electron scattering process. It measures the asymmetry in doubly longitudinally polarized Møller scattering, where both the incident and target electron are polarized in the direction of the beam, and thus is sensitive to the longitudinal polarization of the beam.

The beam polarization is obtained from measuring the asymmetry produced when the beam hits the polarized target. The target is a thin foil of pure iron magnetized by a superconducting solenoid with a field of ~ 4 T in the direction of the beam. The scattered and recoil electrons are focused by a quadrupole magnet and passed through collimators to choose the desired scattering angles, and then defocused by a second quadrupole magnet and detected in coincidence by detectors placed symmetrically on either side of the beam axis. The asymmetry measured by the polarimeter has to be corrected for backgrounds in order to extract the physics polarization asymmetry. Coincidence

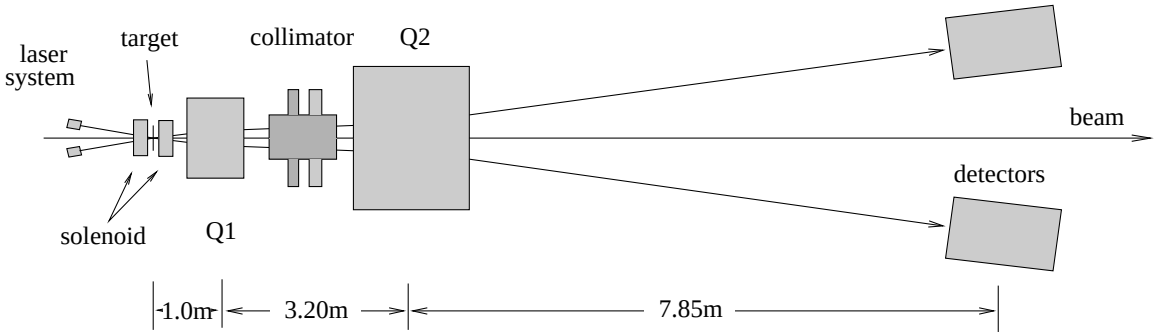

Figure 3.7: Layout of the Hall C Møller polarimeter. The superconducting solenoid is used to drive the pure iron target foil into magnetic saturation. The magnetic field and the foil are oriented perpendicular to the beam.

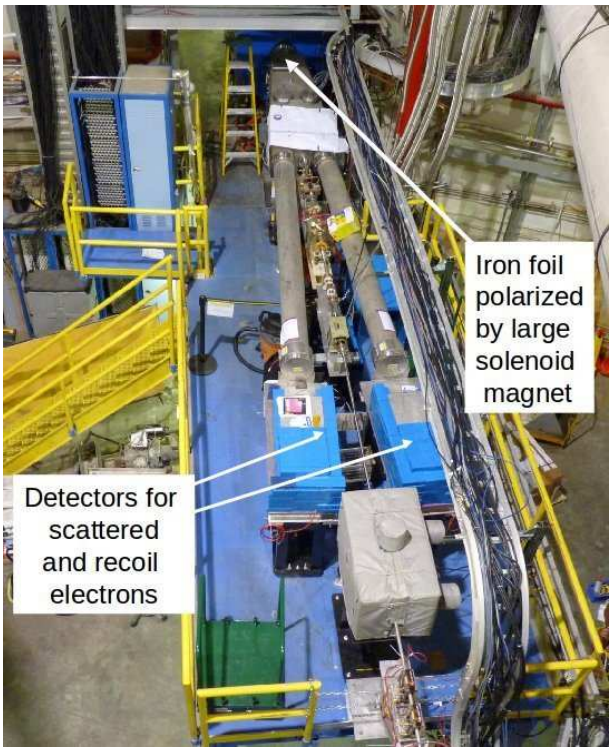

Figure 3.8: Top view of the Hall C Møller polarimeter.

detection of the scattered and recoiling electrons allows suppression of the significant backgrounds from Mott scattering.

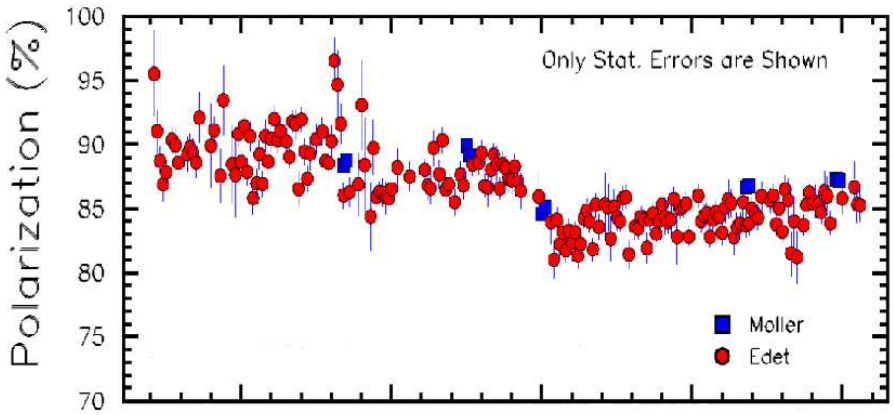

Figure 3.9: Preliminary Møller beam polarization measurements for the first Q-weak production run period (Run I). The x-axis represents the run number. Some preliminary results of the Compton electron detector measurements (see the next section) are also shown.

The most significant systematic uncertainty for the Møller polarimeter is the target electron polarization. The superconducting solenoid provides fields in excess of 3 Tesla, perpendicular to the foil plane, which drives the pure iron foil into magnetic saturation. The electrons in the target can then be polarized parallel (or anti–parallel) to the electron beam direction with a polarization known to better than 0.5%. However, depolarization of the iron foil could happen due to beam–heating effects that limit the maximum beam current that the Møller polarimeter can handle. With no rastering of the electron beam [7], the Møller polarimeter can be used up to 2 μA; with a beam rastering area of $\sim$ 4 mm^2, it can be used with beam currents up to 10 μA. A typical operation of the polarimeter will need about 15 minutes/run to reach $\sim$ 1% statistics. During Q-weak production running, measurements have been taken every 3 – 4 days. Fig. 3.9 shows some preliminary results of the Møller beam polarization measurements. The measured polarization has typically been better than 85% with less than 1% uncertainty for each run.

[7] The beam position is rapidly moved within a small area by magnetic coils to reduce the effects of heat build-up at a point where the beam hit on the target.

3.4.2 Compton Polarimeter

A new Hall C Compton polarimeter is being used for the Q-weak experiment. The Compton polarimeter provides a non-invasive continuous, on-line measurement of the beam polarization at full beam current. The apparatus for the Compton polarimeter includes a magnetic dipole chicane, a green light laser, a photon detector, and an electron detector, as shown in Fig. 3.10. The polarization of the electron beam is measured by scattering low-energy photons, generated by a polarized laser system, from the polarized electron beam. The backscattered photons have an energy of order 10 MeV and are detected and energy-analyzed by a photon calorimeter. The recoil electrons are momentum-analyzed using a dipole magnet which separates them spatially from the main beam and detected by an electron detector. The knowledge of the photon energy and electron momentum is used to extract the Compton scattering cross-section asymmetry, from which the electron beam polarization can be determined. During routine production running, the beam is continuously routed through the Compton chicane with the laser turned on. The detector asymmetries are recorded in parallel with the rest of the data for the experiment.

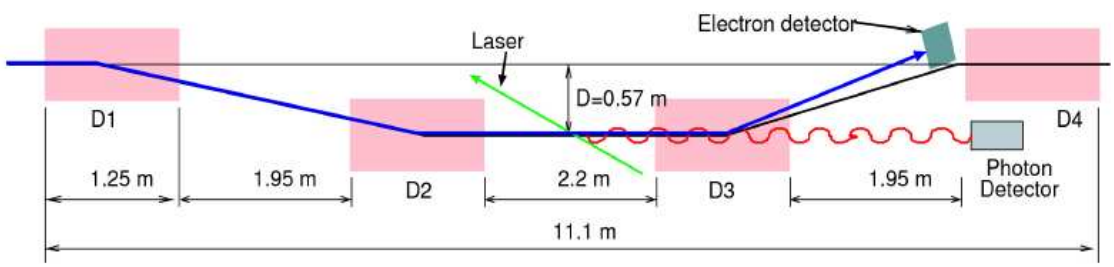

Figure 3.10: Schematic diagram of the Compton polarimeter layout.

Since the backscattered photons are emitted in a narrow cone about the incident electron's direction, the photon detector must be placed on axis with the electron beam. A four–dipole chicane is used to steer the beam to an interaction region, where it will intersect the beam of the high–power laser system (see Fig. 3.11), and then steer it back to its original path. This allows one to position the photon detector downstream of the interaction region with no interference from the electron beam.

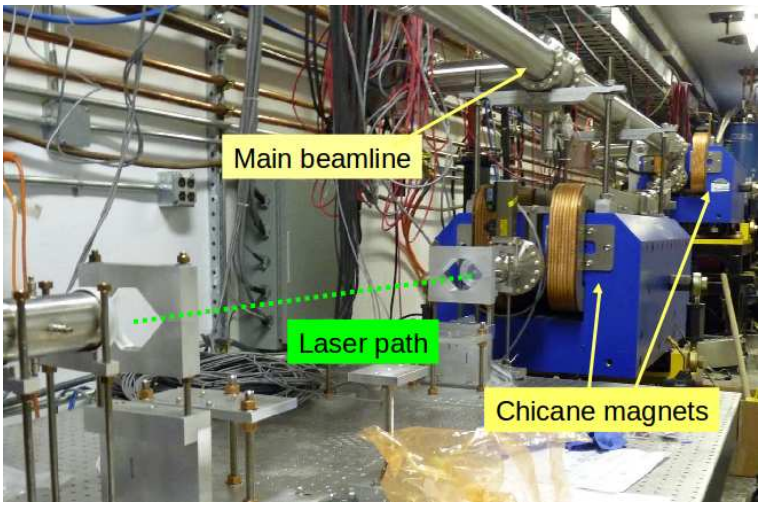

Figure 3.11: Compton region during installation (looking downstream). The Compton dipole chicane is 10.6 m long, located immediately downstream of the Hall C Møller polarimeter.

The Hall C Compton polarimeter makes use of a 10 W, 532 nm (green) continuous wave laser with a low-gain cavity (the cavity gain is about 100) and an in-cavity power of 300 W. The photon detector is an undoped CsI scintillator operated in digital integrating mode via waveform digitizer. Since the scattered electron loses some energy during the Compton interaction, it will undergo a larger deflection in the Compton dipole chicane than the primary electron beam. The chicane then acts as an electron spectrometer, and by measuring the energies of the electrons that have been separated from the nominal beam path, one can form the Compton asymmetry using only the electrons.

The electron detector [Martin et al., 2009] consists of semiconductor micro-strips, fabricated from synthetic diamond (the prototyping and test are discussed in reference [Wang et al., 2008]). It is a multi-strip device, used to sense the track of recoil electrons. The strips have 200 μm pitch, will be oriented perpendicular to the bend plane of the magnet, so that each strip will be sensitive to the recoil electron momentum. The shape of the Compton asymmetry in recoil momentum allows a systematically clean determination of the incident electron polarization.

Fig. 3.12 shows a very preliminary beam polarization result measured by using the diamond

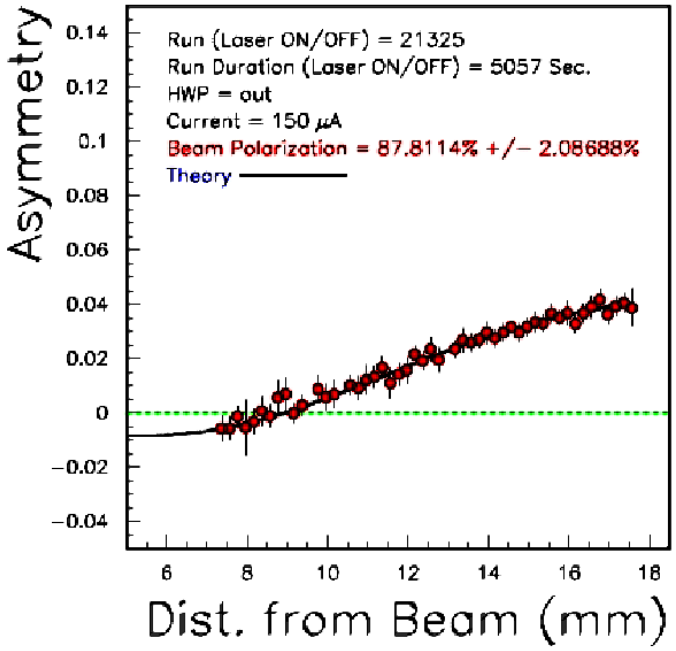

Figure 3.12: Preliminary beam polarization result measured by using the diamond detector.

electron detector of the Compton polarimeter from a commissioning run. The uncertainty is only statistical, but agrees at this level with other beam polarization measurements.

3.5 Liquid Hydrogen Cryotarget System

In order to achieve the statistical precision goal, the Q-weak experiment employs a high beam current and a long target flask to provide a high luminosity. The power deposited by a 180 μA, 1.165 GeV electron beam in a 35 cm long liquid hydrogen target (3.9% radiation length) due to ionization energy loss (at 4.65 MeV/g/cm^2) is about 2120 W (neglecting energy loss in the target windows). Accounting for several hundred Watts of conductive heat losses, circulation fan heat load, reserve heat load for feedback control, etc., the total cooling power for Q-weak target is about 2500 W. The combination of high beam current and a long target flask make the Q-weak liquid hydrogen cryotarget the highest power cryogenic target in the world.

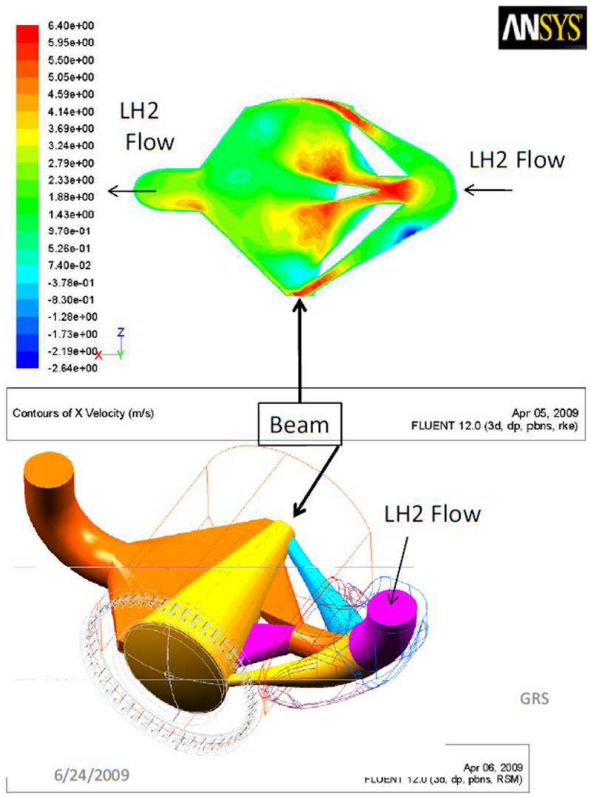

Figure 3.13: Schematic of the transverse flow target. The top figure shows contours in the liquid hydrogen flow velocity and the bottom figure is a CAD model of the actual design [Smith, 2009].

Since the current mode operation of the main Čerenkov detectors makes the experiment particularly sensitive to target density fluctuations, the target was carefully designed to minimize the density fluctuations and associated effects. The target fluid dynamics has been modeled using ANSYS (a fluid dynamics simulation code) in order to minimize possible boiling in the target. The resulting design is that the target liquid and the windsock-shaped liquid hydrogen cell are enclosed in a cylindrical cell with transverse flow, rather than flow along the beam axis (see Fig. 3.13). Simulations have been used to design the body of the target to ensure that the design does not interfere with the scattered electrons that are in the acceptance of the main detectors.

The large Q-weak target cooling load is shared by the JLab End Station Refrigerator (ESR) and

the Central Helium Liquefier (CHL). The ESR supplies about 25 g/s of 15 atm 15 K coolant which returns at 19 K and 3 atm with an enthalpy change $\Delta H = 31$ J/g, corresponding to a maximum cooling power of 775 W (about 30% of what is required for Q-weak). The CHL is able to supply 25 g/s of 3 atm 4 K coolant which can be returned warm to the CHL at 19 K and 1.2 atm, corresponding to a 2575 W of cooling capacity. This combination of resources provides the required cooling power and flexibility to dynamically balance the relative loads on the two refrigerators.

(a) The target scattering chamber shown fed by 4 coolant transfer lines from the top

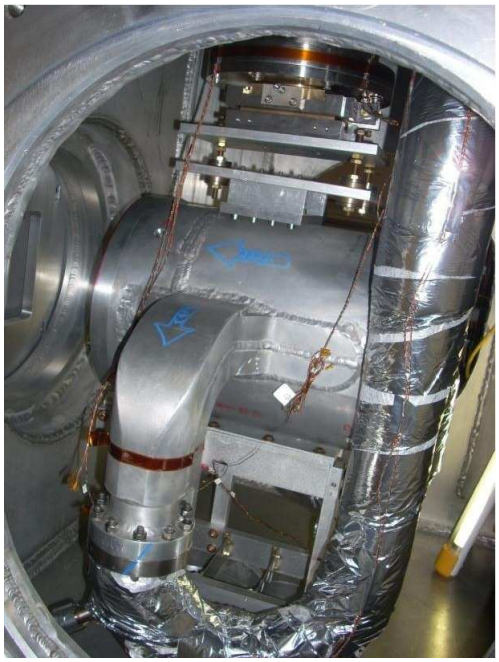

(b) A view of the target cell inside the scattering chamber

Figure 3.14: Photons of target scattering chamber and target cell.

The target is azimuthally symmetric in order to minimize the sensitivity to helicity correlated beam motion. The target window and wall thicknesses are minimized to reduce background contributions to the detector signal. The cell windows are a significant source of background due to the aluminum asymmetry being about a factor of 10 larger than the asymmetry from hydrogen, as well as due to the uncertainty in the theoretical predictions of the scattering rate from aluminum. Therefore, the cell windows were made as thin as possible (76.2 μm thick aluminum) with thinner

nipples where beam is incident on the target.

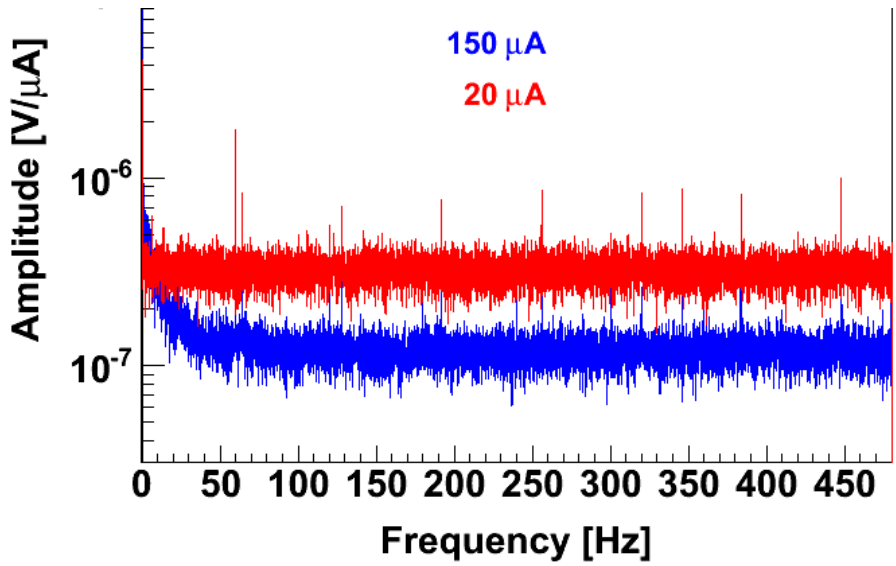

Figure 3.15: Main detector noise frequency spectrum measured for liquid hydrogen target at beam current 20 μA (red) and 150 μA (blue) with 3 mm $\times$ 3 mm raster size. Note that the noise floor is different for the two measurements, due to pedestal subtraction.

The Q-weak liquid hydrogen target operated safely and reliably during the first run cycle from November 2010 to May 2011, at the designed beam current. It was operated routinely with 165 μA of 1.165 GeV electrons and was tested for beam currents of up to 180 μA, without problems. Fig. 3.15 shows the main detector noise frequency spectrum measured for liquid hydrogen target at beam current 20 μA (red) and 150 μA (blue). At very low frequency, the noise at 150 μA is larger than at 20 μA due to random target density fluctuations. However, the additional noise decreases dramatically as the measurement frequency increases. Since the experiment is running at a high helicity reversal rate of 960 Hz, this target density fluctuation noise is not affecting the asymmetry measurement. With a beam raster size of 4×4 mm^2, the density fluctuation noise contribution to the asymmetry widths at 169 μA is only 45 ppm (79 ppm for a 3×3 mm^2 raster).

3.6 Q-weak Spectrometer

The Q-weak spectrometer system consists of a set of acceptance defining collimators, a magnet to focus elastic electrons in the focal plane and to separate these from inelastic events, and a set of tracking detectors to map out the distribution of elastic events on the focal plane, as well as determine the initial momentum transfer.

3.6.1 Collimator and Shield Wall

Three lead collimators were designed and installed in the experiment to define the experiment's angular acceptance and clean up the scattered beam optics, defining the image of elastically scattered electrons in the focal plane and therefore the size and position of the main detectors. Their geometries were refined using simulations. Fig. 3.19 shows the collimator together with a Region 1 GEM chamber. The first collimator serves as the initial cleanup collimator. The second collimator (downstream of collimator one) serves as the acceptance defining collimator. The third collimator (downstream of collimator two) serves as the final cleanup collimator before the beam enters the toroidal magnet. All collimator apertures were carefully surveyed after delivery and collimator positions were surveyed after installation. There is a water cooled tungsten plug with a 14.7 mm diameter aperture in the center of the first cleanup collimator. It is flanged to the downstream beampipe on one end and the target vacuum window on the other, limiting backgrounds from beam scraping on the downstream beam pipe.

Simulation indicates that the room backgrounds are expected to be significant during the asymmetry measurement at high beam current — incident photon rates due to Bremsstrahlung processes will be at the level of 200 MHz in air. A detector shielding hut (see Fig. 3.16), surrounding Region 3, protects the Čerenkov detectors, the Region 3 drift chambers, the trigger scintillators and the focal plane scanner from room backgrounds during the asymmetry measurement (there is also a small shielding hut erected between the first and second collimator, around the Region 1 GEM chambers, and a third shielding enclosure built around 6 racks of electronics used mostly for the tracking sys-

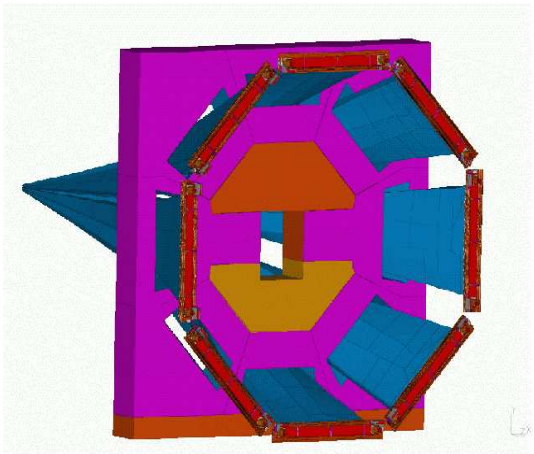

(a) Beam envelopes and main detector modules behind the shield wall

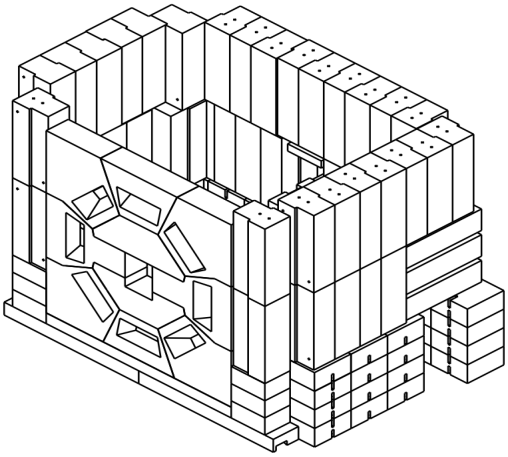

(b) Main detector shielding hut

Figure 3.16: (a) Beam envelops (blue) and main detector modules (red) behind the shield wall. The shield wall is built with barite-loaded concrete (Lego-style fabrication) for high density in minimal space. Stainless steel rebars are used to reinforce the concrete. The apertures have complex geometry with sub-cm tolerances. (b) CAD layout of the detector shield hut, which houses the main detectors, the Region 3 drift chambers, the scintillation counters, and the focal plane scanner.

tem). The Q-weak detector shielding hut is large enough to accommodate the detectors, associated electronics and their support structures. The barite($BaSO_4$)-loaded concrete front wall (wall thickness of 1 meter) of the main detector shielding hut has an aperture for each octant (see Fig. 3.16 (a)) and the apertures are sufficiently large (20 cm upper clearance, 5 cm lower clearance and 3-15 cm side clearance with respect to the main Čerenkov detector) so as to not define the acceptance of the detectors.

Although low energy Møller electrons are deflected out of the detector acceptance by the magnetic field, their large cross-section and corresponding high rate turns the collimators into intense gamma ray sources. A line-of-sight blocking lintel was installed inside the toroidal magnet between the two coils for each octant. The main detector sees about 0.1% yield from background reactions on the collimators, in air, and on the shielding wall. Weighted by the background asymmetry, this constitutes a 1% background.

3.6.2 Toroidal Magnet

The Q-weak toroidal magnet, referred to as "QTOR" in the Q-weak experiment, serves to separate the elastic and inelastic events and is used to focus the elastic electrons onto the main detectors in the focal plane for the asymmetry measurement. It is a resistive iron-free toroidal magnet with an eight-fold symmetric structure. Its' field is produced by a set of eight identical racetrack-shaped coil packages with $\Delta\phi = 45^o$ gaps between them. The coils are driven by a DC power supply with a maximum current of 9 kA.

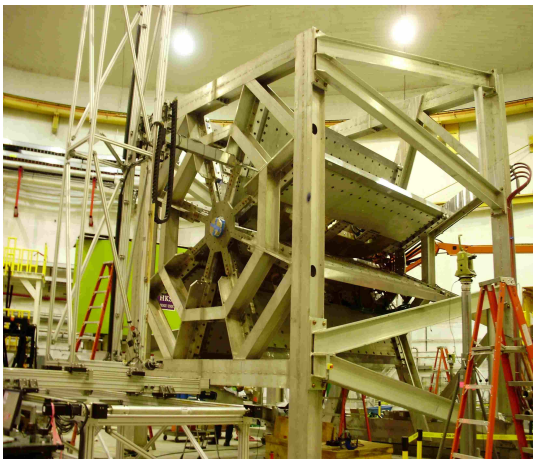

(a) Magnetic field mapping for the QTOR at MIT-Bates with a 3D field mapper.

(b) QTOR shown on the Hall-C floor between the GEM and main detector shielding hut.

Figure 3.17: Q-weak toroidal magnetic field spectrometer.

The QTOR magnet has a field integral of about 0.67 T·m along the central trajectory of the elastically scattered electron. It is optimized to focus elastically scattered electrons for the Q-weak primary beam energy and angle, and is therefore not a momentum focusing spectrometer. There is a strong correlation between the radial coordinate and momentum, so elastic scattering from the liquid hydrogen target appears (poorly focused) at a slightly smaller radius (radius meaning distance from the beam line in the focal plane), while inelastically scattered electrons from threshold pion production intercept the focal plane at slightly larger radius (for a detailed discussion of the QTOR focusing property, see reference [Wang, 2007]). Positive particles with low momenta are

bent inward and prevented from striking the opposite octant by thick shielding around the beamline. The spectrometer focuses most of the collimated elastic electrons into an envelope which is roughly 10 cm tall in the dispersive direction, but about 2 meters wide in the non-dispersive direction. Due to large ϕ-dependent aberrations, some curvature of the elastic event envelope results in a moustache-shaped image on the focal plane (as seen in Fig. 3.2).

In order to achieve the proposed precision in the asymmetry measurement, a lot of work focused on an in-depth study of the magnetic field generated by the QTOR spectrometer, including the magnetic field simulation and development of analysis techniques for field mapping [Wang, 2007]. The actual magnetic field mapping was successfully conducted at MIT-Bates Laboratory[8] (see Fig. 3.17 (a)) using a 3-axis magnetic field mapper. The magnet was fiducialized at MIT-Bates, transported to JLab and installed in the experimental Hall C, where it was remapped and calibrated to verify the installation precision and magnet performance. During production running, the nominal QTOR current setting is 8920 A. Fig. 3.17 (b) shows the installed magnet with the completed main detector shield house.

3.6.3 Tracking Detectors

Since the physics asymmetry is directly proportional to the weak charge of the proton at low Q^2 and the proportionality constant is Q^2, a precise determination of the momentum transfer is critical. The uncertainty in Q^2 directly translates to an additional uncertainty in the extraction of the proton's weak charge. The acceptance-weighted distribution of Q^2, weighted by the analog response of the Čerenkov detectors, needs to be determined to 1% accuracy or better. In addition to the precise Q^2 determination, the tracking system is also used to help determine the 'dilution factor': the contribution of non-elastic scattering events to the Čerenkov detector signal, such as inelastic events from the target, events arising from the detector walls, and any general background in the experimental hall.

There are three regions of tracking detectors being designed and constructed. The Region 1

[8] Bates Linear Accelerator Center of the Massachusetts Institute of Technology, Danvers, USA

tracking detectors, located upstream of the acceptance defining (second) collimator, are gas electron multipliers (GEMs). They are designed to have excellent position resolution for vertex determination. Region 2, located at the entrance of the QTOR spectrometer, houses a set of horizontal drift chambers (HDC). Both the GEMs and HDCs are used to reconstruct the scattering angle of elastically scattered events to high accuracy, by utilizing the spatial separation between them. Region 3, located just upstream of the focal plane with the main detectors, contains a set of vertical drift chambers (VDCs). The VDCs are used to momentum-analyze the scattered electrons, determine the particle trajectories and map the electron detection efficiency across a main detector bar. In addition, a set of trigger scintillators, located between the Region 3 VDCs and the main Čerenkov detectors, provide trigger and event timing reference, and a focal plane flux profile scanner in the bottom (floor) octant is used for Q^2 extrapolation from low current to high current, as well as monitoring the beam optics and rate verification. Each set of tracking chambers (in all three regions) instrument two opposite octants and are rotated to any given octant during tracking measurements.

The tracking detectors are inoperable at high beam current (during asymmetry measurement) since the counting rate per octant at the focal plane is about 800 MHz at 180 μA. For the Q^2 calibration measurements, the beam current is reduced to sub-nA levels to allow the tracking detectors to operate in single event counting mode and the trigger rate is pre-scaled down to provide a manageable data acquisition rate. The tracking detectors (except the GEM detectors) have been fully commissioned and have been used successfully to determine the momentum transfer, measure the electron detection efficiency across the main detectors, and characterize backgrounds. Each of the 8 octants has been characterized with the tracking system. Some details of the tracking detectors are introduced below.

Region 1: Gas Electron Multiplier (GEM)

The Region 1 tracking chambers act as scattering vertex detectors. However, rates at the entrance to the spectrometer will be three orders of magnitude higher than at the focal plane, dominated by low-energy Møller electrons that fall within the collimator acceptance — the elastic rates at a beam

current of 10 nA would approach 45 kHz, a large, low electron momentum (~50 MeV) background due to Møller scattering will be present which is at least a factor of 100 larger than the elastic rate [Forest, 2003]. This large signal from Møller scattering will prevent the use of traditional drift chambers. Hence, the GEM detectors (a high flux micro-pattern gaseous detector used to amplify the ionized charge within a gas chamber and detect charged particles) are chosen for the Region 1 because they are radiation hard and can work at the anticipated rates.

A GEM consists of thin polymer foils, metal-clad on both sides and perforated by holes having a radius on the order of 50 μm in a staggered grid pattern, in which the distance between adjacent holes is on the order of 100 μm. The foil acts as a pre-amplifier when immersed in the gas volume of an ionization chamber. Charge multiplication occurs when the electrons pass through the foil holes (the electrons are produced during ionization of the gas) whose sides have had a electric potential difference applied to produce electric fields on the order of 40 kV/cm. The large amplification, in excess of 10^4 for a multi-stage device, facilitates single particle detection by charge collectors.

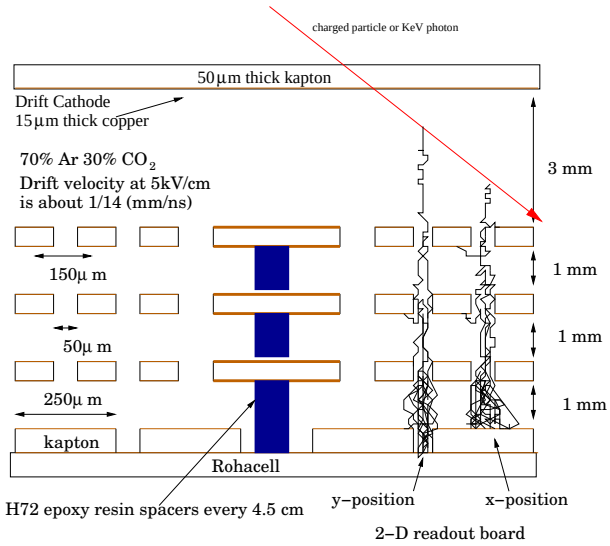

Figure 3.18: Schematic side view of an ionization based tracking chamber with three GEM preamps and a 2-D readout board.

The chambers were constructed from Rohacell and copper clad kapton foils with a fiberglass support structure — the front entrance window to the detector is a sheet of 1 mm thick Rohacell

which supports a copper-clad kapton sheet 50 μm thick, the walls of the ionization region are created using a 8 mm thick fiberglass frames. The charge collector is mounted on the bottom of the ionization chamber and then three GEM foils are stacked on top (see Fig. 3.18). The charge collector has a pitch of 400 μm to provide sufficient resolution. Once charge is accumulated at the collector, pulse shaping and amplification electronics are used to convert a charge equivalent of 500 electrons to a mV signal. The pulse shaping and amplification electronics are incorporated into the multiplexing chip and wire-bonded to kapton leads that are connected to individual charge collector output channels. A multiplexing circuit is used to reduce the number of electronics modules needed to read out the charge collector signals.

The GEM detector has an active area of 10 cm^2, a thickness of ~6 mm and is located just downstream of the first collimator. Two identical detectors are mounted on the opposite sides of the beam on a rail system to move radially into the acceptance for low current (nA) Q^2 current measurements or to move out of the acceptance at high beam currents, , during production running. A rotation system is used to move the detector to different octants (see Fig. 3.19).

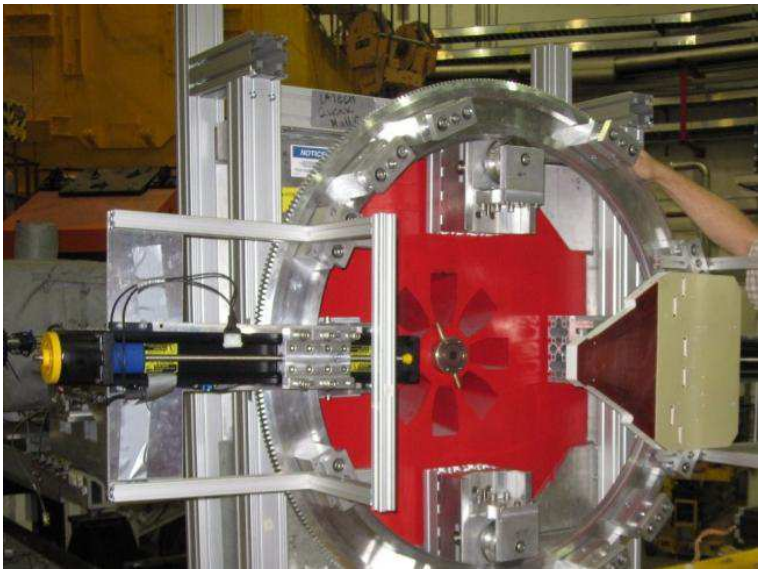

Figure 3.19: Photo of the Region 1 GEM, showing one GEM mounted in the rotation/translation stage prior to completion of the GEM shielding hut.

The design goal for the GEMs is to reach an average tracking efficiency of 99% at an operating event rate of 12 MHz with particle fluxes of 500 Hz/mm^2. To date, the GEMs have not been fully commissioned.

Region 2: Horizontal Drift Chamber

The Region 2 tracking chambers are a set of horizontal drift chambers [9] (HDCs) located just upstream of the QTOR magnet and downstream of the acceptance defining (second) collimator. They are used to establish the initial scattered electron trajectory before the magnet and the interaction vertex by determining the track back to the target — they determine the position and direction of the scattered electrons at the magnet entrance, they can also be used to provide an accurate measurement of the scattering vertex and angle in combination with the Region 1 GEMs, once these become available, and are used to reject the secondary scattering events at the collimator. When combined with the exit angle determination (after the magnet) from the Region 3 tracking detectors and the QTOR field map, the scattered particle's momentum can be determined. With measurements of the scattered particle's momentum and scattering angle, the $\langle Q^2 \rangle$ of elastically scattered electrons can be determined.

The Region 2 HDCs, consisting of two sets of two self-contained chambers (with 42 cm separation between the two chambers), are located 3.15 m (the upstream chamber) and 3.57 m (downstream) from the center of the Q-weak target at a radial distance of about 0.7 m from the beam centerline in a region where the residual field from the QTOR magnet is small (less than 3 G). These chambers have a precision of about 0.6 mrad for the angle determination and a spatial resolution of 170 μm. The measured single plane efficiencies are better than 99%. To reduce multiple scattering, a small amount of material is used in the construction of these chambers. Each chamber has an active area of approximately 50 cm $\times$ 70 cm and a radiation length of 0.075%. In order to keep the chambers out of the flux of scattered particles from neighboring octants, the chamber frames have a trapezoidal shape, being larger at the outer radius side.

[9] Drift chambers are gas-filled devices that contain an array of wires and use a high electric field to detect charged particles from ionization in the gas.

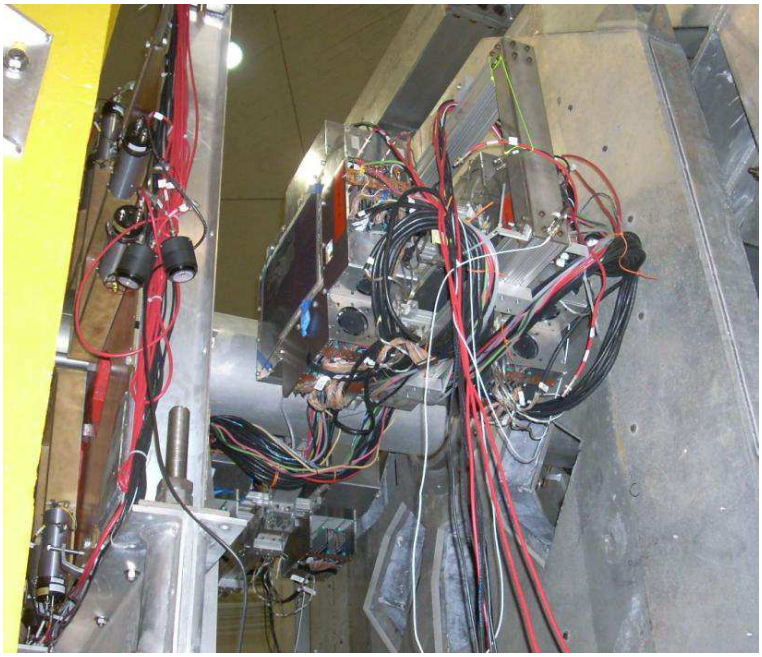

Figure 3.20: Photo of the region 2 HDC's mounted on their motion mechanism, between the 2nd and 3rd collimators.

The chambers are mounted on a small Ferris wheel rotating hub structure on the opposite side of the beam to form two "arms" fixed 180° apart. Each arm can be positioned radially. In order to make alignment more reliable and reproducible, the chambers are pinned to the two positions – "in beam" for the calibration runs and "parked" where they will sit with the protection of the shielding during production running. The arms are attached to a central hub so that they can be manually rotated about the beam pipe. Fig. 3.20 shows a photo of the region 2 HDC's mounted on their motion mechanism.

Region 3: Focal Plane Chambers (VDC)

The Region 3 focal plane chambers are vertical drift chambers (VDCs), a type of drift chamber that tracks the scattered electron by collecting ionization that has traveled in the vertical direction, to determine the location and angle of the scattered electron downstream of the magnetic field.

They are used in conjunction with the Region 2 chambers, to establish the deflection of particles while traversing QTOR, and to map out the origin of the scattered electrons that arrive at the main detectors, so as to measure the average Q^2 distribution of scattered electrons.

The elastic peak at the focal plane has a perpendicular cross-sectional area of $\sim 18 \times 200$ cm^2 (see Fig. 3.2). To cover this area, the VDCs are designed to have an active area of about 50 cm wide, and 2 m long. The chambers are oriented at 45° with respect to the nominal elastic scattering trajectory. Each chamber is 10 cm thick (in beam direction) and has 3 high voltage planes and two wire planes. The sense wires are 25 μm diameter gold-plated tungsten soldered onto photo-etched kapton foils. In order to ensure efficient track reconstruction, the number of wire cells that could be hit by the electrons in each plane are between 4 and 8. The cell spacing is about 5.5 mm which yields an intrinsic position resolution of about 100 μm. Two chambers, each has two wire planes, define the particle trajectory with a set of 4 points, one per wire plane. The two sets of chambers are separated by 30 cm, hence provide excellent position and angle reconstruction. Two packages of chambers (each package consists of two chambers) were constructed. Each chamber has a footprint of 2.3 m (in azimuthal direction) by 1 m (in radial direction), weighs 374 kg, and has 2 planes each with 281 sense wires. The two packages are placed at opposing octants so that two measurements can be made at a time. A total of 4 measurements needs to be made in order to cover the entire detector system.

The two opposing pairs of Region 3 VDCs and their associated trigger scintillators are mounted radially 3 meters away from the beam pipe, supported by a massive rotating support structure known as the Region 3 Rotator, which can be rotated sequentially about the beam line axis, so that tracking data can be obtained in all 8 octants. The entire assembly is placed immediately upstream of the main Čerenkov detectors, inside the shielding hut (see Fig. 3.21). The chambers can slide radially out of direct view of the beam (retracted to a “parked” position) to avoid damage during high current production data-taking and can be repositioned with a measured positioning reproducibility of better than 3 mm.

The measured efficiency of each individual plane is better than 99.8%, and the resolution in

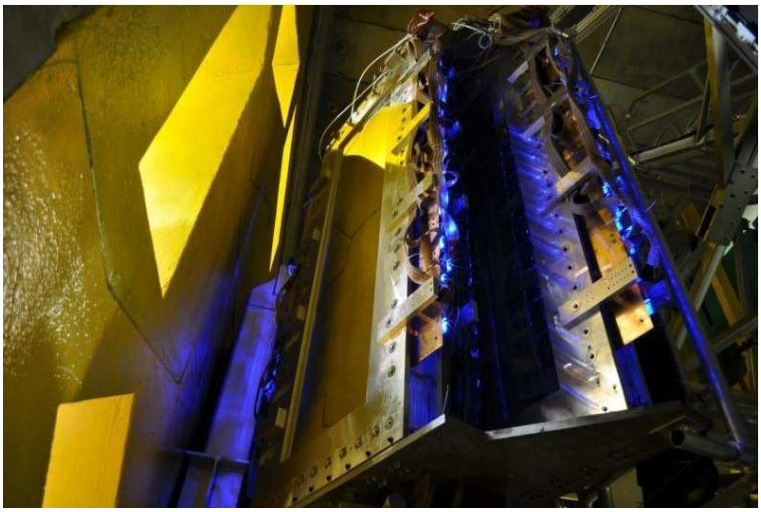

Figure 3.21: Photo of the region 3 VDC's mounted on their motion mechanism in the main detector hut.

an individual plane is 220 μm. Fully reconstructed tracks from a pair of VDCs have a residual of 310 μm.

Scintillation Counters

The event mode calibration system needs a trigger, which is provided by two scintillation counters. The scintillation counters also provide a time reference for the drift chambers and serve as rate indicators while running at lower beam currents. The scintillators are Saint-Gobain BC408 ($C_{10}H_{11}$, Polyvinyl Toluene and Organic Fluors), which produce an energy deposition of 2 MeV/cm for 1 GeV electrons and scintillation yield of 10 photons per keV of energy deposition with a 1 ns rise time, a 2.5 ns FWHM (full width at half maximum), and a 2 ns decay time. Each scintillator is 220 cm long, 30 cm wide and 1 cm thick – slightly larger area than the Čerenkov bars to shadow the main detectors. Their long edge surfaces are diamond milled and the ends are 600 grit sanded. A photograph of one of the two 2 meter long trigger scintillators with PMTs is shown in Fig. 3.22.

The trigger scintillators are supported by aluminum frame and mounted immediately downstream of the Region 3 VDC chamber package. As part of the Region 3 tracking package, they can

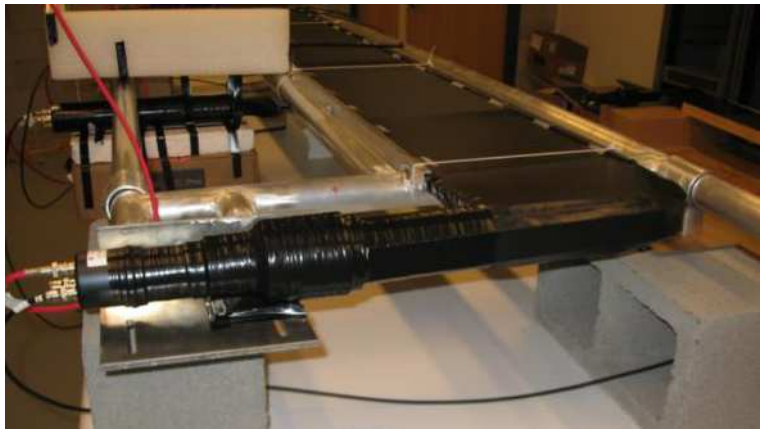

Figure 3.22: Photo of a trigger scintillator on the bench.

travel together with VDCs and cover various octants.

The scintillation light is read out with 3 inch Photonis XP-4312 PMTs through UV transparent "finger" light guides (Adiabatic Lucite) on both ends of the scintillator with a coupling area of 30 cm^2. The photon arrival time at each PMT might be different when the electrons pass through different places on the scintillator due to the path length difference of the photon transportation inside the scintillator. In order to make the trigger timing independent of where the electron passes through the trigger scintillator, a mean-timer[10] is used to decouple the hit position dependence.

The trigger scintillators must have sufficient energy resolution and timing capabilities to identify multi-particle events and veto neutrals. Since plastic scintillators have $\sim$ 1%/cm neutron detection efficiencies, the false triggers from neutrals are minimized by minimizing the thickness of the scintillators to 1 cm, while keeping the thickness large enough for sufficient signal size from the elastically scattered electrons. The timing resolution for the as-built trigger scintillators is measured to be better than 460 ps.

[10] A mean-timer is an electronics module, which takes two timing signals (t_1 and t_2) as inputs, and outputs an average signal $(t_1 + t_2)/2$.

Profile Scanner

During production running conditions, current-mode diagnostics must be employed to check that the beam envelope has the correct shape and position at the detector plane. In addition, as the Q^2 distribution is sampled at low beam currents, any changes at higher currents, such as the target density changes due to target heating, have to be determined. The focal plane flux profile scanner is such a diagnostic device for the Q-weak experiment. It consists of a small active area radiator, operating at counting mode. The scanner can map the rate/light distribution of the main Čerenkov detector at both low beam current and high beam current so that the momentum transfer mapping at low beam current can be extrapolated to high beam current with confidence.

The scanner detector assembly uses two small (1 cm $\times$ 1 cm $\times$ 1 cm) fused silica radiators, each coupled to a 2 inch PMT by an air-core light pipe. High energy electrons passing through the radiators emit Čerenkov radiation in the form of UV and visible light. Quartz is used as the radiator medium because of its radiation hardness and insensitivity to neutral background. Air-core light pipes, their inner surface made from a reflective material, are used to minimize backgrounds arising from interaction of electrons with the light guide material, for example light arising from scintillation or from Čerenkov radiation.

A 2D linear motion system is used to scan the detector assembly in the focal plane. The motion system consists of two stainless-steel ball-screw driven tables and has a motion range of 0.35 m in vertical direction and 2.5 m in horizontal direction. It is driven by servo-motors controlled remotely by a computer. The detector assembly mounted on the motion system can scan over the fiducial area of the main detector (see Fig. 3.23 (a)). Because the maximum electron flux at the focal plane is about 1 MHz/cm^2, the scanner will operate in counting mode. The PMT output pulses are discriminated. Coincidences between the two PMTs are counted in a scaler to generate position-dependent rate information. Scaler rates are synchronized with motion system position information to deduce the electron spatial distribution in the focal plane (see Fig. 3.23 (b)). The scanner also provides a useful trigger when acquiring raster images used to center the beam inside the beam collimator, and to center the targets on the beam. The scanner is also used in QTOR scans, background studies, and

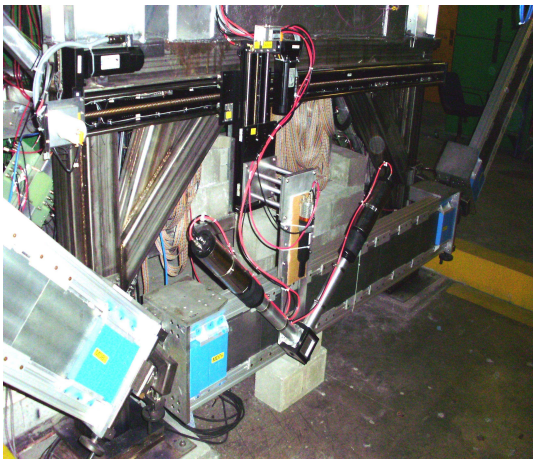

(a) Focal plane profile scanner

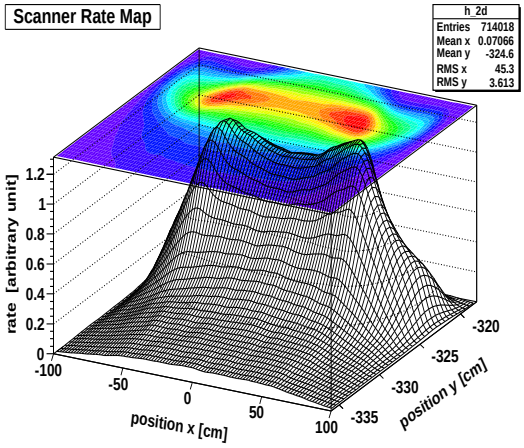

(b) Flux distribution obtained by the scanner.

Figure 3.23: (a) Photo of the focal plane flux profile scanner. (b) Scattered electron flux distribution (in the bottom octant focal plane) obtained by the profile scanner at 10 μA beam current. The x-axis is in horizontal direction, the y-axis is in vertical direction. The z-axis indicates the rate per unit area in an arbitrary unit.

spectrometer optics studies.

3.7 Main Detector

The main detector system employs a set of eight Čerenkov detectors. Each of them consists of two 1 meter long fused silica (Spectrosil 2000 synthetic quartz) bars glued together end-to-end. These radiation hard quartz bars are 18 cm wide and 1.25 cm thick with 200 μm flatness and a 25 Å(RMS) polish. The eight 2 meter long quartz Čerenkov detectors are placed in a special shielding enclosure to reduce the background. All 8 main detector modules are installed on a Ferris wheel structure that supports them at the desired radius. One spare module is used for background measurements. Each detector has two 5 inch PMTs, equipped with two types of custom made PMT bases: one for high gain counting mode calibration running at nA level beam currents and one for low gain current mode production running at beam currents up to 180 μA. The main detector system plays a key role in the Q-weak experiment and forms the main subject of this thesis. The main detector design,

development, construction, installation, commissioning, and associated diagnostic data analysis to verify the performance will be discussed in detail in the following chapter.

3.8 Luminosity Monitor

At very forward scattering angles (less than 1° compared to the central Q-weak scattering angle of about 8°), the scattered electron rate is much higher and the parity violating asymmetry is much smaller. Luminosity monitors (LUMIs – auxiliary current mode detector) can be placed close to the beam line and serve as a "null-asymmetry" monitor and as a target density fluctuation monitor. The luminosity monitor will have a relatively small statistical uncertainty per measurement period as compared to the main detector, due to the high count rates. The physics asymmetry is expected to be very small (about 1% of the main detector asymmetry) due to the low average Q^2 at these very forward angles. The smaller statistical uncertainty make the luminosity monitors much more sensitive to target density fluctuations as well as beam parameter fluctuations (indicated by increasing asymmetry widths); since they are expected to have a much smaller asymmetry than the main detector, a non-zero asymmetry would indicate the presence of a false, helicity-correlated, effect in the experiment. For example, after applying corrections (discussed in section 5.5) for helicity-correlated beam properties to the luminosity monitor, the luminosity monitor should be corrected to zero asymmetry within uncertainties. Otherwise, this is an indication of unaccounted systematic effects that lead to a false asymmetry and need to be investigated.

There are two sets of LUMIs installed in the experiment. The first set is an array of 4 small Čerenkov detectors situated on the upstream face of the acceptance defining (second) collimator (see Fig. 3.24 (a)), looking at scattering angles slightly smaller than that of the mean experiment scattering angle ($\sim 5°$) and will detect mostly Møller electrons. They are 7 cm $\times$ 27 cm $\times$ 2 cm Spectrosil 2000 quartz bars read out with 2 inch Hamamatsu R375 phototubes with quartz windows in photodiode mode, through air-core light guides from each end of the quartz radiators. These detectors see a rate of about 133 GHz, and will be primarily used as target density fluctuation

(a) Four "U"-shaped upstream LUMIs mounted on the upstream face of the primary collimator.

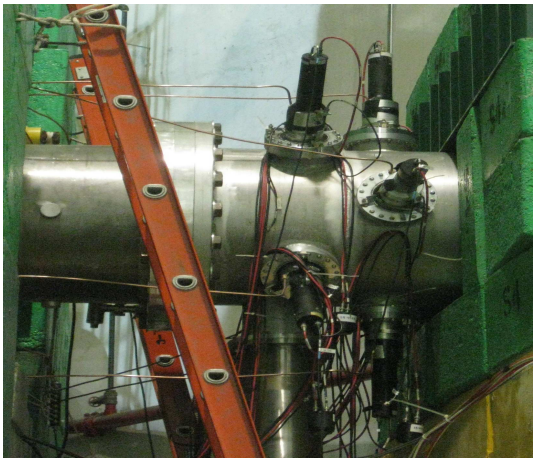

(b) Eight downstream LUMIs installed in the downstream beam pipe at the end of the beamline.

Figure 3.24: Photos of luminosity monitors.

monitors, because they will be relatively insensitive to incident beam angle and energy changes, and will be sensitive to changes in most of the target, with decreased sensitivity to the downstream end of the target. The second set is an array of 8 small Čerenkov detectors located far downstream (17 meters downstream of the Q-weak target), past the main detector and close to the beam dump (see Fig. 3.24 (b) and Fig. 3.1). They are placed symmetrically about the beampipe at a mean scattering angle of about 0.5°, and will be used primarily as null asymmetry monitors to monitor the helicity-correlated beam properties. The downstream LUMIs have sensitivity only to the downstream end of the target. Each of the eight downstream LUMIs consists of a small tapered piece of 4 cm $\times$ 3 cm $\times$ 1.3 cm block of Spectrosil 2000 quartz (same as the Čerenkov radiator). Since the detectors are positioned in a harsh environment, the Čerenkov light is transported away from the quartz radiator located close to the beam centerline via 35 cm long air-core light guides, made out of a reflective aluminum material (Anolux Miro IV PVD [11]), to a Hamamatsu 2 inch R375 phototube with a quartz window, operating in photodiode mode. The active medium of the detectors is inserted into special cups which penetrate the 60 cm diameter beampipe to within 13 cm of the nominal beamline. These

[11] Anomet Inc., http://www.anomet.com/mirfuture.html

detectors see about 100 GHz of scattered electrons and are expected to withstand a dose of 1.8 GRad over the course of the experiment.

Although the designs of the upstream and downstream LUMIs differ, both sets of detectors were instrumented with radiation hard Spectrosil 2000 quartz (the same quartz chosen for the main Čerenkov detectors) to detect the Čerenkov light created by the incident electrons in a specific angular range. Both sets of LUMIs were studied in both current (production) and event (tracking) mode. These linear, unity-gain devices have a large photocathode current under regular operating conditions (about 1 μA) which is comparable to the photoanode current of $\sim 6\,\mu$A, expected for the main detectors, so the same low-noise, high gain I-to-V preamp design developed for the Q-weak main detector (see section 4.5.1) are used for LUMIs. The voltage output from the preamplifiers is then fed into the same chain of digitizing electronics that is used for the main detector.

Parameter	Luminosity monitor	Main detector
$\langle A \rangle$	0.003 ppm	-0.29 ppm
Count rate	29 GHz/det.	0.8 GHz/det.
$\delta A_{\text{stat.}}$, complete experiment	0.0008 ppm	0.005 ppm
$\delta A_{\text{stat.}}$, per pair	0.8×10^{-5}	5×10^{-5}
Energy sensitivity	-0.0020 MeV^{-1}	-0.0020 MeV^{-1}
Angle sensitivity	-260 rad^{-1}	-27 rad^{-1}
Position sensitivity	-20 m^{-1}	-18 m^{-1}

Table 3.5: Luminosity monitor parameters at the nominal 0.75° scattering angle compared to the main detector. The statistical uncertainties on the asymmetry are for all eight LUMIs or main detectors combined. The quoted sensitivities to beam parameter variations are for a single detector, before use is made of symmetry by averaging over detectors.

The expected parameters, such as physics asymmetry, statistical uncertainty, and sensitivities to beam parameter variations for the LUMIs, determined from simulations are compared to the same parameters for the main detectors and are listed in Table 3.5. As a target density fluctuation monitor, the most critical parameter is the LUMIs' statistical uncertainty per helicity pattern as to that of the main detector. If the target density is varying on a time scale comparable to the helicity reversal time (but uncorrelated with the helicity state), it will add in quadrature with the statistical width.

The LUMIs are much more sensitive to target density fluctuations than the main detectors. They are used during diagnostic measurements to determine the optimum target operating parameters (beam raster size, target pump speed, target temperature, etc.). During regular production running, the LUMIs serve as an “early-warning” device to alert to any changes in target and beam operating conditions.

Chapter 4

Main Detector System

4.1 Overview

The Q-weak toroidal spectrometer deflects the scattered electrons away from the beam line and focuses the elastically scattered electrons onto the focal plane to form eight approximately 200 cm wide and 10 cm tall moustache-shaped profiles (see Fig. 4.1). The event rate in the focal plane is 830 MHz per octant. The scattered electrons are detected by eight fused silica (Spectrosil® 2000 synthetic optical quartz) Čerenkov detectors (the concept diagram of the Čerenkov detectors is shown in Fig. 4.2). Quartz was chosen as the active detector material, based on its radiation hardness, its low sensitivity to neutral background (e.g. the absence of scintillation), its uniform response (homogeneity of the material), and low intrinsic noise (secondary absorption and emission of light) [Adam et al., 2005]. The active volume of each of the eight detectors is 200 cm by 18 cm by 1.25 cm and therefore covers the entire elastic profile (including a small amount of inelastic events and target window background; discussed later in a separate section), as determined by the acceptance defining collimator, which selects about 4% of π in θ and about 53% of 2π in ϕ. The active detector volume consists of two optically glued 100 cm long quartz pieces from a single ingot. Two 5 inch (13 cm) photomultiplier tubes (PMT), one at each end of a detector are optically glued to light guides. The light guides are actually simple extension of the active quartz bar itself,

also made of quartz (20 cm×18 cm×1.25 cm), and in turn are optically glued to the active quartz volume. This choice of geometry was mostly based on spatial constraints, as well as financial constraints, accommodating all eight detectors in the focal plane, while covering the entire scattered beam envelope in the chosen acceptance. However, extensive simulations have been carried out, to ensure that the detectors satisfy the basic requirements of the experiment, outlined below. The light guide extensions remove the PMTs from the direct shine of the elastic electron envelope and allow for lead shielding of the PMTs.

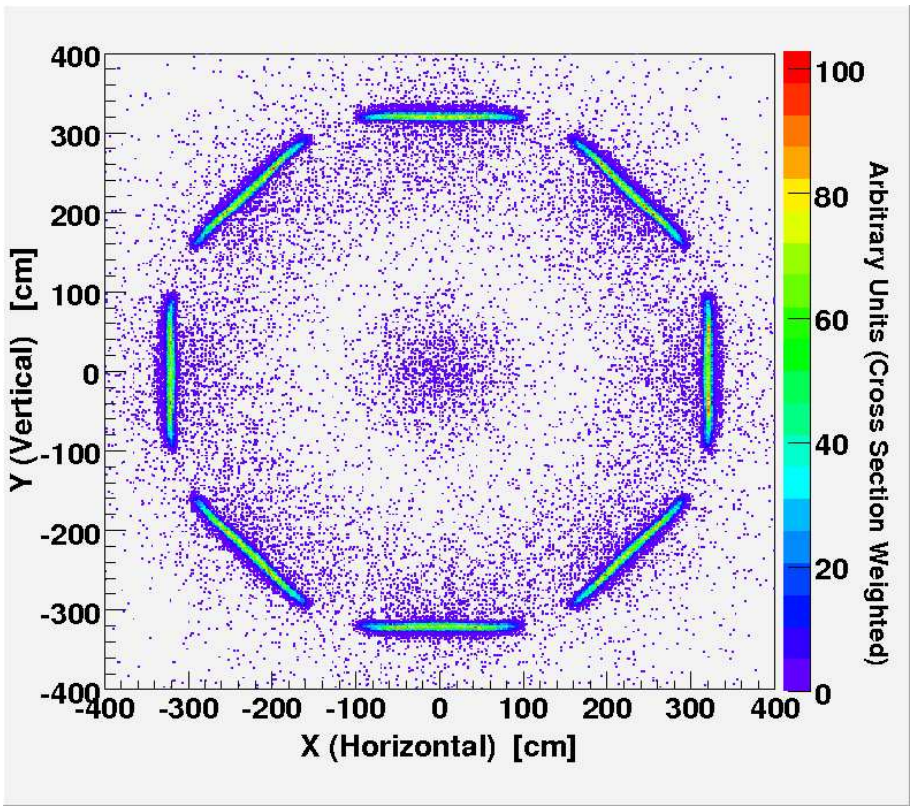

Figure 4.1: Electron flux profile on the focal plane, each beam spot is about 2 m long.

Fig. 4.3 shows the arrangement of the detectors in the focal plane. Fig. 4.4 shows the geometry of a single radiator and the average incident electron trajectory with respect to the detector surface (defined by the surface that is coplanar with the focal plane). As seen from the figures, on average, the scattered electrons traverse a distance of about 1.35 cm with an incident angle of 22°, as they

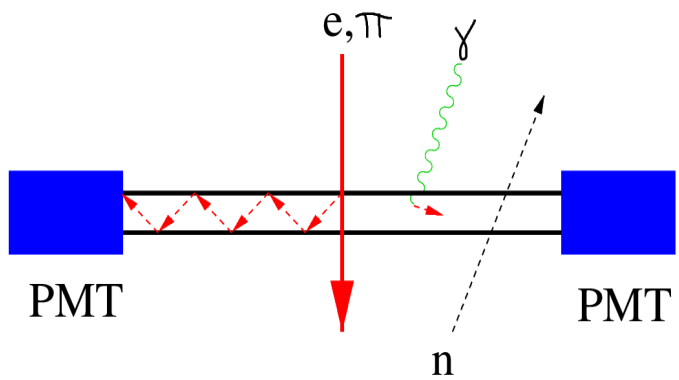

Figure 4.2: Concept diagram of Q-weak Čerenkov detector.

travel through the quartz.

If a relativistic electron of velocity βc that scatters into the quartz detector is moving faster than the speed of light (i.e., its velocity is greater than the local phase velocity of light in the medium), Čerenkov radiation is generated [Leo, 1994]. The Čerenkov photons are emitted at a well defined Čerenkov polar angle (θ_C), uniformly in azimuthal angle (ϕ_C) with respect to the electron trajectory, forming a cone about the electron trajectory:

$$\cos\theta_C(E) = \frac{1}{\beta n(E)}\,, \tag{4.1}$$

where $n(E)$ is the index of refraction of the radiation medium as a function of the energy E of the emitted photon. The Čerenkov radiation threshold is at $\theta_C = 0$, i.e., $\beta = 1/n$. The index of refraction of the fused silica radiator material is $n = 1.482$ at 280 nm (see Table A.3), so the Čerenkov threshold energy for an electron in the quartz bar is

$$E_{\text{th.}} = \sqrt{p^2 + m_e^2} = \sqrt{(m_e\gamma\beta)^2 + m_e^2} = m_e\sqrt{\frac{1}{1-\beta^2}} = m_e\sqrt{\frac{n^2}{n^2-1}} \simeq 0.7\ \text{MeV}, \tag{4.2}$$

in which p is the electron momentum, m_e is the static mass of the electron and $\gamma = (1-\beta^2)^{-\frac{1}{2}}$. Fig. 4.5 shows the momentum threshold of Čerenkov radiation for several charged particles. The average

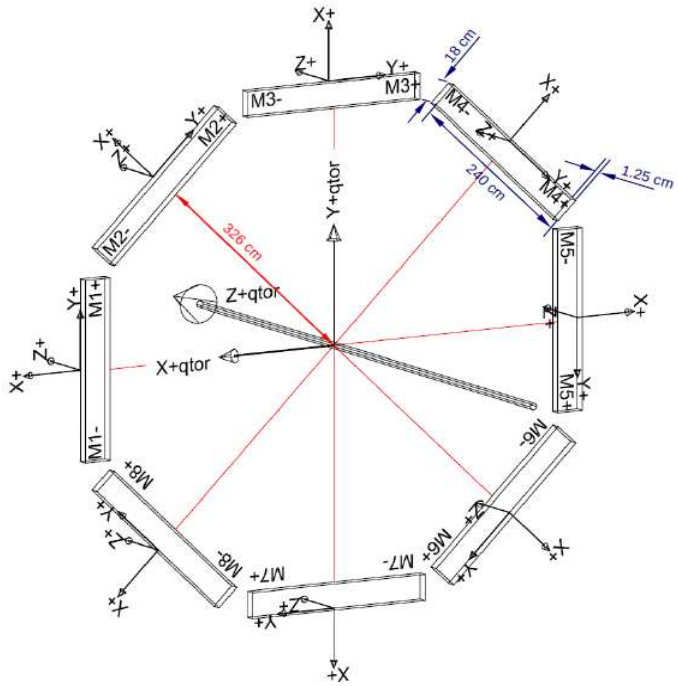

Figure 4.3: Q-weak coordinate systems and schematic layout of the main Čerenkov detectors in the focal plane. There are eight sectors of the QTOR magnet, named as octant 1, octant 2, and so on, respectively. The octants are numbered in the clockwise direction, where octant 1 is the horizontal octant to beam left when looking downstream. The installed QTOR coils are numbered from 2 through 9, with coil 2 located between Octant 3 and Octant 4 (at $\phi = 102.5°$), and the coil numbers increasing in the clockwise direction, as well. The octant numbering convention leads to a natural convention for a right-handed global Cartesian coordinate system — when looking downstream, the positive X axis points to beam left horizontally, the positive Y axis points upward vertically, and the positive Z axis points downstream along the beam axis. The corresponding cylindrical coordinates use the positive X axis as reference for the azimuthal angle ϕ. The ϕ increases in the clockwise direction, thus octant 1 would centered at $\phi = 0$, octant 2 would be centered at $\phi = 45°$, and so on and so forth. Apart from the global coordinates, there are local coordinates defined for each octant. The octant local coordinate system has the positive X axis pointing along the increasing radial direction at the center of the octant, the positive Y axis pointing along the increasing ϕ direction, and the positive Z axis pointing downstream along the beamline. In octant 1, the local coordinates are consistent with the global coordinates. The origins for all coordinates are located at the same point — the geometry center of the QTOR. The main detectors are named as MD1 (or M1), MD2 (or M2), and so on, according to their corresponding octant number. The two PMTs at the ends of each quartz bar are marked as "+" and "−" (or "pos" for "positive" and "neg" for "negative", or "p" for "plus" and "m" for "minus"), according to its Y-location in the local coordinate system. The focal plane is the $Z = 578$ cm plane.

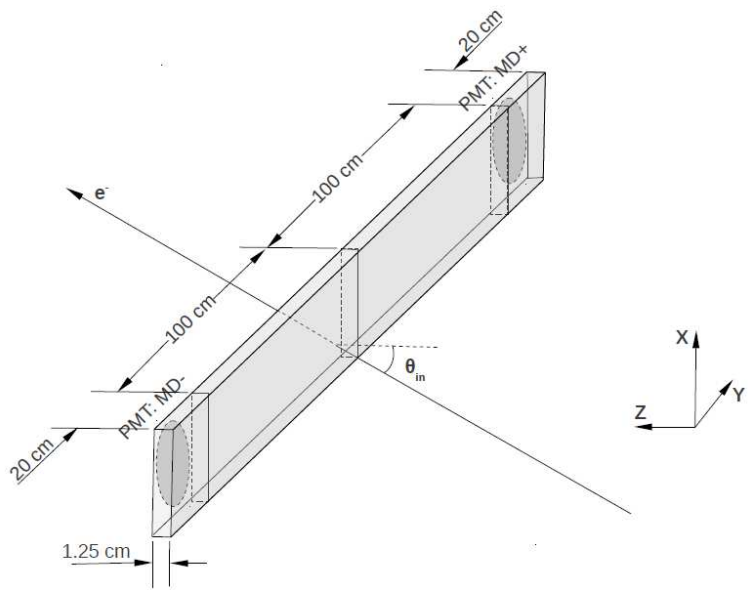

Figure 4.4: The geometry of a single main detector and the average incident electron trajectory with respect to the main detector surface in the local coordinate system of the main detector. The average incident angle (θ_{in}) is 22°.

number of photos produced (N) is given by the Frank-Tamm equation [Frank and Tamm, 1937]:

$$N = \int \frac{\alpha Z^2}{\hbar c}\left(1 - \frac{1}{\beta^2 n^2(E)}\right) dEdx = \int \frac{\alpha^2 Z^2}{r_e m_e c^2} \sin^2\theta_C(E) dEdx \ , \tag{4.3}$$

where $\frac{\alpha^2 Z^2}{r_e m_e c^2} \simeq 370\ \text{eV}^{-1}\text{cm}^{-1}$ for $Z = 1$ (Z is the charge of the particle in unit of the electron charge), x is the path length, traversed by the particle in the medium. The average number of photo-electrons observed ($N_{p.e.}$) is then given by:

$$N_{p.e.} = 370L \int \epsilon(E) \sin^2\theta_C(E) dE \ , \tag{4.4}$$

where L is the total path length of the electron through the radiator in centimeters, ϵ is the overall detection efficiency for collecting the Čerenkov light and transducing it into photo-electrons, E is the photon energy in electron-volts ($E = 2\pi\hbar/\lambda$, λ is the photon wavelength, $\hbar = 197\ \text{MeV} \cdot \text{fm}$ is the reduced Planck constant). ϵ can be factorized as $\epsilon = \epsilon_{\text{coll}}\epsilon_{\text{det}}$ with the geometrical photon

collection efficiency (ϵ_{coll}) varying substantially for different tracks while the photon detection efficiency (ϵ_{det}) remains nearly track independent. In the following discussion, the detected number of photo-electrons $N_{p.e.}$ might be directly referred to as "light yield" instead of the actual light yield N, to involve in the efficiency of light collection and light detection.

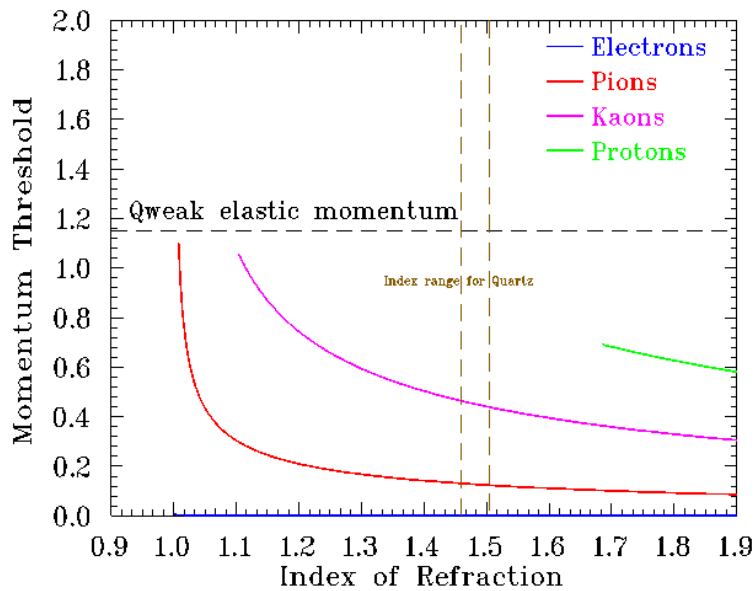

Figure 4.5: Momentum threshold of Čerenkov radiation for several charged particles [Mack, 2002].

For Q-weak scattered electrons of about 1.1 GeV ($p = m_e\beta\gamma = 1.1$ GeV, $\beta \simeq 1$), the Čerenkov angle is $\theta_C = \arccos(1/n\beta) \simeq 47°$. From Eqn. 4.3 and 4.4, each electron produces on average 1000 optical photons between 200 nm (6.19 eV) to 800 nm (1.55 eV), most of which are in the UV range and at shorter wavelength (see Fig. 4.6). These are emitted in a $\sim$ 47 cone (with respect to the incoming electron trajectory). From Monte Carlo simulation, about 250 photons of these arrive at both PMT photocathodes (meaning about 125 photons per photocathode) by total internal reflection (TIR), and the detected number of photo-electrons is about 16 - 20. Therefore, the total collection efficiency (ϵ_{coll}) is about 25% and the the detection efficiency (ϵ_{det}) is about 7%.

Total internal reflection occurs at medium boundary if the light incident angle is larger than a particular critical angle with respect to the normal to the surface. The critical angle (θ_{TIR}) is

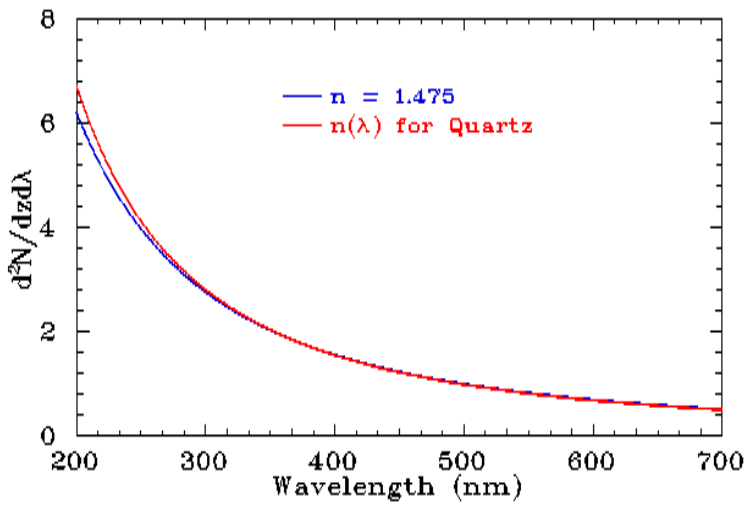

Figure 4.6: Čerenkov light wavelength distribution — the number of photons per nm wavelength per cm track length (see Eqn. 4.29) versus wavelength.

determined by refractive index:

$$\sin\theta_{TIR} = \frac{n_{\text{air}}}{n_{\text{quartz}}} \,. \tag{4.5}$$

Table 4.1 lists the alignment tolerances of Čerenkov angle with respect to the critical angle of the total internal reflection for various refractive index. Fig. 4.7 shows the Čerenkov angle and the TIR critical angle versus the refractive index.

refractive index n	θ_C ($\beta \simeq 1$) [degree]	θ_{TIR} [degree]	Alignment tolerance [degree]
1.30	39.7	50.2	
1.35	42.2	47.7	
1.40	44.4	45.5	
1.45	46.3	43.6	2.8
1.50	48.1	41.8	6.4
1.55	49.8	40.1	9.6
1.60	51.3	38.6	12.6

Table 4.1: The alignment tolerances of Čerenkov angle with respect to the critical angle of the total internal reflection for various index of refraction.

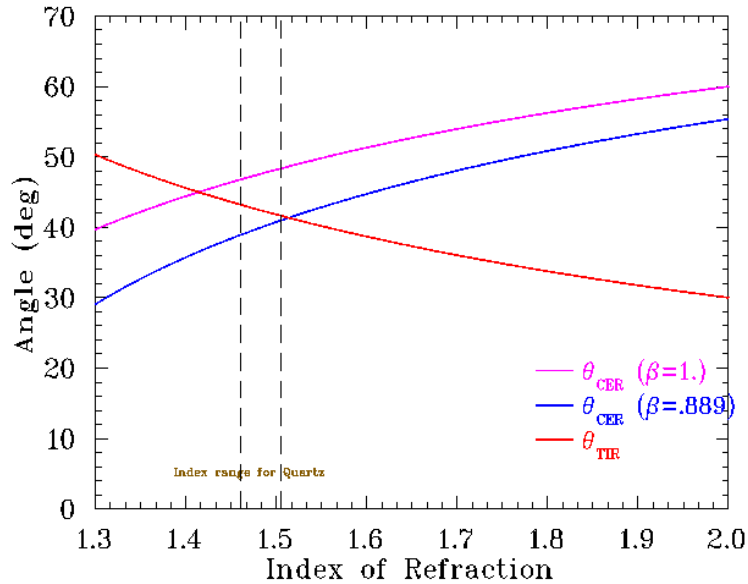

Figure 4.7: Čerenkov angle and TIR critical angle versus the refractive index [Mack, 2002]. The black dashed lines indicate the refractive index range of quartz. Assuming perpendicular incidence, Čerenkov light is trapped by total internal reflection when the magenta curve for Čerenkov angle (θ_{CER}) crosses above the red curve for TIR critical angle (θ_{TIR}). Čerenkov light from $\beta \simeq 1$ particle is trapped for $n > 1.425$. So the light from the 1.1 GeV electron is trapped in quartz bar. The light from background particle with $\beta < 0.889$ cannot be trapped in quartz bar.

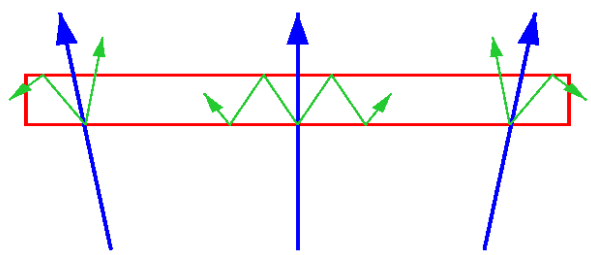

Figure 4.8: Čerenkov lights (magenta) escape from quartz bar (red) due to non-perpendicular incidence of the beam (blue).

Not the entire Čerenkov cone can be trapped since the beam incidence is not perpendicular to the quartz bar surface (see Fig. 4.8). Many photons are lost due to bevelled edges on the quartz and slight index of refraction mismatches between the three optical coupling materials used in the detector construction (UV transmitting glue, quartz and PMT window glass). The amount of light

produced by a given electron track and the efficiency with which this light is transported to the PMTs depends closely on the geometry and the orientation of the detectors, relative to the incoming electron trajectory. The 130 mm PMTs convert the Čerenkov light to a current, with a peak quantum efficiency of about 23% at 270 nm. So with about 8 photo-electrons per PMT photocathode per electron track and an event rate of about 830 MHz per detector the estimated cathode current for each PMT is about 1.1 nA. In production runs the PMTs are operated with a 7 stage base providing a low gain of between 1000 and 2000, depending on the overall efficiency of the detector and the exact event rates (including backgrounds). The nominal PMT anode current is then around 2 μA. The previous chapter discussed the considerable soft (photon) background from electron bremsstrahlung during high current running. To increase the signal to background ratio the addition of a lead pre-radiator (a sheet of lead in front of the quartz active volume, as seen by the scattered electrons) was modeled (see Fig. 4.9). After initial test, all Q-weak detectors are now equipped with pre-radiators. A detailed discussion of the various consequences and benefits of the pre-radiator are discussed in a separate section below. Details about the simulations that were performed to model the detector and make specific design, geometry, and position choices are given in a separate section below.

To achieve the goal measurement accuracy for Q-weak within the available beam time requires high event rates which, in turn requires detector current mode operation. Current mode operation does not allow event/threshold cuts and no discriminator settings can be applied, so that backgrounds must be suppressed by a particular detector design (e.g. pre-radiator) and material choice (i.e. quartz). The effects of various backgrounds in the main detectors are discussed in a separate section. Current mode operation also means that all noise sources must be properly accounted for and suppressed as much as possible (e.g. small excess noise beyond counting statistics). Anything that contributes to the RMS width in the current mode signal stays in the signal, regardless of the origin (backgrounds, shower activity, electronic noise, etc.). The contribution from excess noise factors is reduced for higher number of photo-electrons created at the cathode of a PMT. The higher the number of photo-electrons, the closer the detectors will operate to the elastic electron counting

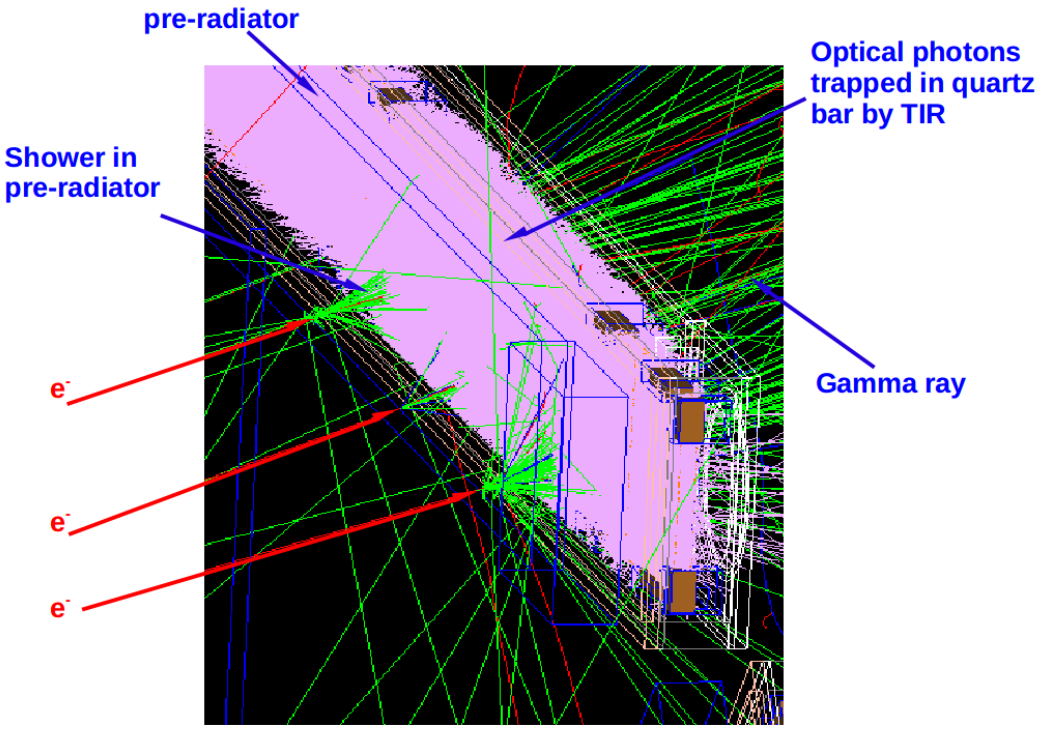

Figure 4.9: Simulated shower activities in the lead pre-radiator.

statistics limit. Even more importantly, the higher the number of photo-electrons, the higher the mean current out of the PMTs and the smaller the RMS width in the measured asymmetry. So a higher number of photo-electrons for a given electron event will mean a higher accuracy measurement for a given amount of time. Knowledge of the photo-electron number allows consistency checks with respect to detector yield (current) and asymmetry widths by providing a means to calculate the expected RMS width and compare this to the width seen in the data. Noise sources in the main detector and the performance of the detectors, as seen in the data, are discussed in detail in a separate section of this chapter. Measuring the number of photo-electrons must be done in pulse counting mode, with a careful single photo-electron calibration. This is done at low beam current and requires a different set of bases (higher gain), allowing for a clear separation between single photo-electron counts and actual events. The photo-electron efficiency tests and measurement results are described in detail in a separate section. The high gain PMT bases are switched

manually with the low gain bases, used during current mode (production) running. Another consequence of current mode running is that any non-linearity in the response of the detector system to small changes in electron numbers (i.e. those that are expected due to parity violation) for different mean currents will translate into variations in the asymmetry mean at different beam currents or for different detector gain settings. This can give rise to an artificially shifted or false asymmetry measurement. Detector non-linearity has been measured on the bench and again during data taking, using current mode runs. Non-linearity tests are discussed in a separate section. Due to their length the main detectors produce a slight position dependent light yield. For an electron event that traverses the active detector volume close to one of the edges, the relatively large distance optical photons from that event have to traverse before reaching the PMT at the opposite end will result in more light loss than for an electron event that traverses the detector close to a given PMT. When combined with the fact that the scattered electron momentum profile on a detector is not uniform (e.g. different electron intercept points on the detector surface correspond to a slightly different Q^2), as well as the fact that the electron rate across the bar is not uniform, this creates a small Q^2 bias. This is another unique problem in current mode operation which can also produce shifted or false asymmetries, but can be largely removed by adding the two PMT signals for each detector, before forming asymmetries (see chapter 3). The light yield mapping, rate distribution, and Q^2 bias tests and measurement results are discussed in a separate section.

In current mode, the PMT anode signal is pre-amplified immediately after the PMT and then routed directly into a set of integrating ADCs. When the experiment switches to low current pulsed mode, the bases are switched, with the low gain base remaining attached to the signal cable that runs to the pre-amplifier. The high gain base anode signal is attached to a different set of fast amplifiers, before being routed to a typical counting mode DAQ setup. Both setups are further described in a separate section below.

Continuous monitoring must be performed to check for gain stability and yield versus asymmetry or yield versus beam current stability. Periodic monitoring must be done for single photoelectron calibration and light transmission. To facilitate the periodic tests, each main detector is

equipped with a set of LEDs. Some important parameters, such as the measured gains for the PMT bases, single photo-electron numbers, are given in section A.1 in the appendix.

4.2 Design Criteria

The main detector is designed to measure the parity violating asymmetry; the most important factor is therefore the statistical uncertainty of the asymmetry measurement. The asymmetry (A) is measured in a "quartet" helicity pattern. The statistical uncertainty in the asymmetry due to counting statistics is:

$$\Delta A_{\text{count}} = \frac{\delta A}{\sqrt{N_{\text{pat}}}} , \tag{4.6}$$

where N_{pat} is the total number of helicity patterns in the measurement and δA is determined by the counting statistics, given by the standard deviation of A.

The measured asymmetry A in a single helicity pattern is given by

$$A_{\text{pat}} = \frac{N^+ - N^-}{N^+ + N^-} , \tag{4.7}$$

where N^+ and N^- are the number of scattered electrons detected by the main detector in the "+" and "−" helicity states, respectively. The derivatives of A with respect to these are:

$$\frac{\partial A}{\partial N^+} = \frac{1}{N^+ + N^-} + \frac{N^+ - N^-}{(N^+ + N^-)^2} = \frac{2N^-}{N_{\text{tot}}^2} , \tag{4.8}$$

$$\frac{\partial A}{\partial N^-} = \frac{-1}{N^+ + N^-} - \frac{N^+ - N^-}{(N^+ + N^-)^2} = \frac{-2N^+}{N_{\text{tot}}^2} , \tag{4.9}$$

where $N_{\text{tot}} = N^+ + N^-$ is the total number of detected electrons in this pattern. For the present discussion, The measurements are assumed to be independent and therefore the covariance is zero. Thus the uncertainty is obtained by

$$\sigma^2 \simeq \frac{(4N^-)^2}{N_{\text{tot}}^4}\sigma_{N^+}^2 + \frac{(4N^+)^2}{N_{\text{tot}}^4}\sigma_{N^-}^2 . \tag{4.10}$$

The Poisson distribution gives the uncertainties on N^+ and N^-, i.e., $\sigma_{N^+} = \sqrt{N^+}$ and $\sigma_{N^-} = \sqrt{N^-}$. Using the fact that the asymmetry is small, such that $N^+ \simeq N^- \simeq \frac{1}{2}N_{\text{tot}}$, and substituting the expressions for σ_{N^+} and σ_{N^-} into Eqn. 4.10 yields

$$\sigma^2 \simeq 4\frac{(N^-)^2N^+ + (N^+)^2N^-}{N_{\text{tot}}^4} = \frac{4N^+N^-}{N_{\text{tot}}^3} \simeq \frac{1}{N_{\text{tot}}} \,. \tag{4.11}$$

Therefore, the uncertainty of the asymmetry for the entire period of measurement is determined as

$$\Delta A_{\text{count}} = \frac{\delta A}{\sqrt{N_{\text{pat}}}} = \frac{\sigma_A}{\sqrt{N_{\text{pat}}}} = \frac{1}{\sqrt{N_{\text{tot}}N_{\text{pat}}}} = \frac{1}{\sqrt{N_{\text{el.}}}} \,, \tag{4.12}$$

where $N_{\text{el.}} = N_{\text{tot}} \times N_{\text{pat}}$ is the total number of electrons detected by the detector in the entire measurement. For example, assuming the beam current normalized rate measured in one detector is 4.4 MHz/μA, the total electron rate at 150 μA beam current on all detectors will be 5.3 GHz. At a 960 Hz helicity reversal rate, the detected electron number is 2.2×10^7 per quartet pattern. Therefore, based on pure counting statistics (Eqn. 4.11), the expected asymmetry width σ_A will be 213 ppm per quartet.

Eqn. 4.12 simply follows from counting statistics. However, there are noises in the detector and electronics which contribute additional random uncertainties, such as the shot noise caused by the fluctuations in the number of photo-electrons per incident scattered electron and the thermal noise produced by the feedback resistors in the preamplifier and DAQ. If the contribution from all noise sources, i.e., the quadrature sum of all additional random uncertainties, is absorbed in a single factor α, one obtains

$$\Delta A = \Delta A_{\text{count}} \sqrt{1 + \alpha^2} \,. \tag{4.13}$$

The factor α is referred to as the excess noise factor, and the "excess noise" in the measurement of A is the fractional amount by which the statistical uncertainty in A exceeds the counting statistics value:

$$\text{excess noise} = \sqrt{1 + \alpha^2} - 1 \,. \tag{4.14}$$

The excess noise directly affects the beam time required to reach the goal statistical precision. The number of total detected electrons is given by

$$N_{\text{el.}} = s \int i_{\text{beam}}\, \hat{R}_{\text{det}}\, dt\ , \tag{4.15}$$

where $\hat{R}_{\text{det}}$ is the detector accepted electron rate normalized to beam current i_{beam}. The factor s is the "live time" ratio of the measurement, which is defined as:

$$s = 1 - \frac{\text{helicity state reversal settling time}}{\text{helicity pattern duration}}\ . \tag{4.16}$$

The factor s appears here because the "settling time" (T_{settle}, which is the time needed to settle the Pockels cell after a helicity state reversal) needs to be omitted for the asymmetry calculation. For a helicity state reversal rate of 960 Hz, $T_{\text{settle}} = 70\ \mu$s and $T_{\text{stable}} = 972\ \mu$s out of a total of $1/960\text{Hz} = 1042\ \mu$s, so the "live time" ratio s is $972/1042 = 0.933$.

Assuming a constant beam current I_{beam} and using Eqns. 4.12, 4.13 and 4.15, one has

$$N_{\text{el.}} = s\, \hat{R}_{\text{det}}\, I_{\text{beam}}\, T_{\text{beam}} = \left(\frac{\sqrt{1+\alpha^2}}{\Delta A} \right)^2\ , \tag{4.17}$$

which gives the integrated beam time

$$T_{\text{beam}} = \frac{1+\alpha^2}{s\, \hat{R}_{\text{det}}\, I_{\text{beam}}\ (\Delta A)^2}\ . \tag{4.18}$$

The integrated beam time is proportional to the excess noise factor squared. Without considering possible background contributions, the factor α is dominated by detector intrinsic noise and the most important performance criteria for the main detector is therefore the detector excess noise or resolution.

The electron detection efficiency in the main detectors depends on the amount of collected light at the photocathode and the corresponding number of photo-electrons emitted from the cathode.

The number of photo-electrons emitted from the cathode is Poisson distributed around the mean. In other words, the variance of the detected number of photo-electrons is given by

$$\sigma_{\mathrm{pe}} = \sqrt{n_{\mathrm{pe}}}\,, \tag{4.19}$$

where n_{pe} is the mean number of photo-electrons. For large values of n_{pe}, the distribution becomes Gaussian. The relative uncertainty in the mean number of photo-electrons is then

$$\frac{\sigma_{\mathrm{pe}}}{n_{\mathrm{pe}}} = \frac{1}{\sqrt{n_{\mathrm{pe}}}}\,. \tag{4.20}$$

This relation gives the lower limit for detector resolution, but other processes usually contribute as well and increase the excess noise. These include random electrical noise, the charge collection in the PMT (multiplication noise at the dynodes), position dependent light yield, and shower fluctuations in the pre-radiator and radiator itself (this includes only source due to the main detector itself. Contributions from other sources, such as target boiling is not considered here).

The nature of the Q-weak current mode signal (tiny changes at fast helicity reversal rate on top of a DC current) requires the detector to have a good linearity, to correctly measure the small rate changes in the detector due to the parity signal (i.e. to avoid false asymmetries). Reference [Mack, 2004] gives an evaluation of the requirement for the detector linearity by calculate the digitized detector response $R(I)$ (e.g. ADC channels) in terms of beam current I. $R(I)$ is a function of the number of scattered electrons striking the quartz detector (N):

$$R(N) = a + bN + cN^2, \tag{4.21}$$

where a, b, c are coefficient, and c represents a small quadratic detector response. An ideal detector would be perfectly linear with no offset ($a = c = 0$). The average scattered electron rate striking the

detector can be estimated with the luminosity (L) by:

$$N_{\pm} = kL(1 \pm PA_{PV}), \tag{4.22}$$

which includes the helicity-dependent effect of the physics asymmetry A_{PV} and beam polarization (P). The scattering cross-section and detector acceptance are absorbed in a constant k, and the subscripts $\pm$ represent one or the other helicity state. The luminosity is proportional to the beam current and the target density:

$$L = \rho I = \rho_0(1 + \beta I)I = \rho_0 I + \rho_0 \beta I^2, \tag{4.23}$$

where the target density variation with beam current is parameterized by $\rho(I) = \rho_0(1 + \beta I)$. ρ_0 is the nominal target density (without density fluctuation due to beam heating effects), and β is a coefficient. Above expressions yield the system response:

$$R_{\pm}(I) = a + bk\,(1 \pm PA_{PV})\left[\rho_0 I_{\pm} + \rho_0 \beta I_{\pm}^2\right] + c\left[k\,(1 \pm PA_{PV})\left(\rho_0 I_{\pm} + \rho_0 \beta I_{\pm}^2\right)\right]^2 . \tag{4.24}$$

To second order in I, and first order in A_{PV}, this becomes

$$R_{\pm}(I) = a + bk\rho_0(1 \pm PA_{PV})I_{\pm} + \left[bk\rho_0\beta(1 \pm PA_{PV}) + ck^2\rho_0^2(1 \pm 2PA_{PV})\right] I_{\pm}^2 . \tag{4.25}$$

The coefficients of the $I_{\pm}^2$ term represent the nonlinearity. These terms arise both from target density changes (via the β parameter) and detector nonlinearities (via the c coefficient). Thus, there appears to be no benefit in having a detector chain with linearity far better than relative magnitude βI, which past experience suggests is $O(1\%)$. Therefore, a detector chain linearity of an order of smaller at $O(0.1\%)$ level would not limit the overall linearity, and the detector system nonlinearity of less than 1% would be acceptable (see reference [Mack, 2004] for a detailed analysis of the detector nonlinearity and how the asymmetry measurement is affected by the nonlinearities). A system with

nonlinearity that is 1-2 orders of magnitude smaller than this criterion would be ideal, since the corrections for nonlinearities in the detector system are then negligible.

From above discussion, a larger light yield improves the noise properties and brings the experiment closer to counting statistics. In order to operate close to counting statistics, we demand that the additional statistical contribution to the measured asymmetry be less than 5% [Mack, 2002]:

$$\sqrt{1 + \left(\frac{\sigma_{p.e.}}{N_{p.e}}\right)^2} < 1 + 5\%, \tag{4.26}$$

where $N_{p.e.}$ is the observed number of photo-electrons and $\sigma_{p.e.}$ is the RMS of the number of photo-electrons. Assuming $\sigma_{p.e.} = \sqrt{N_{p.e.}}$, the number of photo-electrons should be greater than 10.

During production running, the detectors will be operated in current-mode since the high rate makes it impossible to count individual events, the PMTs and bases were specifically selected (designed) to operate well at low gain and produce a continuous stable current signal. Current mode operation makes event cuts impossible and therefore forces the detectors to be well designed (or selected) to satisfy the following requirements:

- the detectors must be insensitive to pion background and photon background,
- the detectors must operate close to counting statistics with low thermal noise, so that the RMS width in the detector signal is dominated by single event photo-electron numbers.
- the detectors must be insensitive to radiation damage and soft backgrounds,
- the detectors must operate with modest Q^2 bias and less than 1% integral nonlinearity,
- the detectors must incorporate engineered solutions to minimize or monitor cross-talk between the apparatus and the helicity reversal signal.
- the detectors have mechanical and optical properties which are stable over the lifetime of the experiment,

While the main detector itself has limited use in tracking mode (e.g. in the determination of the momentum transfer), aside from using it as an alternative trigger, some of the performance diagnostic tests for the main detectors are done in tracking mode. The most important diagnostics include light yield uniformity tests across the bar (related to Q^2 bias) and the determination of the number photo-electrons per scattered electron event (detector efficiency). These two tests are related and are discussed in detail, later on in this chapter. In order to perform these tests, the main detectors must also be able to operate in pulse mode and this requires high gain operation (as opposed to the low gain operation in current mode mentioned above). The main detectors therefore operate with two different sets of bases, one for low gain current mode operation during production running and one for high gain pulse mode operation during tracking mode runs. Both of these are discussed in detail further on in this chapter.

As mentioned above, the main detectors consist of a set of eight 200 cm long, 18 cm wide and 1.25 cm thick quartz bars. The bars consist of two optically glued two 100 cm long, 18 cm wide and 1.25 cm thick polished synthetic quartz pieces. Each long quartz bar has two 20 cm long, 18 cm wide and 1.25 cm thick rectangular quartz light guides coupled to its two ends, and each quartz light guide has a 130 mm photomultiplier tube (PMT) attached on its surface. The extensions keep the PMTs out of the main envelope of scattered electrons and allow the PMTs to be lead shielded. This choice of geometry was mostly based on spatial constraints, accommodating all eight detectors in the focal plane, while covering the entire scattered beam envelope in the chosen acceptance. As further described below, the geometry and position of the detectors was validated using extensive electron and optical photon simulations. In current mode, the PMT anode signal is pre-amplified immediately after the PMT and then routed directly into a set of integrating ADCs. When the experiment switches to low current pulsed mode, the bases are switched, with the low gain base remaining attached to the signal cable that runs to the pre-amplifier. The high gain base anode signal is attached to a different set of high speed amplifiers, before being routed to a typical counting mode DAQ setup. Both setups are further described below. The detectors are mounted coplanar with the focal plane, as shown in Fig. 4.3.

4.3 Simulations and Detector Design

The detector design is based on extensive Monte Carlo simulations, which have been compared (and to some degree benchmarked) with commissioning and production data. Simulations were done to study the light production and transport in the quartz bar, to study effects of quartz bar surface properties, to determine quartz bar and light guide shapes and geometries, quartz bar tilt angle, to study the effect of position dependent light yield, etc. Apart from the studies of detector design and performance, simulations were also performed to study background and Q^2 distribution. These simulations address questions that are not only important to the detector design itself, but also very important to understanding the entire experiment.

The simulations discussed in this thesis have been developed based on the Geant4 framework [1]. The basic method is to set up detailed as-built geometries of the detectors and shielding, implement the as measured magnetic field of the spectrometer. Particles in the simulations are tracked from the target to the detectors. The scattered electron events are generated by an event generator and the target forms the source within the simulation. By turning on all relevant physics processes along the particle trajectories, the detector response can be simulated for various chosen geometries, which remains the only thing to be changed, provided the relevant physical processes are properly implemented. The simulation results are benchmarked by comparing them to independent experimental results wherever possible and the resulting deviations are then used to modify the simulation code until consistent results are obtained or a reasonable uncertainty can be assigned to the simulations results. The detector design is optimized through several such iterations.

In the simulation, the primary scattering event is generated independently by an event generator, including the e-p elastic scattering in the target, elastic and quasi-elastic electron scattering on the aluminum nuclei in the target cell windows. The latter process was considered explicitly because its asymmetry is about ten times greater at a given scattering angle than it is for e-p elastic scattering in the liquid hydrogen target. The implemented physical processes include all electromagnetic pro-

[1] Developed at CERN, Geant4 is an object oriented programming framework for the simulation of the passage of particles through matter. It is a toolkit including useful libraries to describe matter, interaction and particle transportation.

cesses and low energy hadronic processes above a cut value[2]. This allows for secondary e-p elastic and inelastic scattering in the target, Møller scattering in the target, generation of electromagnetic shower products in the target and any other geometry implemented in the simulation. The Čerenkov and scintillation light production in the main detector quartz bars are the major physics processes of interests.

A complete simulation of the signals expected in the detector, using the geometrical setup shown in Fig. 4.10 was performed. The simulation had all the geometry shown in the figure, except the aluminum beam-pipe and its lead shielding. The main detectors are implemented in particular

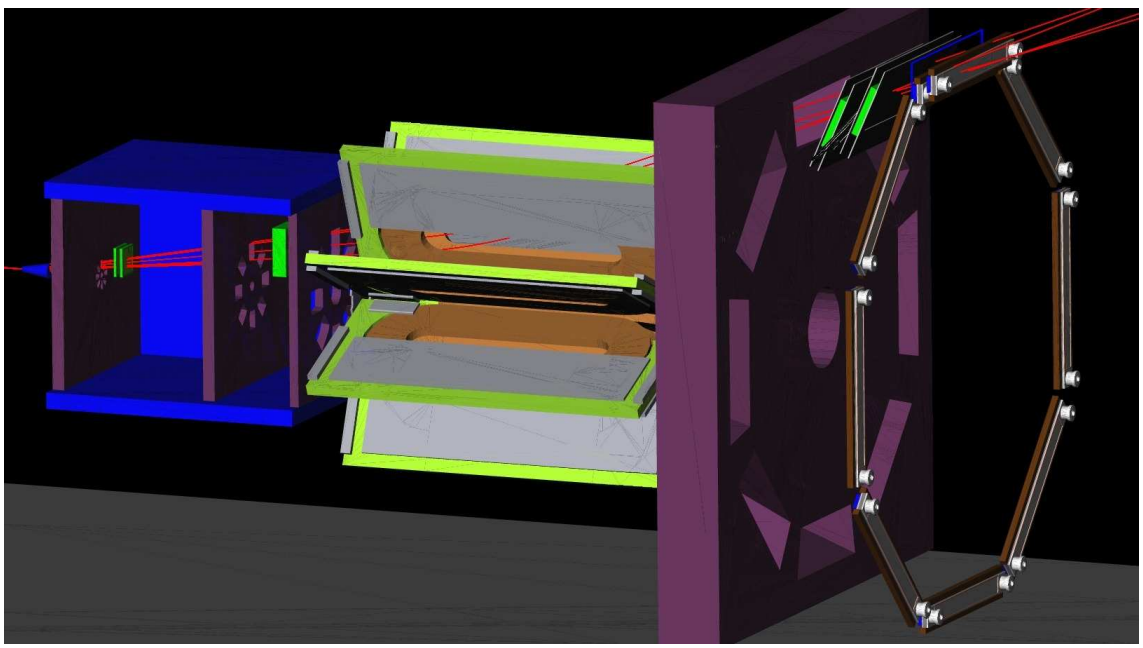

Figure 4.10: Visualization of Q-weak Geant4 simulation. From left to right, the geometries of the liquid hydrogen target cell and its aluminum scattering chamber window, the first collimator, the Region 1 GEMs, the second collimator, the Region HDCs, the third collimator, the QTOR spectrometer, the shielding wall,the Region 3 VDCs, the trigger scintillator and the main detectors are shown, together with a few simulated trajectories of the elastic scattered electrons. The as-built dimensions are used for the target, the collimators, and shielding wall, which are especially important with respect to Q^2 simulations and rate predictions.

[2]Cut value defines the extent to which a particle is tracked. Cuts are defined in distance, which are converted into energy based on the material. The cut value is 1 mm in this simulation.

detail, as shown in Fig. 4.11, including the quartz bars, glue joints, lightguides, PMTs, detector housing, PMT housing, PMT lead shield, pre-radiator, quartz bar holders and detector windows (covers). As many details as possible were modeled in the simulation, such as the small mismatch between two quartz bars. The simulation also investigated the consequences (e.g. light loss) of possible defects, such as quartz bar and/or light guide misalignment, oversized bevels and chipped edges. The rectangular light guides were 20 cm long, 1.25 cm thick and 18 cm wide without any reduction in width or thickness. The geometry of the light guides and PMT attachment for the main Čerenkov detectors is selected based on light transmission and collection performance, as well as by the spatial constraints set by the distance between neighboring detectors and freedom for position adjustability in the radial direction, while keeping the PMTs out of the scattered beam profile as much as possible. In the simulations, the detectors were initially placed 570 cm downstream of the QTOR center (in the simulated focal plane) and 326 cm radial distance from the beam center. These numbers were replaced with as-installed numbers (578 cm downstream of the QTOR center and 335 cm radial distance from the beam center).

The implemented detector geometry was used in simulations with the Čerenkov process turned on, to determine the overall efficiency of the detectors for various design choices, such as detector thickness, pre-radiator thickness and light guide geometry. The simulation included all relevant material properties, including wavelength spectra, index of refraction, surface reflectivity (specifically of the PMT photocathode), and surface roughness (specifically of the quartz pieces). For example, prototype tests and simulations showed that the size and polish quality of the bevels was important. The simulations indicated (as compared to the prototype tests) that the unpolished bevels on a quartz bar prototype reduced the number of photo-electrons by about 40%. Based on this, the final quartz bars have polished bevels of less than 0.5 mm.

The quartz bar thickness was optimized using simulations by finding a compromise between the need to maximize photo-electron yield and the need to minimize shower noise [Gericke, 2005]. In other words, the optimal quartz bar thickness was determined by simultaneously minimizing contributions to the Q-weak uncertainty from photo-electron and electron shower noise. The simulation

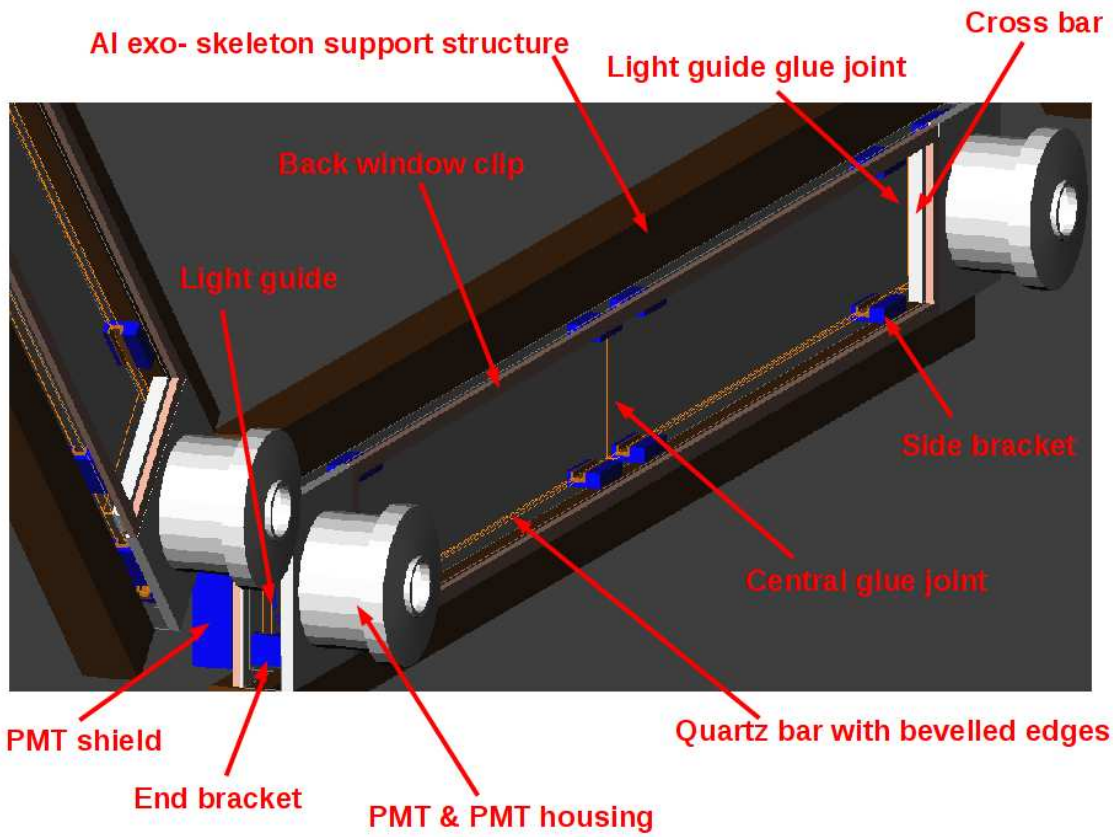

Figure 4.11: Visualization of the main detector implementation in the Q-weak Geant4 simulation. The detector housing is removed so that the inner structure can be seen.

was performed for several different detector thicknesses between 0.5 and 3 cm. The distribution of the combined noise factors shows a minimum around 1 cm thickness. The number of photo-electrons increases by a about a factor of two over a range of thickness from 1-2 cm. The optimum thickness appears to be 2-2.5 cm, with a shallow minimum which depends on the surface reflectivity assumptions. However, the net excess noise is a nearly model-independent $\sim 3\%$. A thickness of 1.25 cm was selected to conservatively provide enough photo-electrons while keeping the excess noise from shower generation (about 1%/cm) under control.

A similar procedure was performed to find the ideal thickness for the pre-radiator. Simulations were performed with the lead radiator thickness varied between 1 and 4 cm. The shower maximum

in terms of the number of secondary particles produced and light yield reach a maximum at about 2 cm, while the excess noise has a minimum at about the same thickness, as shown in Fig. 4.12. Based on this, the thickness for the lead pre-radiator was chosen to be 2 cm.

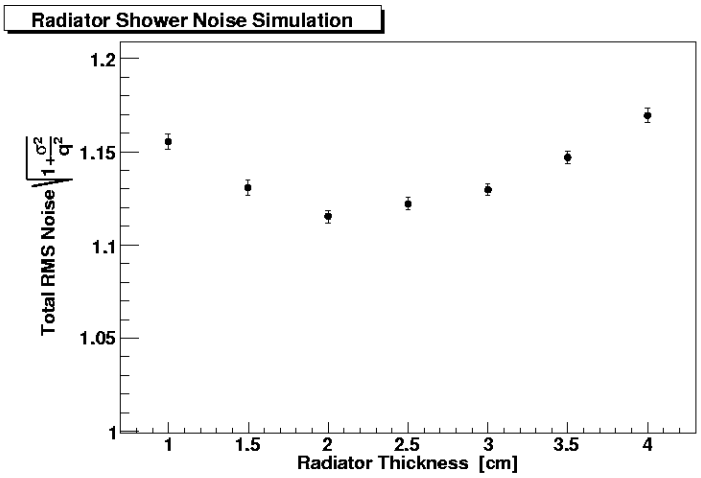

Figure 4.12: Preradiator shower noise

The optimal Čerenkov detector light guide geometry was determined by simulating the light yield for various configurations, such as with the PMT on the edge or on the face of the light guide for rectangular, trapezoidal, or wedge guide geometries, or without light guide (PMT on the active quartz volume edge only). It appears that the rectangular light guide with the PMT on the face of the guide produces the largest mean number of photo-electrons and that the geometry has no significant effect on the excess noise due to light yield variations [Gericke, 2006b].

The detector tilt angle (defined in Fig. 4.13(a)) was also optimized through a series of simulations. Simulations were carried out to determine the excess noise as a function of detector tilt angle (see Fig. 4.13(b)), the light yield uniformity as a function of electron hit positions along the length of the quartz bar and tilt angle, as well as the uniformity of the Q^2 distribution across the quartz bar. The light yield is significantly more uniform for a zero tilt angle, albeit being less than for other angles. Considering the complications of design and installation, the optimal tilt angle is zero – perpendicular to the beam direction. The requirement for the number of photo-electrons per

detector (more than 10 p.e., see section 4.2) still can be met at zero tilt angle.

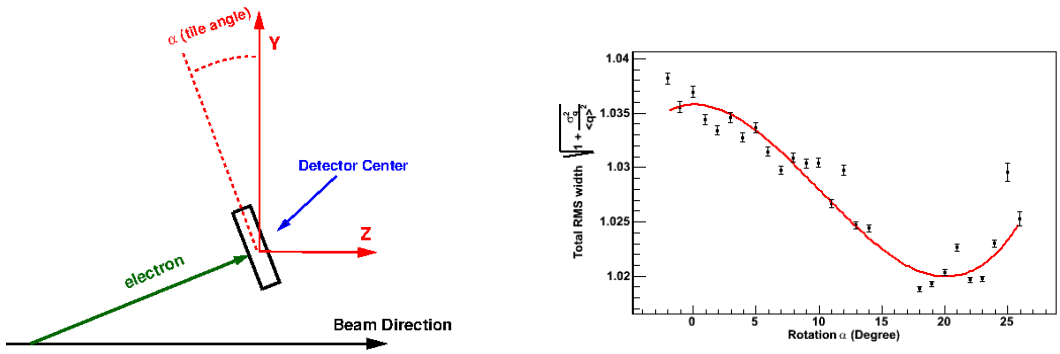

(a) Definition of the tilt angle

(b) Noise vs tilt angle

Figure 4.13: Main detector tilt angle simulation. Due to the fact that the excess noise varies by only 1.5% for the various tilt angles, but especially since the light yield uniformity across the bar is significantly better (see below), a 0 degree tilt angle was chosen.

The simulation studies of total light yield in the detector indicate that the light yield could be different as the electron incident position changes. Fig. 4.14 shows the simulated total light yield spectrum and the light yield correlation between the two PMTs on the same quartz bar, without the pre-radiator. These were simulated at zero detector tilt angle (see Fig. 4.13 (a)). This is the nominal angle, for which the Čerenkov bars are perpendicular to the beam. The long tail toward higher light yield in Fig. 4.14 (a) and the curvature of the light yield correlation in Fig. 4.14 (b) is an indication that the light yield is dependent on the electron incident positions – a combined effect of the shower activities in the quartz bar, the various path lengths of the traversed electrons in the quartz bar, and the various light transmission distances in the quartz bar.

In order to verify this position dependence, simulations were performed to determine the light yield distribution as a function of electron hit position on the quartz bar. Fig. 4.15 (a) shows the light yield distribution along the quartz bar, while Fig. 4.15 (b) shows the light yield distribution across the quartz bar (radial direction, as defined by the coordinate system). The position dependent light yield (nonuniformity of light yield) can be seen in the plots — the light yield is approximately uniform across the quartz bar with some edge events (the electrons hit on the edge of the quartz bar

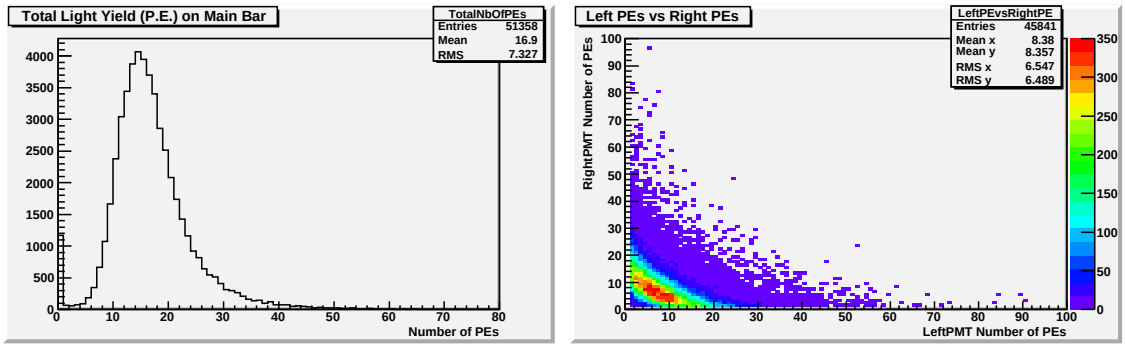

(a) Total light yield in the Čerenkov bar (b) Correlation of light yields in left and right PMTs

Figure 4.14: Total light yield and light yield correlation between two PMTs

at the inner radius side) which produce a smaller amount of lights (as seen in Fig. 4.15 (b)), but the light yield is much more nonuniform along the quartz bar. This nonuniformity can be more clearly

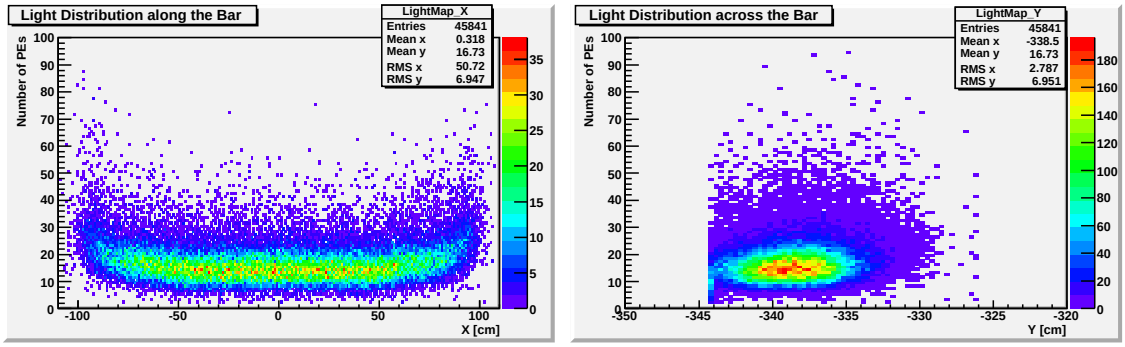

(a) Variation of light yield along the Čerenkov bar (b) Variation of light yield across the quartz bar

Figure 4.15: Position dependent light yield on the Čerenkov bar. The colored axes indicate the rate of electrons in arbitrary unit.

identified by plotting the light yield profile along the quartz bar, as seen in Fig. 4.16, which shows the variation of light yields (from the left hand side PMT, right hand side PMT and the sum of both PMTs) along the Čerenkov bar at zero tilt angle.

The hit position dependence of the light yield will affect not only the excess noise in the detector, but also the light-weighted $\langle Q^2 \rangle$ determination, and therefore needs to be optimized. This dependence with respect to the detector tilt angle (see Fig. 4.13) was studied in the simulation and the

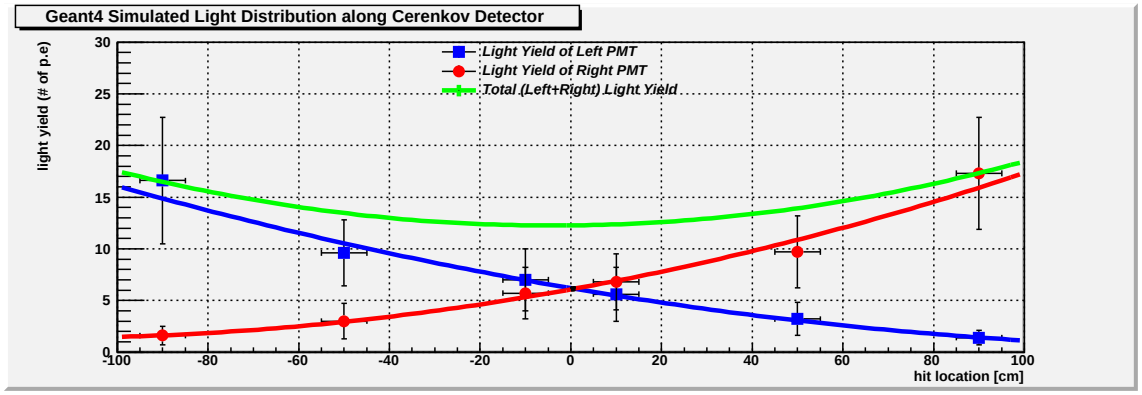

Figure 4.16: Simulated variation of the light yield as a function of electron hit positions along the Čerenkov bar at zero detector tilt angle.

result indicated that the non-uniformity is minimized at zero detector tilt angle. For example, when the detector tilt angle is 22 degrees, so that the mean electron central trajectory is perpendicular to the quartz bar front surface, the total light yield is higher than it is for the configuration with the detector at zero tilt angle, but the non-uniformity of the light yield is along the bar increases, as seen in Fig. 4.17. The simulated light yield distributions were benchmarked with cosmic ray tests and during commissioning with beam (see section 4.6.3), with good agreement between the simulation and the tests.

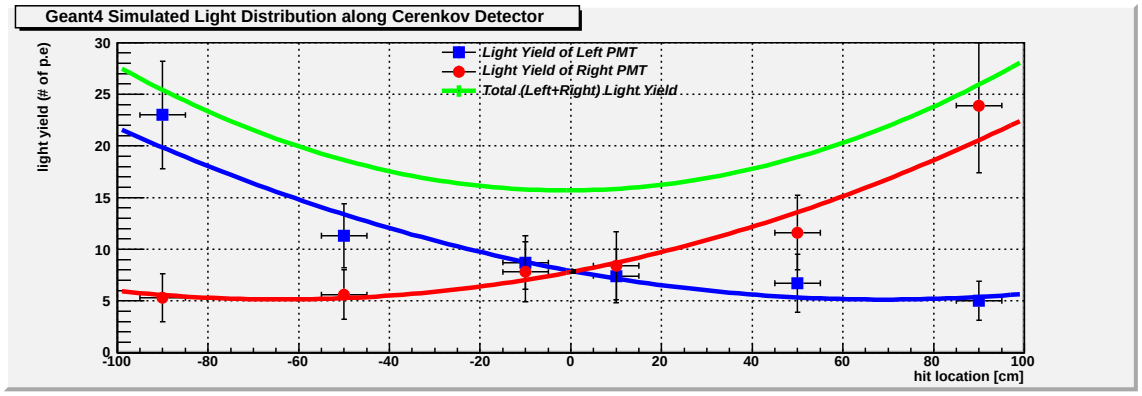

Figure 4.17: Simulated variation of the light yield along the Čerenkov bar, with the mean electron trajectory at normal incidence on the quartz bar).

The parity violating asymmetry is proportional to Q^2, so the $\langle Q^2 \rangle$ needs to be determined with an uncertainty of less than 0.5% (see Table 3.1). The determination of $\langle Q^2 \rangle$ requires knowledge of the acceptance, cross section, and radiative corrections for bremsstrahlung. Simulations indicate that the Q^2 is not uniformly distributed on the detector plane, as seen in Fig. 4.18. In addition, each event which is accepted by the main detector will produce different amount of light, depending on its hit location on the quartz bar (see the event rate distribution in Fig. 3.2 and Fig. 3.23). The convolution of nonuniform Q^2 and light yield distributions produces a slight $\langle Q^2 \rangle$ bias, which must be taken into account. To remove any remaining bias, the Q^2 for each electron track must be weighted by the light produced by that electron in the detector, to get the light-weighted $\langle Q^2 \rangle$.

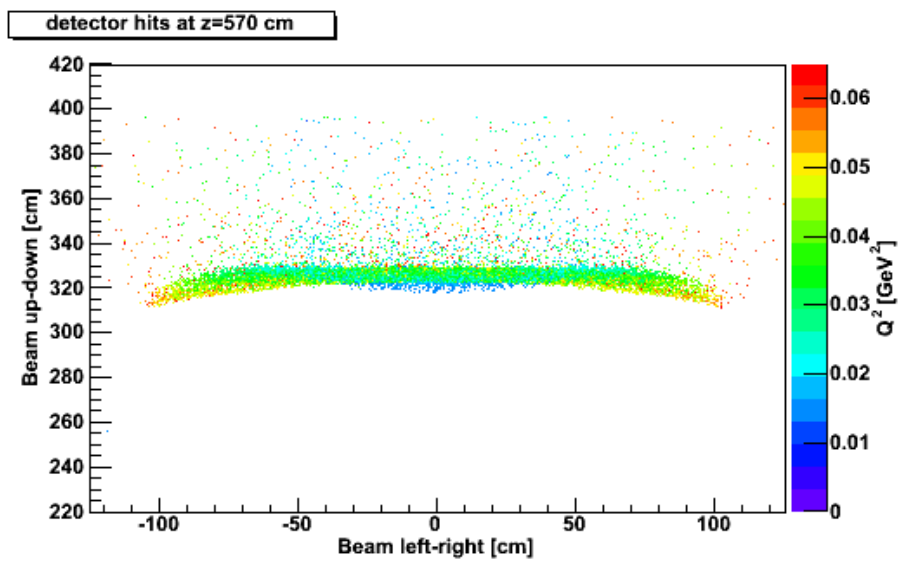

Figure 4.18: Elastic event distribution by Q^2

For example, simulations and data indicate that events near the middle of the radiator will have a lower light yield (see Fig. 4.16, 4.47 and 4.48). Lower Q^2 events are focused in the center of the detector. The combination of the two effects then biases the Q^2 upward by about 1.5%, as seen in Fig. 4.19.

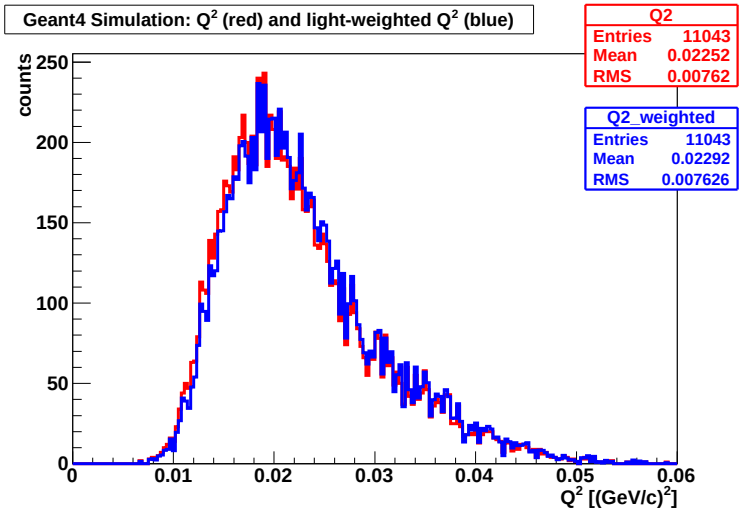

Figure 4.19: Momentum transfer determined from simulation. The red curve indicates the Q^2 distribution before light-weighting, and the blue curve indicates the light-weighted Q^2 distribution.

4.4 Detector Construction

4.4.1 Radiator and Light Guide

As mentioned above, the purpose of the main detectors is to detect the electrons in the elastic envelope while, as much as possible, suppressing all forms of background. This includes background from material activation and shower activity, neutral background and electrons other than those in the elastic envelope. Particles below the Čerenkov threshold do not produce a signal in the detectors. This includes low energy photons and neutrons. In addition quartz is known to be a poor scintillator. This was verified by bench measurements (this is discussed below). Together with the fact that quartz is very radiation hard, it is the material of choice for Q-weak. The most important properties and specifications for the main detectors radiators and light guides are summarized in Table 4.2.

When selecting radiator material, a major concern is radiation hardness. The detectors will acquire a radiation dose of approximately 100 kRad by the end of the experiment (see section 4.6.1 for a simple dose estimation). This high dose environment could rapidly damage the light transmission for many other commonly used detector materials, such as Lucite, for example. As mentioned

Parameter	Value
Material	Spectrosil® 2000 synthetic fused silica
Quartz Bar Dimension	200 cm × 18 cm × 1.25 cm
Light Guide Dimension	20 cm × 18 cm × 1.25 cm
Polishing Quality	Optical polish (25 Å RMS)
Bevel Size (beveled on every edge)	1.5 mm
Detector position z	577 cm from QTOR magnet center
Detector radial position r	331 cm from beam axis

Table 4.2: Čerenkov radiator and light guide parameters

in the overview, every scattered electron that hits the detector at a different location has a slightly different Q^2 (see Fig. 4.18). So radiation damage, giving rise to a decrease in optical transmission, will produce a Q^2 bias, since more light will be detected for some Q^2 values than for others (see the simulated distributions of light response and Q^2-dependence in section 4.3). Since Q-weak has a finite Q^2 acceptance, this bias would shift the mean Q^2 value that is ultimately used to extract the weak charge of the proton from the measured asymmetry. A 4% measurement of the proton weak charge requires a 0.5% determination of the average Q^2 and a radiation damaged detector would make it hard to satisfy this requirement. An additional problem would be that the amount of radiation damage is time dependent, and would cause the effective mean Q^2 to shift with time. Of course, all of this comes together with a general decrease in light yield, causing the statistical efficiency of the experiment to diminish with time.

The synthetic fused silica by Saint-Gobain Quartz[3], the Spectrosil® 2000 material, is selected for the radiator and light guide because this material is sufficiently radiation-hard [4] for the Q-weak application and produces negligible light via scintillation and luminescence. The Spectrosil® 2000 has exceptional purity (contaminants at the ppm level, bubble-free and fluorescence-free), low luminescence, low scintillation, excellent optical transmission from 180 nm in the deep UV through

[3]Saint-Gobain Quartz, http://www.quartz.saint-gobain.com/

[4]This type of quartz was used successfully in PEP II at SLAC — no observable radiation damage after a 2 GRad dose [Ecklund et al., 2001]. The same grade of quartz is also being used in the HAPPEx-II experiment [Acha et al., 2007] for the very forward angle (less than 1°) luminosity monitors [Glesener, 2005] with ~1-2 GRad over the course of the entire run.

to 2000 nm in the IR. The key properties of Spectrosil® 2000 are listed in Table 4.3.

Property	Value
Density	2.21 g/cm^3
UV Transmittance	$\geq$ 99.5% (at 193.4 nm), $\geq$ 99.9% (at 248 nm), 10 mm pathlength
IR Transmittance	$\geq$ 95.0% For wavelengths below 2000 nm, 10 mm pathlength
Refractive Index	see Table A.3 (1.4667 at 435.83 nm, for example)
Refractive Index Homogeneity	$< 25 \times 10^{-6}$, up to 200 mm
SiO_2	$\geq$ 99.999%
Bubbles	< 0.03 mm^2/100 cm^3

Table 4.3: Material properties of Spectrosil® 2000 synthetic fused silica

The length (200 cm) and width (18 cm) of quartz bar are determined by the elastic beam spot size on the focal plane, which are enough to cover the entire elastic region in one octant with minimum inelastic contaminations. The thickness (1.25 cm) was optimized using simulations, by balancing the competing aspects of maximizing light yield and minimizing shower activity and background, since shower activity increases excess noise and thicker detectors are more sensitive to background (see section 4.3). The systematic variations in bar thickness are ± 250 μm (or 1%), with point-to-point variations in thickness due to 25 Å RMS polishing. In order to reduce costs, 100 cm long quartz bars were purchased and then glued in to the 200 cm long active volume of the detector. All surfaces are polished with a standard optical-grade finish. All edges are beveled to $\approx$1.5 mm to avoid being easily chipped. The detectors are instrumented with 130 mm PMTs and bases, optically attached to the active quartz volume by light guides, as explained in the overview.

Each optical assembly is 2.40 m long, including two 100 cm long radiators and two 20 cm long light guides. These pieces were glued together, resulting in three main glue joints: light guide to radiator, radiator to radiator and radiator to light guide. Fig. 4.20 shows the quartz bars and light guides in the process of being glued together to form a optical assembly). The 130 mm PMTs are directly glued onto the face of the light guide. The optical glue used to attach the quartz pieces and the PMTs is SES406 by Shin-Etsu [5]. The glue was chosen for its mechanical strength, stable light

[5] Silicone elastomer made by Shin-Etsu Chemical Co., Ltd.

transmission under high radiation doses. The glue was tested for radiation damage for doses up to 1 MRad at a ^{60}Co facility (the Nuclear Services of North Carolina State University). In order to get reliable glue joints, surface priming, glue mixing ratio, glue layer thickness and gluing procedure had been carefully studied and a controlled gluing procedure was established (see Appendix A.2 for a detailed description of the gluing procedure).

Figure 4.20: Assembly of the quartz components of the main detector. Two of the eight assemblies are shown.

4.4.2 Preradiator

Soft backgrounds (e.g. low energy photons) are present everywhere and come from every direction. Photons with energies at or below $\mathcal{O}(100)$ keV will not produce light in the detectors, since quartz does not scintillate [Mack, 2007]. However, photons above that energy can pair produce inside the quartz and the electron-positron pair can make Čerenkov light. Extensive simulation (see section 4.3) studies were carried out to determine the benefits (and the consequences) of using a lead

pre-radiator in front of the quartz (as viewed by an incoming scattered electron, shown in Fig. 4.9). The benefits are two fold: (1) soft photon background from primary electron bremsstrahlung, which is incident on the detector from the same general direction as the scattered beam envelope, is reduced by absorption in the lead pre-radiator and (2) the electrons in the scattered envelope shower in the pre-radiator, producing on average 8 outgoing electrons of slightly lower energy for every incoming electron. Each of the shower electrons makes as much light as the single incoming electron would have, so that the pre-radiator provides a large gain in the signal, while the isotropic background remains the same. The former benefit is a simple shielding mechanism, while latter actively increases the signal to background ratio.

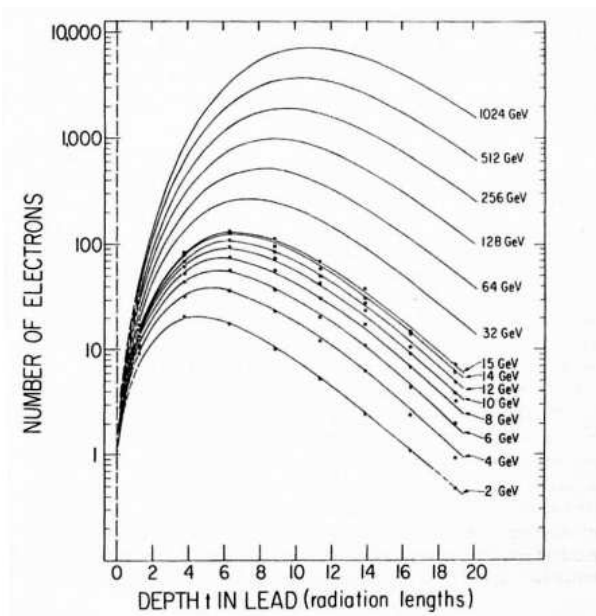

Figure 4.21: Shower profile in lead. The number of electrons should be multipilied by a normalization factor of 0.79 [Müller, 1972].

Lead radiation length is 0.5 cm [Nakamura et al., 2010]. Shower maximum is reached at about 4 radiation lengths as shown in Fig. 4.21. The pre-radiator for the main detectors was correspondingly chosen to be 2 cm thick.

Although the pre-radiator will improve the signal to background ratio, the light yield fluctuations

due to fluctuations in the number of the shower particles produce additional excess noise. In the design process, simulations were used to show that a minimum of 12% in excess noise is achieved for a 2 cm pre-radiator thickness (see Fig. 4.12). The apparent disadvantage of running with a pre-radiator is therefore a correspondingly longer running time (about 370 additional hours). However, the resulting reduction in relative background contribution to the signal more than makes up for this additional time requirement.

During commissioning, half of the main detectors had pre-radiators installed and the other half were bare. A suite of studies and tests was performed for all detectors, including background studies, beam position sensitivity tests, light yield tests, and RMS noise studies. Based on a comparison of the results between the two sets of detectors, it was decided to equip all detectors with pre-radiators for production running.

4.4.3 Photomultiplier Tubes

To convert the Čerenkov light to a current signal, the main detectors use 130 mm photomultiplier tubes (PMT), with S20 photocathode, UV transmitting glass window, SbCs dynodes and DC coupling with an electrostatic shield at cathode potential. The PMT dimensions are shown in Fig. 4.22. The model of PMT is 9312WKB (was D753WKB), made by Electron Tubes (ET Enterprises Ltd.). This is a custom variant of model 9312KB with enhanced UV sensitivity. 9312KB itself is the S20 photocathode version of model 9390KB which is a cheap, compact, 130 mm diameter photomultiplier with blue-green sensitive bi-alkali photocathode and 10 stages of high gain, high stability, SbCs dynodes with linear focus design for good linearity and timing (see below for a discussion on PMT linearity). 9312WKB is sensitive in the wavelength range from 200 to 900 nm, with a peak quantum efficiency of about 23% at 270 nm (see Fig. 4.24).

The material and size of the PMT window have been selected based on considerations of light yield and detector performance stability with the purpose of maximizing the number of photoelectrons and reducing effects of radiation damage in the detectors. The number of Čerenkov photons produced (N) per unit path length of a particle (dx) with charge Ze and per unit energy interval

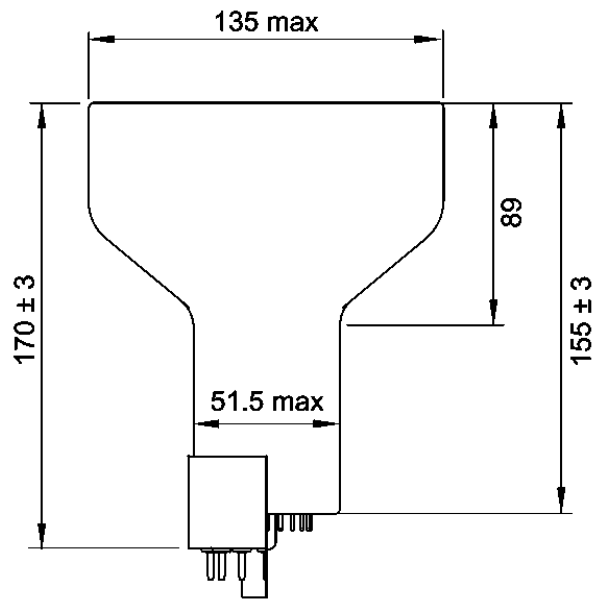

Figure 4.22: Dimensions of 130 mm 9312WKB photomultiplier tube. Unit: mm

of the photons (dE), is given by [Nakamura et al., 2010]:

$$\frac{d^2N}{dEdx} = \frac{\alpha Z^2}{\hbar c}\sin^2\theta_C = \frac{\alpha^2 Z^2}{r_e m_e c^2}\left[1 - \frac{1}{\beta^2 n^2(E)}\right] \tag{4.27}$$

$$\simeq 370\sin^2\theta_C(E)\ \ \mathrm{eV}^{-1}\mathrm{cm}^{-1} \qquad (Z = 1), \tag{4.28}$$

or, equivalently,

$$\frac{d^2N}{dxd\lambda} = \frac{2\pi\alpha Z^2}{\lambda^2}\left[1 - \frac{1}{\beta^2 n^2(\lambda)}\right]. \tag{4.29}$$

The wavelength distribution of the Čerenkov light ($d^2N/dxd\lambda$ versus λ) for quartz is shown in Fig. 4.6. This shows that most of the light is produced at short wavelength (UV enhanced). To collect as much light as possible, the PMTs used in Q-weak are equipped with UV transmitting glass, as opposed to regular borosilicate glass (see Fig. 4.23).

By selecting PMTs with UV glass windows which have a low wavelength cutoff at roughly 250 nm (i.e., 50% of maximum quantum efficiency) [6], we will be able to maintain a stable detector

[6]This short wavelength cutoff can be raised further, for example, to 350 nm, by gluing filters on the PMT

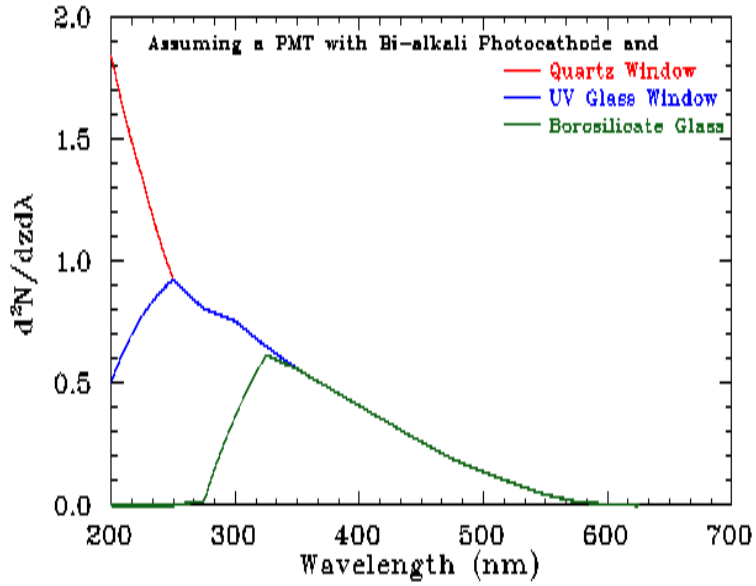

Figure 4.23: Čerenkov light collections by PMT with different PMT window. The window transmission efficiency and the quantum efficiency of a bi-alkali photocathode have been taken into account. [Mack, 2002]

performance and a good light yield even in the case of radiation damage at very low wavelengths. In addition, because of the light loss due to reflection at the PMT window, a larger PMT window with a larger active area results in a better light collection efficiency. A 130 mm PMT provides a photocathode diameter of 110 mm or an active area of ~ 95 cm^2.

The main detector PMTs use a multialkali S20 (Na_2KSb:Cs) photocathode. The S20 photocathode has a peak quantum efficiency of about 23% at about 260 nm and has finite efficiency down to 200 nm (see Fig. 4.24 and Table A.4). By comparison, standard bi-alkali cathodes have a sharp cutoff at about 300 nm, resulting in a lot of light loss. The S20 cathode is therefore well matched to the Čerenkov light wavelengths in quartz.

In addition, the S20 photocathode was selected because it has a low sheet resistance. The main detector PMT photocathode current in current mode operation is on the order of several nA, due to

windows if we find that the quartz bars damage more quickly than found in tests by the BaBar DIRC group [Cohen-Tanugi et al., 2003].

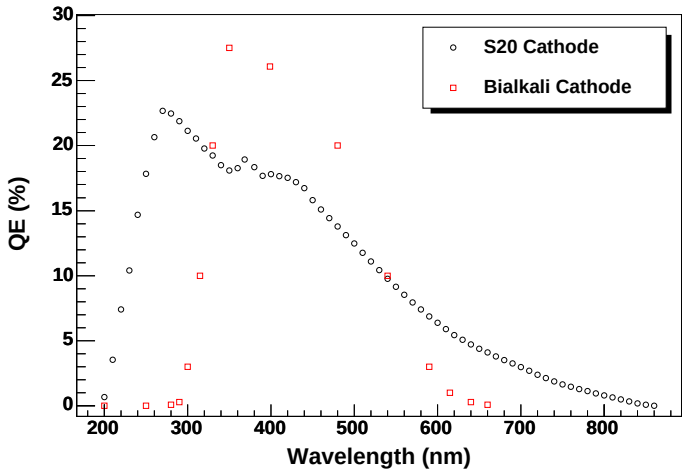

Figure 4.24: Quantum efficiency (QE) for the S20 photocathode with UV glass, as compared to the QE for a regular bi-alkali photocathode with a lime glass window.

the combination of high rates and high photo-electron numbers. This is a relatively high, continuous photocathode current and can produce large potential drops across the face of the photocathode if the photocathode has a high sheet resistance (see reference [Mack, 2005] for a discussion of photocathode voltage drop). For example, use of standard bi-alkali photocathodes would lead to potential drops across the photocathode of many 10's of volts. A non-equipotential photocathode will induce poor electrostatic focusing and cause the loss of a large fraction of the photo-electrons. At high load (larger than 1 nA cathode current), the S20 photocathode has a very low voltage drop over a large photocathode area, since it has 3 orders of magnitude smaller resistivity than standard bi-alkali photocathodes. Therefore, the effects of voltage drop, such as poor electrostatic focusing, loss of collection effciency, and potentially poor linearity, are negligible.

A disadvantage of the S20 photocathode is its higher thermionic emission rate, resulting in a relatively large dark current (a factor of 33 times larger than bi-alkali at 20 °C) which slightly complicates the interpretation of pulsed mode data, for detector efficiency tests. A 130 mm PMT with an S20 photocathode has a typical dark rate of approaching 100 kHz if triggered at 0.5 p.e. (photo-electron) level. This is not an issue in current mode since the dark current dilution is small

(less than 10^{-4}, estimated by:

$$\frac{\text{dark current}}{\text{detector yield}} \sim \frac{100\ \text{kHz} \times 1\ \text{p.e.}}{0.8\ \text{GHz} \times 10\ \text{p.e.}} < 10^{-4}, \tag{4.30}$$

where the full beam current rate is approximately 0.8 GHz, with a ~10 p.e. per track response for one PMT), but it makes it more difficult to quantify soft background pulses consisting of 1 photo-electron in event mode [7].

The main detector PMTs have a 10 stage dynode structure, with SbCs dynodes. Compared to other types of dynode material, SbCs dynodes reduce the so-called "rate effect", which causes the gain in a PMT to vary with the average current in a PMT. This can cause non-linear responses of the PMT to slight changes in electron event rate (such as the expected event rate changes due to the helicity reversal) and therefore constitutes an important possible systematic effect for Q-weak (see section 4.6.2 for a more detailed discussion of the detector non-linearities and associated tests).

A change in elastic electron event rate on the detector may cause the gain of a PMT to shift slightly, even when the bias voltages are perfectly stable and space charge effects are negligible. The electron bombardment of the last few dynodes is considered to cause the secondary emission coefficient to change, leading to a net gain change. The magnitude of the effect can vary by a factor of several between individual PMTs of the same type. This is called the "rate effect" or "short-term instability" although the independent variable is more likely the current or power dissipation on the last several dynodes [Yamashita, 1977] [Yamashita, 1978] [Vincenzi et al., 1984].

The SbCs dynodes are designed to reduce the rate effect [Vincenzi et al., 1984]. However, even with S20 photocathodes, stable voltage dividers, and negligible space charge effects, the residual rate effect with SbCs dynodes might prevent us from meeting the specification of less than 0.1% nonlinearity. The time constant for such gain changes is of order 0.1 second [Mack, 2005]. If the helicity reversal frequency is increased so that the time interval of rate changes is well below 0.1 second, the "rate effect" might be suppressed. The high helicity reversal rate of 960 Hz for Q-

[7] Soft background and dark rate can be disentangled to some extent by varying the beam current since soft background is proportional to beam current, but dark rate does not change with beam current.

weak was chosen in part to suppress effects that could cause false asymmetries, which includes the described “rate effect”.

As mentioned above, with the high event rate in production mode, the expected cathode current is a few nA. To reduce non-linearity effects, such as those described above, the PMTs will be operated at low gain during production running. This is achieved by using only the first 7 dynode stages and keeping the remaining stages and anode at the same bias voltage as dynode 7, as well as operating the PMT at a relatively low bias of around 1100 Volts (see section 4.4.4 on a description of the current mode PMT base). The corresponding anode current is well matched with the 1 MΩ transfer gain current-to-voltage preamplifiers and the current mode integrating ADCs, used to digitize the main detector signal during production running (see section 4.5.2 on a description of the current mode main detector DAQ). Non-linearities are of lesser concern when the main detectors are operated in pulse mode, since the effect itself is reduced (lower power deposition) and because small changes in PMT pulse height have no effect on the data. In pulsed mode, all the dynodes are used and the dynode bias is optimized for relatively high gain so that individual pulses in the quartz bars can be observed. There are no stringent requirements on timing or linearity in this application, but we do need at least 10^6 gain to be able to calibrate the photo-electron efficiency of the main detectors, by measuring clear single photo-electron peaks. However, even if all 10 stages are used to reach a maximum gain of 10^6, the single photo-electron pulse height, when terminated into 50 Ω, is only 0.8 mV. For this reason, fast linear amplifiers will be used to see the single photo-electron peak, instead of using higher gain PMTs which would have resulted in larger non-linearities in production running.

In addition to the build-in electrostatic shield at the cathode potential (inside the PMT itself), there are three other types of add-on shielding: electrostatic shielding, magnetic shielding, and radiation shielding. The electrostatic shielding is implemented in the form of an aluminum PMT housing, which also provide physical protection for the PMT and serves as a light tight housing (see section 4.4.5 for a description of the detector housing and mounting structure). The magnetic

shielding is a double layer, mu-metal case[8] inserted between the PMT housing and the PMT itself (see Fig. 4.28). The mu-metal is floated electrically, to reduce noise pick-up, and insulations were carefully inserted to avoid possible high voltage sparks between the mu-metal and the photocathode. In the experiment, stray fields from QTOR at the PMT locations are less than 0.1 Gauss, hence Earth's field dominates. Sensitivity tests at fixed cathode to first dynode voltage have shown that the earth's field has negligible effects when the PMT is shielded with this double layer mu-metal.

Beam optics simulations show that the main detector PMTs are located outside of the beam envelope. However, upstream multiple scattering events and secondary shower beam can potentially hit the PMT region and produce background in the PMT signal. To reduce this effect, radiation shielding in the form of 5 cm thick lead bricks is mounted just in front of the PMTs and below the PMTs at the inner radius side. This provides 10 radiation lengths attenuation for $\mathcal{O}(1)$ GeV particles (electrons) coming from the upstream direction and from the beamline.

4.4.4 PMT Bases

The main detector PMTs are used alternately in both current and pulsed modes, requiring them to operate over a wide range of gain (10^3 - 10^6). In current mode, the PMTs need to be highly linear and therefore operate at low gain, while in event mode, the PMTs need to have a high gain to obtain single photo-electron resolution. To satisfy both requirements, two types of PMT bases, a set of low gain bases and a set of high gain bases were built, to optimize the PMT gain and linearity in both current mode and event mode.

Considerations of PMT lifetime limit the maximum anode current to about 6 μA, and thus (for a fixed photocathode current of 6 nA) a maximum gain of ~1000. To achieve this low gain, while maintaining the high inter-dynode voltages required for linear operation, only the first 7 active stages of the PMT are used. The remaining stages are tied together electrically as a single anode. For pulsed mode operation, the bases are switched to the higher gain bases, which use all 10 dynode stages, to reach a gain of $\sim 2 \times 10^6$.

[8] Mu-metal is a nickel-iron alloy that has very high magnetic permeability so as to screen and attenuate low-frequency magnetic fields.

The PMT gain is determined by a particular high voltage divider design and the applied bias voltage, constrained by the manufacturer's maximum ratings for voltage and total gain. PMT base designs were developed based on simulations, using a simple PMT gain – voltage divider model [Mack, 2005]. The PMT gain for stage i can be modeled as:

$$G_i = \beta_i V_i^{\alpha_i} \ , \tag{4.31}$$

where V_i is the voltages applied on stage i, β_i and α_i are gain parameters. For n active dynodes, the total gain can be expressed as:

$$G = \prod_{i=1}^{n} G_i = \prod_{i=1}^{n} \beta_i V_i^{\alpha_i} \ . \tag{4.32}$$

Assuming the gain parameters are the same for all stages, approximate values of β_i and α_i then can be derived from the vendor's catalog, and improved and refined through prototype tests. The PMT base can be modeled as a voltage divider network, containing ideal resistors and zener diodes (zener diode is used to provide a fixed voltage for a certain dynode). This model is used to calculate the currents, voltages and nominal gains for an unloaded base, at zero anode current, and to estimate the changes in PMT gain at vary anode current by solving the nonlinear problem of determining the state of a voltage divider as the load varies. This model does not include other PMT performance limiting factors, such as the dynode rate effect, the space charge effects. The exact properties of the base-PMT assemblies were determined during bench testing on prototypes and on the final bases [Anderson, 2006] [Gericke, 2006a] [MacEwan, 2010].

The current mode PMT base is critical for production parity-violation measurements. The principal requirements are less than 0.1% nonlinearity at 10^3 gain and 6 nA photocathode current [Mack, 2005]. The voltage divider incorporates two zener diodes to fix the bias voltage between the cathode and first dynode and to keep the first-stage multiplication noise independent of applied high voltage. The zener diodes are also used on the final stage where the amplified currents are largest, to try and keep the currents stable and reduce possible non-linearities. All other stages are identical resistor stages (see Fig. 4.25). At fixed supply voltage, any change in the voltage across

one resistor (ΔV) must be equal and opposite to the voltage change ($-\Delta$V) in the other resistor, thus the net gain for these two stages does not change to first order in ΔV. In practice, in order to yield high linearity, the resistive dynodes need to be well matched.

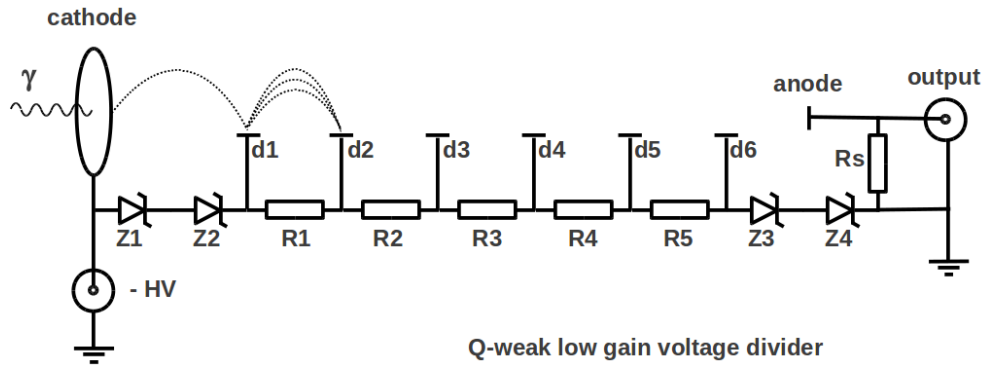

Figure 4.25: Schematic diagram for the low gain current mode PMT base. The voltage drop between the cathode-d1 region is due to two 140 V, 5 W rated zener diodes ($Z1, Z2$) and the same for the final stage (Z3, Z4). R1 – R5 are identical 1 kΩ/0.5 W resistors. Rs is a 10 kΩ/0.5 W load/safty resistor.

A load/safety resistor (1-10 kΩ) is added in the divider between the anode and ground to keep the anode at the ground potential if the anode output is disconnected from the preamplifier. Subsequent reconnection of the preamplifier to the anode could potentially damage the preamplifier if the anode is charged. In some pulsed mode applications, the peak current can greatly exceed the divider current, so some local storage of charge is needed beyond the dynode stray capacitance. In our current mode application, the divider current is at least 100 times larger than the anode current and should be able to recharge the dynodes to their nominal voltages on pico second time scales after a small perturbation such as a statistical fluctuation or a major perturbation such as a spark. Therefore, the current mode divider does not include any reservoir capacitors. Modern high voltage power supplies have very low ripple, so the current mode divider also does not include decoupling filter capacitor to minimize stored energy which could damage the power supply or the PMT in the event a spark is generated [Mack, 2005].

By increasing or decreasing the high voltages, the gain can be adjusted by a factor of 4. All cur-

rent mode PMT and base assemblies were fully tested and characterized during bench tests and then again during detector commissioning. The full set of bench and commissioning tests is described in section 4.6.

The pulsed mode PMT base is needed for event mode measurements which will be used to search for background and to map out the electron hit position dependent response of the detector. The principle requirements for the pulsed mode divider are reasonable linearity, sufficient gain and bandwidth to achieve single photo-electron resolution, since much of a 1-10 MeV low energy photon background may show up as single photo-electrons in the detectors and dilute the measurements. Hence, to obtain background spectra which can be interpreted in terms of a fractional dilution, it is important that the detector be linear over a dynamic range of roughly 1-100 photo-electrons.

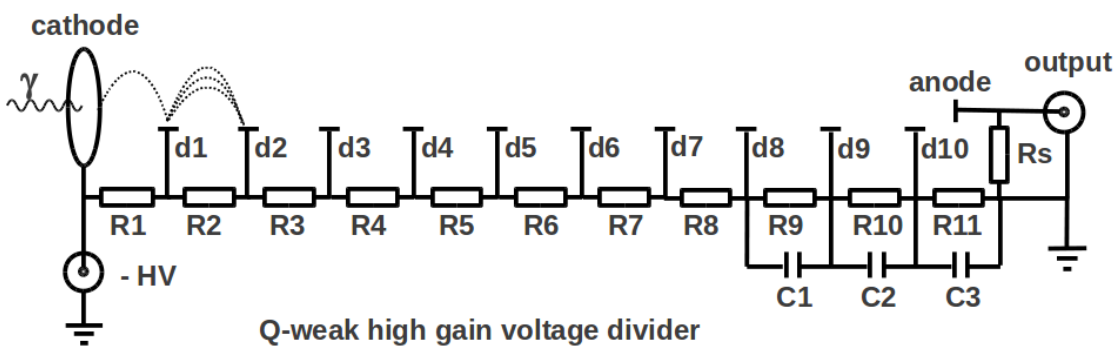

Figure 4.26: Schematic diagram for the high gain pulsed mode PMT base. R1 is a 180 kΩ/2 W resistor. R9 is a 112 kΩ/2 W resistor. Rs is a 1 MΩ/0.5 W load/safty resistor. Other resistors are 56 kΩ/0.5 W. C1 – C3 (100 nF) are reservoir capacitors.

The divider design (as shown in Fig. 4.26) is a compromise between the requirements for reasonable gain, linearity, and stability with respect to rate changes. Because of the low photo-electron number (10 p.e. per PMT without pre-radiator, 50 p.e. per PMT with pre-radiator), relatively low gain (10^6), and long risetime for this PMT (of order 10 ns), the peak currents are estimated only at the level of:

$$\frac{(50\text{ p.e.}) \times (1.6 \times 10^{-19}\text{ C}) \times 10^6}{10\text{ ns}} \sim 1\text{ mA}, \tag{4.33}$$

which which also means there wouldn't be a large amount of nonlinearity (the manufacturer spec-

ified PMT nonlinearity is less than 1% at this level of peak current). Good pulse linearity can be assured by using low inductance reservoir capacitors on the final base stages. The divider includes a 1 MΩ load/safety resistor between the anode and ground to prevents the anode from charging up when disconnected. In addition, reflections from patch panel impedance mismatches would appear as low amplitude pulses or oscillations that could complicate the analysis of background contributions that produce low amplitude pulses. The load/safety resister is also used to back-terminate the divider so as to minimize the reflections. Like the current mode PMT bases, the pulsed mode PMT base assemblies were fully tested and characterized on the bench and during commissioning.

4.4.5 Main Detector Mounting and Support Structure

The main detector mounting and support structure consists of a housing for each quartz and PMT assembly, a so-called exoskeleton around each housing, and a general support structure for all eight detectors, referred to as the Ferris wheel (see Fig. 4.32). The housing provides the mounting structure for the glued quartz and PMT assemblies and are designed to minimize tension on the various glue joints and torsion on the bar itself, which could destroy total internal reflection. The housing also provides light tight dark environment for the detectors. The housing is mounted inside the exoskeletons, which are designed to reinforce the mechanical strength of the main detector housing and provide mounting structures for PMT lead radiation shields and the lead pre-radiators. The exoskeletons also provide the mounting interface to the overall support structure (the Ferris wheel). The Ferris wheel locates the main detectors at their designed places in the focal plane (according to the simulated location of the scattered beam envelope). The attachment of the exoskeletons to the Ferris wheel incorporates manual radial motion capabilities with a range of about 15 cm. The final position of the detectors was carefully surveyed. All survey and alignment markers are attached to the quartz-PMT housings. The Ferris wheel incorporates cable trays and work platforms with ladders, for maintenance access. All the mechanical structures were built with aluminum in order to provide a “low-Z” (short radiation length hence less shower background) and iron-free (to avoid the possibility of being magnetized) environment around the detectors. Use of other materials was

restricted to places where extra strength was required. This included bolts, where the stainless steel and copper were used.

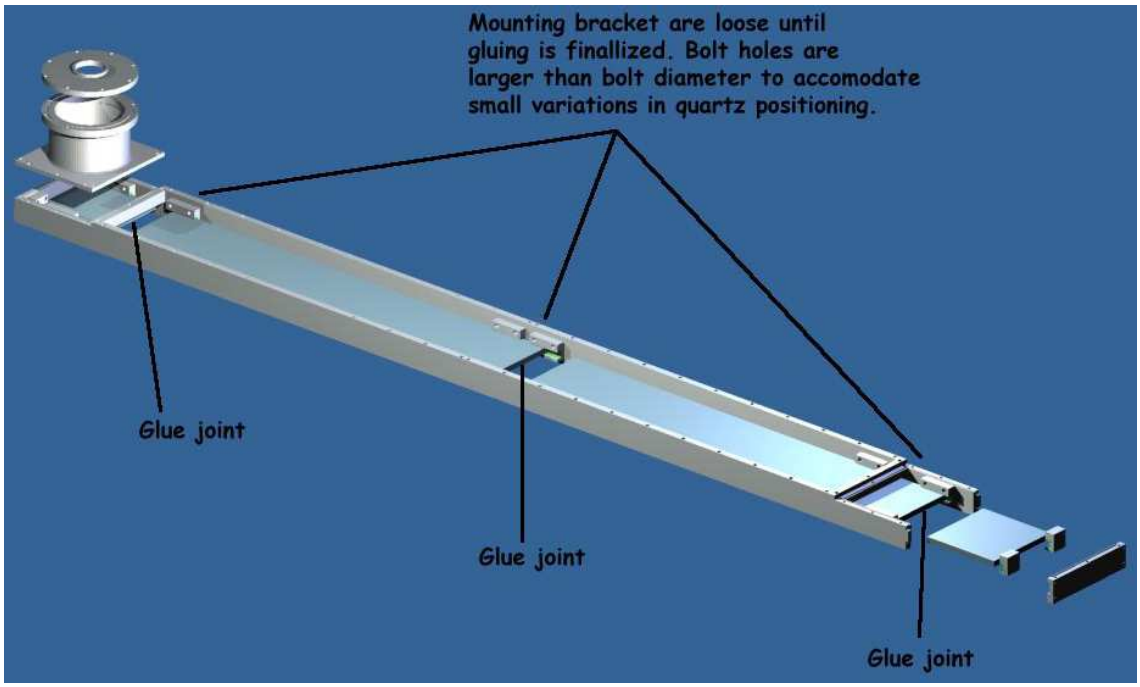

Figure 4.27: Exploded view of the radiator module. The front (entrance) and back (exit) "windows" are not shown. The assembly consists of 38 bolted parts.

The detector housing must satisfy a number of design constraints and requirements, such as light tightness, minimizing light transportation loss, strain and stress free mounting of the quartz bars, supporting quartz bars and glue joints in any orientation, minimizing showering, allowing fairly easy access to service the PMTs and provide easy access to the PMT bases to switch quickly between production (current) and tracking (pulse) mode. Light tight seals are implemented by using gaskets and black liquid tape. The light transportation loss is minimized by reducing surface contact of housing material with the quartz bars (which destroys total internal reflection). The housing also allows for possible lining on the inside, with reflective material. Showering is minimized by using low-Z materials, and minimizing the amount of material around the detector. The housing consists of an aluminum frame and thin entrance and exit windows, made from Poron – a flexible 0.64 cm

thick black radiation hard elastomer [9]. The window material is stretched across the housing front and back and clamped down by aluminum bars, to ensure that no contact is made with the quartz surface. The exploded view of the detector housing assembly, which includes frame, PMT housing and quartz bar mounting brackets, is shown in Fig. 4.27 (see appendix A.5 for the detailed CAD drawings of the detector housing [Gericke, 2009]).

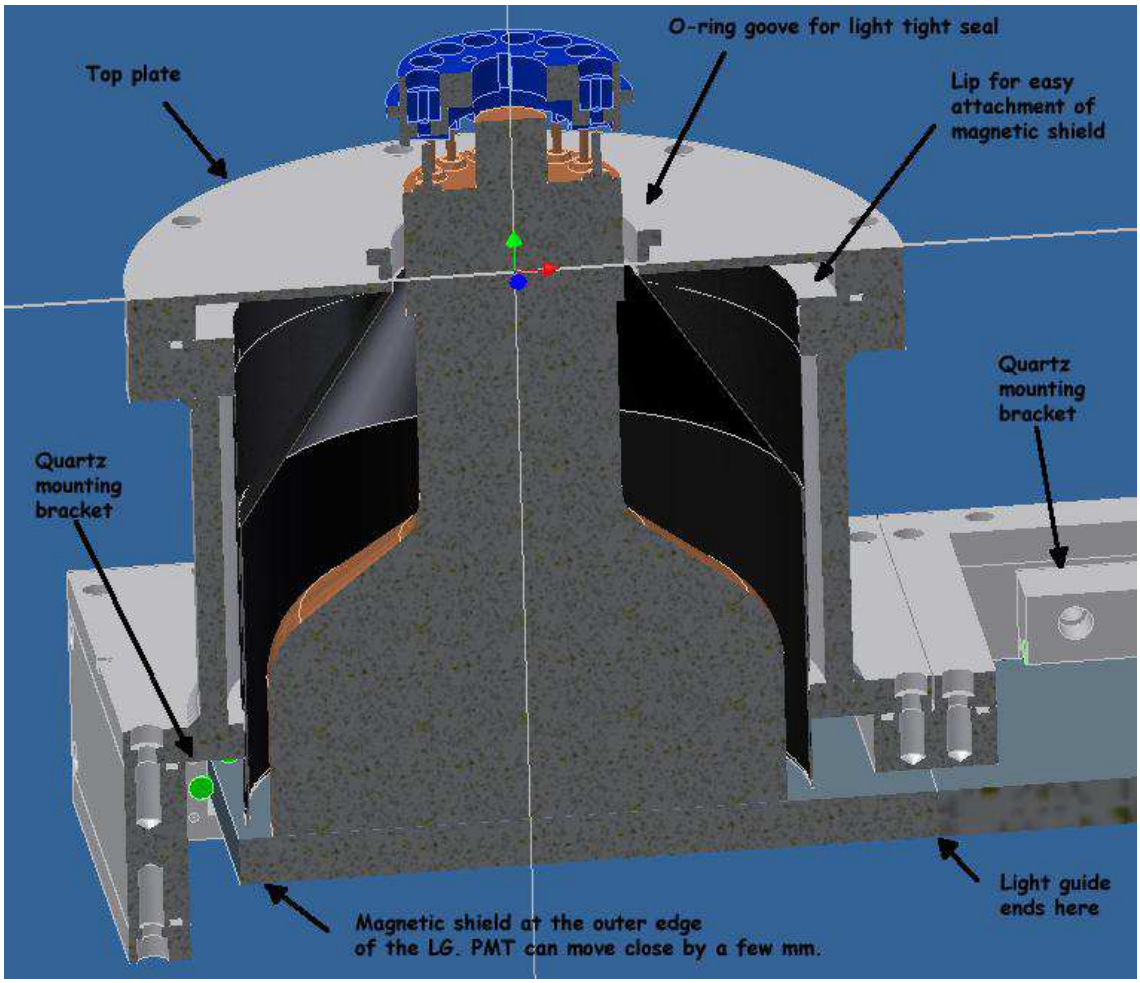

Figure 4.28: PMT housing portion cut along the bar. The positioning of the PMT on the light guide, as well as housing design to accommodate mounting of the magnetic shield, are shown.

[9] Stockwell Elastomerics, Inc. 4749 Tolbut Street, Philadelphia, PA 19136-1512

The aluminum frame (quartz bar housing walls) of the module require the use of stainless steel Helicoil inserts for the tapped holes to prevent stripping of threads. The PMTs housing is located at the outer edge of the module. The tubular region of the PMT housing is welded to the plate that attaches to the quartz housing walls. The design accommodates a ±4 mm variation in the overall length of the quartz bar assembly. The overall length of the module is 95.5 inches (about 243 cm) and the overall width is 9.5 inches (about 24 cm). The thickness and width of the housing walls are 0.75 inch (1.91 cm) and 2 inch (5.08 cm), respectively. The PMT housing (see Fig. 4.28) has a large opening to accommodate variations in PMT positioning on the light guide. The magnetic shielding for the PMT is fixed inside the PMT housing and there are isolated electrical feed-through connectors on the lid (top plate) to drive LEDs inside the detector housing, for diagnostic purposes.

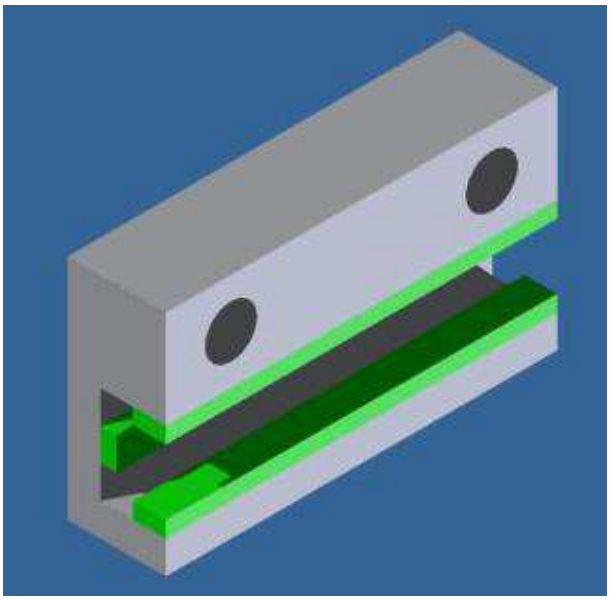

Figure 4.29: Quartz holding bracket with silicone inserts for strain relief and cushioning (7.62 cm long for the side brackets and 5.08 cm long for the quartz bar end brackets.

The quartz bar inside the housing is held by “C-shaped” mounting brackets (see Fig. 4.29). The thinner side of the bracket is towards incident electrons, to minimize electron showering in the brackets. The brackets have a bolt hole diameter that exceeds that of the bolt by about 2 mm, so that they can be adjusted to conform to the glued form of the quartz assembly and can be tightened

without introducing additional strain on the glue joints. Enough pressure needs to be produced by the brackets on the quartz bar and all glue joints to prevent relative motion of the quartz pieces and loss of light coupling when the detector is moved. The brackets essentially allow one to build the housing around the glued quartz bar, rather than having to lift the quartz bar into the housing, which minimizes the stress on the glue joints on the quartz bar.

(a) Assembled main detectors

(b) Detectors stored on a shelf

Figure 4.30: (a) A photo of assembled main detectors with housing but without window material. The gaps between the quartz bar and frame and the thinner brackets on the electron incident side (coming from the bottom in the picture) reduce showering. The bars across the quartz assembly, between the two side walls, shown in the photo are for temporary support of the frame. (b) Five fully assembled main detectors stored on a shelf, and completely tested for light tightness and optical coupling with cosmic rays.

An in-situ mounting scheme for the quartz bar and the PMTs was used in assembling the quartz-PMT assembly and the housing, with the purpose of protecting glue joints and accommodating the small variations of component size and shape. The basic procedure used was: gluing the two half quartz bars to get the full length quartz bar, mounting the entire quartz bar and light guide assembly in its final position inside the housing when the glue is settled (building the housing around the quartz bar), then attaching the PMT housing as well as the PMT itself with the glue applied on the PMT window before attaching the top plate, centering the PMT with the designed top plate opening, removing the PMT housing after the glue on the PMT window is settled, cleaning the quartz bar assembly, reattaching the PMT housing and covering the detector with the poron windows to close

up the detector entirely. The photo in Fig. 4.30 (a) shows the assembled detector with housing before covering the detector with the poron windows. The photo in Fig. 4.30 (b) shows the fully assembled detectors stored on a shelf.

The detector optical assembly and housing must be reinforced by a frame of extruded aluminum struts – the exoskeleton (see Fig. 4.31). As mentioned above, the exoskeleton performs several jobs, such as stabilizing the housing, supporting the lead radiation shielding for the PMTs, supporting the panels of lead pre-radiators, and providing interface points for attachment with radial adjustment (see below). The exoskeleton was designed to safely support 500 lbs (about 227 kg) of weight in different orientations with minimal deflection.

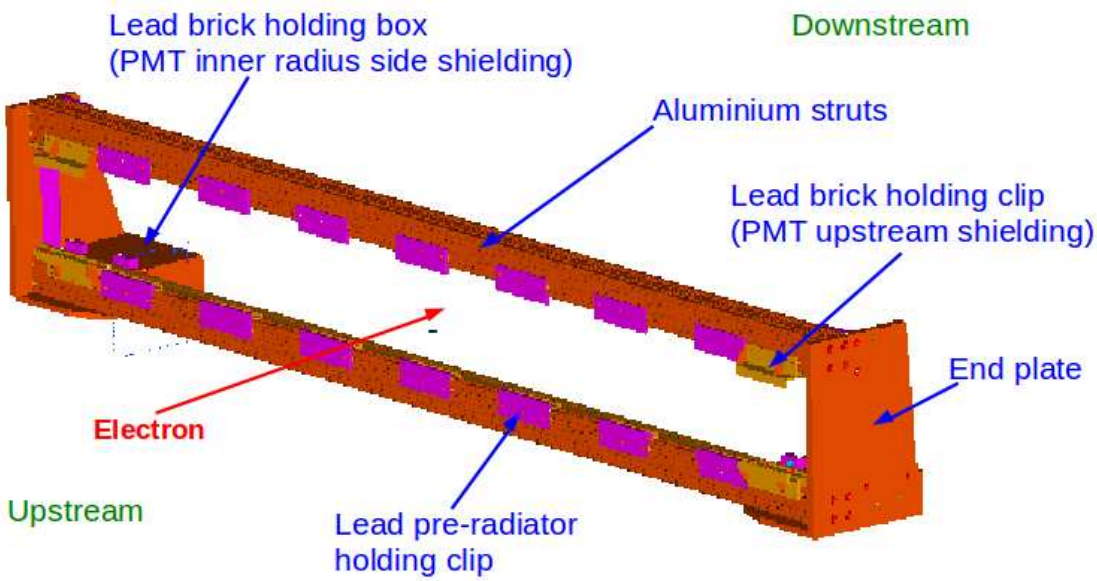

Figure 4.31: Exoskeleton of the detector optical assembly and housing. The detector optical assembly and housing are loaded into the exoskeleton from the downstream side.

The exoskeleton has clips at the upstream side. These clips are used to clamp the 2 cm thick pre-radiator tiles and 5 cm thick lead bricks for shielding the PMT. Another set of lead brick PMT shields are inserted into holding boxes attached to the bottom of the exoskeleton at the PMT position to shield the radiations against beamline background.

A Ferris wheel was designed to support the Q-weak main detectors (see Fig. 4.32). The Ferris wheel has an octagonal structure which lines up the eight main detectors with the scattered electron beam profiles on the focal plane, as created by the eight sector QTOR. The Ferris wheel is located just downstream of the focal plane with access platforms (not shown) and detector supporting arms. The main detectors are mounted on the supporting arms in each octant (see the schematic view of the main detector array mounted on the Ferris wheel in Fig. 4.32).

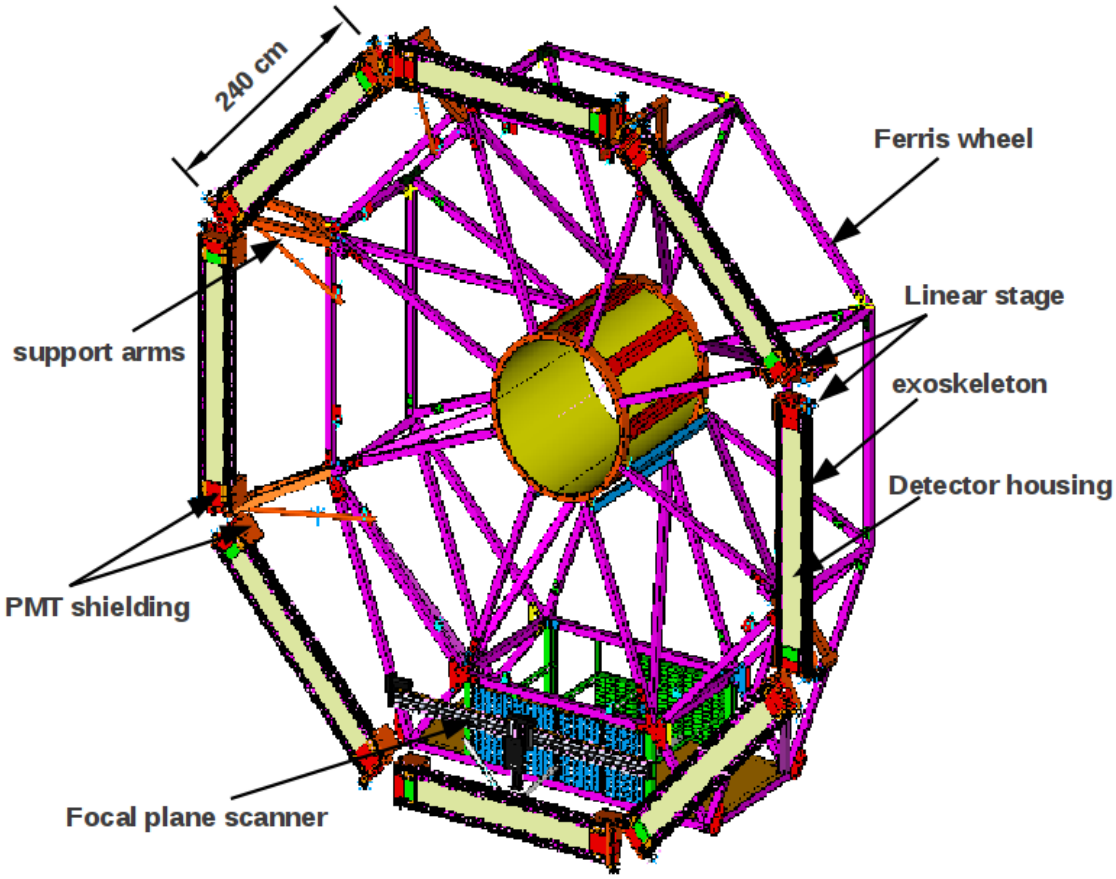

Figure 4.32: Schematic view of the main detector array mechanical support structure. The detector modules, including detector assembly and exoskeleton, are mounted on the Ferris Wheel (purple) with detector support arms (orange).

The detector radial positions within the support structure can be adjusted, to compensate for

any possible variation in electron optics, as compared to the simulation predicted scattered electron profile, and to cancel out any small survey and alignment errors. The radial adjustment devices are ball-screw linear translation stages with encoders so that the position can be fine-adjusted with high reproducibility. The translation linear stages are attached to the hard end plates of the exoskeleton and their movable tables are bolted on the support arms (see Fig. 4.33). A ~15 cm moving range of the table gives enough flexibility for the radial position adjustment.

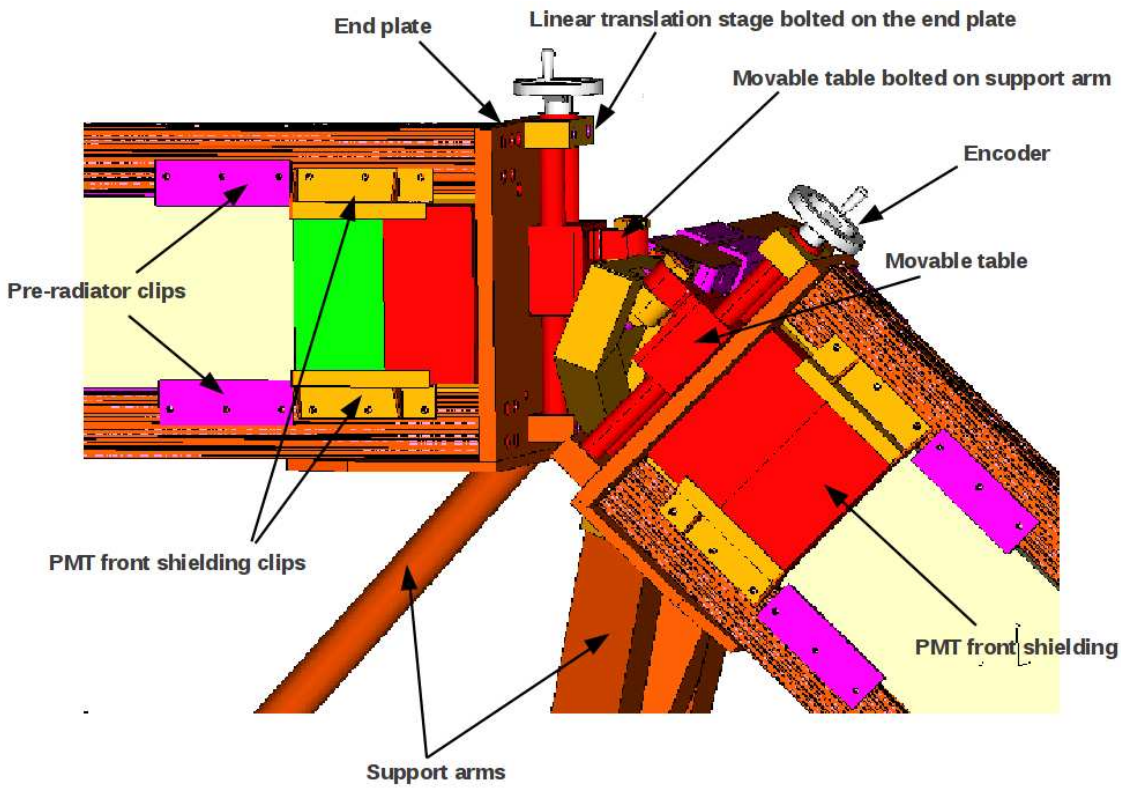

Figure 4.33: Schematic view of the radial adjustment (looking downstream). The pre-radiator clips (purple) and the PMT front radiation shield clips (orange) on the exoskeleton are also shown.

4.4.6 Diagnostic System

The detector performance, such as electronic noise level, and the signal processing electronics needs to be checked periodically. The detector system noise performance can be checked by introducing low noise inputs during occasional beam-off periods. These test signals need to have a comparable amplitude to the beam on signal. By replacing the signal from elastic electrons with an equivalent amount of LED light into the PMT, the statistical noise width can be reduced by a factor of $1/\sqrt{N_{\text{p.e.}}}$ [10]. Running the main detectors with LEDs is also a sensitive test for such excess noise sources as after-pulsing or sparking.

An even more sensitive test (approaching the shot noise limit) is to replace the light sources altogether with a current source at the input to the I-to-V amplifier. The shot noise limit is more than 2 orders of magnitude smaller than the electron track statistical uncertainty, so a current source could allow a sensitive test of amplifier and ADC noise.

Because the LED and current source runs have so little noise compared to the counting statistics of electron tracks, the time needed to identify excess noise at a significant level is very short. For example, if an excess noise factor of 10% is considered a threshold for concern, from Eqn. 4.13 and 4.14, the counting statistical uncertainty would be only increased by $\sqrt{1+(10\%)^2}-1 = 0.5\%$. This would yield a 100% change in the predicted noise level of an LED run or a 1000% change in the expected level using a current source. Thus, even one second would be plenty of time to make a determination of whether the apparatus itself (in the absence of beam) was a significant source of excess noise. By monitoring these noise levels intermittently throughout the experiment, we will be able to track potentially increasing noise levels from radiation damage to the amplifier, etc.

Each battery source is an electrostatically shielded box, containing a 9 V battery and a resistor. They are configured either as a voltage source or as a current source, and can be used to test the current mode front-end electronics and make measurements of the electronics pedestal contribution to the signal. The battery sources were installed close to the PMTs and preamplifiers. Each main

[10] A more careful analysis is required which takes the single photo-electron resolution into account, but the simple scaling argument above is only optimistic by perhaps $\sqrt{2}$.

detector includes a set of 2.5 mm green LEDs [11], installed at either end of the housing, one close to each PMT. The LEDs are used to simulate the light production in the quartz bar, check the light transportation, calibrate the single photo-electron spectrum, and validate noise level.

The LEDs in the detectors are driven either by a DC power supply or a pulse generator to perform single photo-electron calibrations and linearity tests. Due to the nonidentical response of each individual PMT to the LED light, a power supply distribution panel is needed to provide light emission adjustment for individual LED. The LED power supply distribution panel [Wang, 2010] (as shown schematically in Fig. 4.34) is powered by either an external DC power supply or an external short pulse generator. For the LED light emission stability, a mirrored current source drive circuit on each LED with light emission feed back would have been ideal. However, a regulated voltage source was chosen to simplify the circuit.

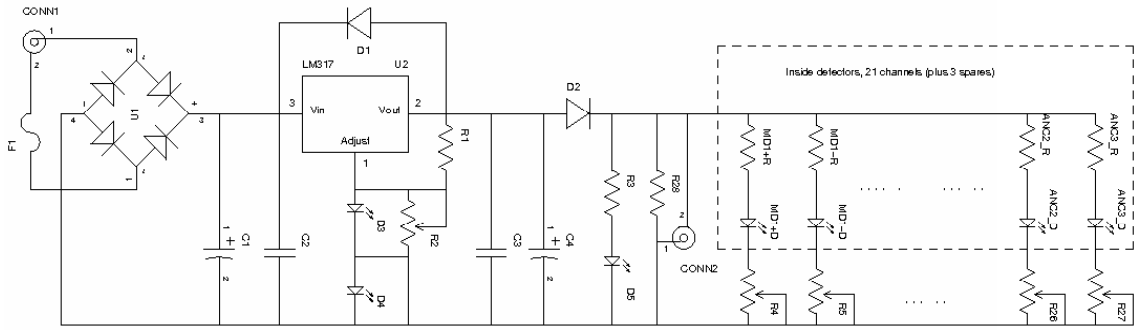

Figure 4.34: Schematic diagram of LED power distribution panel.

The luminous intensity of an LED (I) has a temperature dependence as: [Schubert, 2006]

$$I = I_0 \exp[-(T - T_0)/T_1], \tag{4.34}$$

where I_0 is the luminous intensity at $T_0 = 300$ K, T_1 is LED characteristic temperature and $T_1 \sim 100$ K. The LED light emission will exponentially decrease with increasing temperature. This temperature drift has large effects on the PMT output, especially at the beginning when the

[11] The green LEDs have ~560 nm wavelength. A better performance can be acquired by using blue LEDs (~470 nm) or UV LEDs (<400 nm) whose wavelengths are closer to the wavelengths of produced Čerenkov lights in the quartz bar.

LED starts to warm up. In order to avoid using a complicated temperature compensation circuit to produce constant LED luminosity, the LEDs will be turned on in advance, before making a diagnostic measurement. Short time measurement should then be made after LEDs have stabilized, to reduce the effects of luminosity drift.

4.5 Electronics and Data Readout (DAQ)

To make a precise measurement of a parity violating asymmetry possible, suppression of noise and systematic effects is paramount. In principle, the faster the helicity reversal, the better the suppression. To see how this works, it is most convenient to look in the frequency domain. With an unpolarized beam, the signal from one of the main detector PMTs would be a DC current of about 6 μA with noise from various sources, mostly the shot noise but with slow drifts in the detector gain and other experimental components. If the electrons are longitudinally polarized, the current will be decreased slightly in the positive helicity state and increased slightly in the negative helicity state. If the helicity repeatedly reversed at some frequency, then the "parity signal" would be a small, mostly square-wave signal superimposed on the the DC (mean) component, including the drifts.

To extract the small parity signal from the other drifts, we integrate the signal over each helicity state and take the difference between the positive and negative states. Any drift or fluctuation in the signal with a significantly lower frequency than the helicity reversal frequency will "look" like a constant DC offset over a small range of consecutive helicity states. If a particular pattern is chosen (such as "$+ - -+$" or "$- + +-$") from a sequence of consecutive helicity states to calculate the asymmetry (rather than simply using "$+ - + - + - \ldots$"), then the parity violating component can be separated from slower drifts, even if these increase or decrease linearly with time, over the helicity pattern. Any signal fluctuations (noise) at frequencies that are significantly larger than the helicity reversal frequency will be integrated over by electronic filtering in the ADCs and by software integration. The challenge in all aspects of the experimental design is to ensure that all fluctuations in the signal (other than the parity signal) with a frequency at or close to the chosen helicity reversal

are (1) random with respect to the helicity state and (2) small in amplitude compared to the expected parity signal. If these two conditions can be satisfied then these fluctuations will average to a zero mean within an uncertainty that becomes part of the overall experimental uncertainty.

4.5.1 Electronics

As described before, the Q-weak experiment will run both in low beam current counting/event mode for calibration and in integration/current mode for asymmetry measurements. Two independent sets of electronics – event mode electronics and current mode electronics, are designed for the main detector to run in these two different modes. In event mode, the beam current is reduced to $\sim$ nA level so that the event rate is reduced drastically. The detectors can then work in pulse counting mode and individual pulses can be processed. The event mode electronics use conventional techniques to measure charge, timing and rate, etc, and will not be discussed in detail here. In current mode, the beam current is increased to $\sim 150\ \mu$A or higher, to meet the requirement of measuring the ~ -0.3 ppm parity-violating asymmetry with a statistical precision of 5×10^{-9} in about 2500 hours. This beam current will produce an event rate of about 800 MHz in each of the 8 octants. This is too high for conventional pulse counting techniques. Custom made electronics[12] are needed for current mode measurements. Details of the current mode electronics are introduced below.

A block diagram of the Q-weak current mode front-end electronics is shown in Fig. 4.35. The figure shows how a $5\ \mu$A current signal is produced from the high count rate in one of the 8 detectors. It is assumed that typically 50 photo-electrons will be released at the photomultiplier tube (PMT) cathode for each event [13]. The gain of the photomultiplier will then be adjusted to yield $5\ \mu$A at the anode under normal running conditions. The current signal from the photomultiplier tube goes to a low noise trans-impedance (current-to-voltage) preamplifier located close to the PMTs. At the output end, the amplifier provides a line driver, capable of maintaining the signal amplitude over the more than 100 meter distance to the DAQ room, where the signal is digitized by VME based digital

[12] Designed and built by researchers at TRIUMF and the University of Manitoba.

[13] Simulation, bench and beam test (see related sections in this chapter) showed that, on average, about 8 photo-electrons per event can be detected by a single PMT on a bare quartz bar (without pre-radiator); about 50 photo-electrons per event can be detected by a single PMT if the quartz bar is equipped with a 2 cm thick lead pre-radiator.

integrators located in the electronics cage outside the experimental area. The whole system must be very low noise so that beam-off null asymmetry tests can be made in a short time.

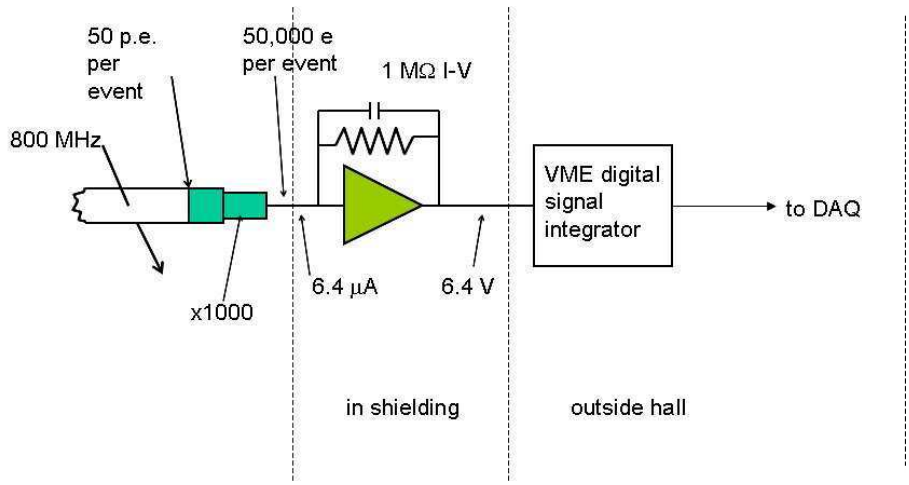

Figure 4.35: Schematic of the current mode signal chain.

The 5 μA signal from a PMT with beam on the detectors is considerably noisier than a 5 μA signal from a battery because it is made from large, 50,000 e charge lumps rather than from single electrons. This "shot noise" [14], i.e. the standard deviation of current fluctuations, is given by

$$i_{\text{shotnoise}} = \sigma_I = \sqrt{2QI\Delta f}\ , \tag{4.35}$$

where I is the current, Q is the charge quantum, and Δf is the equivalent noise bandwidth. If the bandwidth is limited by a simple one-pole low-pass filter with half-power frequency f_{-3dB}, the equivalent noise bandwidth is $\frac{\pi}{2} f_{-3dB}$. If the limit is set by integrating the signal for T seconds, the equivalent noise bandwidth is $\frac{1}{2T}$.

The custom VME signal integrators must integrate the signal over a time period depending on the helicity reversal rate. Two schemes have been considered. In the '120 Hz' scheme, each helicity state will last 1/30 second. The current mode electronics will integrate the current over the helicity

[14]Shot noise is a type of electronic noise that occurs when the finite number of particles that carry energy (such as electrons in an electronic circuit or photons in an optical device) is small enough to give rise to detectable statistical fluctuations in a measurement.

state in four 1/120 second blocks. The scheme would be insensitive to noise at multiples of the 60 Hz power line frequency; the factor of 4 in over sampling would let us check if significant line noise was being canceled by the 1/30 second integral. In the '1 kHz' scheme, each helicity state will only last 1/250 seconds, and the charge will be digitized as four, one millisecond long, integral blocks. There are many reasons for choosing the faster reversal, such as suppression of beam line noise or target boiling noise. Prior experience with liquid hydrogen target [Armstrong et al., 2003] indicates that the noise from target boiling is limited to low frequencies, and that bubbling is not seen on a time scale of a few ms. This observation has been validated by the Q-weak data, as seen in the main detector signals (see Fig. 3.15). The need for four integral blocks per helicity state is not as clear as for the '120 Hz' case, but the electronics were designed to preserve that capability.

This integration method requires that the analog signal bandwidth is small compared to the sampling rate, so that the signal is approximately constant over one time bin. Limiting the analog bandwidth is also important so that signal frequencies higher than twice the sampling rate do not 'alias' [15] back into the passband. Therefore, the digital integrator has a sharp cutoff filter built in. However, the analog bandwidth cannot be made too low. Too low a bandwidth will give too little spread in the individual samples and will not average out 'least bit' ADC noise. Also, the signal we are looking for is a small current synchronized with the helicity state; a very small bandwidth could slow the response of the electronics, resulting in that the real signal cannot be followed. When looking at in the time domain, the dead time between helicity states (about 70 μs) is much larger than the signal rise-time, so the current is steady on its new value before integration begins.

Table 4.4 summarizes the main noise sources under different running modes. The main noise source during production data taking is shot noise due to the random arrival of electrons at the detectors (i.e. counting statistics). Preamp noise cannot be lower than the thermal noise (Johnson noise) in the 1 MΩ feedback resistor. This white noise, with a density $e_R = 4k_BTR_f$ (where k_B is Boltzmann's constant in joules per kelvin, T is the resistor's absolute temperature in kelvins, and R is

[15] Aliasing refers to an effect that causes different signals to become indistinguishable (or aliases of one another) when sampled. It also refers to the distortion or artifact that results when the signal reconstructed from samples is different from the original continuous signal.

Condition	Noise on 1/120 s integral (ppm)	Noise on 1/1000 s integral (ppm)
Beam-ON shot noise	430	1240
Shot noise during LED tests	61	175
Shot noise during battery tests	1.9	5.5
Preamplifier noise	0.7	2.0
Digital integrator noise	1-2	1-2

Table 4.4: Comparisons of noise contributions from different sources. This noise is reduced during beam off tests when the charge quantum of the 5 μA signal is smaller. It is assumed $Q = 50000$ electrons for beam on, $Q = 1000$ electrons for LED tests, and $Q = 1$ electron for battery tests. If other sources of noise are small compared to shot noise, then the time to achieve a given statistical precision is proportional to the square root of charge quantum (see Eqn. 4.35).

the resistor value in Ohms, $e_R = 127nV/\sqrt{\text{Hz}}$ at room temperature), is added in quadrature with the shot noise. The input resistor also contributes noise, the size of which depends on the capacitance of the input cable. Simulations at TRIUMF indicate around 400 nV/$\sqrt{\text{Hz}}$ [Ramsay, 2006]. Since the amplifier noise for a modern preamp is several factors of ten below this, we assume the resistor noise dominates. As a fraction of 5 V, it is 2 ppm for a 1 ms integration. For the VME based digital signal integrator, the noise depends on details of the design, but is effectively one or two least significant bits on a 20 bit number. Internally, the integrators use 18 bit ADCs with typically 0.5 LSB RMS noise that is further reduced by averaging multiple (500 to 1000) samples over the integration period.

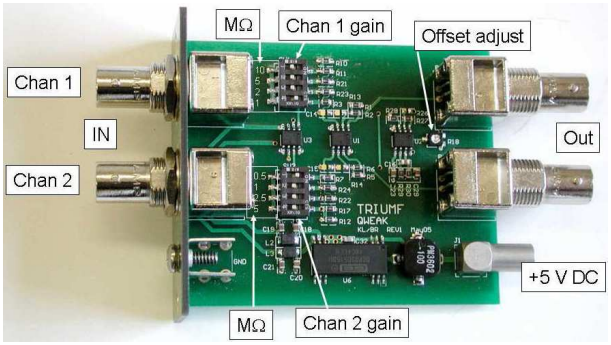

Figure 4.36: Photo of the low-noise preamplifier built at TRIUMF.

The current mode PMT anode signal is sent to a nearby, high gain, current to voltage (I-to-V) operational front-end amplifier through a low-capacitance coaxial cable. The photo of the low noise preamplifier is shown in Fig. 4.36. The schematic diagram of the amplifier design is shown in Fig. 4.37. The design is based on 5 m of RG-62 cable on input. The inputs are protected with a combination of resistors and diodes. The noise in the preamp is dominated by the combination of input cable capacitance (longer cable means more input capacitance and increasing noise), the value of the input protection resistor and the feedback resistor. A bandwidth of 30 kHz will follow a helicity reversal settling time of 70 μs. The I-to-V amplifier is followed by a cable-driving stage with an optional offset voltage. This stage must drive the large capacitive load (more than 100 m RG-58 cable to the VME digital integrator in the counting house).

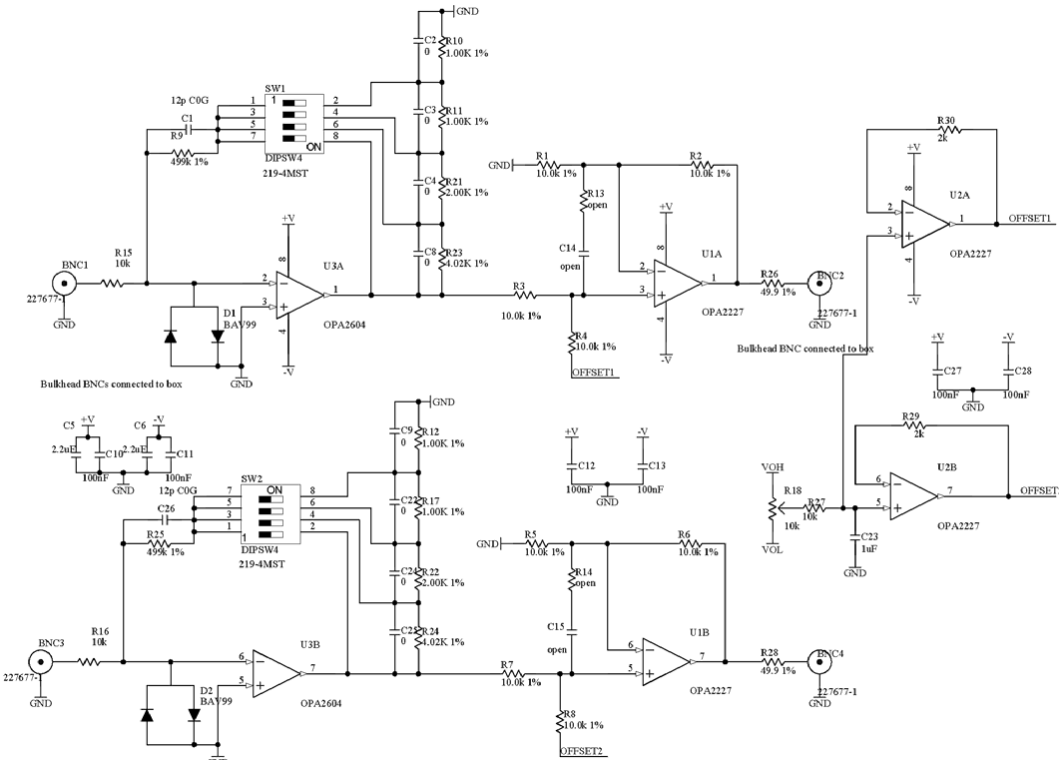

Figure 4.37: Schematic diagram of TRIUMF low noise trans-impedance preamplifier.

The main detector pre-amplifiers have a bandwidth of 26 kHz and trans-impedance gain of 0.5

MΩ, 1 MΩ, 2 MΩ, 4 MΩ [16]. For a typical PMT anode current of negative 6 μA and a trans-impedance gain of 1 MΩ, the inverting I-to-V amplifier gives an output of positive 6 V.

The custom VME digital integrator is located outside the experimental area due to concerns about single-event upsets and long term radiation damage. The block diagram of the design is shown in Fig. 4.38. An instrumentation amplifier at the input provides common mode noise rejection and is followed by an anti-aliasing[17] filter. The combination of front-end trans-impedance amplifier and anti-alias filter allows the system settling time and noise bandwidth to be controlled separately. An 18-bit ADC operates at a fixed sampling rate, being controlled by signals derived from external clock and gate signals. The combination of 18-bit precision and fast sampling allows us to spread even our lowest noise signal over 9 channels (FWHM). The output of each ADC in the module is summed for a selectable number of samples and made available to the DAQ system through the VME interface. All control, summation and VME logic resides in a Field Programmable Gate Array (FPGA).

The method of integration is a simple rectangular approximation. The integration scheme is as follows. The integration period, T, is divided into n equal time bins of width Δt and the signal is sampled at the middle of each bin; the integral is Δt times the sum of the samples.

Each VME module consist of eight integrator channels. The module takes −10 V to +10 V input signals at 10 kΩ input impedance on quasi-differential isolated BNC connectors (the BNC outer conductor is connected to ground by a 100 kΩ resistor) for input signals. The module is gated by an external NIM signal (e.g. MPS trigger) and clocked by a 20 MHz NIM signal from the accelerator source. An internal gate and an internal 20 MHz clock can be self-generated by the module, for testing. The sampling rate is set as a fraction of the clock, from 68 ksps (kilo samples per second) to 500 ksps with 20 MHz clock. The input signals are filtered with a 50 kHz, 5-pole anti-aliasing filter and then integrated by the 18 bit ADC at a sampling rate selectable up to 500

[16]The Q-weak luminosity monitors use the same pre-amplifiers, but with different gain and bandwidth. The luminosity monitor pre-amplifiers have a bandwidth of 17 kHz and trans-impedance gains of 0.5 MΩ, 1 MΩ, 25 MΩ, 50 MΩ.

[17]Anti-aliasing means removing signal components that have a higher frequency than is able to be properly resolved by the recording (or sampling) device. This removal is done before (re)sampling at a lower resolution. Anti-aliasing is often done using an analog anti-aliasing filter to remove the out-of-band component of the input signal prior to sampling with an analog-to-digital converter.

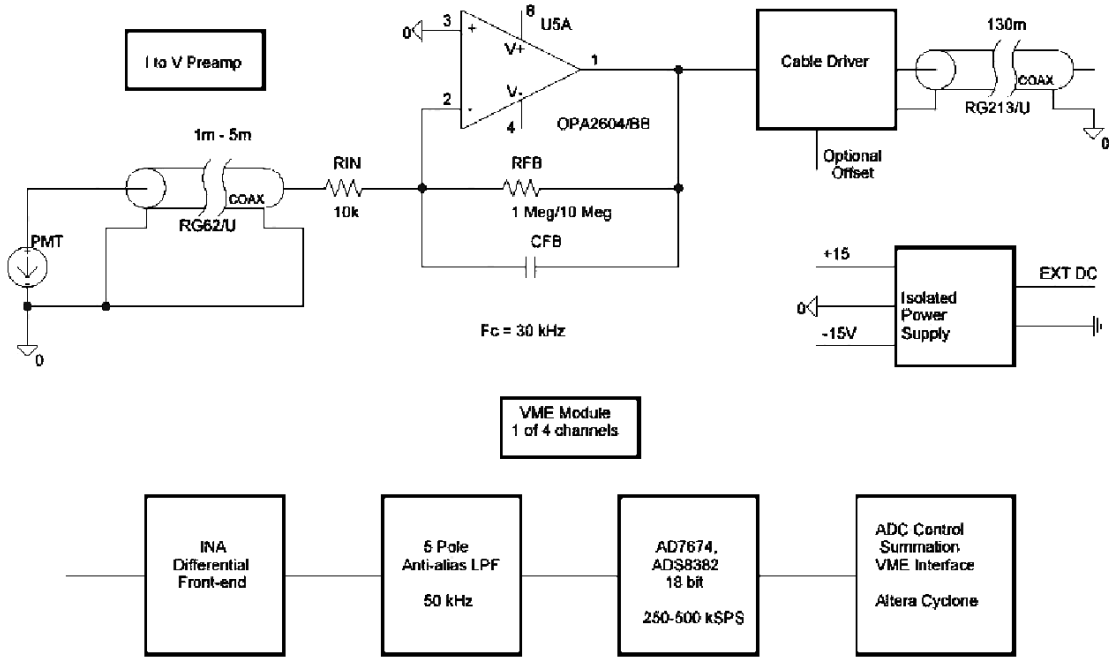

Figure 4.38: The top figure is a schematic showing how a current signal at the PMT anode (left) becomes a voltage signal at the ADC inputs in the counting house (right). The bottom figure is a block diagram of one of the VME sampling ADC modules.

ksps. Integration time is software selectable – set as a fixed number of samples (e.g. 2000 samples = 4 ms at 500 ksps). The integration can be started at a selected time (gate-to-trigger delay) after the leading edge of the gate, then runs for the pre-set number of samples. The overall sum of the integration is available to the DAQ software on the VME bus as a 32-bit data word. It can also be divided into 4 sub-blocks (time intervals) as selected through the VME. The sum fills up in 1/30 s at 500 ksps with no dead time between the intervals. The outputs are buffered inside the VME module (individual block sums and the total sum are stored for each of the 8 channels) so that the previous helicity integral can be read out while the next one is being integrated. The main registers of the module used for setting operation parameters are listed in Table 4.5.

The principal requirement for the main detector high voltage system is to provide isolated (from other electronics), stable and low noise high voltages so that the PMTs can be operated safely over

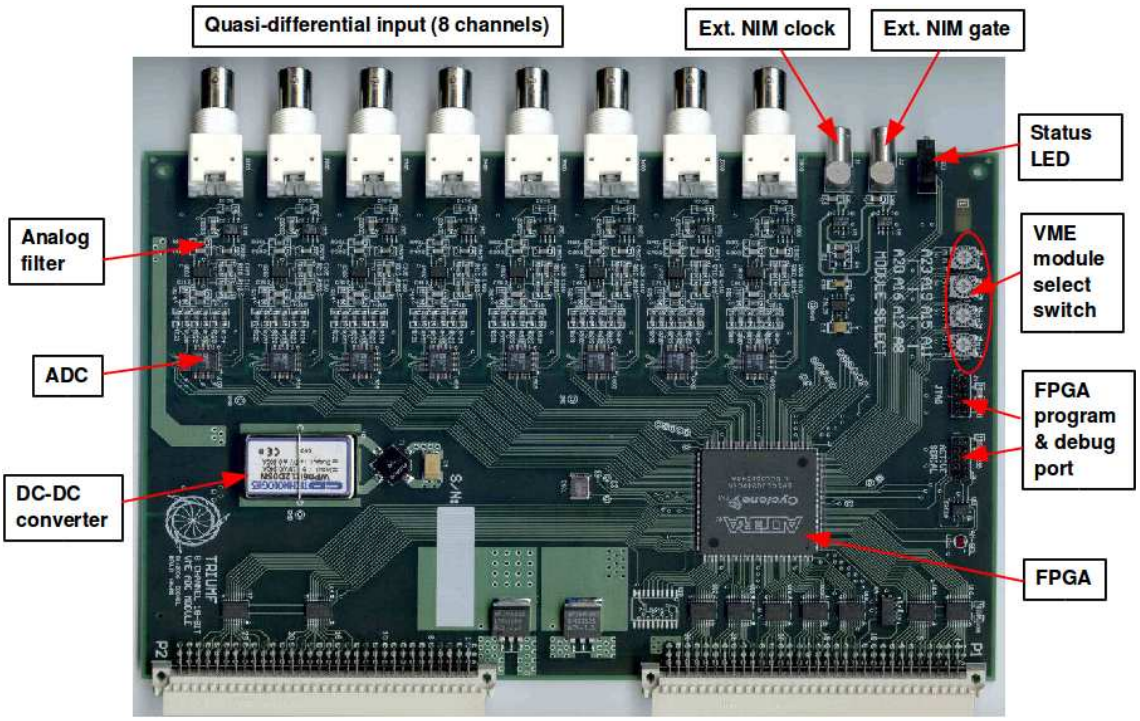

Figure 4.39: Photo of the TRIUMF VME digital integrator (18-bit 500 kHz sampling ADC). The on-board FPGA sums samples during a helicity state, giving an equivalent precision of ~ 25-bits.

VME Register	Value	Operation Parameter
PERIOD_MULT	$[0, 255]$	Sample Frequency = SystemClock/(PERIOD_MULT + 40)
SAMPLE_PER_BLK	$[1, 16383]$	Total Samples = (SAMPLE_PER_BLK) $\times$ (Number of Blocks)
GATE_DELAY	$[0, 255]$	Gate to Trigger Delay = 2.5 μs + (Sample Period $\times$ GATE_DELAY)
INT_GATE_FREQ	$[1, 65535]$	Internal Gate Frequency = (100 kHz)/(INT_GATE_FREQ)

Table 4.5: Main registers of the TRIUMF VME integrator.

the long period of experiment without introducing significant noise (60 Hz pickup), or systematic effects in the form of helicity correlated HV changes. The maximum current for both current mode and event mode PMT bases is 3 mA, which is consistent with the CAEN[18] high voltage power supplies. The CAEN A1733N cards are used for the main detectors.

The CAEN A1733N cards can provide negative 3 kV up to 3 mA per output channel, and are

[18]CAEN - Costruzioni Apparecchiature Elettroniche Nucleari S.p.A. - is a provider of electronic instrumentation for radiation and low light sensors, located at Viareggio, Italy.

hosted by CAEN SY2527 high voltage mainframe, powered from an isolation transformer. Separate high voltage mainframes are used for event mode PMT bases and current mode PMT bases. There are a total of 55 channels for the main detector system, as listed in Table 4.6. To ensure

Event mode PMTs	16 (1 per PMT, 2 PMTs per detector, 8 detectors)
Background detector	2 (1 per PMT, 2 PMTs)
Event mode spares	8 (1 per octant)
Event mode total	26
Current mode PMTs	16 (1 per PMT, 2 PMTs per detector, 8 detectors)
Background detector	2 (1 per PMT, 2 PMTs)
Current mode spares	8 (1 per octant)
Auxiliary detectors	3 (1 per detector)
Current mode total	29

Table 4.6: High voltage channel arrangement of the main detector system

DC isolation, each PMT base was connected to its pre-amplifier and high voltage supply. Channel to channel interconnection or intermediate grounding was avoided. The CAEN HV system has a potentiometer-adjustable high voltage limit, which will trip in the event of overcurrent, and will alarm in the event of under-voltage or over-voltage. The HV control/status software for the HV system allows one to quickly download current mode or pulsed mode HV settings along with some administrative protection, and to read back both the HV and the current drawn by the PMT bases.

An AC power line phase monitor was built for giving a phase reference to the DAQ system, to test for 60 Hz AC power line pickup. It takes AC power line signals (110 V) and reduces the amplitude to about 5 V by using an isolated transformer so that the TRIUMF digital integrator can be used to digitize this signal. The phase monitor consists of two isolated outputs, which have opposite phases with respect to each other, feeding into the TRIUMF digital integrator (10 K input impedance) through two BNC connectors. The output signal amplitudes (Vpp) of the phase monitor can be adjusted through a panel mount potentiometer. The signal quality is determined by the quality of the transformer. Normally, a small commercial transformer has considerable waveform distortion. In order to reduce clipping, ring effects and distortion of the output waveform, a resister

is used to limit the primary current of the transformer to reduce saturation and damp the ring current off.

4.5.2 Data Acquisition

The experiment requires two distinct modes of data acquisition: current mode measurement of the main detector signals, and low current tracking mode measurements, in which individual particles will trigger the DAQ (pulse counting). These two DAQ schemes will be implemented as two essentially independent systems with separate hardware in separate crates and with individual DAQ/analysis software, with some sharing of beamline instrumentation electronics. Beam feedback is analyzed in real-time to calculate helicity correlated beam properties such as current, position and energy to provide prompt diagnostic information. The results of these calculations can be used to feedback on the beam and reduce these effects.

The data flow in the DAQ chain is the transformation of the data from the detectors and the detector control into CODA (CEBAF [19] Online Data Acquisition) format for further physics analysis. CODA is a software tool kit of data acquisition system, designed and commonly used at Jefferson lab, for the data acquisition management, monitoring and storage of data. The Q-weak CODA system consists of several embedded ROCs ("readout controllers") running the VxWorks real-time kernel and communicating with back-end Linux processes (event builder, event transfer, event recorder). The entire chain is controlled by the run control GUI through the run control server. The data is stored on disk/tape as raw data files, which can be decoded and analyzed by using the Q-weak analysis software.

The Q-weak analysis software includes the CODA event decoder, the track reconstruction engine, and the parity analysis engine. Its framework is designed such that each major hardware component will be represented by a subsystem class. The main detector class is the utmost important subsystem which contain routines to unpack the raw data, perform calibrations and event processing, fill histograms and Ntuples, and communicate processed data to other classes for further

[19] Continuous Electron Beam Accelerator Facility.

processing.

The main mode of the experiment is the parity production (current) mode, which produces high rates in the main detectors, resulting from the high luminosity due to a thick target and large beam currents. The preamplified main detector PMT signals are sampled by the integrating ADCs. These ADC modules integrate the current from each of two photomultiplier tubes on each main detector. The electronics and the parity mode DAQ work at a 960 Hz helicity reversal rate[20]. The integrated signals are readout at the helicity reversal rate, with a data rate of about 4.5 Mb/s (independent of beam current). The main detector current mode data acquisition is designed for experimental asymmetry measurements, so the readout of the TRIUMF ADC modules (described in section 4.5.1) forms the core of the DAQ system.

In addition to digitizing the current from the main detector PMTs and several background detectors, the same type of ADC is used to digitize beam line information which is collected at the same rate as the main detector data. The beam line data includes BCMs, BPMs and luminosity monitors. The ADCs for these signals are located in a separate crate so that any small helicity correlations in beam parameter signals will not affect the main detector ADCs.

The rate and volume of data for main detector current mode acquisition is modest compared to typical DAQ and analysis capabilities. Assuming a 32 bit data word per ADC channel, 16 ADC channels for the main detectors, and a 50% overhead for headers, the main detector event size is about 64 bytes. With a readout rate of 1000 Hz, the main detector data rate is about 64 kilobytes per second. However, the beamline instruments occupy a large number of ADC channels, resulting in a total data rate of about 4.5 MB/s. At this rate, a 2500 hour run would produce a data set of about 40 TB.

The Q-weak apparatus will be partially instrumented with tracking detectors as described in section 3.6.3, in order to study the experimental acceptance and background. Measurements with the tracking system will be done at low beam current, so that individual particles can be tracked through the magnet. For this mode of measurement, the main detector PMT pulse amplitude spectrum and

[20] until now the JLab helicity reversal rate has always been 30 Hz

timing information will be recorded. The tracking data acquisition operates in pulse counting mode, triggering on individual particles. The front-end electronics are all VME [21] modules, using CAEN V792 charge ADC for PMT amplitudes, the JLab F1 TDC for timing signals, and JLab SIS3801 scaler for event counting. The tracking DAQ can be operated as an independent system, with the option of reading beam line information. This DAQ has event read-out rates up to 6 kHz.

All vital parameters in the experiment are monitored in real time and a few percent of the data is analyzed on-line (meaning within minutes of taking the data). A first pass analysis (with a minimum of data quality cuts and linear regression) of the complete data set taken during a shift is processed in about 48 hours, depending on availability of computing resources.

4.6 Bench/Beam Testing and Detector Diagnostics

Since the main detectors are used to measure the parity violating asymmetry with high accuracy, their performance needs to be carefully established. For current mode measurements this primarily means measuring how close the detectors operate to counting statistics, how linear they are, and how insensitive to background they are. For the first two aspects, another important consideration is how stable they are, or can be expected stay, over the lifetime of the experiment. The determination of the main detector counting statistics performance requires measurements of photo-electron yield and electronic noise performance. This quantity (sometimes referred to as detector resolution) is expressed in terms of excess noise above single event counting statistics ($\sigma/\sqrt{N}$) and gives rise to a non-zero width in the signal. Linearity refers to both linearity with respect to yield variations as well linearity with respect to distance between a given PMT and the electron hit location. The former could produce false asymmetries or at least additional contributions to the RMS width in the signal, if it is not controlled. The latter would produce a non-zero Q^2 bias, if it is not controlled, as discussed before. Long term stability of these effects is determined primarily by effects of radiation damage, electronic stability and general aging (specifically of the PMTs). The following describes

[21] VME is a computer bus standard, widely used for the electronics in the field of nuclear and particle physics.

some tests that were done on the bench, before the detectors were installed, and data that was taken after the detectors were installed, and provides the performance condition of the main detectors at the beginning and during the first Q-weak run cycle.

4.6.1 Radiation Hardness

For a 1 GeV electron the total mean stopping power in fused silica (density 2.2 g/cm^3) is about 1.7 MeV/(g/cm^2) (see reference [Nakamura et al., 2010]). The stopping power can also be calculated with the ESTAR program[22]. Assuming an electron rate of 800 MHz distributed uniformly over a 200 cm $\times$ 12 cm area (the approximate size of high rate region of the scattered electron profile on the detector) with an average incident angle of 22° for 2500 hours, the deposited energy on a 1.25 cm thick quartz radiator is:

$$\begin{aligned} &8 \times 10^8 \text{ Hz} \times 1.7 \text{ MeV}/(\text{g/cm}^2) \times 2.2 \text{ g/cm}^3 \times 1.25 \text{ cm}/\cos(22^\circ) \times 2500 \text{ hrs} \times 3600 \text{ sec/hr} \\ &= 3.7 \times 10^{16} \text{ MeV} , \end{aligned} \tag{4.36}$$

so the absorbed dose (deposited energy/mass) is estimated as:

$$3.7 \times 10^{16} \text{ MeV}/(2.2\text{g/cm}^3 \times 200 \text{ cm} \times 12 \text{ cm} \times 1.25 \text{ cm}) = 5.6 \times 10^{12} \text{ MeV/g} , \tag{4.37}$$

i.e., average does[23] is about

$$5.6 \times 10^{12} \text{ MeV/g} \times (100 \text{ Rad}/6.24 \times 10^9 \text{ MeV/g}) = 9.0 \times 10^4 \text{ Rad} \sim 100 \text{ kRad} . \tag{4.38}$$

The highest rate on the radiator is about 1.2 MHz/cm^2, corresponding to an absorbed dose of 400 kRad. Therefore, allowing for non-uniformities and showering, a maximum value of 0.4 MRad is assumed. A pre-radiator placed in front of the quartz bar will increase the dose by a factor of about

[22] http://physics.nist.gov/PhysRefData/Star/Text/ESTAR.html

[23] The unit of absorbed radiation dose is Rad, which is defined as the dose causing 0.01 joule of energy to be absorbed per kilogram of matter. 100 Rad = 6.24×10^9 MeV/g.

7 for 1 GeV electrons and the main detectors should therefore be insensitive up to about 700 kRad radiation damage.

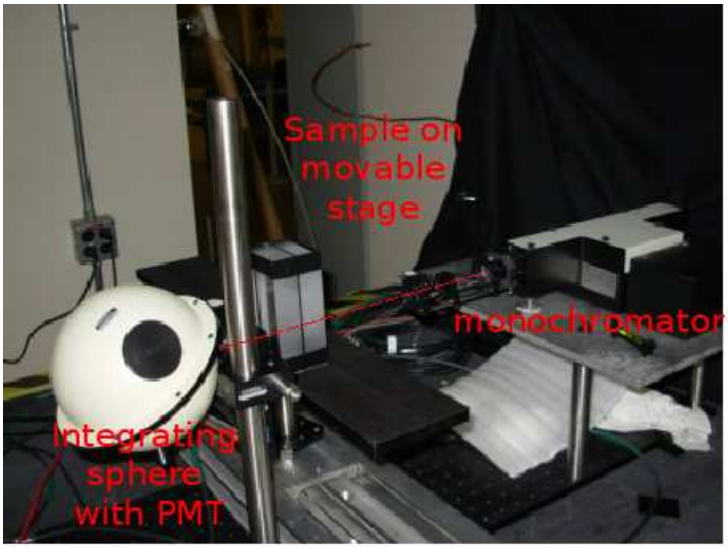

Figure 4.40: Setup for radiation damage measurement.

In order to determine the radiation hardness of the main detectors, several fused silia samples were irradiated with a ^{60}Co to 1.1 MRad, at the Nuclear Services of North Carolina State University, then the light transmission was measured. Fig. 4.40 shows the setup for the light transmission measurement. The setup consists of a monochrometer that shoots a beam of light with specified frequencies through the quartz samples. The traversed light is detected by a PMT in the integrating sphere. By applying Fresnel corrections [Hecht, 2002], an absolute transmission measurement with uncertainties of ± 0.2% was achieved. From the Fig. 4.41, a few percents loss due to radiation damage to a glue joint could be seen, but the fused silica showed no change after 1.1 MRad irradiation[Mack, 2007].

In addition, a prototype of the TRIUMF low noise preamplifier was exposed to 18 kRad (exceeded the 1 kRad specification by more than an order of magnitude) at the Jefferson laboratory ^{137}Cs irradiation facility. During and following the irradiation, no significant performance deterioration and increase in noise were seen [Mack, 2006].

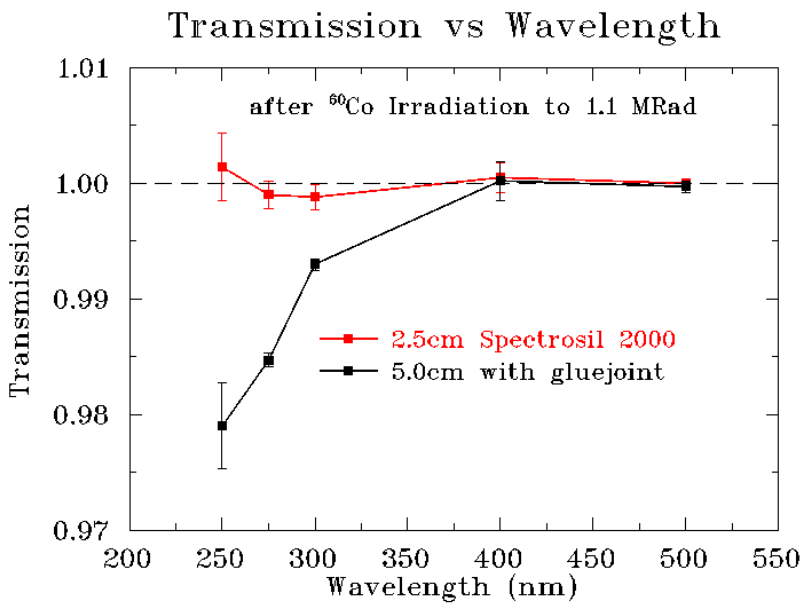

Figure 4.41: Light transmission after irradiation.

4.6.2 PMT-Base Linearity

From section 4.2, the detector system nonlinearity of less than 1% would be acceptable. The electronics including preamplifier and TRIUMF digital integrator are linear to within 1 part in 10^4 [Ramsay, 2006]. The nonlinearity is dominated by the contributions from the PMT and base, since there could be a significant nonlinear response in the PMT-Base combination, such as a gain shift due to the dynode rate effect (the manufacturer catalog value is 0.05 % / μA), and the space charge effects near the anode. Any nonlinear response in the PMT which causes small current changes around some mean DC current could cause a false asymmetry (if it is correlated with the helicity sequence) and increase the asymmetry RMS width.

The PMT-Base linearity was tested on the bench with a sensitive two-LED technique. In this technique, one LED is operated in DC mode to provide a relatively large, adjustable mean cathode current, while the other LED is operated in AC mode as a small, fixed-magnitude signal, as shown

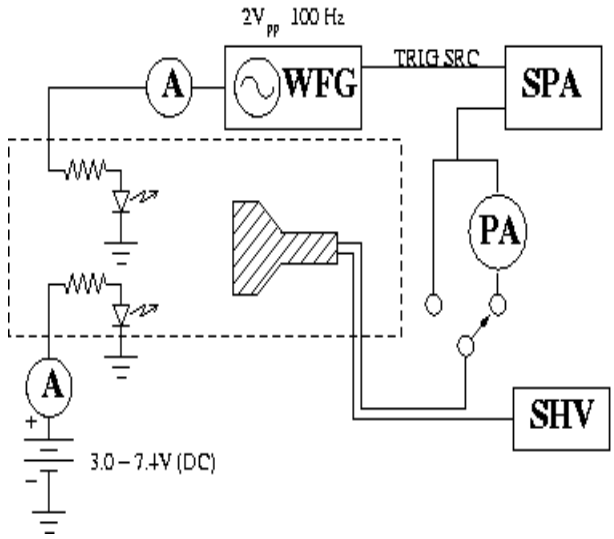

Figure 4.42: The differential non-linearity measurement of the low gain PMT-Base combination using two LEDs: one producing a DC offset and the other producing a small additional AC change. A waveform generator (WFG) produces a sequence of pulses to drive the AC LED, while a spectrum amplifier (SPA) and a picoammeter (PA) measures the PMT anode current.

in Fig. 4.42. The AC component can be measured separately from the DC component by using either a lock-in-amplifier or a spectrum analyzer, which can be phase locked to the AC LED signal (the latter was used for this study). The measured variations in the AC signal amplitude (at the PMT anode), as a function of DC anode current are then used to constrain the non-linearity of the PMT by placing an upper bound on its size (in the absence of an actual observed non-linearity).

Non-linearity equal to any change in the AC $V_{\rm pp}$ amplitude. The AC V_{pp} amplitude around the mean DC offset were repeatedly measured using a spectrum analyzer (SPA). The measurements were repeated for various DC offsets and the results (see Fig. 4.43) showed an upper bound of 0.05% non-linearity at the load of 6 μA with PMT bases providing a gain of 2000 (note that Q-weak is currently running at a PMT base gain of 200). Therefore, the main detector PMT-Base combination is known to be linear to between 10^{-5} to 10^{-4}. The two LEDs technique can be extended to directly applied on the main detectors which are instrumented with two diagnostic LEDs.

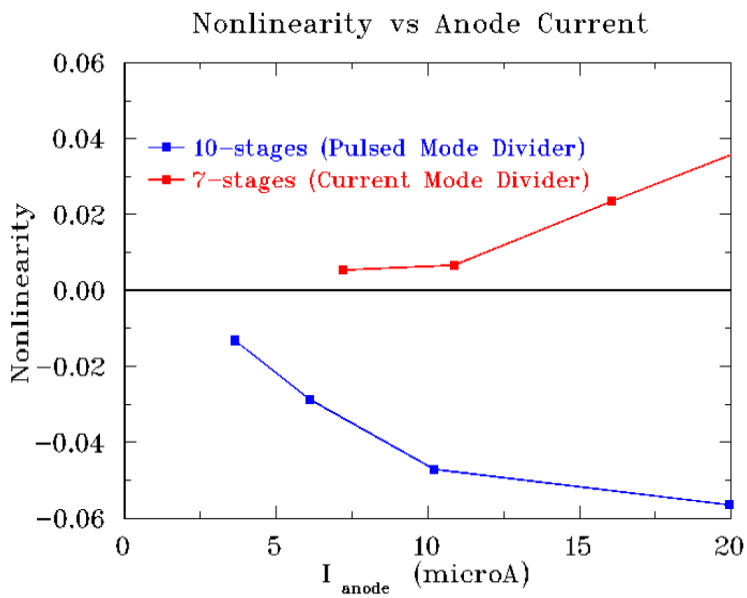

Figure 4.43: PMT-Base linearity (%) versus PMT anode current. During production run, the PMT is operated in the 7-stages current mode at an anode current of about 6 μA.

4.6.3 Detector Performance

The main detector system including detectors, electronics and shielding is expected to have good performance in many aspects. For example, the system is required to be easily switched from one running mode to another for production parity violation asymmetry measurement (current mode) or for background studies and Q^2 measurement (pulse counting mode). This is realized by switching PMT bases with different gain settings: current mode base gain 200, event mode base gain 2×10^6. Apart from these types of operational performance, the other performance of detectors were mostly studied through simulations, bench tests, beam tests and data analysis on production runs. These performances are mainly represented by radiation hardness, light yield, linearity, resolution and efficiency, as discussed below.

The pedestals are the detector yield measured during beam off period at nominal detector operation conditions and settings. The pedestal is determined by the preamplifier offset and background (such as the PMT dark currents) at no-beam condition and its RMS width reflects the electronics

chain noise level. The stability of detector pedestal in current mode (Y_{ped}) directly relates to the detector yield determination and thus affects the detector linearity and asymmetry calculation.

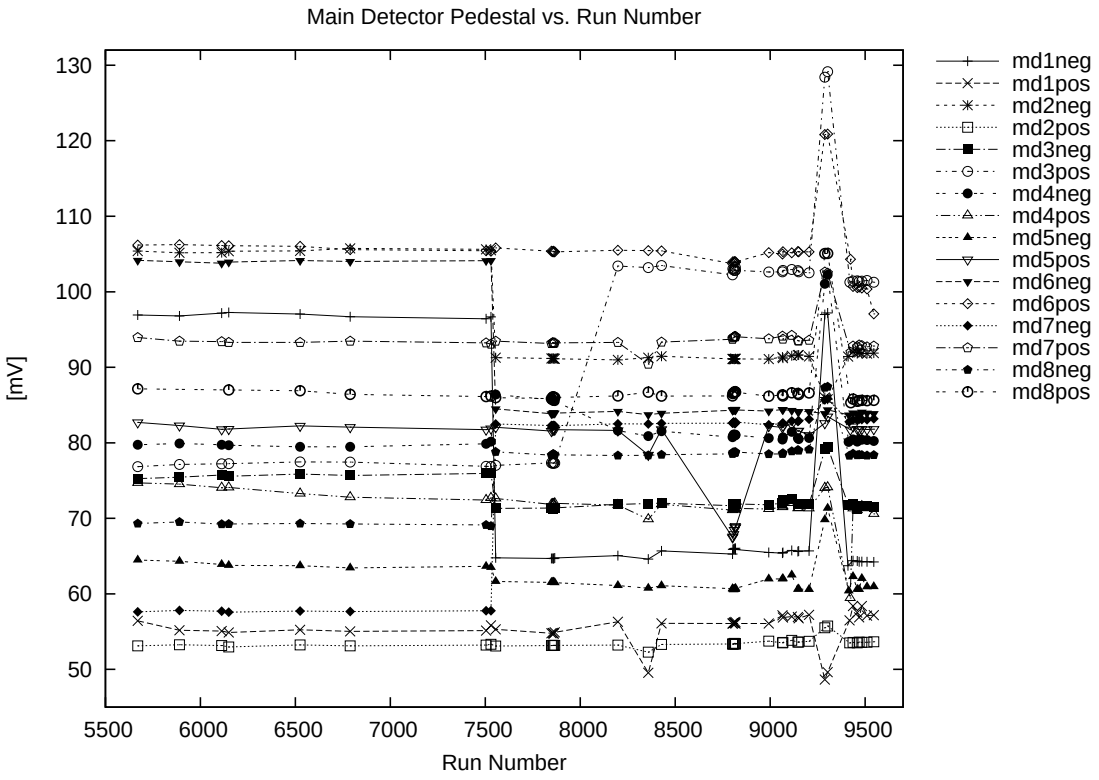

Figure 4.44: Main detector pedestal vs. run number (the lines are just for guiding eyes).

In order to monitor the main detector pedestal stability over time, pedestal versus run number and the pedestal variance for a selected period are plotted in Fig. 4.44 and Fig. 4.45, respectively. The large shifts in pedestals are mainly due to hardware changes such as switching PMT bases and pre-amplifiers. As an example, over this running period, a maximum RMS change of about 24 mV on the 73 mV mean pedestal of detector "md1neg" can be observed. Fig. 4.45 indicates that the pedestals indeed are very stable over a long period of time of running.

The number of photo-electrons detected by the PMT has a dependence on the electron hit position, caused by the Čerenkov light transportation loss in the optical assembly. The Čerenkov light production and transportation were studied using Monte Carlo simulations and tested extensively

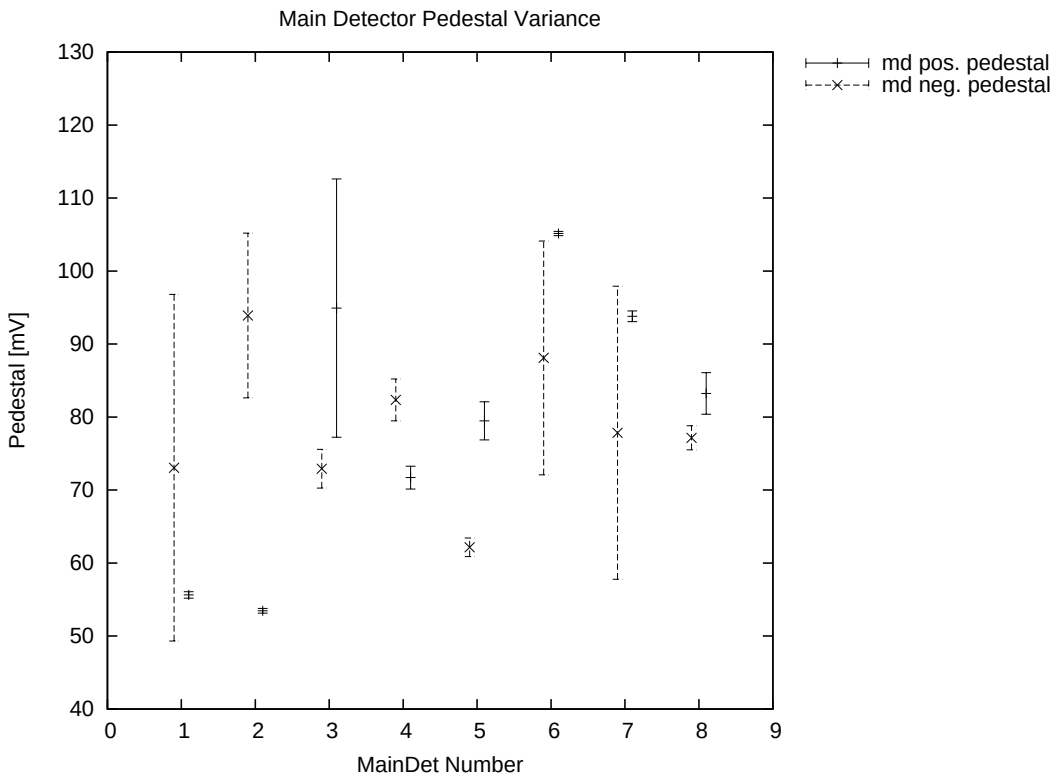

Figure 4.45: Main detector pedestal variance.

with cosmic ray muons. For the cosmic muon test, the setup consisted of a fully assembled main detector sandwiched between two scintillators. The scintillators have small active areas so that the positions and angles of incident cosmic ray can be approximately defined. The coincidence of two scintillator signals form a trigger for the electronics to digitize the pulse generated by the Čerenkov light in the quartz bar. Fig. 4.46 shows an example result of a light yield spectrum (pulse amplitude spectrum), in which the single photo-electron peak can be clearly identified. However, the muon track is only nominally perpendicular to the detector surface, so the finite angle acceptance of the trigger scintillators may significantly broaden the widths (muons traverse the detector at various angles and therefore broaden the photo-electron spectrum).

The position-dependent response of the detector was studied by moving the trigger scintillators to different positions along the quartz bar. The number of photo-electrons from each PMT and the

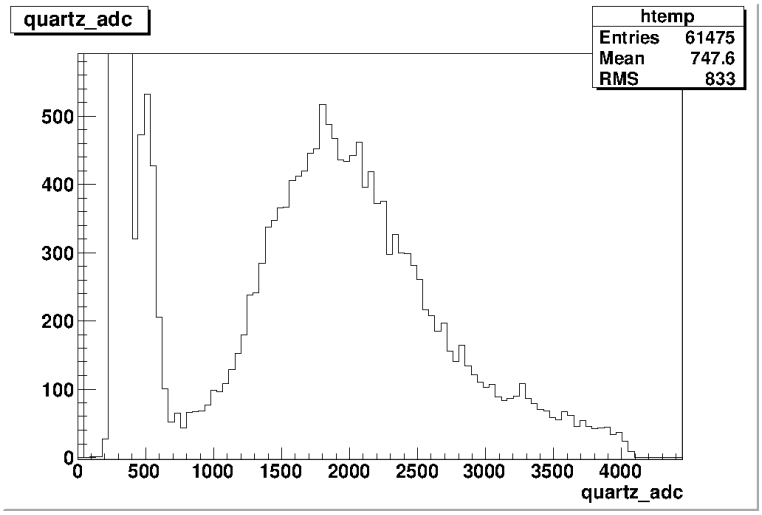

Figure 4.46: Representative pulse height distribution in cosmic ray test.

sum of photo-electrons are plotted with respect to the incident position of cosmic ray. As shown in Fig. 4.47, the mean number of photo-electrons is about 20 and a certain nonlinearity can be seen due to light transportation loss, which agrees with the simulation expectation (see Fig. 4.16 for reference). This nonlinearity suggests that the two PMTs on the same quartz bar should be gain-

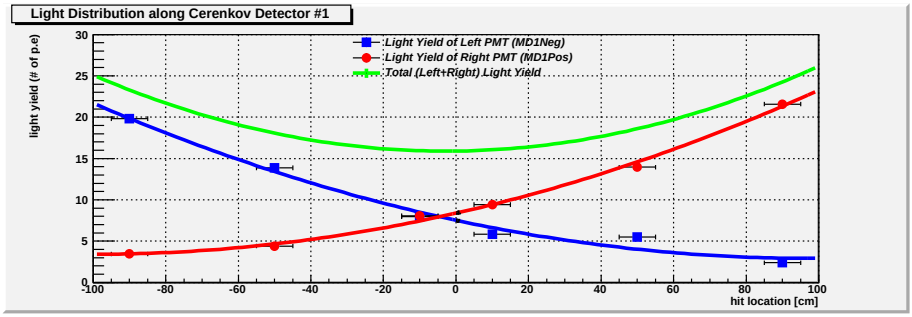

Figure 4.47: Light yield distribution on the Čerenkov detector 1

matched and the PMT yield signals from the two bar ends should be summed so that the total light yield is independent of position to within a few percent. For example, the plots in Fig. 4.48 generated from the event mode run data confirmed this expectation. The summed light yield from two PMTs has a flatter distribution along the quartz bar (see Fig. 4.48 (a)), especially at the middle region.

Since the middle region has much higher rate than the region close to the PMTs (see Fig. 4.48 (b)), the effects of the non-uniformity of light yield are further suppressed.

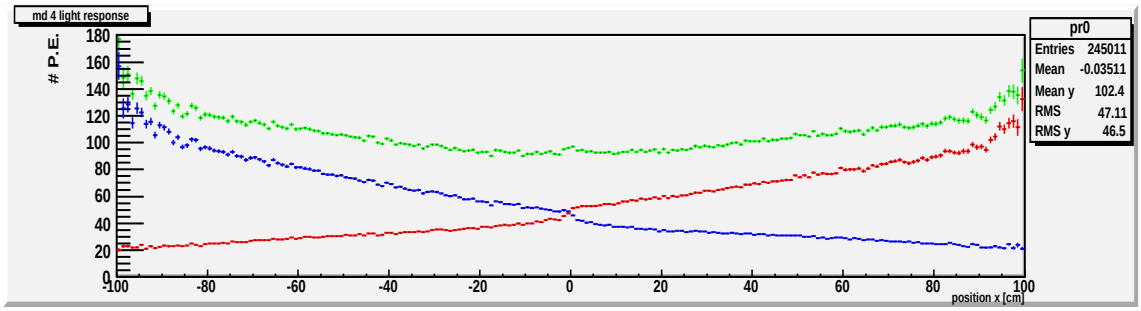

(a) Light yield distribution along the quartz bar: number of photo-electrons in md4m PMT (blue), number of photo-electrons in md4m PMT (red), summed number of photo-electrons (green).

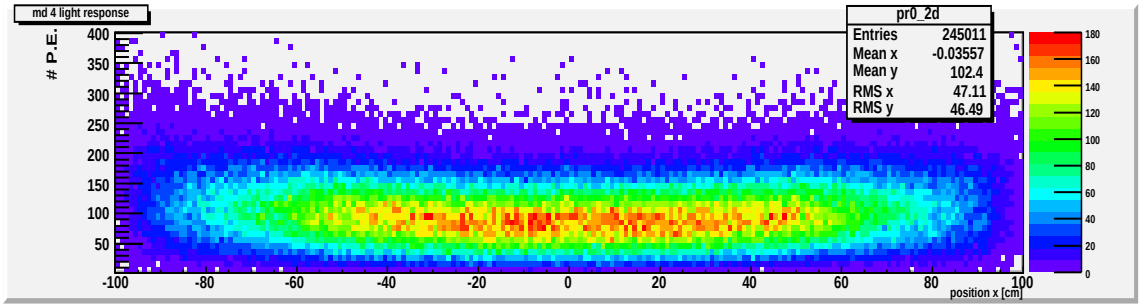

(b) Light yield distribution along the quartz bar with rate indicated by the colored axis.

Figure 4.48: Hit position dependent photo-electron yield on the pre-radiated main detector 4, using data from event mode run 8676. The summed mean light yield is ~ 100 photo-electrons per track (a factor of ~ 6 more light than the bare bar which has no a pre-radiator.)

The light yield non-uniformity discussed above, together with the non-uniform Q^2 distribution on the quartz bar produces a small Q^2 bias. Simulations suggest this effect will shift the $\langle Q^2 \rangle$ by about 1.5% (see section 4.3 for reference). For the as-installed detectors, the reconstructed individual tracks from event mode runs give the distribution of Q^2 on the main detectors. By weighting these Q^2 with the main detector light yield distribution, the light weighted $\langle Q^2 \rangle$ can be acquired (the details of Q-weak track reconstruction and momentum determination are discussed in references [Pan, 2010] [Deconinck, 2009]). Fig. 4.49 shows an example of the accepted Q^2 distribution and main detector light yield weighting using event mode run 8658. The $\langle Q^2 \rangle$ is shifted upward by about 1.6%, which agrees with the simulation expectation.

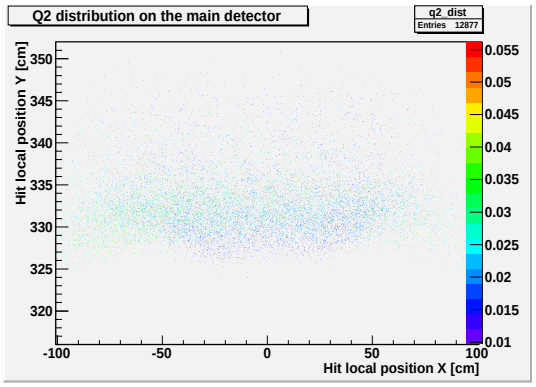

(a) Main detector accepted Q^2 distribution on the quartz bar. The colored axis indicates the Q^2 values in unit of $(\text{GeV/c})^2$.

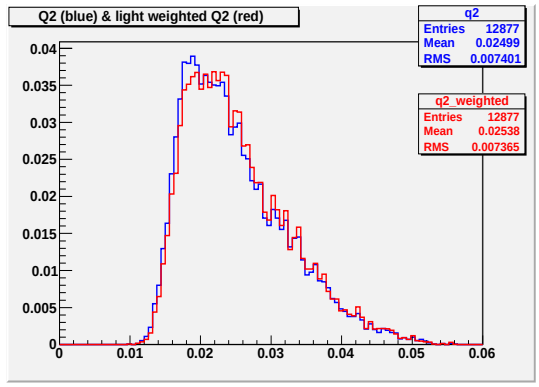

(b) Histogram of accepted Q^2 with (blue line) and without (red line) main detector light yield weighting. Unit: $(\text{GeV/c})^2$

Figure 4.49: Accepted Q^2 distribution and light weighting.

As discussed in section 4.2, the detector resolution essentially determines whether or not the experiment operates close to counting statistics. Eqn. 4.20 gives the best resolution that the main detector can reach. From the data, the detector resolution can be obtained from the full width at half maximum (FWHM = 2.354σ where the factor 2.354 relates the standard deviation of a Gaussian distribution to its FWHM) of the light yield spectrum – the ADC spectrum in event mode (see Fig. 4.51). The detector resolution is then defined as:

$$R = \frac{\sigma}{\text{mean} - \text{pedestal}} \,. \tag{4.39}$$

The resolution R indeed is the major portion which contributes to the factor α in Eqn. 4.14[24], thus it can be used to estimate the excess noise.

Fig. 4.50 shows a simulated total photo-electron yield on the main detector. The position dependent photo-electron yields and the electron showing in the quartz bar add a long tail on the spectrum, resulting in a lower detector resolution. Considering only the shot noise from photo-electron yield

[24]There are also other sources such as target density flutuation that contribute to the excess noise.

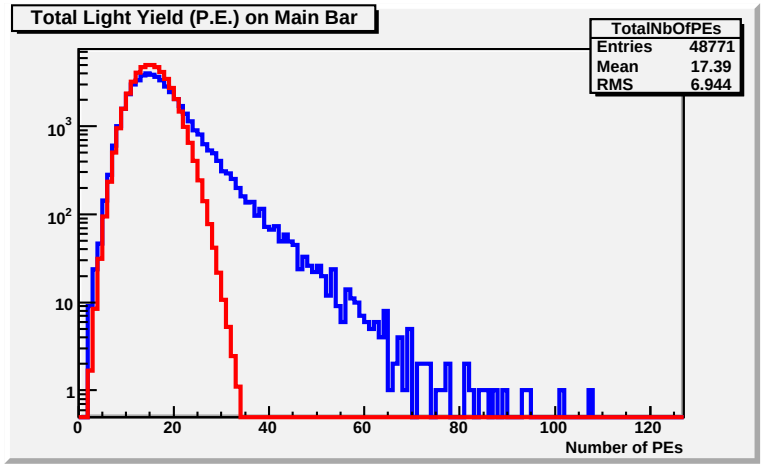

Figure 4.50: Simulated total light yield on the main detector without pre-radiator (blue line). An ideal Poisson distribution (red line) centered at 16 p.e. is showed for comparison.

fluctuations with mean value centered at 16 p.e., for example, the best resolution that the main detector can reach is $1/\sqrt{16} = 0.25$, corresponding to an excess noise factor of $\sqrt{1+0.25^2} = 1.031$. The detector signals have a much broader spectrum, due to other noise contributions, such as the showing in pre-radiator, the target density fluctuations and background. A typical ADC spectrum of a pre-radiated main detector is shown in Fig. 4.50, giving a resolution of 47% and excess noise factor of 1.105 (i.e., 10.5% excess noise).

From Eqn. 4.20, a larger photo-electron number implies a better detector resolution. The shower in the pre-radiator will increase the light yield, but the shower flutuation will also add statistical spread. Therefore, a good pre-radiator design is essential to minimize the excess noise (as discussed in section 4.4.2). Analysis on the Q-weak event mode data gives that the average resolution for detectors with and without pre-radiators are 46% and 47%, respectively. The preradiated detector has a higher resolution than the detector without a pre-radiator, meaning that there is large width contributions from background. This also indicates that the pre-radiator design has been optimized.

If the integrated beam time required to reach the statistical uncertainty goal of the asymmetry measurement due to pure counting statistics is T_{count} and the actual integrated beam time required

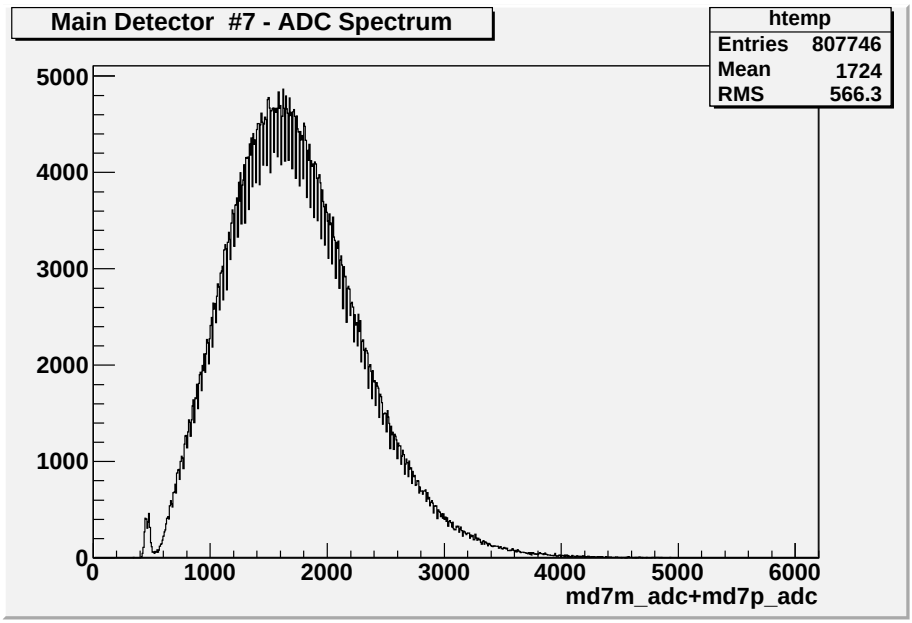

Figure 4.51: An example of a main detector ADC spectrum (Run 8672, Detector 7). The x-axis indicates the ADC channel number, corresponding to the number of photo-electrons. The y-axis indicates the number of counts in each ADC channel. The pedestal of the spectrum represents the offset of electronics chain.

to reach the same goal is T, then we have

$$T_{\text{count}} = \varepsilon \cdot T \ , \tag{4.40}$$

where ε is the efficiency of the detector system. By using Eqn. 4.18, it is easy to find

$$\varepsilon = \frac{T_{\text{count}}}{T} = \frac{1}{1+\alpha^2} \ . \tag{4.41}$$

For 16 p.e. light yield, for instance, the excess noise factor is 1.031 and the highest efficiency the detector can reach is $1/1.031^2 = 94.1\%$. For the as-installed detector with a 47% resolution and an excess noise factor of 1.105, the efficiency is $1/1.105^2 = 81.9\%$ [25].

In order to reach the statistical uncertainty goal within a limited beam time, the detector effi-

[25] This includes all effects from the entire experiment.

ciency must be high, therefore, the excess noise must be small for the Q-weak experiment. Apart from the shot noise discussed above, another excess noise source is the electronic noise which is dominated by the current noise of the preamplifier and the ADC at 0.2 ppm/$\sqrt{\text{Hz}}$. Although an individual read of the 18 bit ADC has a least bit error of 7.6 ppm at 1/2 full scale (dynamic range), this is reduced to a negligible level by rapid sampling. Noise sources in the radiator and PMTs are of equal or greater importance to the electronic noise. The shower fluctuations in the 1.25 cm thick quartz bars contribute about 2.5% excess noise. Other sources of excess noise are mostly electron luminosity-independent (such as cosmic rays striking the PMT glass envelope). Individual PMTs could show excess noise from luminosity-dependent multiplication noise, sparking, or after-pulsing. Multiplication noise can be thought of as the single photo-electron resolution and is a relatively small effect for large photo-electron numbers. Sparking can result from the charging up of insulated structures or (in a current-mode application) failure to hold the electrostatic shield at cathode potential. After-pulsing is due to the ionization of residual gas (or helium contamination), yielding large, late “echos” of the original signal.

The main detector performance, such as the widths via resolution, linearity in helicity-correlated corrections and backgrounds, impacts the uncertainty of the asymmetry measurement in many places. As discussed above, a critical performance criteria for the main detectors is how close they operate to counting statistics, so that the measurement can reach the statistical uncertainty goal within the requested beam time. However, this is really a measure of how well the experiment as a whole is working, since the measured asymmetry width includes the effect of the main detector resolution together with all of the effects of various backgrounds, target noise/boiling, measured beam properties, detector noise, etc. in quadrature. The best way to evaluate this crucial metric is to compare the measured asymmetry width with that expected from a simulation based exclusively on counting statistics for a single helicity quartet. The difference (in quadrature) is a measure of the excess noise in the experiment, the reduction of which was one of the primary commissioning goals.

Taking a specific run, production run 8911 for example. The event rate is 6.12 GHz for the 165

μA beam current during that run. With a helicity reversal rate of 960 Hz, a settling time of 70 μs, and a measured detector resolution (with the pre-radiators) of 46%, which contributes 10.1% excess noise above counting statistics (the combined excess noise of showering, photo-electron statistics, and nonuniform light collection), the expected asymmetry width is

$$\begin{aligned}\sigma &= \frac{1}{\sqrt{N}} \times \sqrt{1+\alpha^2} \qquad (4.42)\\ &= \frac{1}{\sqrt{6.12\times 10^9\ \text{Hz} \times \left(\frac{1}{960\ \text{Hz}} - 70\times 10^{-6}\ \text{s}\right)\times 4}} \times \sqrt{1+(46\%)^2}\\ &= 205\ \text{ppm} \times 110.1\% = 226\ \text{ppm},\end{aligned}$$

i.e., a 226 ppm asymmetry width should be seen. Adding a 70 ppm width contribution due to the target boiling (an upper limit for boiling derived from the data), and using a measured beam current monitor (BCM) resolution of 67 ppm for a pair of BCMs, and adding the contributions in quadrature, the lowest asymmetry RMS width we should be able to see is about:

$$\sigma_{\text{expected}} = \sqrt{\sigma^2_{\text{det}} + \sigma^2_{\text{target}} + \sigma^2_{\text{BCM}}} = \sqrt{226^2 + 70^2 + 67^2}\ \text{ppm} = 246\ \text{ppm}. \qquad (4.43)$$

An asymmetry width of 254 ppm was measured for that run, using the average of two BCMs for normalization. That means for this example the unaccounted for excess noise is

$$\sigma_{\text{unaccounted}} = \sqrt{\sigma^2_{\text{measured}} - \sigma^2_{expected}} = \sqrt{254^2 - 246^2}\ \text{ppm} = 63\ \text{ppm}. \qquad (4.44)$$

From more recent runs, 230-240 ppm widths were observed, with target boiling contribution of about 50 ppm, after some improvements on the BCM resolution and shielding to suppress the background.

As seen in Fig. 4.52, with an asymmetry width of 250 ppm, the 2.1% statistical uncertainty goal for the asymmetry measurement will be met in the remaining beam time, assuming a real-

istic, overall operation efficiency of 50% to account for periodic tracking measurements, Møller measurements, beam studies, equipment and beam down time.

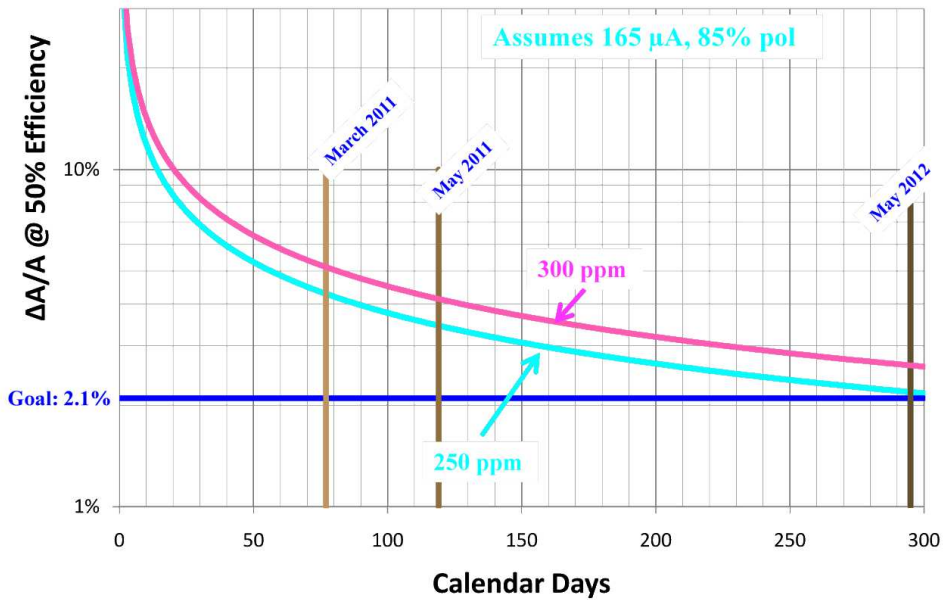

Figure 4.52: A plot of the expected uncertainty as a function of calendar days of beam at an overall operation efficiency of 50% [Smith, 2011].

4.7 Auxiliary and Background Detectors

To monitor background contributions and electronic noise leakage into the various detector parts, a set of auxiliary detectors have been constructed and placed at specific locations around the main detectors. The detectors include one complete assembly (identical to the main detectors) placed close to the beam line, just downstream of the focal plane as a beam line background monitor and three smaller dark boxes with a PMT low gain base assembly in various configurations, which are further described below.

Auxiliary detectors 1 and 2 are identical. They consist of a dark box containing a bare PMT (without quartz or any other active material), shielded with double layers of mu-metal, a current

mode PMT base and a LED light source (see Fig. 4.53). Auxiliary detector 1 was placed in a well shielded fixed location. This particular configuration of LED light, PMT, and low gain base delivers a low noise signal (~ 10 ppb/shift) to provide a noise floor reference for the main detector electronics chain. Auxiliary detector 2 is placed next to the PMT of any chosen main detector. Instead of being at a fixed location like auxiliary detector 1, it is movable, so that it can function as a "PMT background" detector. Auxiliary detector 3 has almost the same structure as detectors 1 and 2, but has a light guide extension (identical to the ones used on the main detectors) glued to it in the same configuration as the PMTs are glued to the light guides in the main detectors. Auxiliary detector 3 is also movable. It is placed next to the PMT of any of the main detector to serve as a "PMT+lightguide background" detector. The LED in auxiliary detectors 2 and 3 are only used for PMT performance checkout.

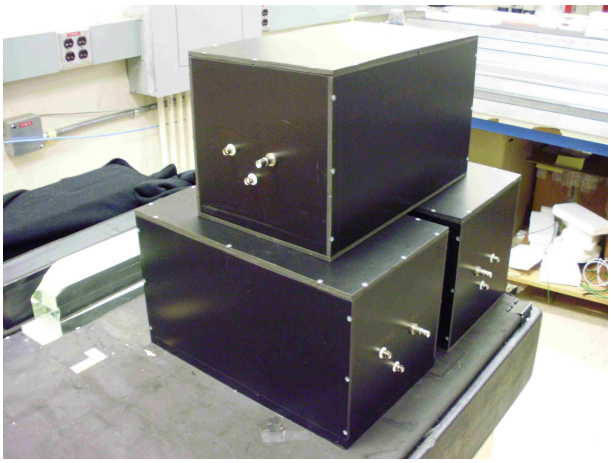

(a) Three completed auxiliary detectors

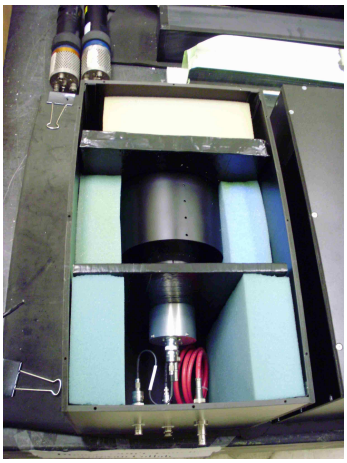

(b) A view of the inner structure of an auxiliary detector

Figure 4.53: Photos of auxiliary detectors

4.8 Summary

The main detector system is a critical subsystem of the Q-weak experiment. It includes 8 Čerenkov detectors working either in current mode for production asymmetry measurement or in pulse count-

ing mode for Q^2 determination and background studies. Each detector is an optical assembly, including two 130 mm PMTs coupled to a fused silica radiator and light guides. The detector are operated in current mode, due to the high event rate of more than 800 MHz per detector. The current signal from the PMTs is amplified and converted to a voltage signal by an I-to-V amplifier and then digitized with an 18 bit integrating ADC. A very challenging requirement for the detector system is to run these detectors in both current mode and pulsed mode. The solution was to use a single PMT with two different voltage dividers, and with separate readout and DAQ chains.

A major criterion was to build a stable, and linear detector system with minimum noise and background sensitivity. The detector radiation hardness is important for long term stability and was tested by exposing fused silica and preamplifier samples to doses higher than those expected in the experiment, without significant damage. Tests showed that the PMT-Base combination has a very good linearity.

The detector system has been installed, tested, and commissioned over a few months of commissioning period in 2010. Basic performance/acceptance criteria have been met and the detectors have shown to be working at the design specifications. For example, the electronics noise was shown to be < 16 ppm at 1 kHz, well below the acceptance criteria (< 50 ppm). With beam, 16 photo-electrons per electron track for non-preradiated detector, were seen on average, which is well above the acceptance criteria of 10 photo-electrons per track. With the 2 cm thick lead pre-radiators in front of the main detectors, the number of photo-electrons per track is about 7 times higher. The detectors have made the transition from commissioning to production running and were operated without major problems during the first run cycle from November 2010 to May 2011.

Chapter 5

Analysis

This chapter introduces the basic analysis schemes and methods for obtaining the physics asymmetry from data. The analysis of a subset of the production data is presented, with a preliminary result for a 6% statistical uncertainty asymmetry measurement.

5.1 Overview

The road from data to the proton's weak charge can be represented by the following simplified expressions:

$$A_{\text{phys}} = A_{\text{raw}} f(P_b, Y_{bkg}, x, x', y, y', E, I, \ldots) \,, \tag{5.1}$$

$$A_{\text{phys}} = kQ^2 Q_W^p + kQ^4 B \,, \tag{5.2}$$

where A_{raw} is the raw asymmetry obtained before any corrections are applied to the data. A_{phys} is the physics asymmetry, which is related to A_{raw} through a complicated function f. In order to extract the physics asymmetry from the raw asymmetry, one needs to determine and remove contributions from helicity correlated beam properties $(x, x', y, y', E, I, \ldots)$ and backgrounds (Y_{bkg}). Since the expected size of the measured asymmetry scales with beam polarization (P_b), precise knowledge of the beam polarization is required. Finally, the extraction of the weak charge of the proton (Q_W^p)

requires knowledge of the average momentum transfer (Q^2) and hadronic corrections (B).

The final extraction of the weak charge requires the combination of polarization measurements, momentum transfer measurements, and asymmetry measurements. Each one of these essentially forms a separate experiment and analysis stream and to prevent a possible human bias from entering into the analysis for each, the asymmetry measurements are blinded.

The data is collected in approximately hour long runs (the DAQ runs continuously, but for data handling and "bookkeeping" the runs are started and stopped manually every hour or so). Each run is subdivided into approximately 10 minute long "runlets", which form the individual binary files for storage, and a first pass analysis is performed automatically, with little or no data quality cuts. Further analysis refinements are made during second and third pass analysis.

First, so called, data quality cuts are applied to the raw detector yield data, to eliminate data taken during a beam trip or excursion where the beam is unstable. These cuts are based either on the beam current monitors, or beam position monitors. Run-averaged values are stored in a MYSQL database, further cuts to the data are made on a run-by-run basis during data quality checks. Helicity correlated false asymmetries are then removed using linear regression techniques.

Background dilutions are measured and the asymmetries from the background are either calculated or measured in order to correct the measured asymmetries. To unblind the asymmetry, one of two schemes might be used. One scheme is that, once the various corrections are finalized, the data are unblinded and the asymmetries are then averaged; another scheme is that the un-blinding will not happen until the final blinded asymmetry is calculated from all measured asymmetries. The analysis process from raw asymmetries to the proton's weak charge is summarized in the following steps:

- Data quality checks are performed on a run-by-run basis.
- The blinding factors and helicity correlated corrections are applied.
- The run averaged yields and asymmetries are then used to correct for background asymmetries and other corrections.

- The asymmetries are corrected for beam polarization and unblinded.
- The measured Q^2 from tracking mode runs are then used to calculate the proton's weak charge.

5.2 Data Quality

Before the data undergoes any detailed analysis, as discussed in the following sections, the basic data quality has to be checked and data cuts need to be applied to remove low quality data. Early cuts included those cuts for removing all data taken during hardware failures or glitch, low beam current conditions, large beam jitter or excursions, and short period of time immediately before and after beam trips, as well as cuts on beam periods with large energy variations. Cuts were applied in such a way as to remove as little physics data as possible, while removing as much substandard quality data as possible and without introducing biases. Further cuts might be applied, such as a helicity gate cut, which removed the data if the helicity gates were lost due to the delay in the event builder and transfer of the DAQ, or a charge asymmetry cut, which removed data with large charge asymmetry. Some data cuts are made manually. For example, the feedback cut, which ensured that only data taken with the proper beam feedback were accepted. Some dedicated runs, such as the beam modulation runs, are omitted from the parity data analysis by not labeling them as production runs.

The detector yields provide a direct way to check the detector performance and data quality during a run[1], by looking at individual PMT yields, and comparing them with estimated values. A rough rate calibration can be done at a beam current of less than 100 nA, where the rate on a single detector is about 4.5 kHz/nA. After a measurement of the absolute beam charge with the injector Faraday cup, one can determine the yield to ± 5%. The drop in yield in going from low to high beam current due to beam heating needs to be checked. Periodic event mode runs between

[1]The yields are preferred to diagnose detector performance rather than asymmetries, although the asymmetries can remove many detector flaws that are not helicity correlated . However, because there is an inherent loss of information when calculating asymmetries, some useful information might be suppressed.

current mode production runs provide ADC spectra which are checked to make sure PMTs are not in danger of saturating. For every production runlet, one can plot the beam normalized yield versus time and watch for large drifts and spikes in the time domain. One can also calculate a DFT (discrete Fourier transform) and look for deviations from $1/f$ noise to diagnose any electronic noise pickup if an increase in the asymmetry RMS widths is observed. Plots of the run averaged values of the yield and asymmetry in each main detector PMT are checked as well. If these quantities were significantly different (varied outside of the error) in a particular octant or run, as compared to the mean from a range of runs, then the data for that octant or run would be eliminated. Detector yield and asymmetry drifts with time are also considered. If a large drift in the yields or asymmetries could not be correlated with large deviations in one of the beam parameters, the data would be eliminated.

At the accelerator source, an insertable half wave plate (IHWP) can be used to reverse the helicity sign and therefore switch the sign of the physics asymmetry, without changing the signal that reports the helicity. This can be used to look for false asymmetries due to the electronics and provides a consistency check, since the corresponding experimental asymmetry is supposed to reverse sign. A general idea of the quality of the data can be obtained by plotting the normalized yields and asymmetries as a function of octant number and run number for a given period of running time in which the IHWP have been placed in both IN and OUT states. The raw asymmetries are expected to be reversed with the IHWP IN and OUT.

Several methods are used to plot the detector data in order to study possible systematic effects. The first one was to look at the way asymmetries are distributed on a run by run basis. Since each run is approximately one hour long, this method looks for systematic effects on 12 to 24 hour timescales (the period for which the HWP was in the same state). Runs are grouped into "slugs" [2], where members of the same slug had the same configuration (such as the insertable half-wave plate setting to change the asymmetry sign setting). Since the source configuration was changed every day, a plot of the asymmetry versus slug covers several day long timescales. The average asymmetries

[2] In Q-weak, a "slug" is a set of data with a common sign for the slow reversals, i.e. given combination of IHWP, and Wein filter configuration.

are obtained from both plots by an uncertainty weighted average over all values. Adding the two resulting asymmetries (from averaging both HWP state sets separately), a zero value should be obtained to within the statistical uncertainty (see Fig. 5.6).

Additional tests for systematic effects are performed on the data, such as comparing the asymmetries obtained from each PMT, each detector and several detector combinations. The results from these tests should be consistent with each other. Only the combination of all main detectors is used to calculate the overall main detector asymmetry.

5.3 Raw Asymmetries

As described in the previous chapter, there are eight main detectors, each of them with two PMTs. The signal from every PMT is integrated over a helicity window time-slot and recorded. The first step towards determining the raw asymmetry is to measure and subtract the pedestals from the raw signals. The pedestals are acquired in separate beam-off pedestal runs.

The charge-normalized yield of each main detector PMT is determined by:

$$Y_{\mathrm{PMT}} = R \times F \times Q \times N \times G_{\mathrm{PMT}} \times G_{\mathrm{Amp}} \,, \tag{5.3}$$

where R is the scattered electron rate of about 800 MHz at 180 μA for in a given octant, F is the factor accounting for the increase in rate due to shower effect in the main detector pre-radiator (F ~6-7), N is the average number of photoelectrons produced by the Čerenkov light ($N \simeq 8$ per PMT without pre-radiator), Q is the electron charge ($Q = 1.6 \times 10^{-19}$ C), G_{PMT} is the gain of the PMT (G_{PMT} ~200), and G_{Amp} is the trans-impedance (transfer gain) of the low noise pre-amplifier ($G_{\mathrm{Amp}} = 1$ MΩ).

The raw data acquired by the DAQ system provide the yield for each main detector PMT in each helicity window, as well as beam parameters and information of helicity states. Once the pedestals are removed, PMT yields are normalized to the beam charge (current integrated over one helicity window) and stored as charge-normalized yields. Because the yield is proportional to the beam

charge, the yields are normalized to charge to remove the dependence of the asymmetry on helicity correlated charge fluctuations and noise present in the beam. The raw asymmetry obtained from a PMT per helicity pattern (a "quartet" pattern of pseudo random helicity states "$+--+$" or "$-++-$") is calculated from the normalized PMT yield

$$A^{\text{raw}}_{\text{PMT}} = \frac{(Y^{1+}_{\text{PMT}} + Y^{2+}_{\text{PMT}}) - (Y^{1-}_{\text{PMT}} + Y^{2-}_{\text{PMT}})}{(Y^{1+}_{\text{PMT}} + Y^{2+}_{\text{PMT}}) + (Y^{1-}_{\text{PMT}} + Y^{2-}_{\text{PMT}})} , \tag{5.4}$$

where the superscripts 1 and 2 indicate respectively the yields for the first and second "+" or "−" helicity states and the yields in the negative helicity states are subtracted from those in the positive states in the numerator. The raw asymmetry obtained from a single helicity pattern is referred to as "pattern asymmetry".

When calculating the asymmetry for a particular detector, the two PMTs gains need to be matched (because of yield non-uniformity across the bar and Q^2 biasing, as discussed in the previous chapter) so that a detector yield can be formed by combining and averaging the two PMT yields:

$$Y_{\text{det}} = \frac{g_{\text{neg}} Y_{\text{neg}} + g_{\text{pos}} Y_{\text{pos}}}{2(g_{\text{neg}} + g_{\text{pos}})} . \tag{5.5}$$

The factors g_{neg} and g_{pos} are the software gain matching factors for the negative side and positive side PMTs on that detector, respectively, to compensate unmatched PMT yields. The individual PMT yield can also be weighted by $1/\sigma^2_{Y_{\text{PMT}}}$ ($\sigma_{Y_{\text{PMT}}}$ is the statistical width of the PMT yield) while calculating the average. However, this is not suitable for Q-weak since that would increase the sensitivity to beam noise. In fact, the symmetric design of the experiment means that all PMTs have nearly identical yields. As a result, the statistical variations among different PMTs are small. Using the detector yield Y_{det}, the detector raw asymmetry can be calculated as

$$A^{\text{raw}}_{\text{det}} = \frac{(Y^{1+}_{\text{det}} + Y^{2+}_{\text{det}}) - (Y^{1-}_{\text{det}} + Y^{2-}_{\text{det}})}{(Y^{1+}_{\text{det}} + Y^{2+}_{\text{det}}) + (Y^{1-}_{\text{det}} + Y^{2-}_{\text{det}})} . \tag{5.6}$$

The raw asymmetry for a combination of several (N) detectors or the raw asymmetry for a combi-

nation of all detectors can be obtained in a similar way, i.e.,

$$A^{\text{raw}}_{\text{comb}} = \frac{(Y^{1+}_{\text{comb}} + Y^{2+}_{\text{comb}}) - (Y^{1-}_{\text{comb}} + Y^{2-}_{\text{comb}})}{(Y^{1+}_{\text{comb}} + Y^{2+}_{\text{comb}}) + (Y^{1-}_{\text{comb}} + Y^{2-}_{\text{comb}})} \tag{5.7}$$

with

$$Y_{\text{comb}} = \frac{\sum_i^N \left(g^i_{\text{neg}} Y^i_{\text{neg}} + g^i_{\text{pos}} Y^i_{\text{pos}}\right)}{2N \sum_i^N \left(g^i_{\text{neg}} + g^i_{\text{pos}}\right)} . \tag{5.8}$$

Another way to obtain the combined asymmetries is that the detector asymmetries are all separately calculated and then combined via uncertainty (statistical width) weighted averages, as:

$$A^{\text{raw}}_{\text{comb}} = \sum_i^N \frac{A^{\text{raw}}_{\text{det},i} \sigma^{-2}_{A^{\text{raw}}_{\text{det}},i}}{\sigma^{-2}_{A^{\text{raw}}_{\text{det}},i}}. \tag{5.9}$$

However, the statistical width $\sigma^{-2}_{A^{\text{raw}}_{\text{det}}}$ can only be obtained after the first round of data analysis (or use the values from previous runs by assuming there are no changes in the statistical widths of detector raw asymmetries).

The mean raw asymmetry and RMS width for each run (or runlet) can be determined either by fitting a histogram filled with the raw pattern asymmetries of a combination of all PMTs to Gaussian distribution, or by direct calculation as:

$$\langle A^{\text{raw}}_{\text{comb}} \rangle = \frac{1}{N} \sum_{\text{pattern}}^N A^{\text{raw}}_{\text{comb,pattern}} , \tag{5.10}$$

$$\sigma_{A^{\text{raw}}_{\text{comb}}} = \sqrt{\frac{1}{N} \sum_{\text{pattern}}^N \left(A^{\text{raw}}_{\text{comb,pattern}} - \langle A^{\text{raw}}_{\text{comb}} \rangle\right)^2}. \tag{5.11}$$

In the following discussion, $A^{\text{raw}}_{\text{comb}}$ will be used to represent the mean raw asymmetry. Typical measured main detector asymmetries are shown in Fig. 5.1, The figure legends show the asymmetry width in the array of 8 detectors around the beam axis, with the central histogram showing the combination of all eight detectors. These results were obtained at a beam current of 150 μA.

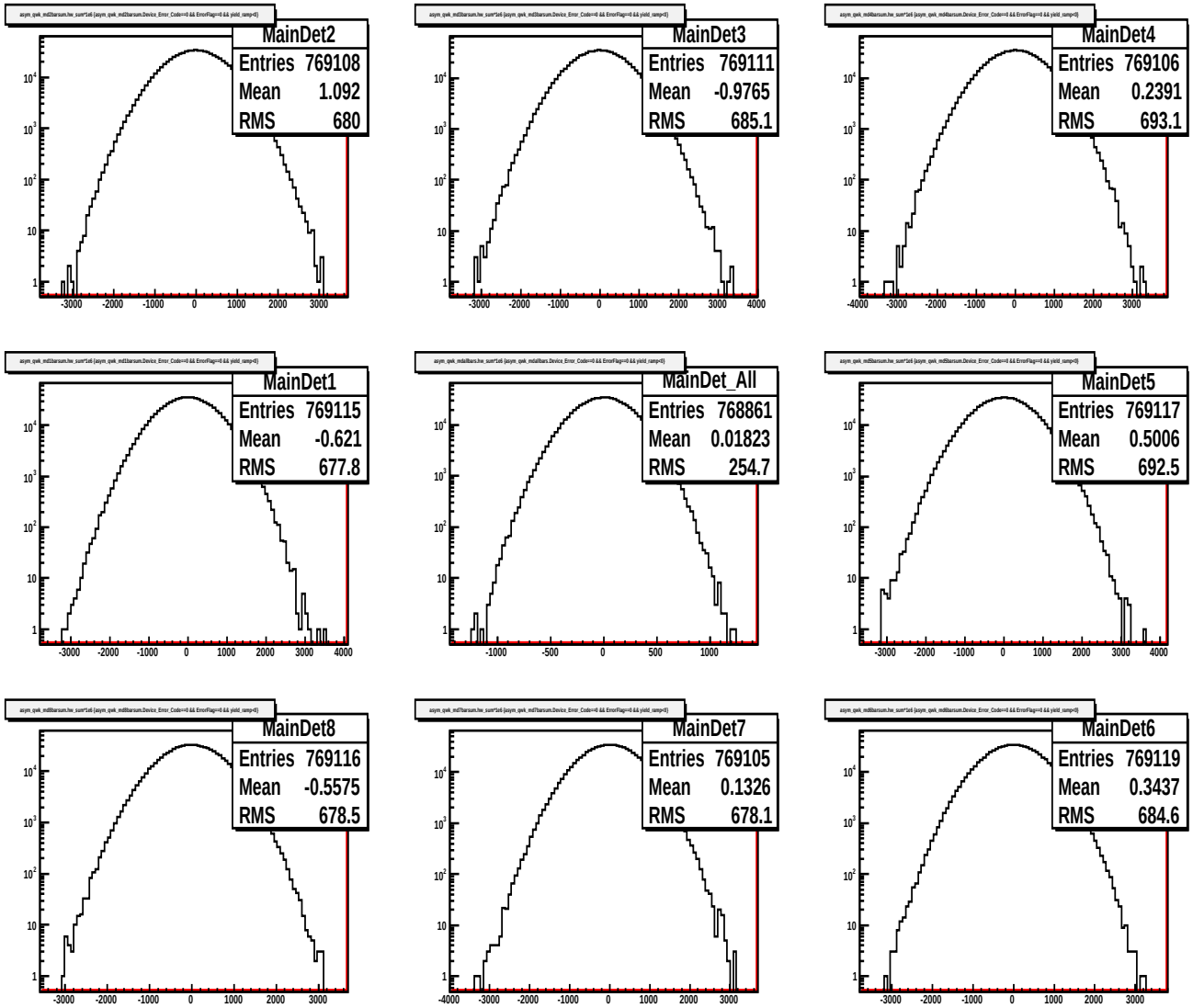

Figure 5.1: Array of measured asymmetries from the main detectors arranged as seen by the beam. In each plot, the x-axis indicates the asymmetry (unit: ppb), the y-axis indicates the number of counts, in log-scale.

5.4 Blind Analysis

To prevent human bias entering during the extraction of the weak charge result from asymmetry, the data is "blinded", following an algorithm in which the raw asymmetries are shifted by a fixed amount and then multiplied by a factor of 1 or -1 (determined by the status of the insertable half wave plate):

$$A_i^{\text{blinded raw}} = \pm(A_i^{\text{raw}} + A') \,, \tag{5.12}$$

where A' is the shift introduced in the blind analysis. The theoretical prediction for the asymmetry is ~ -300 ppb, so A' was chosen to fall in the interval between -60 to $+60$ ppb (20% of the asymmetry, which is much larger than the anticipated experimental uncertainty). All cuts and systematic studies are performed on the "blinded" data. Once the analysis has completed, the data will be "unblinded", revealing the real asymmetry. It should be pointed out that the data from the other detectors is not blinded, only the main detector parity data is blinded.

5.5 Corrections for Helicity-Correlated Beam Properties

The goal of constraining systematic uncertainties from each source for the Q-weak experiment is that the systematic uncertainties are not more than the statistical uncertainty for the measurement of the parity asymmetry, i.e., no more than 6×10^{-9}, and that corrections are known to 10% (see Table 3.1 – the anticipated experimental uncertainties, for reference).

The measured asymmetry can have a component from false asymmetries due to helicity correlated beam properties. The raw asymmetry (A^{raw}) has to be corrected for the residual false asymmetry in the beam which affects both the central value of the raw asymmetry and its width. The electron beam can be described by six parameters: charge (intensity), energy, x and y angle (x', y'), and x and y position. The helicity correlations (i.e., the asymmetries) of these parameters are measured by using beam position monitors (BPMs). The correlation between beam and raw detector asymmetries is linear to first order. Consequently, it is possible to remove the helicity correlated beam

contributions by applying a least squares linear regression to the raw asymmetry results. There are basically two methods to do linear regression: linear regression on the asymmetries (every multiplet of MPS periods is regressed on) and linear regression on the yields (every MPS period is regressed on). The linear regression on the asymmetries is done by plotting the asymmetry correlations, i.e., the asymmetries of all PMTs (or detectors and detector combinations) versus the asymmetries of six beam parameters. By applying a linear fit to the data, the regression slopes S_{ij} are obtained for every PMT/detector i, and beam parameter P_j. The regressed asymmetry A_i^{reg} is then given by

$$A_i^{\mathrm{reg}} = A_i^{\mathrm{raw}} - \sum_j^6 S_{ij} A_j^{\mathrm{beam}} \,, \tag{5.13}$$

where A_j^{beam} is the asymmetry for beam parameter P_j and the regression slopes (also called the correlation matrix elements) $S_{ij} = \frac{\partial A_i^{\mathrm{raw}}}{\partial A_j^{\mathrm{beam}}}$. Eqn. 5.13 can also be expressed in terms of the charge-normalized detector yield Y^{det} as

$$A_i^{\mathrm{reg}} = A_i^{\mathrm{raw}} - \sum_{j=1}^6 \frac{1}{2Y_i^{\mathrm{det}}} \frac{\partial Y_i^{\mathrm{det}}}{\partial P_j} \Delta P_j \,, \tag{5.14}$$

where $\Delta P_j = P_j^+ - P_j^-$ is the beam parameter difference between the two helicity states. Eqn. 5.14 is the expression of linear regression on the yields. The measured beam parameters can be used to extract slopes, $\frac{1}{Y}\frac{\partial Y}{\partial P_i}$. Since the regression slopes varied over time, they are calculated on a run-by-run basis, which is enough to minimize the statistical uncertainties of the fit.

The linear regression on the asymmetries is a well defined method since the asymmetries have no inherent lower limit and are therefore symmetric and Gaussian. However, this method might hide the effects of beam parameter correlations. The linear regression on the yields is a more natural method, but this method might encounter issues in case that the yield values are small.

The regression slopes can be extracted using the natural beam motion (jitter). It also possible to use the method of beam modulation — a dithering method to study the slopes by deliberately causing large position, angle or energy differences in the beam. The beam modulation can be

performed periodically by using a set of corrector magnets between the entrance to the hall and the target to move the beam in x and y, in order to measure the sensitivity of the detectors to beam motion. The charge asymmetry and energy differences can also be studied by deliberately inducing large effects at the source. However, the effects of beam parameter correlations might be large when the beam is dithered.

The asymmetry per run (A_{run}) and its statistical width (σ_{run}) are given by a Gaussian fit to the regressed asymmetry distribution of the combination of all main detectors ($A^{\text{reg}}_{\text{comb}}$). The statistical uncertainty per run (δA_{run}) is then obtained from σ_{run} and the number of helicity patterns ($N^{\text{pat.}}_{\text{run}}$) in that run:

$$\delta A_{\text{run}}(\text{stat.}) = \frac{\sigma_{\text{run}}}{\sqrt{N^{\text{pat.}}_{\text{run}}}} \,. \tag{5.15}$$

Fig. 5.2 gives an example from a specific run, showing distributions of these corrections. Fig. 5.3 – 5.5 give some example results for the sensitivities and corrections versus runs, where Fig. 5.3 shows the sensitivities to x, y, x', y', energy and charge asymmetry in runs 10810 – 10915, and Fig. 5.4 shows corrections to the combination of all detectors asymmetry due to variations in x, y, x', y', energy, and charge asymmetry. The sum of all of these contributions is shown in Fig. 5.5. The energy change is measured with the BPMs at at a location where the energy dispersion is high. A sensitivity of 500 ppm/mm corresponds to roughly −2 ppm/ppm in energy. Do the variation of the cross-section with energy would produce a sensitivity of −2 ppm/ppm. Simulations show that movement of the scattered electron profile across the width of the detectors with energy would change that to −1.5 ppm/ppm. Charge asymmetries are measured using BCMs. The main detector sensitivity to a charge symmetry is ∼1.7%, in agreement with measurements made at where deliberate large charge asymmetries were introduced. Starting at around run 10830 charge sensitivities were seen to be small and negative, due to a change of calibration and a pedestal change for the BCMs.

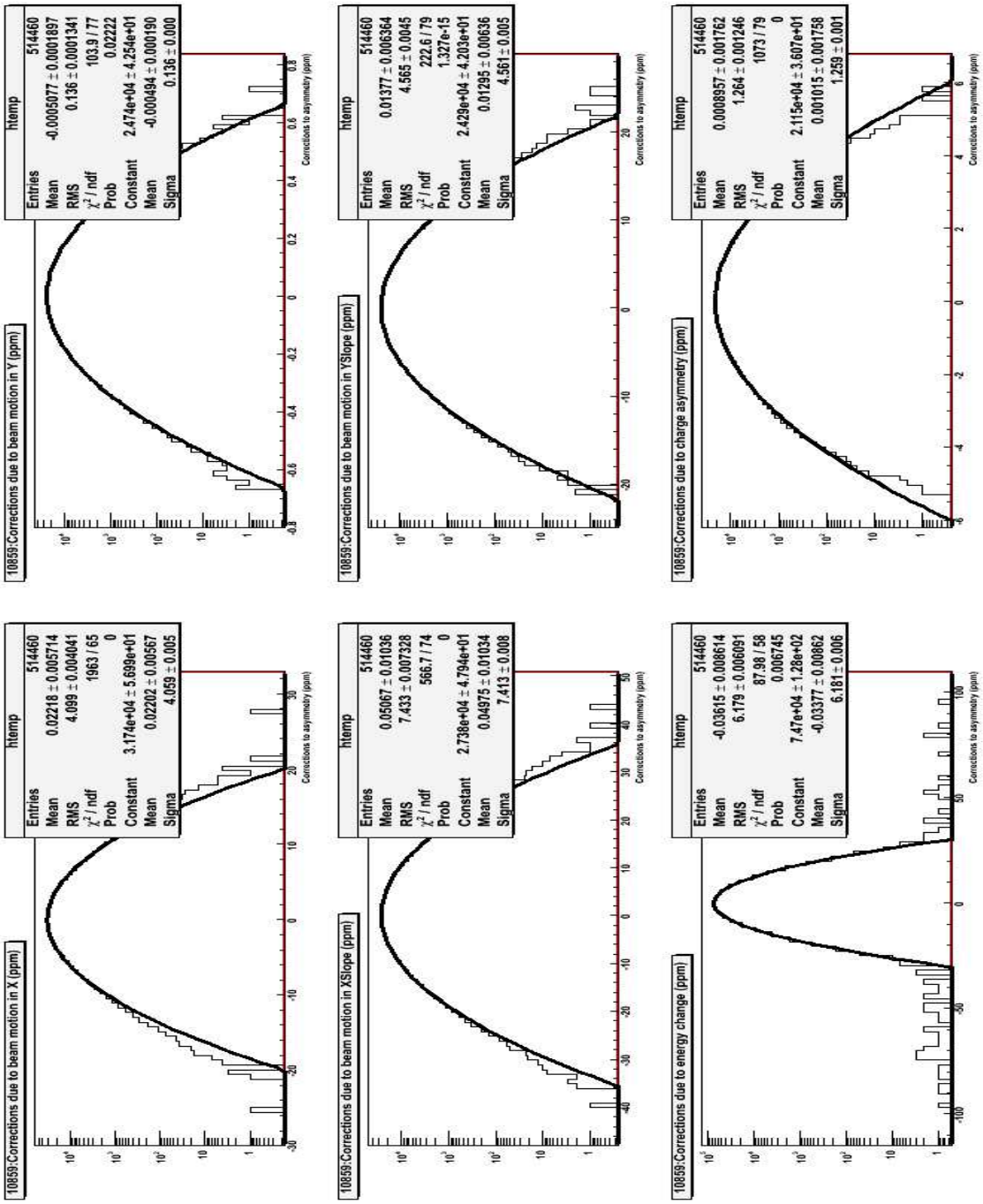

Figure 5.2: Distributions of helicity-correlated beam property corrections.

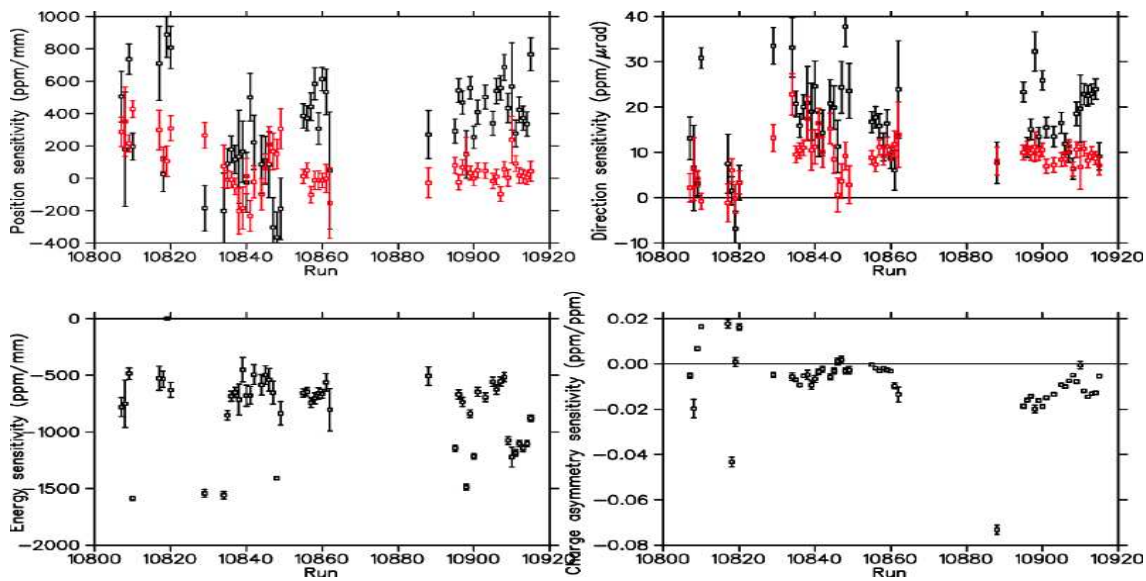

Figure 5.3: Sensitivities to x, y, x', y', energy and charge asymmetry. x and x' sensitivities are shown in black, y and y' in red.

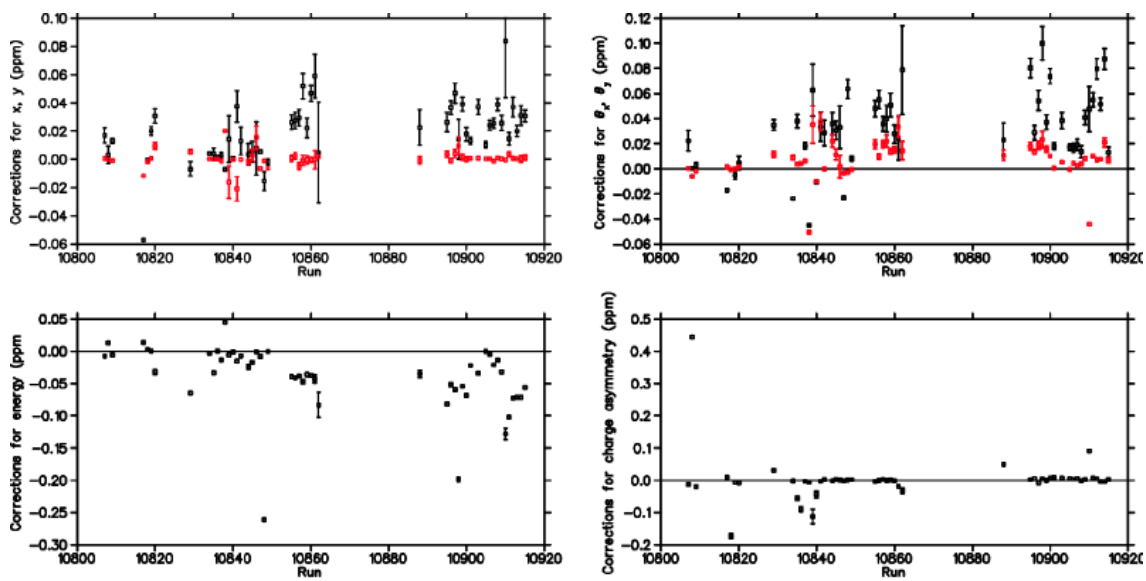

Figure 5.4: Helicity-correlated beam property corrections to the combined detector asymmetry, for all detectors. The corrections are applied using the extracted sensitivities, multiplied by observed variations of beam properties after helicity reversals. Corrections are of the order of tens of ppb.

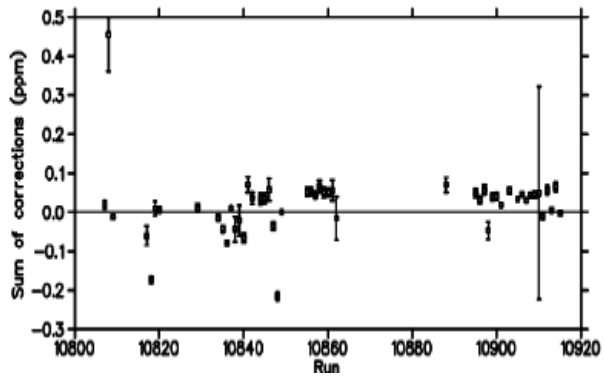

Figure 5.5: Helicity-correlated beam property corrections to the combination of all main detectors asymmetry. The corrections are from the extracted sensitivities multiplied by observed changes of beam properties on helicity reversal. Corrections are of the order of tens of ppb.

5.6 Background Corrections

The experimental asymmetry obtained after regression still includes the contributions from various backgrounds. Neglecting radiative corrections, the experimental asymmetry (A^{exp}) is given by the detector yield difference over detector yield sum as:

$$A^{\text{exp}} = P_b \frac{A_{\text{ep}} Y_{\text{ep}} + \sum_j A_j Y_j}{Y_{\text{ep}} + \sum_j Y_j} , \tag{5.16}$$

where P_b is the beam polarization during production running, determined by the Møller and Compton measurements [3], A_{ep} denotes the elastic e-p scattering asymmetry that is to be extracted, Y_{ep} is the beam-current-weighted detector yield due to the elastic e-p scattering, A_j denotes a particular type of background asymmetry, and Y_j is the beam-current-weighted detector yield due to a

[3]The well developed analysis schemes and methods for obtaining the beam polarization and the associated systematic effects, such as the transverse polarization contributions to the asymmetry measurement, are treated elsewhere, including other thesis and papers. See, for example, references [Gaskell et al., 2007] [Armstrong et al., 2007] [Birchall, 1988] [Maas et al., 2005b] [Kaufman, 2007].

particular type of background. This expression can be rewritten as:

$$A_{\mathrm{ep}} = \frac{1}{P_b}\left(A^{\mathrm{exp}} + \sum_j A^{\mathrm{exp}}\frac{Y_j}{Y_{\mathrm{ep}}} - P_b\sum_j A_j\frac{Y_j}{Y_{\mathrm{ep}}}\right) . \tag{5.17}$$

Then, if one defines $f_j = Y_j/Y_{\mathrm{ep}}$ as the beam-current-weighted fractional yield and takes $A_j^{\mathrm{exp}} = P_b A_j$ as the experimental asymmetry due to a particular background j, the elastic physics asymmetry A_{ep} can be written as

$$A_{\mathrm{ep}} = \frac{1}{P_b}\left[A^{\mathrm{exp}} + \sum_j \left(A^{\mathrm{exp}} - A_j^{\mathrm{exp}}\right) f_j\right] . \tag{5.18}$$

Therefore, in order to determine the physics asymmetry A_{ep} of the elastic e-p scattering, both the beam-current-weighted fractional yield, f_j, and the difference of the experimental asymmetries, $A^{\mathrm{exp}} - A_j^{\mathrm{exp}}$, must be measured or well bounded so that the corrections for each type of background can be made [4].

Because the measurement techniques are very different for different types of background, they are separated into prompt (hard) and non-prompt (soft) background. The hard background mainly involves contributions from the aluminum target windows, including elastic events and quasi-elastic events. These are measured using aluminum dummy targets at different QTOR field settings. Due to the large asymmetry from elastic electron-aluminum scattering, this type of background is significant and must be measured precisely. From simulation, the asymmetry-weighted fractional yields are 11.1% and −3.3% for elastics and quasi-elastics, respectively. Another important source of background comes from the inelastic pion-electroproduction, which contributes about −0.5% to the asymmetry-weighted fractional yield and is measured by lowing the QTOR field. The soft backgrounds mainly involve MeV level photons and e^+e^- events from beamline and collimators, and contribute about 0.4% and 0.1%, respectively. These are measured by plugging the selected collimator openings and shielding the beam pipe. Soft backgrounds also includes neutron events. Since the main detector quartz radiators are not sensitive to neutrals, they make tiny contributions ($\simeq$ 0.4%).

[4] In this discussion, the quoted values of background contributions are from calculation, simulation and past experience. The Q-weak collaboration will release the results when the measurements and detailed analysis are fully completed.

The background detectors in the detector hut is used to measure this type of background. In addition, quartz radioluminescence of the detector might contribute to the soft background. Measurements during beam off intervals (by looking at suspicious decay pattern in the pedestal immediately after beam off) determine that this type of background is negligible.

Unlike the linear regression that is made at the helicity pattern or multiple helicity patterns level to remove contributions from the helicity correlated beam properties, the background corrections should be made at the individual run level. If the beam polarization, detector linearity and background contributions have been stable over the entire run period, the background corrections could be also made at the final stage, when all the production data is acquired and the overall experimental asymmetry is extracted (i.e., at the very end of the experiment and data analysis, when there is enough information and statistical significance).

5.7 Physics Asymmetry

The physics asymmetry at the individual run level is obtained after all the systematic effects have been regressed out. To calculate the parity-violating asymmetry over N runs, the asymmetry per run (A_{run}) will be weighted by the statistical width in the asymmetry distribution for that run:

$$A_{PV} = \frac{\sum_{\text{run}}^{N^{\text{run}}} A_{\text{run}} w_{\text{run}}}{\sum_{\text{run}}^{N^{\text{run}}} w_{\text{run}}} , \tag{5.19}$$

where

$$w_{\text{run}} = \frac{1}{\sigma_{\text{run}}^2} \tag{5.20}$$

is the weight obtained from the statistical width σ_{run} in each run. The overall parity-violating asymmetry is given by the weighted mean of all runs. The overall statistical uncertainty of the weighted mean asymmetry is calculated from the RMS value of the statistical uncertainty of each

run, i.e., RMS(δA_{run}(stat.)), and the number of runs:

$$\delta A_{PV}(\text{stat.}) = \frac{\text{RMS}(\delta A_{\text{run}})}{\sqrt{N^{\text{run}}}} = \frac{1}{\sqrt{N^{\text{run}}}}\sqrt{\frac{1}{N_{\text{run}}}\sum_{\text{run}}^{N^{\text{run}}}(\delta A_{\text{run}})^2} = \frac{1}{N^{\text{run}}}\sqrt{\sum_{\text{run}}^{N^{\text{run}}}(\delta A_{\text{run}})^2}\,. \tag{5.21}$$

For a quick estimation of the overall statistical uncertainty, one could assume that each run has approximately the same number of helicity patterns $\langle N_{\text{run}}^{\text{pat.}}\rangle$ and the σ_{run} for each run is very close to an average value $\langle\sigma_{\text{run}}\rangle$ such that δA_{run} for each run is close to an average value $\langle\delta A_{\text{run}}\rangle$, then the uncertainty on the the total asymmetry δA_{PV}(stat.) can be estimated from Eqn. 5.21 as:

$$\delta A_{PV}(\text{stat.}) = \frac{\langle\delta A_{\text{run}}\rangle}{\sqrt{N^{\text{run}}}} = \frac{1}{\sqrt{N^{\text{run}}}}\frac{\langle\sigma_{\text{run}}\rangle}{\sqrt{\langle N_{\text{run}}^{\text{pat.}}\rangle}} = \frac{\langle\sigma_{\text{run}}\rangle}{\sqrt{N_{\text{total}}^{\text{pat.}}}}\,, \tag{5.22}$$

where $N_{\text{total}}^{\text{pat.}}$ is the total number of helicity patterns accumulated in the experiment. This equation is essentially the same as Eqn. 4.12. For smaller data sets or larger data sets rather than runs, such as runlets (subsets of a run) or a slugs (multiple runs), the above equations also hold.

As discussed in the previous section, variations of beam properties with helicity can lead to false asymmetries, hence the helicity correlations should be kept as low as possible. The corrections are based on measured sensitivities and residual correlations. If the helicity correlations are sufficiently small, the measured parity asymmetry, A_{meas} can be written in terms of the physics asymmetry, A_{PV}, as:

$$A_{\text{meas}} = A_{PV} + \sum_{i=1}^{n}\left(\frac{\partial A}{\partial P_i}\right)\Delta P_i, \tag{5.23}$$

where beam parameter P_i changes upon helicity reversal to $P_i^{\pm} = P_i \pm \Delta P_i$. The detector sensitivities $\partial A/\partial P_i$ can be determined from natural variation of beam parameters or by modulating the relevant beam parameter. The helicity-correlated beam parameter differences, ΔP_i, are measured continuously during data-taking. From the sensitivity of the apparatus to beam parameter variations and the measured beam parameters, the corrections due to small helicity correlations can be determined — essentially, these corrections are obtained through the linear regression. The uncertainty of ΔP_i

is estimated as the variance of ΔP_i:

$$\delta(\Delta P_i) = \sqrt{\frac{1}{N}\sum_n (\Delta P_{i,n} - \langle \Delta P_{i,n} \rangle)^2}\,, \tag{5.24}$$

where $\langle \Delta P_{i,n} \rangle$ is the run averaged value of ΔP_i and the summation is over N runs. Then the uncertainty in the asymmetry due to helicity-correlated beam properties is determined as

$$\delta A_{\text{beam}} = \sqrt{\sum_i \left[\frac{\partial A}{\partial P_i}\delta(\Delta P_i)\right]^2}\,. \tag{5.25}$$

This is an uncertainty with a value close to zero if it is already taken into account in the asymmetry due to linear regression. From Eqn. 5.18, the uncertainty in asymmetry due to background corrections is

$$\delta A_{\text{background}} = \frac{1}{P_b}\sqrt{\sum_j \left[\left(A^{\text{exp}} - A_j^{\text{exp}}\right)\delta f_j\right]^2 + \sum_j \left[f_j\,\delta\left(A^{\text{exp}} - A_j^{\text{exp}}\right)\right]^2}\,. \tag{5.26}$$

The uncertainty in asymmetry due to beam polarization is calculated as

$$\delta A_{\text{polarization}} = \left|\frac{A^{\text{exp}}}{P_b^2}\delta P_b\right|\,. \tag{5.27}$$

The systematic uncertainty and the significance of the observed asymmetry are then

$$\delta A_{\text{syst.}} = \sqrt{\delta A_{\text{beam}}^2 + \delta A_{\text{background}}^2 + \delta A_{\text{polarization}}^2}\,, \tag{5.28}$$

$$S_{A_{PV}} = \frac{A_{PV}}{\sqrt{(\delta A_{\text{stat.}})^2 + (\delta A_{\text{syst.}})^2}}\,. \tag{5.29}$$

Fig. 5.6 shows an example plot of the asymmetry for the combination of all main detectors versus Wien setting and IHWP status, which includes all Q-weak run I production parity data taken from February 11, 2011 to May 13, 2011 [Rajotte, 2011]. The data of the first 25% statistical uncertainty measurement (data taken from January 13, 2011 to February 10, 2011) is not included

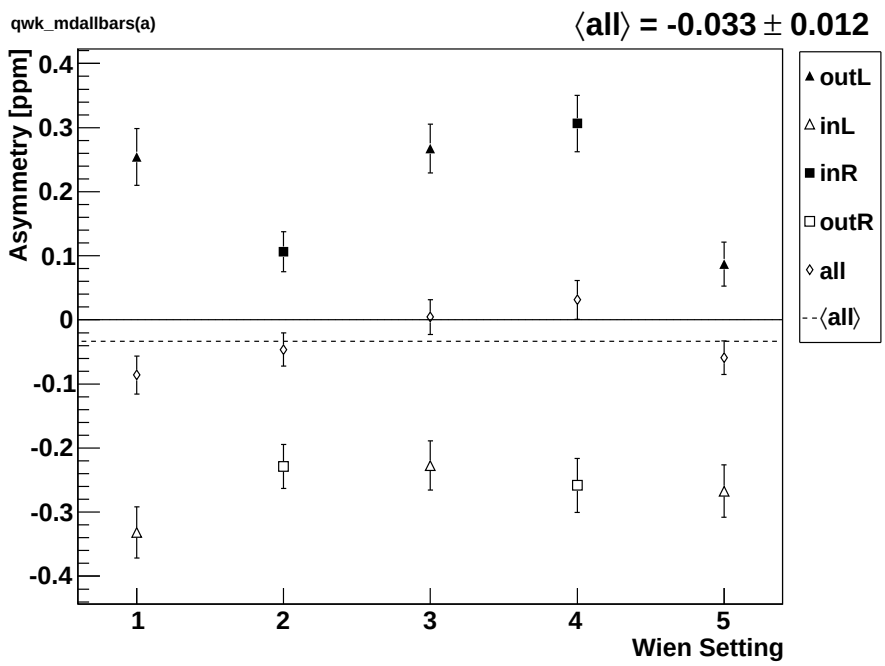

Figure 5.6: Asymmetries from different runs/slugs are grouped according to the IHWP and Wien settings (the data has not been corrected for the asymmetry sign reversals due to IHWP status change). The open diamond marker indicates the statistical width weighted average value of two groups which have the same Wien setting but opposite IHWP status. The dashed line indicates the grand average of all asymmetries. The data has not been corrected for asymmetry sign reversals, and the uncertainties are only statistical.

in the plot and the following calculations, because that data was assigned a different large blinding factor (larger than 60 ppb). The corresponding run/slug list and the regressed data are showed in Table 5.1. The measured asymmetry from the data (not being normalized to beam polarization) is found to be

$$A_{\text{meas}} = -211 \pm 12\,(\text{stat.}) \pm 60\,(\text{blinding factor})\ \text{ppb}\,. \tag{5.30}$$

This is a blinded result with 5.7% statistical uncertainty. With more production data to reduce the statistical uncertainty, upon completing the experiment, Q-weak will be the most precise measurement to date of any asymmetry in electron scattering.

Wien (#/Flip)	Run range	Slug range	Date (2011)	Asymmetry [ppm] (IHWP IN)	Asymmetry [ppm] (IHWP OUT)
0/R	08964-09812	< 40	13/01 - 10/02	0.113 ± 0.043	−0.351 ± 0.036
1/L	09939-10186	42-58	11/02 - 22/02	−0.332 ± 0.040	0.214 ± 0.044
2/R	10196-11129	59-80	22/02 - 05/04	0.106 ± 0.031	−0.229 ± 0.034
3/L	11131-11390	81-98	05/04 - 14/04	−0.227 ± 0.038	0.237 ± 0.038
4/R	11391-11711	99-116	14/04 - 28/04	0.307 ± 0.044	−0.218 ± 0.042
5/L	11714-11735	117-136	28/04 - 13/05	−0.267 ± 0.041	0.087 ± 0.034

Table 5.1: Q-weak Run-I asymmetry data. The data has not been corrected for asymmetry sign reversals, and the uncertainties are only statistical.

5.8 Hadronic Structure Contributions

The parity-violating asymmetry expression contains contributions from nucleon structure form factors. They increase in relative importance as one moves away from $Q^2 = 0$. To consider the impact of these contributions on the extraction of the weak charge, the asymmetry which involves the quantity of interest, Q_W^p, is written as follows:

$$A_{Q_W^p} = A_{PV} - A_{hadV} - A_{hadA} \,. \tag{5.31}$$

The second term involves the vector electromagnetic and weak hadronic form factors. It reduces to the $Q^4 B(Q^2)$ term in Eqn. 2.107 for small Q^2. The third term involves the e-N axial-vector form factor G_A^e. These terms are kept separately, because there are two different types of experiments that are used to constrain them with different kinematic dependences.

The Q-weak experiment aims to determine $A_{Q_W^p}$ (and therefore Q_W^p) from the measured physics asymmetry A_{PV}. The values of the hadronic terms (A_{hadV} and A_{hadA}) are determined by results from parity-violating electron scattering experiments at higher Q^2, that are more sensitive to these terms.

The estimates for A_{hadV} and A_{hadA} are

$$A_{hadV} = -101 \text{ ppb} , \tag{5.32}$$

$$A_{hadA} = -12 \text{ ppb} , \tag{5.33}$$

given in reference [Qweak-Collaboration, 2004]. Assuming a value of $Q_W^p = 0.0716$ (with all radiative corrections included), the $A_{Q_W^p}$ can be estimated to be about -180 ppb. The acceptance averaged values of the asymmetry in the experiment is expected to close to -293 ppb, including 61% contributions from $A_{Q_W^p}$, 35% contributions from A_{hadV} and 4% contributions from A_{hadA}. The uncertainties on the hadronic terms are

$$\delta A_{hadV} = 2.83 \text{ ppb} , \tag{5.34}$$

$$\delta A_{hadA} = 2.16 \text{ ppb} , \tag{5.35}$$

as explained in reference [Qweak-Collaboration, 2004], which imply a 1.5% and a 1.2% contributions to the fractional uncertainty on Q_W^p from the vector hadronic component and from the axial hadronic component, respectively. The total estimate of the uncertainty stemming from hadronic structure contributions is obtained from the combination of the two estimates for the uncertainties on the vector (1.5%) and axial (1.2%) hadronic components in quadrature. The final estimate for the fractional uncertainty on Q_W^p from hadronic structure is 1.9%. The total contribution to the uncertainty on Q_W^p is then written as:

$$\frac{\delta Q_W^p}{Q_W^p} = \sqrt{\left(\frac{\delta A_{PV}}{A_{Q_W^p}}\right)^2 + \left(\frac{\delta A_{hadV}}{A_{Q_W^p}}\right)^2 + \left(\frac{\delta A_{hadA}}{A_{Q_W^p}}\right)^2} . \tag{5.36}$$

5.9 The Proton's Weak Charge and Weak Mixing Angle

After removing the hadronic contribution, the proton's weak charge and the weak mixing angle can be determined from

$$A_{Q_W^p} = -\frac{G_F Q^2}{4\pi\alpha\sqrt{2}} Q_W^p \,, \tag{5.37}$$

$$Q_W^p = 1 - 4\sin^2\theta_W + \text{radiative corrections} \,, \tag{5.38}$$

where the radiative corrections were discussed in section 2.6.

Table 3.1 contains a brief summary of the key uncertainties for this experiment, which were estimated through simulations and calculations. These values will be updated and replaced by measured uncertainties, as the the data analysis and data collection progresses. An extensive set of sensitivity measurements has shown that the Q-weak experiment is statistics limited and a 4% measurement of the weak charge should be achievable by the end of May 2012.

As an exercise, the proton's weak charge and the weak mixing angle can be calculated by using the 5.7% asymmetry measurement data considered in this thesis. Because the statistical uncertainty of the 5.7% asymmetry measurement and the blinding factor are far larger than the systematic uncertainty, the systematic corrections (except the contributions from hadronic structure and the helicity-correlated beam parameters which have been corrected in the regression) and radiative corrections will be neglected. By using a beam polarization value of 89% (determined by the polarization measurements), the values of the $A_{Q_W^p}$, Q_W^p and the weak mixing angle at $Q^2 = 0.026$ (GeV/c)^2 (with an uncertainty of about 5% [5], determined from the calibration runs and weighted by the main detector light yield responses) are found to be

$$A_{PV} = -237 \pm 14\ (\text{stat.}) \pm 67\ (\text{blinding factor})\ \ \text{ppb} \,, \tag{5.39}$$

$$A_{Q_W^p} = -124 \pm 14\ (\text{stat.}) \pm 67\ (\text{blinding factor})\ \ \text{ppb} \,, \tag{5.40}$$

[5] The uncertainty is simply estimated by using the tracking detector geometry and resolution.

$$Q_W^p = 0.053 \pm 0.006 \text{ (stat.)} \pm 0.029 \text{ (blinding factor)} , \tag{5.41}$$

$$\sin^2\theta_W = 0.2368 \pm 0.0015 \text{ (stat.)} \pm 0.0072 \text{ (blinding factor)} , \tag{5.42}$$

where the blinding factor involved in each calculation is treated as an uncertainty term.

Table 5.2 gives a comparison between the theoretical prediction (see [Nakamura et al., 2010], [Erler et al., 2003] and [Erler and Ramsey-Musolf, 2005b]) and the very preliminary Q-weak 5.7% statistics measurements for the proton's weak charge and the weak mixing angle at $Q^2 = 0.026$ $(\text{GeV/c})^2$. The Q-weak results are in agreement with the Standard Model prediction on the level of the statistical uncertainty and the uncertainty due to blinding analysis factor.

	Theoretical prediction	Q-weak 5.7% measurement (blinded)
Q_W^p	0.0716 ± 0.002	0.053 ± 0.030
$\sin^2\theta_{W_{\overline{\text{MS}}}}$	0.2385 ± 0.0006	0.2368 ± 0.0074

Table 5.2: Comparison between theoretical prediction and Q-weak 5.7% statistics measurement.

Chapter 6

Conclusion and Outlook

The Q-weak experiment had been constructed and successfully commissioned. As a key subsystem, the main Čerenkov detectors were designed to perform measurements of parity violating asymmetries in e-p scattering. The commissioning data demonstrates that this detector system is sufficiently low noise to allow operation at counting statistics in the Q-weak integrating current mode.

The goal of the Q-weak experiment is to measure the parity-violating asymmetry in elastic electron-proton scattering to a precision of ~4%, which translates into a measurement of $\sin^2\theta_W$ at $Q^2 = 0.026\ (\mathrm{GeV/c})^2$ to a precision of ~0.3%. The asymmetry measured by the Q-weak experiment during the 2010-2011 first run cycle is

$$A_{PV} = -237 \pm 14\ (\mathrm{stat.}) \pm 67\ (\mathrm{blinding\ factor})\ \ \mathrm{ppb}\ . \tag{6.1}$$

This asymmetry was measured at a momentum transfer of

$$Q^2 = 0.026 \pm 0.002\ \ (\mathrm{GeV/c})^2\ . \tag{6.2}$$

The proton's weak charge and weak mixing angle at $Q^2 = 0.026\ (\mathrm{GeV/c})^2$ obtained from the mea-

sured A_{PV} are

$$Q_W^p = 0.053 \pm 0.006 \text{ (stat.)} \pm 0.029 \text{ (blinding factor)} , \tag{6.3}$$

$$\sin^2\theta_W = 0.2368 \pm 0.0015 \text{ (stat.)} \pm 0.0072 \text{ (blinding factor)} , \tag{6.4}$$

These very preliminary results are in agreement with the theoretical predictions at their current uncertainties.

The experiment has completed the first run cycle and has succeeded in measuring the proton's weak charge to about 8%. The aim is to improve this to 4% during Phase II, from Fall 2011 to Spring 2012. If the Q-weak experiment achieves the goal precision in the remaining running period, it will be the most precise determination of the parity violating asymmetry in electron-proton scattering to date, and will provide the first direct measurement of the proton weak charge. At the precision goal of 0.3% for $\sin^2\theta_W$, the Q-weak measurement will be sensitive to new physics effects at scales up to ~2.5 TeV, complementing studies from collider experiments. The Q-weak results will be sensitive to new physics models, such as additional neutral gauge bosons, extensions to the Standard Model that include supersymmetry, and the existence of leptoquarks (bosons with nonzero baryon and lepton number). In addition, since the Q-weak experiment will measure $\sin^2\theta_W$ at approximately the same momentum transfer as the SLAC E-158 experiment, the results from both experiments should complement each other and provide more clues regarding the nature of possible new physics phenomena.

The measurement of parity-violating asymmetries with high precision has become an important tool for studying new physics beyond the Standard Model. The success of the Q-weak experiment will establish confidence in the ability to measure asymmetries to an accuracy at the ppb level in future high energy electron scattering experiments.

Appendix A

Miscellaneous Details of the Main Detector

A.1 Detector Parameters

A.1.1 Detector and PMT serial number

Detector	MD1	MD2	MD3	MD4	MD5	MD6	MD7	MD8
Serial No.	4	3	1	5	6	2	7	8

Table A.1: Main detector serial number.

	MD1	MD2	MD3	MD4	MD5	MD6	MD7	MD8	AUX1	AUX2	AUX3
Neg	119	109	104	124	129	105	106	110	115	132	128
Pos	121	107	122	135	134	108	126	111			

Table A.2: PMT serial number for each detector

A.1.2 Transmission spectrum and refractive index of fused silica

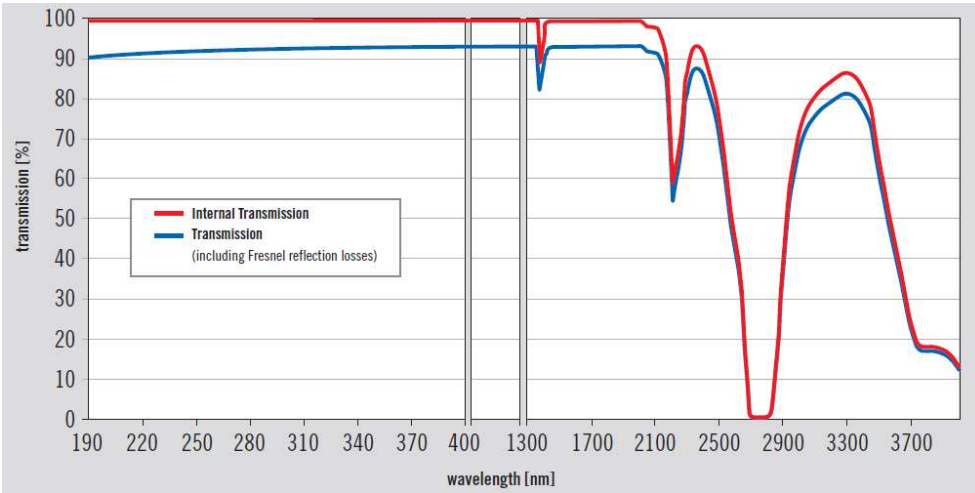

Figure A.1: Typical transmission spectrum of Spectrosil® 2000 synthetic fused silica. Sample thickness: 10 mm

Wavelength (nm)	1128.95	1064.00	1060.00	1013.98	852.11	706.52	656.27
Refractive Index (n)	1.44887	1.44963	1.44968	1.45024	1.45247	1.45515	1.45637
Wavelength (nm)	643.85	632.80	589.29	587.56	546.07	486.13	435.83
Refractive Index (n)	1.45670	1.45702	1.45840	1.45846	1.46008	1.46313	1.46669
Wavelength (nm)	404.66	365.01	334.24	312.66	253.73	248.30	248.00
Refractive Index (n)	1.46962	1.47454	1.47975	1.48447	1.50547	1.50838	1.50855
Wavelength (nm)	228.87	214.51	206.27	194.23	193.40	193.00	184.95
Refractive Index (n)	1.52109	1.53365	1.54259	1.55884	1.56014	1.56077	1.57495

Table A.3: Refractive index of Spectrosil® 2000 synthetic fused silica.

A.1.3 PMT quantum efficiency

Wavelength (nm)	200	210	220	230	240	250	260
Quantum Efficiency (%)	0.68	3.55	7.40	10.4	14.6	17.8	20.6
Wavelength (nm)	270	280	290	300	310	320	330
Quantum Efficiency (%)	22.6	22.4	21.8	21.1	20.5	19.7	19.2
Wavelength (nm)	340	350	360	370	380	390	400
Quantum Efficiency (%)	18.4	18.0	18.2	18.8	18.3	17.6	17.7
Wavelength (nm)	410	420	430	440	450	460	470
Quantum Efficiency (%)	17.6	17.5	17.1	16.7	15.8	15.0	14.4
Wavelength (nm)	480	490	500	510	520	530	540
Quantum Efficiency (%)	13.7	13.1	12.4	11.7	11.0	10.4	9.77
Wavelength (nm)	550	560	570	580	590	600	610
Quantum Efficiency (%)	9.15	8.53	7.95	7.39	6.87	6.38	5.90
Wavelength (nm)	620	630	640	650	660	670	680
Quantum Efficiency (%)	5.45	5.07	4.71	4.39	4.10	3.79	3.51
Wavelength (nm)	690	700	710	720	730	740	750
Quantum Efficiency (%)	3.25	2.98	2.68	2.40	2.13	1.88	1.65
Wavelength (nm)	760	770	780	790	800	810	820
Quantum Efficiency (%)	1.47	1.30	1.13	0.96	0.80	0.65	0.48
Wavelength (nm)	830	840	850	860	870	880	900
Quantum Efficiency (%)	0.33	0.18					

Table A.4: Typical quantum efficiency of 9312WKB PMT with S20 photocathode.

A.1.4 PMT saturation voltage and current

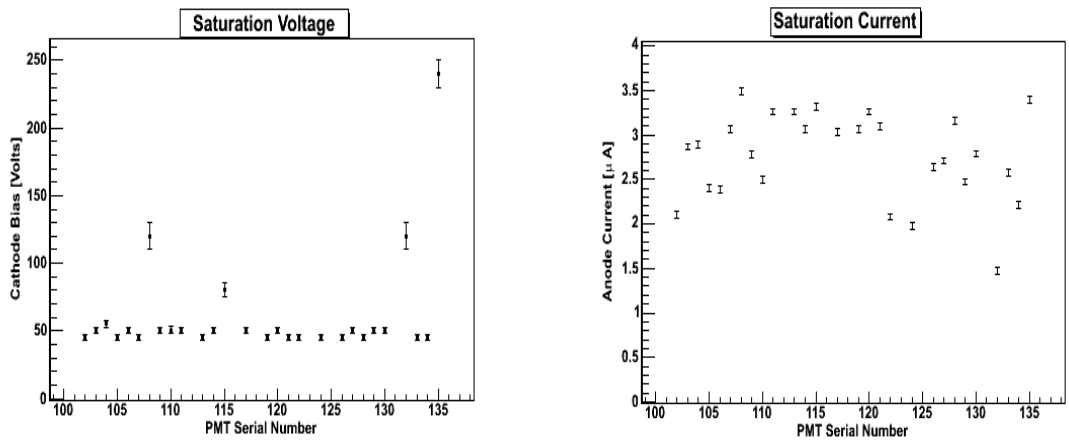

(a) Saturation voltages for all PMTs

(b) Saturation currents for all PMTs

Figure A.2: Measurement were taken with a 370 nm LED as a light source. The PMTs were working in photodiode mode (read the photo-current from the first dynode) with a cathode bias voltage up to a few hundred volts. Record anode current as a function of supply voltage and find the current and voltage at which the PMT saturates.

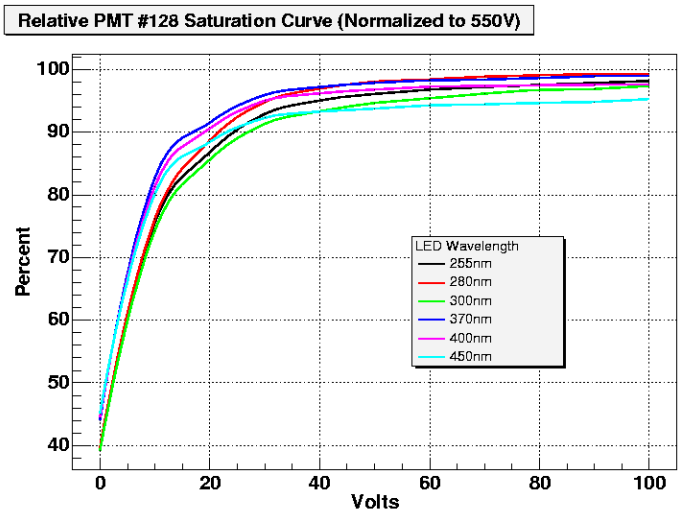

Figure A.3: Saturation as a function of wavelength for the reference PMT (serial No. 128).

A.1.5 Gain tests for current mode PMT bases

HV [V]	1300	1250	1200	1150	1100	1050	1000	950	900	850	800
Base #					Gain						
101	7062	4678	3052	1940	1206	718	409	221	112	53	22
102	7022	4527	2943	1883	1171	700	400	218	110	52	22
103	7024	4562	2936	1855	1153	690	387	209	106	49	20
104	7347	4735	3072	1959	1215	726	408	225	114	54	22
105	6599	4263	2754	1753	1084	646	364	198	101	47	19
106	7221	4647	2983	1895	1178	702	400	218	112	53	22
107	6199	3955	2558	1625	1000	596	339	184	94	44	18
108	6696	4269	2771	1758	1081	646	370	200	102	48	20
109	6406	4042	2630	1673	1039	626	359	197	101	48	20
110	6129	3873	2491	1572	973	581	332	180	92	43	18
111	6045	3753	2453	1571	969	579	329	178	91	43	18
112	5972	3768	2416	1540	951	567	322	175	89	42	17
113	5675	3683	2387	1529	935	556	317	172	88	41	17
115	6507	4099	2666	1691	1055	631	359	196	100	47	19
117	5977	3705	2407	1531	951	563	321	174	89	42	17
118	7922	5030	3376	2045	1262	744	423	229	116	54	22
119	7642	4877	3159	1987	1222	728	410	221	112	52	21
120	7439	4717	3037	1931	1194	704	399	217	109	51	21
121	7310	4653	2973	1902	1174	698	398	217	111	52	21
122	7406	4638	4694	1892	1174	702	398	217	110	52	21
123	7769	4929	3194	2033	1260	749	428	230	117	55	23
124	7428	4611	2969	1900	1193	711	407	224	114	54	23

Table A.5: Gain measurements for the current mode low gain PMT bases. Measurements were taken with a reference PMT (serial No. 128). Bases 114 and 116 are eliminated due to their abnormal high gain.

Base #	101	102	103	104	105	106	107	108	109	110	111
HV [V]	1079	1082	1084	1078	1090	1081	1100	1091	1095	1102	1103
Base #	112	113	115	117	118	119	120	121	122	123	124
HV [V]	1104	1106	1094	1104	1075	1078	1080	1082	1082	1075	1080

Table A.6: Bias voltages at a PMT gain of 1000. Measurements were taken with a reference PMT (serial No. 128). Bases 114 and 116 are eliminated due to their abnormal high gain.

A.1.6 Single photo-electron calibration

	MD1	MD2	MD3	MD4	MD5	MD6	MD7	MD8
Neg.	14.0	22.0	20.4	22.1	22.8	28.7	24.6	27.8
Pos.	16.7	38.5	20.4	22.4	30.1	25.3	16.1	12.3

Table A.7: Single photo-electron calibration I (October 5, 2011). Unit: number of charge ADC channels per photo-electron (and 0.1 pC/ch).

	MD1	MD2	MD3	MD4	MD5	MD6	MD7	MD8
Neg.	11.9	18.4	20.7	16.9	20.4	25.1	16.4	24.9
Pos.	18.2	37.9	19.0	22.8	28.0	25.9	29.2	12.2

Table A.8: Single photo-electron calibration II (November 2, 2011). Unit: number of charge ADC channels per photo-electron (and 0.1 pC/ch).

	MD1	MD2	MD3	MD4	MD5	MD6	MD7	MD8
Neg.	12.4	11.2	12.9	21.0	12.0	13.3	14.7	11.9
Pos.	17.0	15.8	13.8	18.5	17.9	18.6	16.4	11.4

Table A.9: Single photo-electron calibration III (March 14, 2011). Unit: number of charge ADC channels per photo-electron (and 0.1 pC/ch).

A.1.7 Typical current mode yield

Detector	Yield [V/μA]	RMS [V/μA]
MD1−	0.034363	5.9×10^{-5}
MD1+	0.039068	6.7×10^{-5}
MD2−	0.026691	4.3×10^{-5}
MD2+	0.044260	7.2×10^{-5}
MD3−	0.043711	7.2×10^{-5}
MD3+	0.023393	3.8×10^{-5}
MD4−	0.025374	4.3×10^{-5}
MD4+	0.038453	6.3×10^{-5}
MD5−	0.036681	6.0×10^{-5}
MD5+	0.045696	7.6×10^{-5}
MD6−	0.039137	6.3×10^{-5}
MD6+	0.032705	5.3×10^{-5}
MD7−	0.032501	5.3×10^{-5}
MD7+	0.038210	6.2×10^{-5}
MD8−	0.039887	6.5×10^{-5}
MD8+	0.044247	7.2×10^{-5}

Table A.10: Typical current mode yields of main detectors.

A.1.8 High voltage and pre-amplifier settings

	MD1	MD2	MD3	MD4	MD5	MD6	MD7	MD8	
HV [V]	1200	1300	1100	950	1100	1200	1200	1200	Neg.
I [μA]	1492	1617	1374	1184	1369	1496	1494	1496	
HV [V]	1200	1100	1200	1050	900	1100	1000	1200	Pos.
I [μA]	1496	1371	1494	1309	1121	1366	1248	1495	

Table A.11: High voltages and currents of event mode high gain bases (March 5, 2011).

	MD1	MD2	MD3	MD4	MD5	MD6	MD7	MD8
Neg.	114.5	122.4	93.5	106.9	107.6	117.3	109.8	120.3
Pos.	105.8	94.6	102.5	124.6	117.0	110.6	120.7	120.3

Table A.12: Pre-amplifier offset settings (July 27, 2010). Unit: [mV]

	MD1	MD2	MD3	MD4	MD5	MD6	MD7	MD8	
HV [V]	880	820	850	800	820	840	850	815	Neg.
PMT gain	200	200	200	200	200	200	200	200	
HV [V]	850	850	805	850	805	820	810	855	Pos.
PMT gain	200	200	200	200	160	200	200	160	

Table A.13: Current mode PMT high voltage and gain settings (the voltages were lowered by 10 V on January 21, 2011).

Parameter/setting	Value
Estimated event rate per detector	4.4 kHz/nA
Pre-amplifier gain setting	2 MΩ
PMT gain setting	200
PMT anode leakage (dark current)	<1 nA
Average photo-electron yield per detector	110 p.e./event

Table A.14: Typical current mode parameters and settings for the Q-weak Run-I. All main detectors were equipped with pre-radiators.

A.2 Gluing Procedure

1. Surface preparation (surface cleaning and polishing are critical to good adhesion):

   (a) Clean a fresh razor blade with isopropyl alcohol (IPA), then strip the surface to be glued (as well as about 1 – 2 cm along the sides) to remove any insoluble coatings.

   (b) Wipe down the surface of interest with IPA to remove any fingerprints, permanent marker writing, or thick, gummy residues from tape, etcetera. Clean down about 1 –2 cm on the sides helps reduce contamination.

   (c) Use soap and water to remove the IPA residue. Rinse with distilled water.

   (d) First polish: Lightly scrub the area to be glued for a few minutes with 0.05 micron MicroPolish. Scrub 1 cm down the sides as well. Add distilled water to keep the polish wet.

   (e) First rinse: Wipe the sides off with no-linting wipes (such as KimWipes) wetted with distilled water. Then remove polish from the main face using KimWipes wetted with distilled water using a uni-axial motion. Change wipe after each pass, and change directions between wipes so that one end does not end up cleaner than the other.

   (f) Second polish and rinse: Using less polish, repeat the last two steps.

   (g) Carefully dry the surface with a heat gun and inspect the surface with light. If necessary, repeat the above steps 2 or 3 times except the first razor blade step.

2. Glue preparation:

   (a) Tumble the glue components in case components have separated.

   (b) Put the low viscosity hardener (CAT-1202) into a clean plastic cup first, then add the higher viscosity base (SES-406, the main component of the silicon rubber glue). The glue volume ratio and pumping time are listed in Table A.15 for reference.

   (c) Stir glue thoroughly with a clean, dry stirring rod. Mix as much air in as possible.

(d) Pump the glue until most bubbles are gone to remove air and any absorbed water which could affect performance. Control the pumping time (less than 1 hour) to make sure the glue is still keep low viscosity after pumping.

Glue joint	Hardener CAT-1202 [ml]	Base SES-406 [ml]	Pumping time [min]	Cure time [hr]
PTM window to light guide	2.0	40	60	>72
light guide to quartz bar	4.4	40	30	>48
central glue joint	5.0	40	20	>48

Table A.15: Parameters for preparing optical glue.

3. Dispense glue:

   (a) Use two wire-chamber wires as spacers and tape them on the prepared gluing surface (for the central glue joint only). This is to keep a uniform thickness of the glue layer when gluing the two pieces of quartz bars together.

   (b) Fill a syringe with glue from the middle of the cup. Empty the syringe most of the way and refill it. This gets rid of most air bubbles and dilutes any contaminants that might be on the inside of the syringe.

   (c) Squeeze out remaining air bubbles and apply glue on the prepared surface.

   (d) Align the quartz bars (quartz light guide or PMT) and glue them together.

   (e) Pull out the spacer slowly and make sure no air bubble left inside the glue joint. Do not wipe off any excess glue.

4. Final quality check and cleaning:

   (a) After 48 hours cure time, test the glue joint by putting one end of the quartz bar on the

table and lifting the other end after the glue cured. Redo the above gluing procedure if there are any breaking glue joints.

(b) Remove excess glue with a razor blade, then follow the surface preparation procedure to clean the entire optical assembly.

Figure A.4: Photo of the main detector optical assembly in the gluing and cleaning process.

A.3 Detector Installation

A coordinate system and naming convention are defined in section 4.1 and used for the detector installation. For convenience, there are rotation angles defined for survey and alignment purpose. These rotation angles are yaw angle — rotation angle about Y axis, pitch angle — rotation angle about X axis and roll angle — rotation angle about Z axis.

Based on the sub-mm errors of the quartz bar mismatch and quartz bar location with respect to the radiator module as the detectors are assembled, the required tolerances for detector judicialization, survey and alignment should be matched to $\sim$ 1 mm so that the installation will not introduce additional positioning uncertainty.

The location tolerances are determined in the global coordinates: for x,y locations, 1 mm tolerance is corresponding to the $<$ 1 mm quartz bar errors, for the z location, because the about 25 degree electron incident angle will cause the electron profile to move up/down about 5 mm if the quartz bar z location was changed about 10 mm, 2 mm tolerance is proper, which corresponds to 1 mm errors on x and y. The rotation tolerances are determined in the detector local coordinates: for the yaw angle, 1 mm error over the 200 mm detector width gives about 1.5 mrad error, for the pitch and roll, 1 mm error over 2000 mm detector length gives about 0.2 mrad error. Note that the sub-mm errors are physical, thus the above tolerances are the best that could be achieved when the detectors are installed. As long as the symmetry requirements are meet, some specifications need to be weaken where the fine adjustment is not available and it would require using the crane to install shims, or drilling/rewelding the arms.

After loading the detector module into exoskeletons, the detectors are fiducialized using CMM[1] on the registration points, edges and surfaces of quartz bars. Because there are small differences of the quartz bar length, width and thickness, as well as small mismatch between two half-sized quartz bars as they are glued together, the registration points, edges and surfaces need to be defined as references for survey and alignment. The registration surface is the front surface of the quartz bars towards the incoming scattered electrons; the registration edges are the outer radius edges of

[1] A CMM is a coordinate measuring machine for measuring the physical geometrical characteristics of an object.

the quartz bar on the registration surface [2]; the registration point is the outer radius end of the quartz bar center glue joint. These references are best aligned when the detector is assembled and their positions are transferred to several survey monuments fixed on the exoskeleton of the detector through fiducialization.

The detectors are craned to position, fixed on the supporting arms (see Fig. A.5 (a)), then surveyed by using a laser tracker. The survey monuments on the exoskeletons are target holders for laser tracker. The use of laser tracker and the ability of detector fine adjustment in radial direction made the detector alignment easier and accurate. A photo of the installed main detector octagonal array is shown in Fig. A.5 (b) with the main detectors just downstream of the vertical drift chambers before the shielding house was erected around them. The photo in Fig. 3.23 also shows a closer view of two bottom detectors, as well as the focal plane scanner which can be moved around in the bottom octant to help characterize the main detector at higher beam currents where the VDCs cannot be used. The final survey on the installed detectors showed that the registration point of each detector was located to an average radial position of 344.0 cm (with a RMS value of 0.24 cm) to the beam and an average Z-location of 577.9 cm (with a RMS value of 0.54 cm) downstream of the QTOR center, i.e., the quartz bar center was located at $X = 335.0$ cm, $Z = 578.5$ cm in its local coordinate system.

[2]The outer radius edges of the quartz bar are chosen as registration edges because these edges are located in between the elastic events region and the inelastic events region.

(a) Photo of a main detector being installed.

(b) Octagonal main detector array shown between the region 3 chambers, and the main detector access platform.

Figure A.5: Main detector installation photos

A.4 Detector Survey Results

The main detectors survey results are shown by the table in Fig. A.6, which contains the as-found coordinates in both the Q-weak global coordinate system and the main detector local coordinate system as defined in section 4.1. Additionally the movements in the local system are shown. The first group of coordinates are the as-found locations of the quartz bars in the global (QTOR) coordinate system, with the origin at the center of the QTOR magnet. Units are meters. The second group of coordinates describes the as-found locations in the local coordinate system for each individual detector.

	Qtor Coord System					Local Quartz Bar Coords				
Detector Side	X (M)	Y (M)	Z (M)	phi ang (deg)		Local X (cm)	Local Y (cm)	Local Z (cm)		Ri component
MD1+	3.4379	1.2568	5.7743	0		343.79	125.68	577.43		343.782
MD1-	3.4357	-1.2578	5.7715			343.57	-125.78	577.15		343.666
MD2+	1.5418	3.3227	5.7788	45		343.97	125.93	577.88		343.965
MD2-	3.3174	1.5422	5.7678			343.62	-125.52	576.78		343.518
MD3+	-1.2580	3.4371	5.7726	90		343.71	125.80	577.26		343.712
MD3-	1.2566	3.4429	5.7803			344.29	-125.66	578.03		344.029
MD4+	-3.3266	1.5417	5.7836	135		344.24	126.21	578.36		344.162
MD4-	-1.5455	3.3168	5.7774			343.82	-125.25	577.74		343.910
MD5+	-3.4390	-1.2576	5.7808	180		343.90	125.76	578.08		344.048
MD5-	-3.4418	1.2570	5.7820			344.18	-125.70	578.20		344.099
MD6+	-1.5343	-3.3312	5.7848	225		344.05	127.06	578.48		344.210
MD6-	-3.3144	-1.5551	5.7868			344.33	-124.40	578.68		344.293
MD7+	1.2596	-3.4427	5.7875	270		344.27	125.96	578.75		344.322
MD7-	-1.2550	-3.4407	5.7827			344.07	-125.50	578.27		344.125
MD8+	3.3099	-1.5508	5.7758	315		343.70	124.39	577.58		343.844
MD8-	1.5344	-3.3314	5.7779			344.06	-127.07	577.79		343.931

Figure A.6: Main detector survey result.

A.5 CAD Drawings of Preradiator, Radiator Box and Exoskeleton

Each pre-radiator consists of 2 end pieces (Fig. A.7) and 6 T-bar pieces (Fig. A.8).

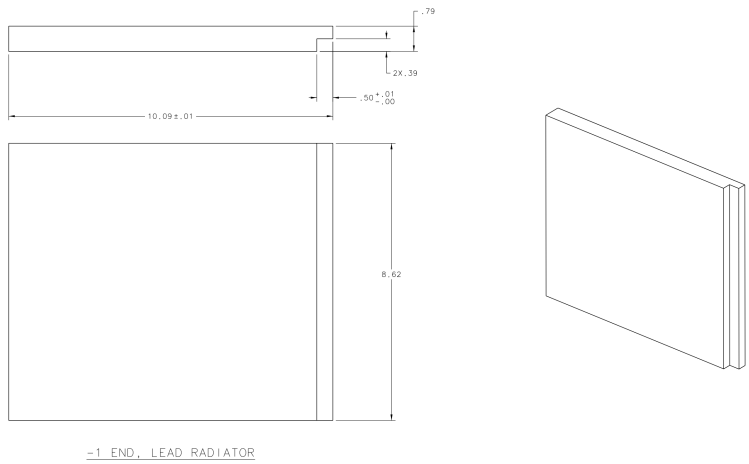

Figure A.7: Preradiator end piece. Material: lead (Pb) with 2-5% antimony (Sb).

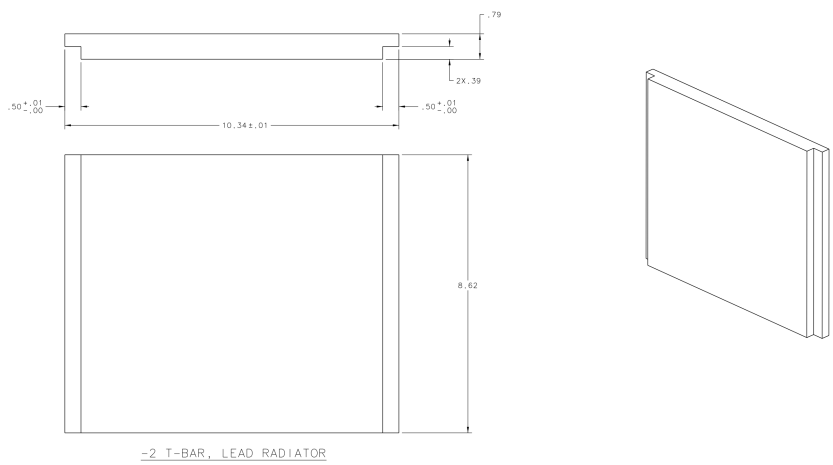

Figure A.8: Preradiator T-bar piece. Material: lead (Pb) with 2-5% antimony (Sb).

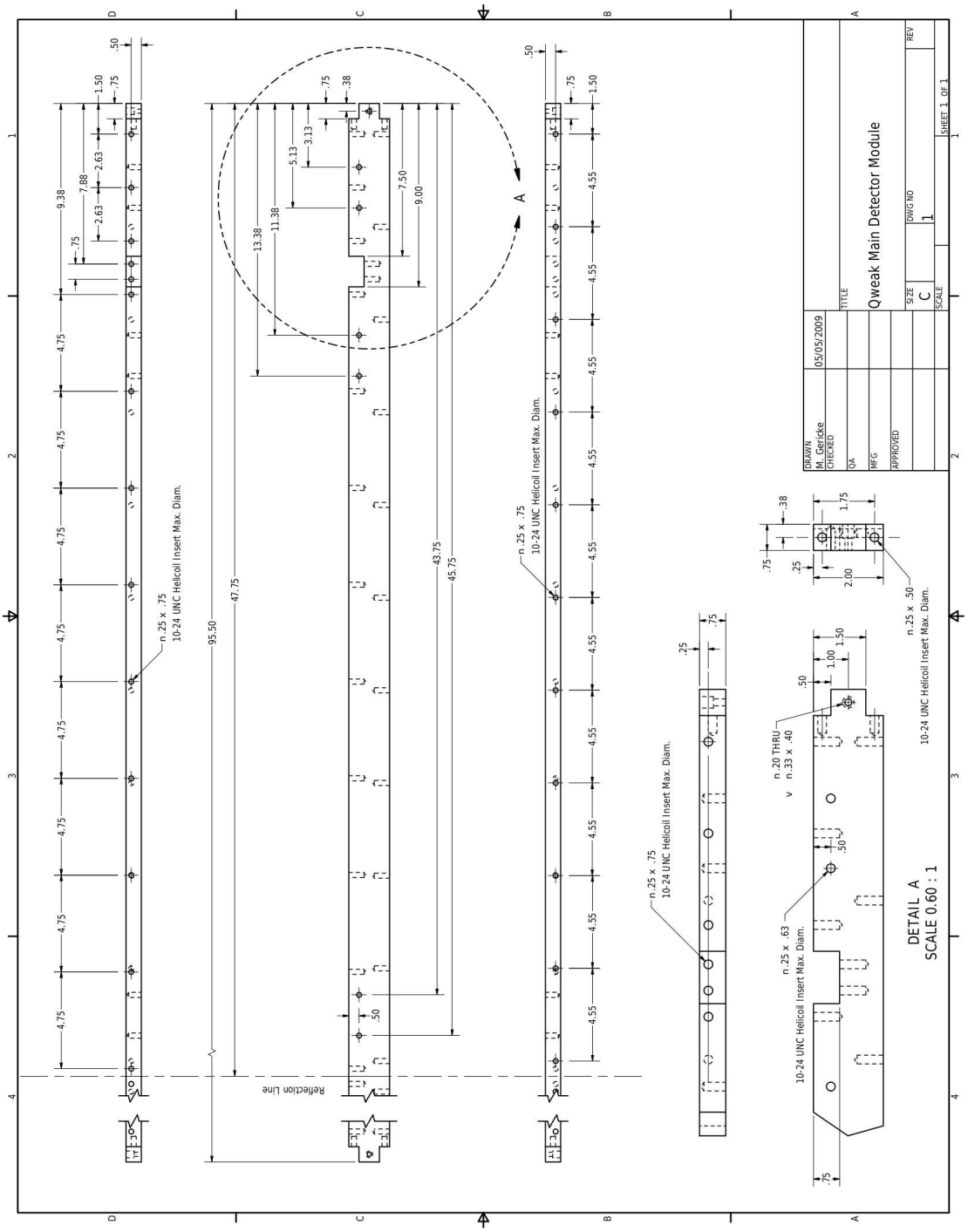

Figure A.9: Radiator box CAD drawing 1 of 10.

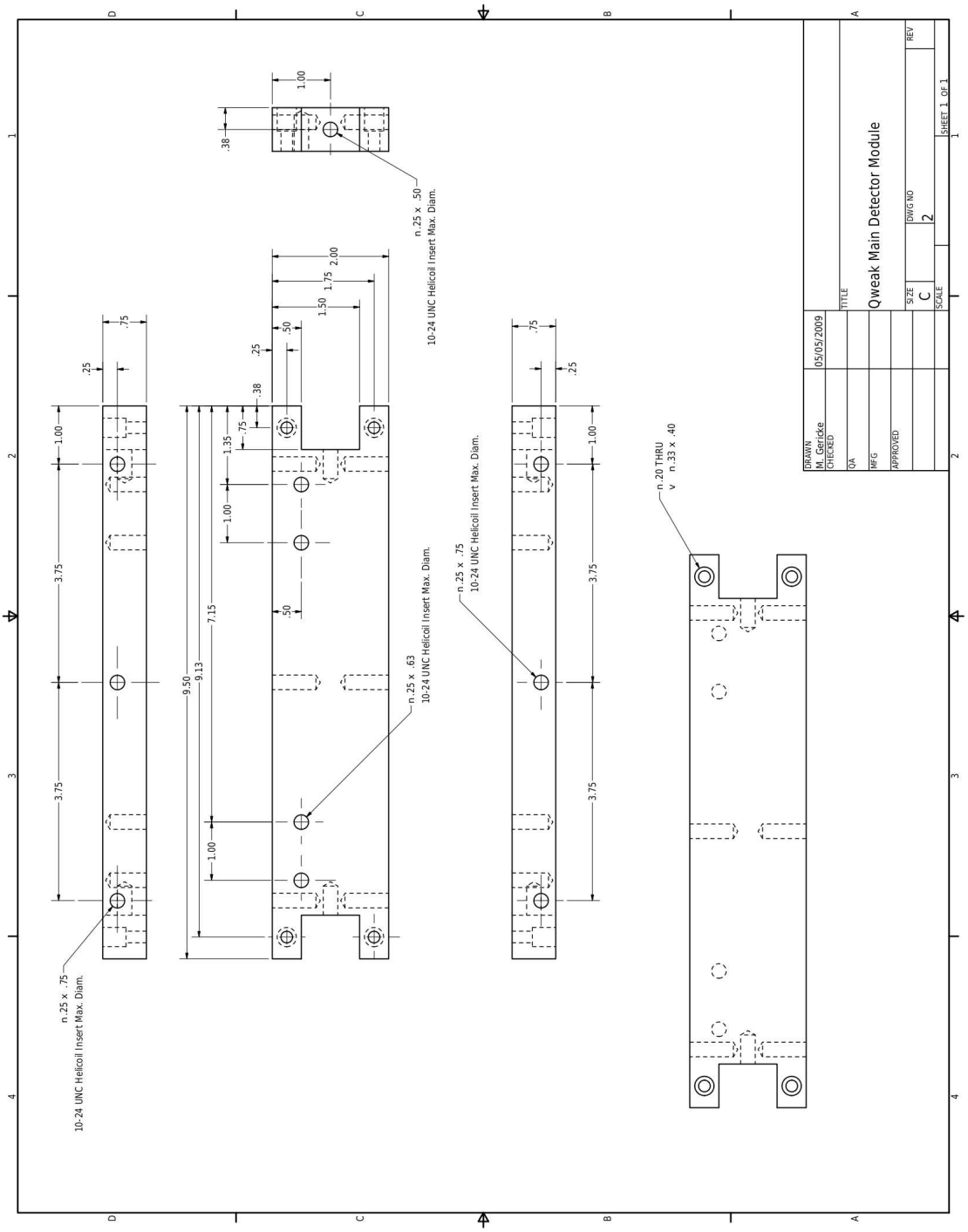

Figure A.10: Radiator box CAD drawing 2 of 10.

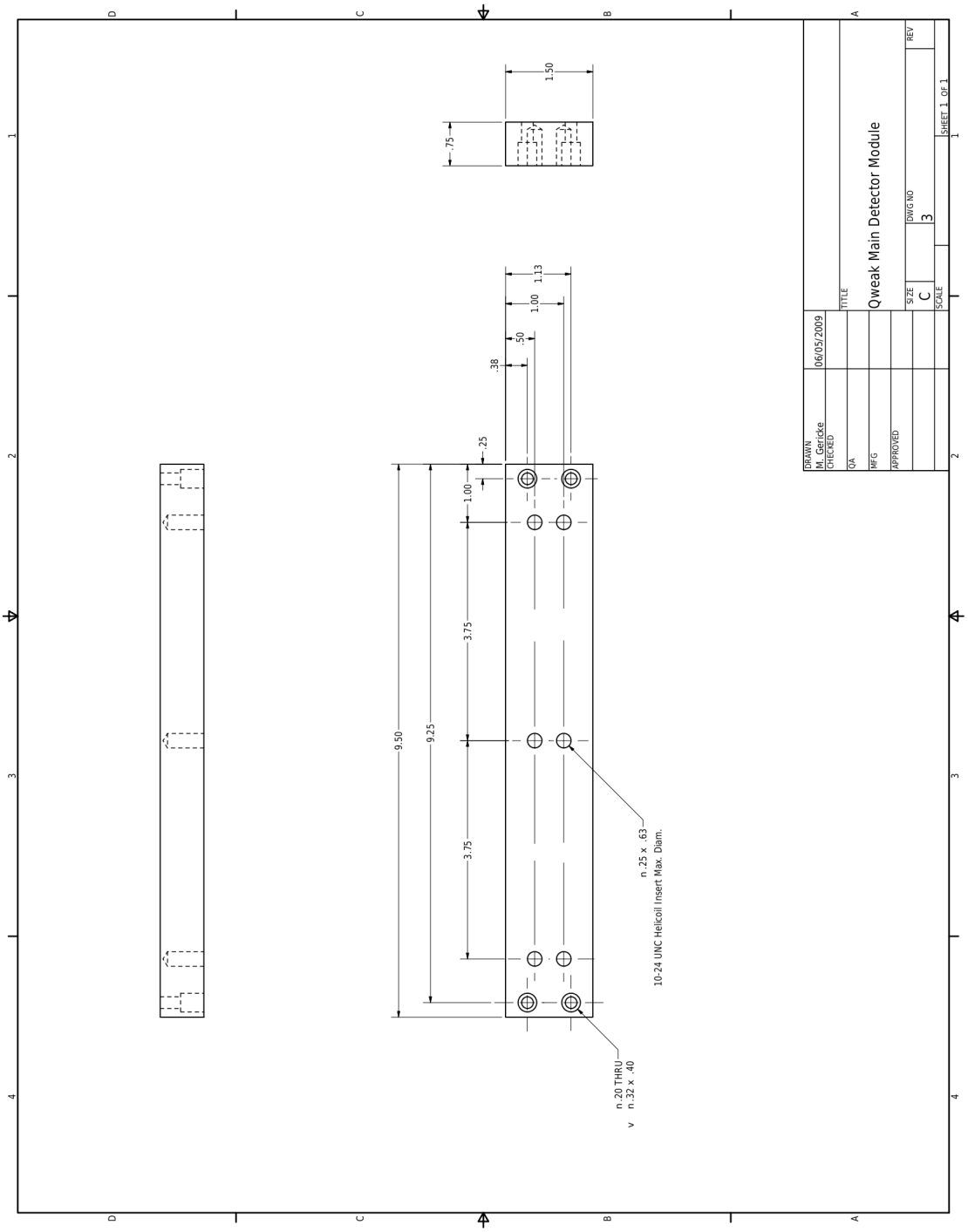

Figure A.11: Radiator box CAD drawing 3 of 10.

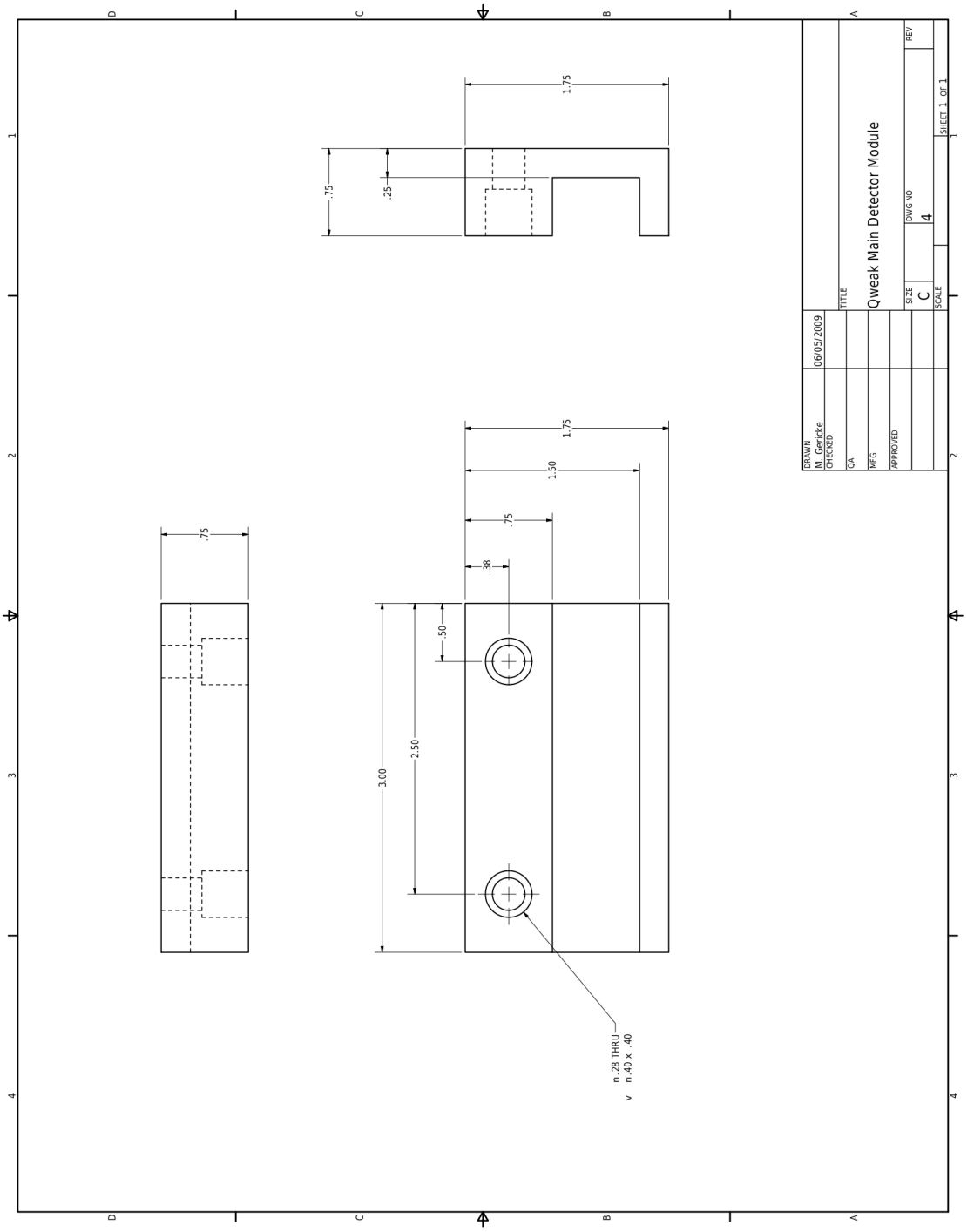

Figure A.12: Radiator box CAD drawing 4 of 10.

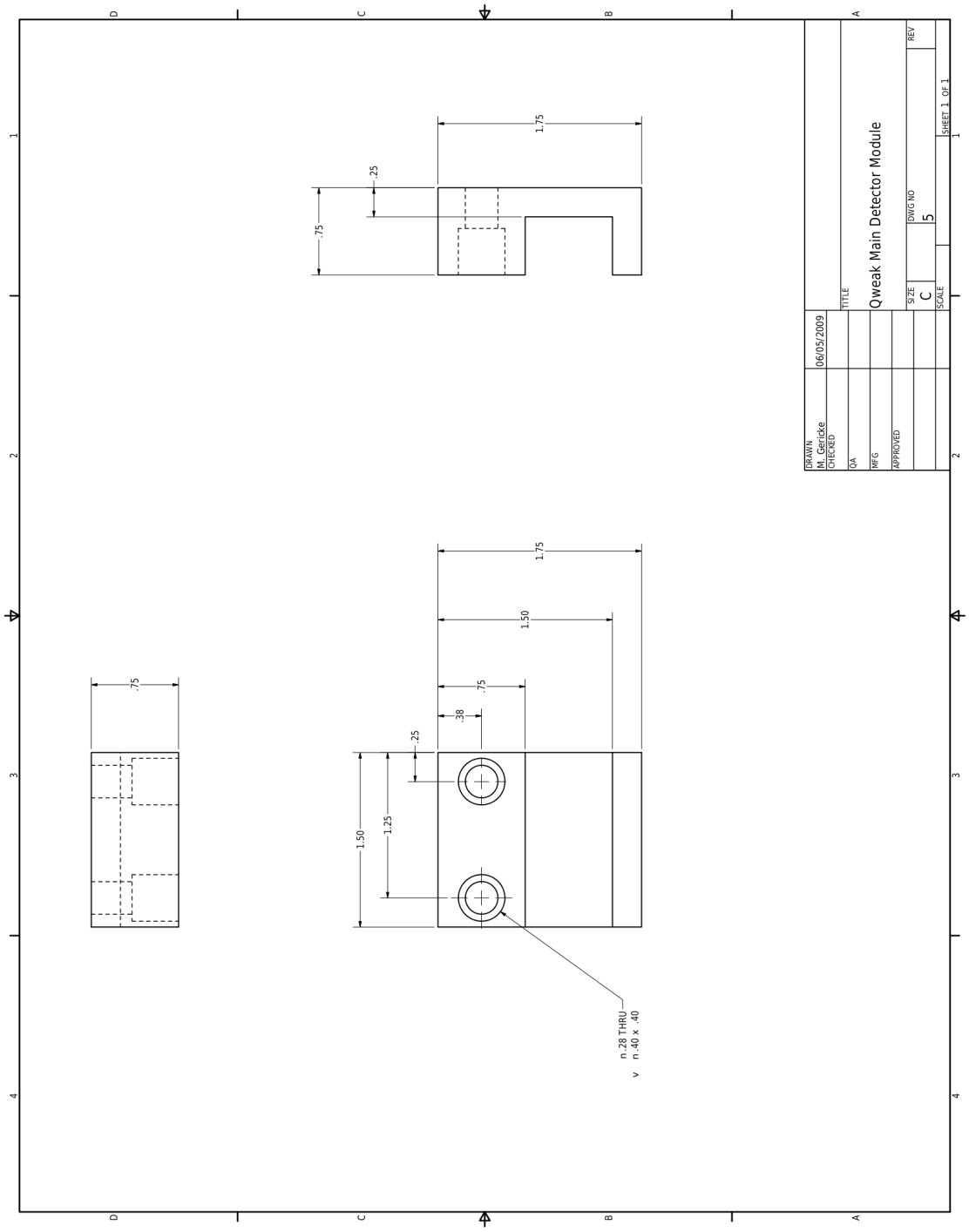

Figure A.13: Radiator box CAD drawing 5 of 10.

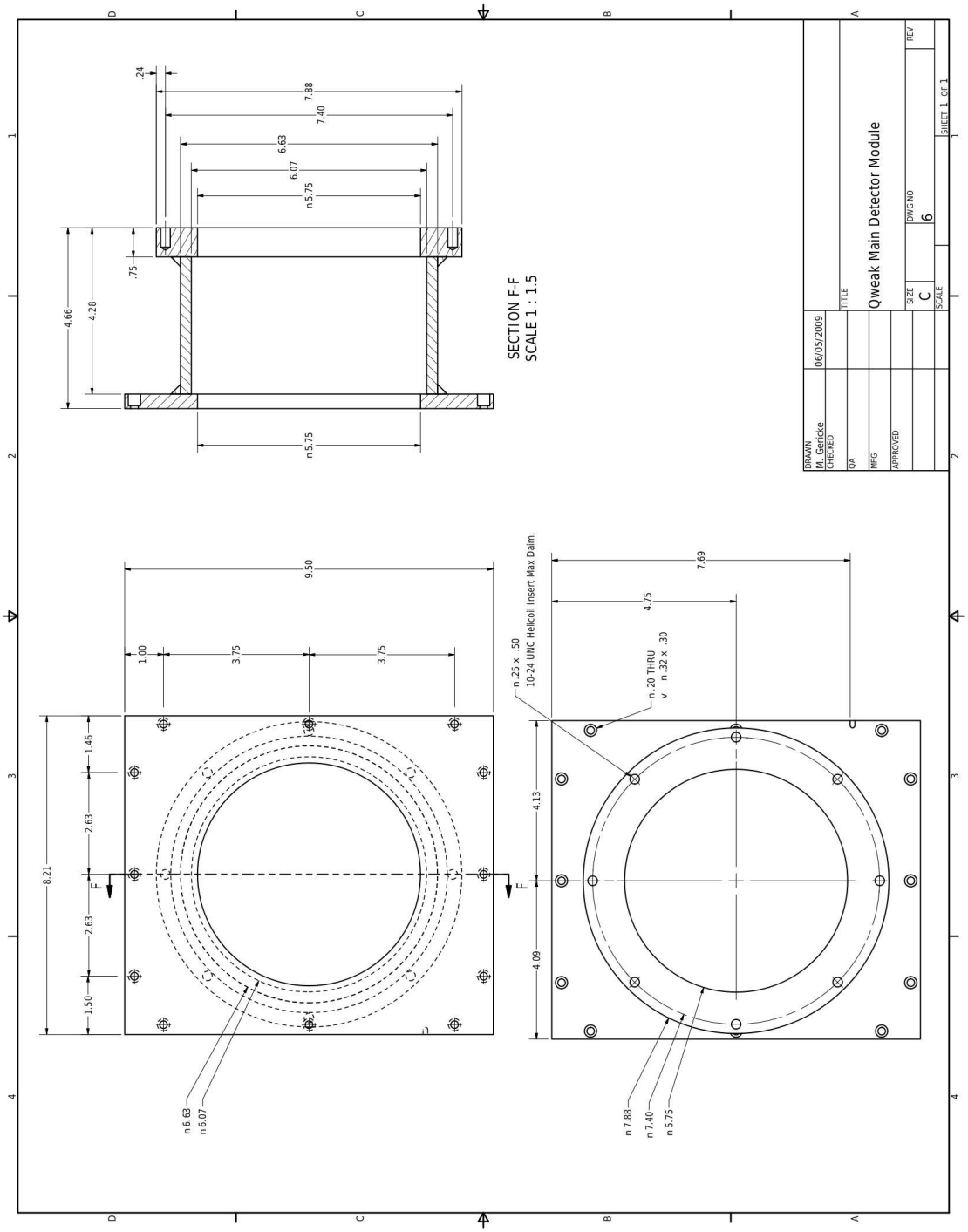

Figure A.14: Radiator box CAD drawing 6 of 10.

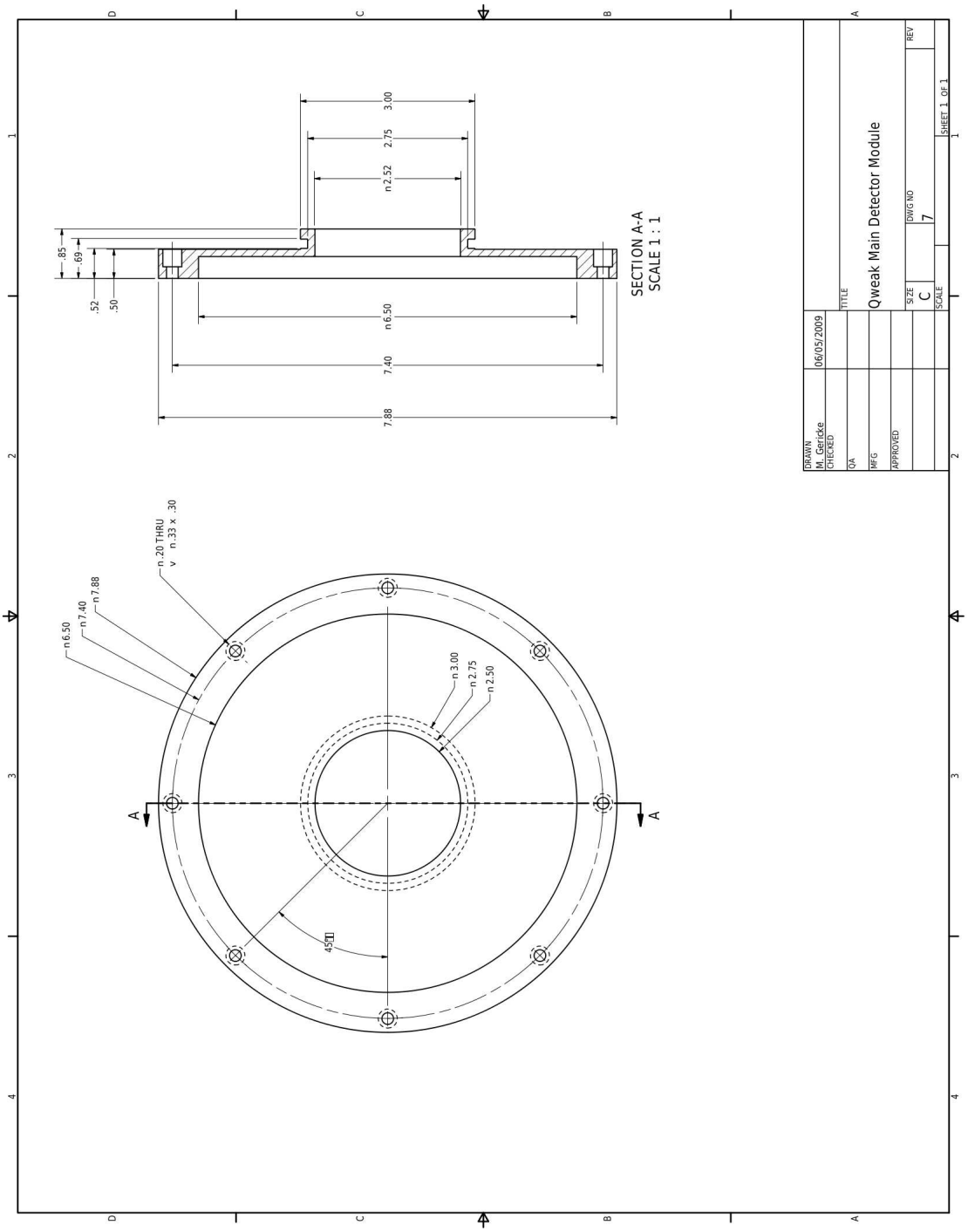

Figure A.15: Radiator box CAD drawing 7 of 10.

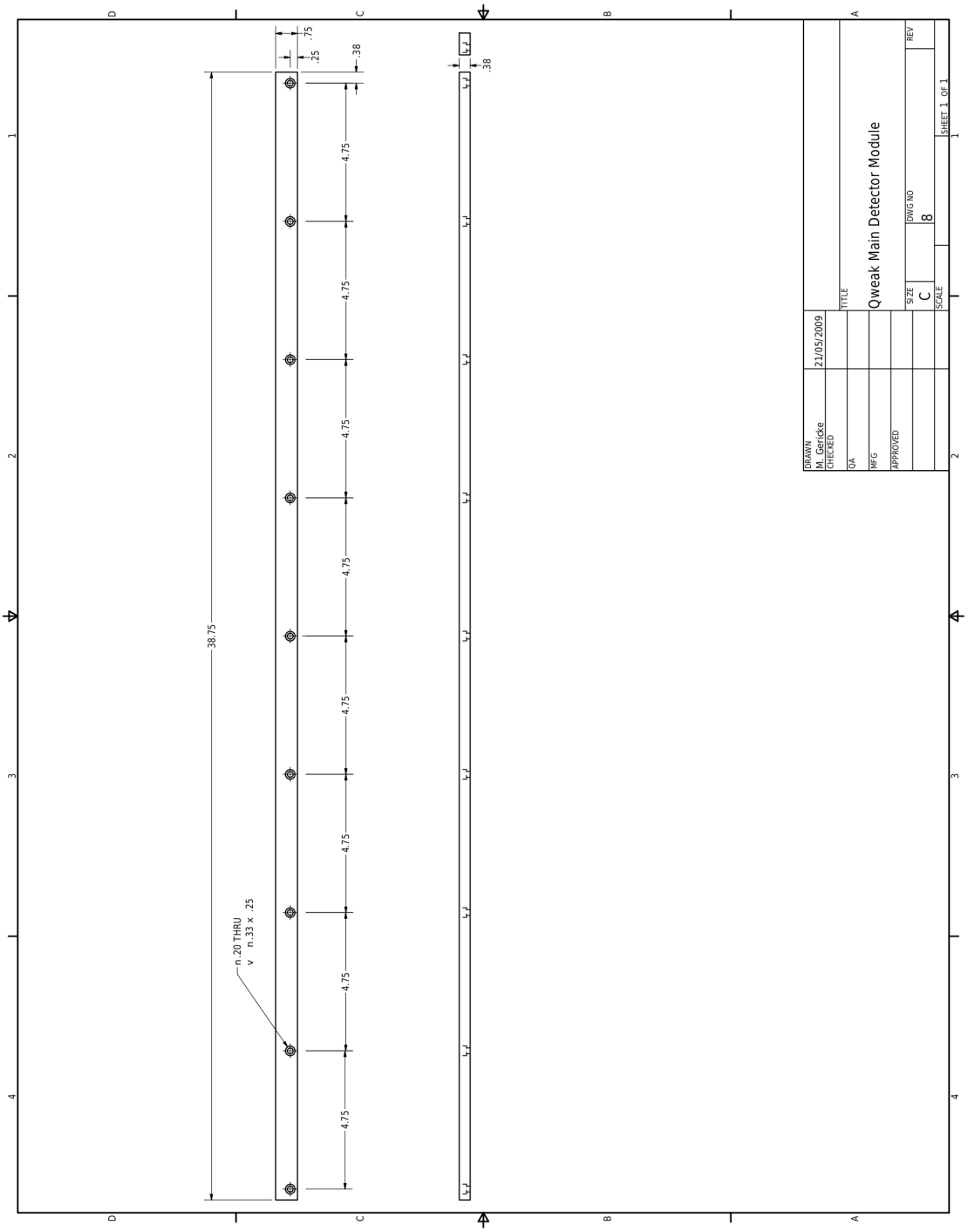

Figure A.16: Radiator box CAD drawing 8 of 10.

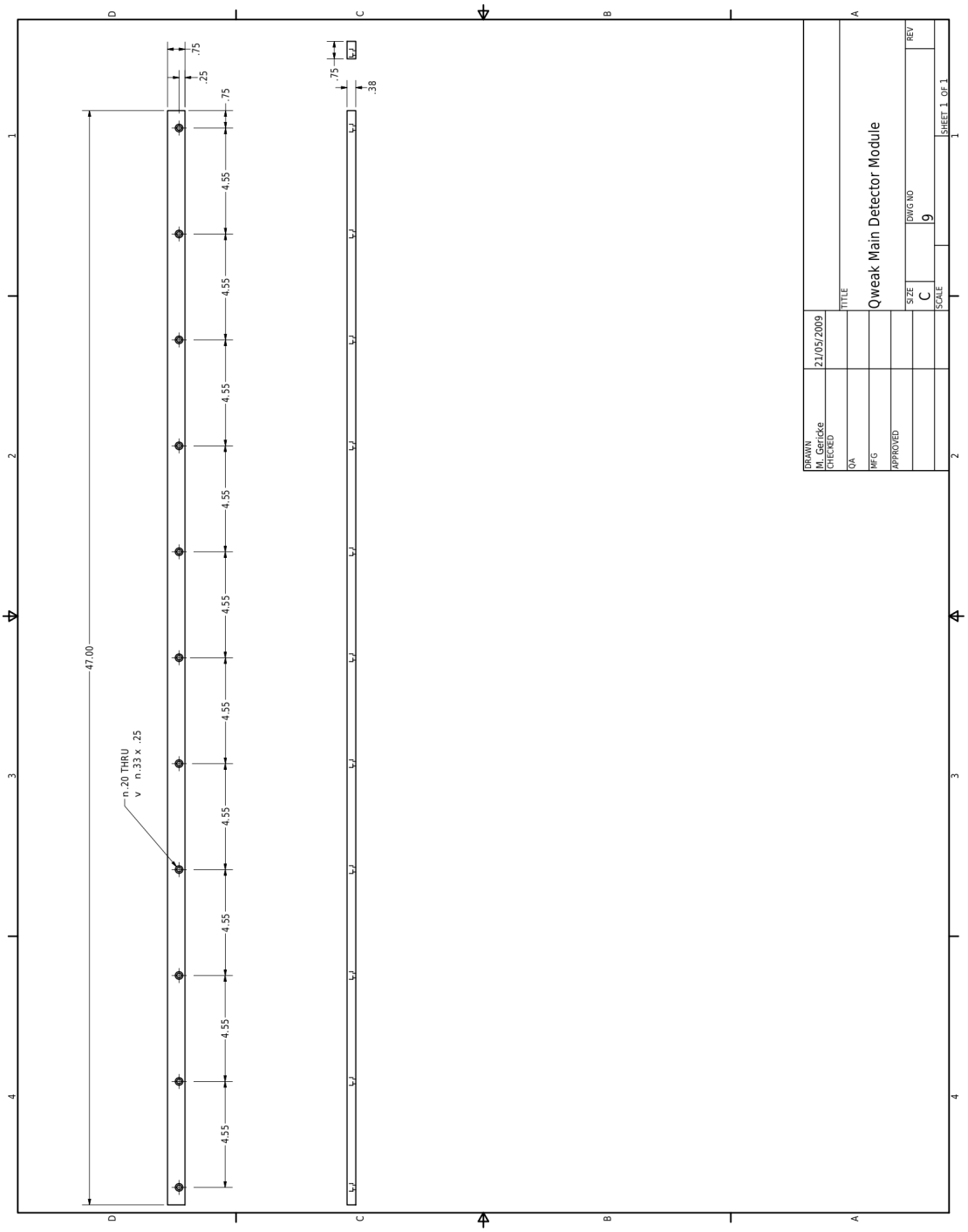

Figure A.17: Radiator box CAD drawing 9 of 10.

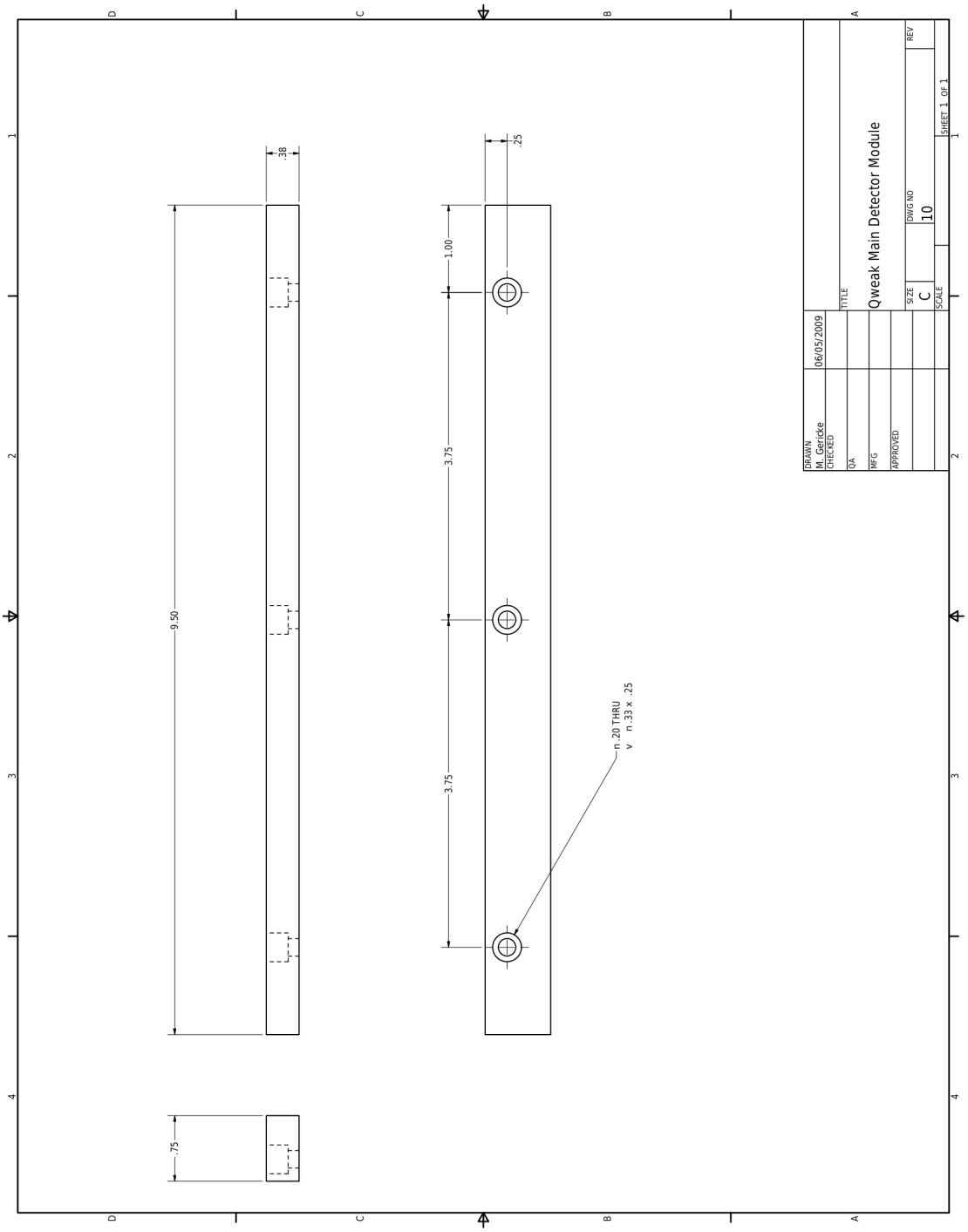

Figure A.18: Radiator box CAD drawing 10 of 10.

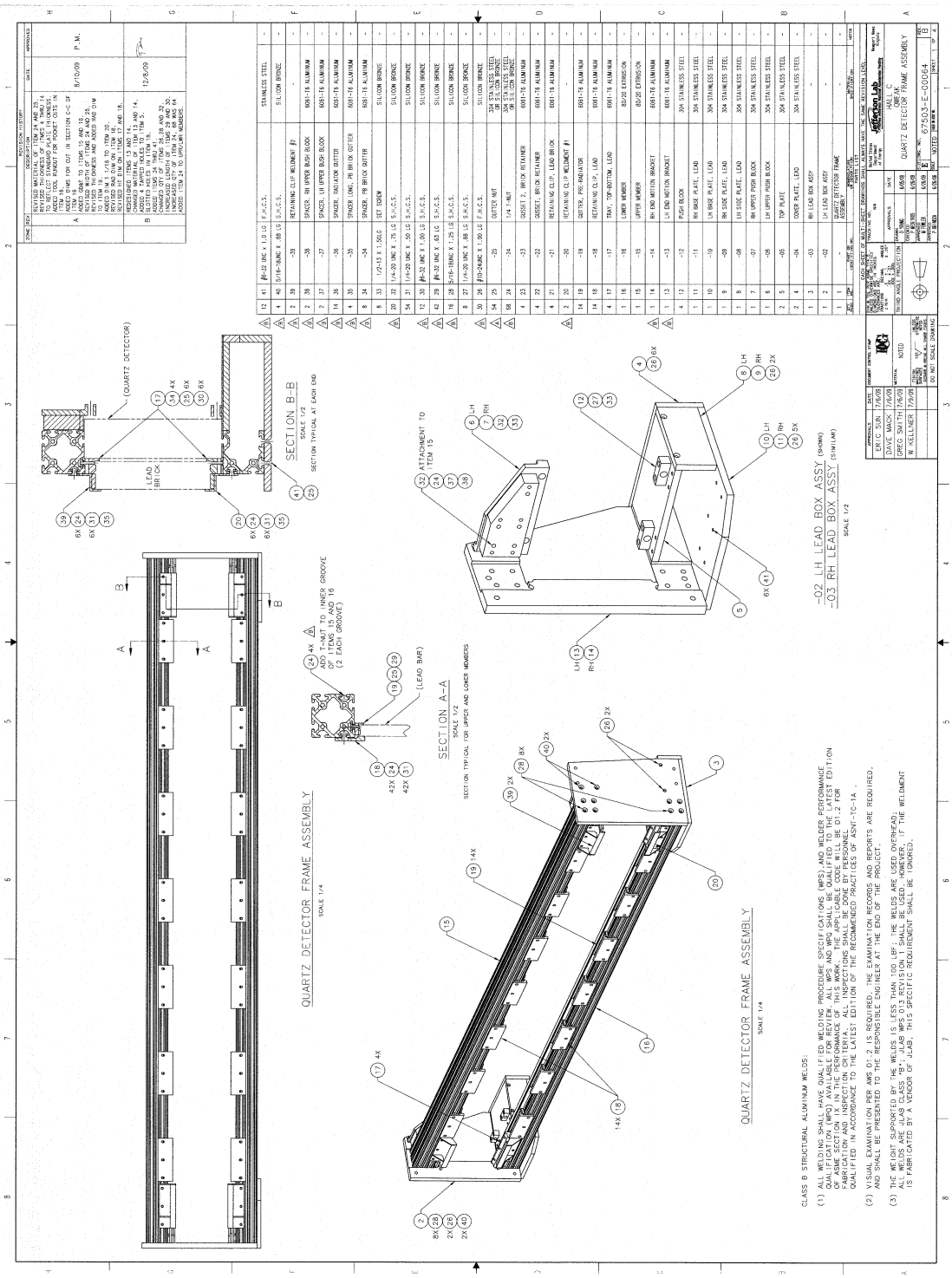

Figure A.19: Exoskeleton CAD drawing 1 of 4.

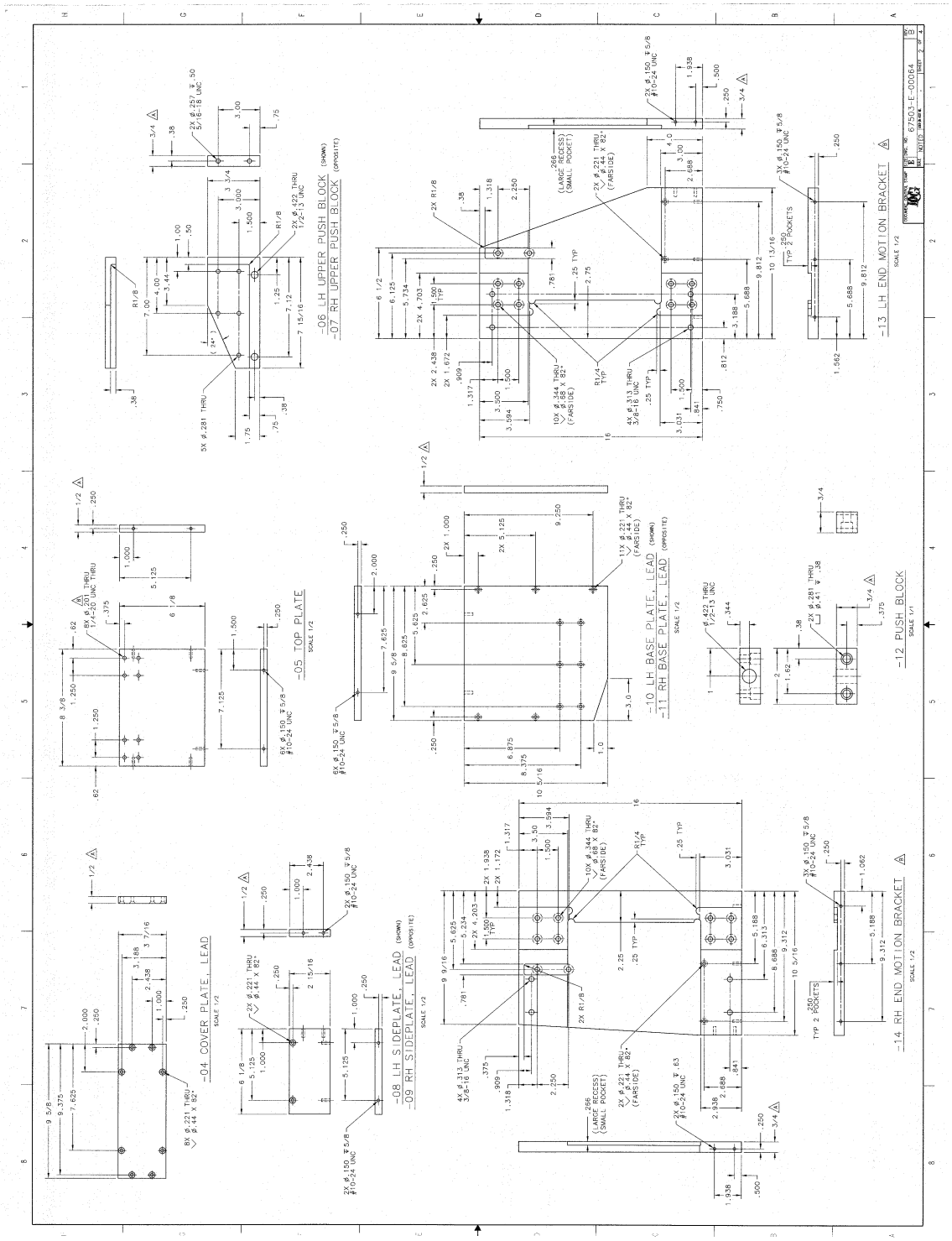

Figure A.20: Exoskeleton CAD drawing 2 of 4.

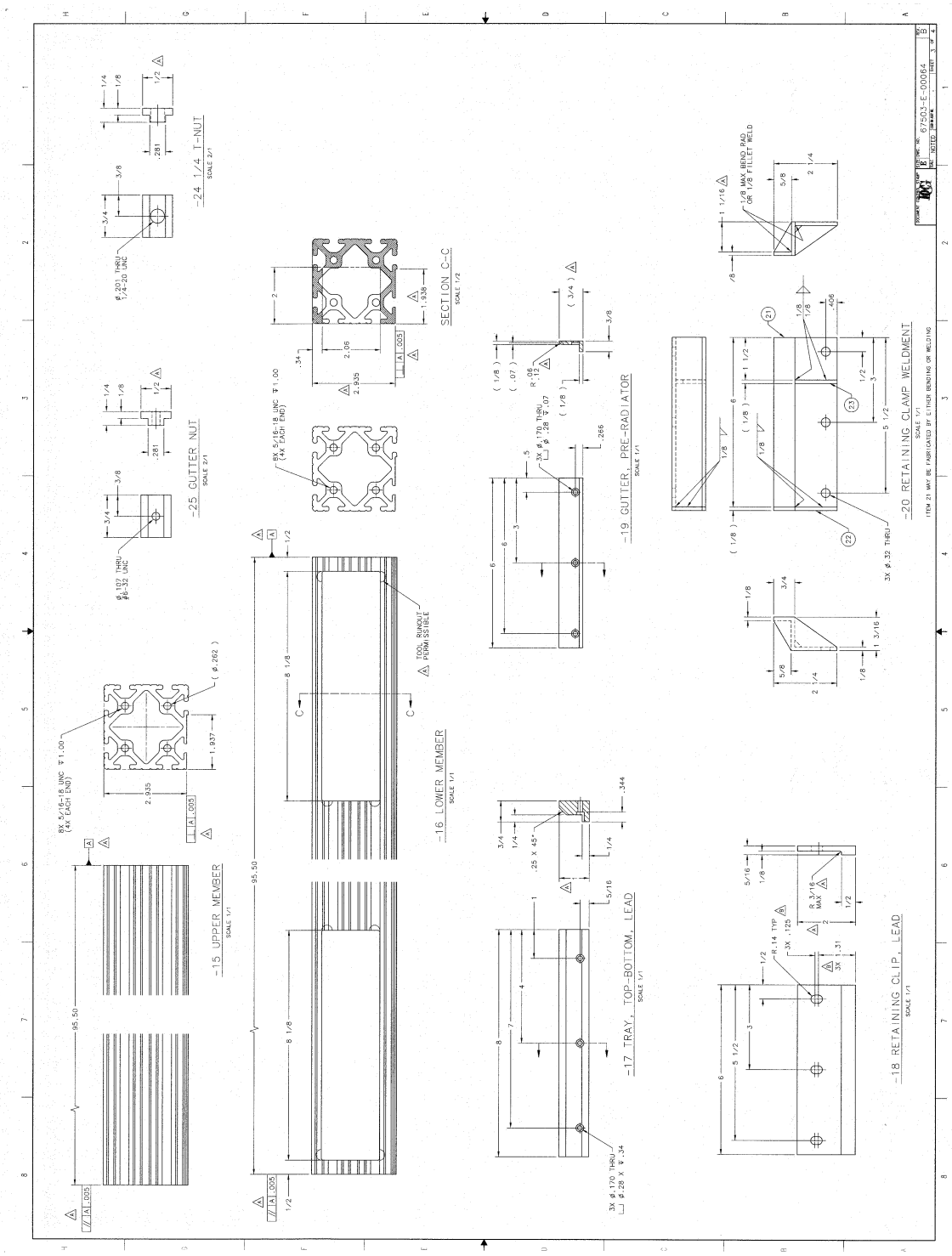

Figure A.21: Exoskeleton CAD drawing 3 of 4.

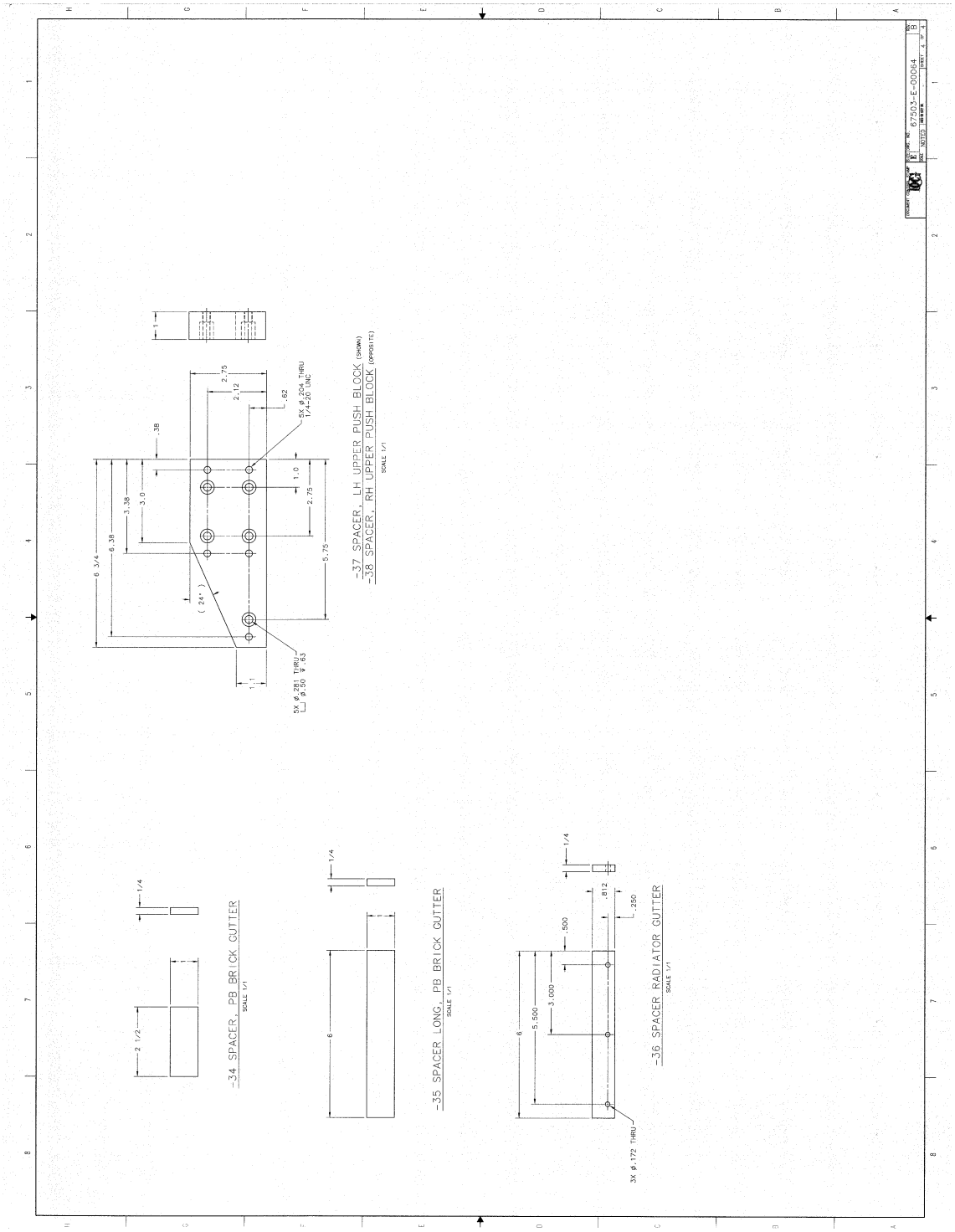

Figure A.22: Exoskeleton CAD drawing 4 of 4.

Appendix B

My Contributions to the Q-weak Experiment

I have been working on several different subsystems of the Q-weak experiment. The following list summarizes my major contributions to the experiment.

- Main Čerenkov detector system:

    1. contributed to design of the main detector,
    2. performed a Geant4 Monte Carlo simulation to study the detector performance,
    3. constructed all 9 main Cerenkov detectors (including one full-sized background detector),
    4. designed and built 3 auxiliary detectors,
    5. designed and built the main detector diagnostic system (LED test system and phase monitor),
    6. built up the main detector electronics chain,
    7. installed the main detectors system,
    8. set up and conducted the main detector cosmic ray tests,

9. conducted the beam tests for the main detectors,
10. completed the main detector commissioning.

- QTOR magnetic spectrometer:
  1. calculated the magnetic field map for the Monte Carlo simulation and track reconstruction program,
  2. performed the QTOR magnetic field mapping at MIT-Bates and at JLab,
  3. contributed to the field mapping data analysis.
- Hall-C Compton polarimeter:
  1. prototyped the first diamond strip detector,
  2. tested the diamond detector and characterized the detector on bench,
  3. prototyped and tested the diamond detector front-end electronics.
- Focal plane scanner:
  1. designed and built the scanner motion control system,
  2. participated in the installation and commissioning of the scanner detector.
- DAQ/analysis:
  1. wrote the main detector class to decode and process the main detector data,
  2. wrote the blinding analysis class to perform the blinding analysis on the asymmetry data,
  3. analyzed a subset of tracking and production data.

Appendix C

The Q-weak Collaboration

Q-weak Collaboration Spokespersons

Carlini, Roger (Principal Investigator)	Thomas Jefferson National Accelerator Facility
Finn, J. Michael	College of William and Mary - (deceased)
Kowalski, Stanley	Massachusetts Institute of Technology
Page, Shelley	University of Manitoba

Q-weak Collaboration Members

Androic, Darko	University of Zagreb
Armstrong, David	College of William and Mary
Asaturyan, Arshak	Yerevan Physics Institute
Averett, Todd	College of William and Mary
Balewski, Jan	Massachusetts Institute of Technology
Beaufait, Joseph	Thomas Jefferson National Accelerator Facility
Beminiwattha, Rakitha	Ohio University
Benesch, Jay	Thomas Jefferson National Accelerator Facility
Benmokhtar, Fatiha	Christopher Newport University
Birchall, James	University of Manitoba

Cates, Gordon	University of Virginia
Cornejo, Juan	College of William and Mary
Covrig, Silviu	Thomas Jefferson National Accelerator Facility
Dalton, Mark	University of Virginia
Davis, Charles	TRIUMF
Deconinck, Wouter	College of William and Mary
Deng, Xiaoyan	University of Virginia
Diefenbach, Juergen	Hampton University
Dow, Karen	Massachusetts Institute of Technology
Dunne, James	Mississippi State University
Dutta, Dipangkar	Mississippi State University
Ent, Rolf	Thomas Jefferson National Accelerator Facility
Erler, Jens	University of Mexico
Falk, Willie	University of Manitoba
Forest, Tony	Idaho State University
Franklin, Wilbur	Massachusetts Institute of Technology
Furic, Miroslav	University of Zagreb
Gaskell, David	Thomas Jefferson National Accelerator Facility
Gericke, Michael	University of Manitoba
Grames, Joseph	Thomas Jefferson National Accelerator Facility
Grimm, Klaus	Louisiana Tech University
Hashemi Shabestari, Mitra	Mississippi State University
Higinbotham, Douglas	Thomas Jefferson National Accelerator Facility
Holtrop, Maurik	University of New Hampshire
Hoskins, Joshua	College of William and Mary

Ihloff, Ernie	Massachusetts Institute of Technology
Johnston, Kathleen	Louisiana Tech University
Jones, Derek	George Washington University
Jones, Donald	University of Virginia
Jones, Mark	Thomas Jefferson National Accelerator Facility
Jones, Richard	University of Connecticut
Joo, Kyungseon	University of Connecticut
Kargiantoulakis, Emmanouil	University of Virginia
Kelsey, James	Massachusetts Institute of Technology
Keppel, Cynthia	Hampton University
King, Paul	Ohio University
Kohl, Michael	Hampton University
Korkmaz, Elie	University of Northern British Columbia
Leacock, John	Virginia Polytechnic Institute and State University
Leckey, John	College of William and Mary
Lee, Anna	Virginia Polytechnic Institute and State University
Lee, Jeong Han	Ohio University and The College of William and Mary
Lee, Lawrence	TRIUMF
Lung, Allison	Thomas Jefferson National Accelerator Facility
Luwani Zurmbonwi, Ndukum	Mississippi State University
MacEwan, Scott	University of Manitoba
Mack, David	Thomas Jefferson National Accelerator Facility
Magee, Joshua	College of William and Mary
Mahurin, Rob	University of Manitoba
Mammei, Juliette	Virginia Polytechnic Institute and State University

Martin, Jeffery	University of Winnipeg
McHugh, Martin	George Washington University
Meekins, David	Thomas Jefferson National Accelerator Facility
Mei, Jiawei	Thomas Jefferson National Accelerator Facility
Michaels, Robert	Thomas Jefferson National Accelerator Facility
Micherdzinska, Anna	George Washington University
Mkrtchyan, Arthur	Yerevan Physics Institute
Mkrtchyan, Hamlet	Yerevan Physics Institute
Munroe, Richard	Christopher Newport University
Myers, Katherine	George Washington University
Narayan, Amrendra	Mississippi State University
Nuruzzaman, nfn	Hampton University
Opper, Allena	George Washington University
Pan, Jie	University of Manitoba
Paschke, Kent	University of Virginia
Phillips, Sarah	University of New Hampshire
Pitt, Mark	Virginia Polytechnic Institute and State University
Poelker, B.	Thomas Jefferson National Accelerator Facility
Rajotte, Jean-Francois	Massachusetts Institute of Technology
Ramsay, W. Desmond	University of Manitoba
Ramsey-Musolf, Michael	University of Wisconsin-Madison
Roche, Julie	Ohio University
Sawatzky, Bradley	Thomas Jefferson National Accelerator Facility
Seva, Tomislav	University of Zagreb
Silwal, Rupesh	University of Virginia

Simicevic, Neven	Louisiana Tech University
Smith, Gregory	Thomas Jefferson National Accelerator Facility
Smith, Timothy	Dartmouth College
Solvignon, Patricia	Thomas Jefferson National Accelerator Facility
Souder, Paul	Syracuse University
Spayde, Damon	Hendrix College
Subedi, Adesh	Mississippi State University
Subedi, Ramesh	George Washington University
Suleiman, Riad	Thomas Jefferson National Accelerator Facility
Tsentalovich, Evgeni	Massachusetts Institute of Technology
Tvaskis, Vladas	University of Winnipeg
van Oers, W.T.H.	University of Manitoba
Waidyawansa, Buddhini	Ohio University
Wang, Diancheng	University of Virginia
Wang, Peiqing	University of Manitoba
Wells, Steven	Louisiana Tech University
Wood, Stephen	Thomas Jefferson National Accelerator Facility
Yang, Siyuan	College of William and Mary
Young, Ross	The University of Adelaide
Zhamkochyan, Simon	Yerevan Physics Institute
Zhao, Zhiwen	University of Virginia
Zheng, Xiaochao	University of Virginia
Zou, David	Massachusetts Institute of Technology

Figure C.1: Q-weak Collaboration picture (TRIUMF, 2008).

Bibliography

[Abbiendi et al., 2001] Abbiendi, G. et al. (2001). Precise determination of the Z resonance parameters at LEP: 'Zedometry'. *Eur. Phys. J.*, C19:587–651.

[Abbiendi et al., 2004] Abbiendi, G. et al. (2004). Tests of the standard model and constraints on new physics from measurements of fermion-pair production at 189-209 GeV at LEP. *European Physical Journal C*, 33(2):173–212.

[Abbiendi et al., 2006] Abbiendi, G. et al. (2006). ALEPH, DELPHI, L3, OPAL and SLD Collaborations, LEP electroweak working group, SLD electroweak and heavy flavour groups. *Phys. Rept*, 427:257.

[Abe et al., 2000a] Abe, K. et al. (2000a). First direct measurement of the parity-violating coupling of the Z^0 to the s quark. *Phys. Rev. Lett.*, 85(24):5059–5063.

[Abe et al., 2000b] Abe, K. et al. (2000b). High-precision measurement of the left-right Z boson cross-section asymmetry. *Phys. Rev. Lett.*, 84(26):5945–5949.

[Abe et al., 2001] Abe, K. et al. (2001). Improved direct measurement of leptonic coupling asymmetries with polarized Z bosons. *Phys. Rev. Lett.*, 86(7):1162–1166.

[Abreu, 1993] Abreu, P. (1993). DELPHI collaboration: A measurement of B meson production and lifetime using Dl^- events in Z^0 decays. *Zeitschrift für Physik C Particles and Fields*, 57:181–181.

[Acha et al., 2007] Acha, A., Aniol, K., Armstrong, D., Arrington, J., Averett, T., Bailey, S., Barber, J., Beck, A., Benaoum, H., Benesch, J., et al. (2007). Precision measurements of the nucleon strange form factors at $Q^2 \sim 0.1$ GeV^2. *Physical review letters*, 98(3):32301.

[Ackerstaff, 1997] Ackerstaff, K. (1997). Measurement of the branching fractions and forward-backward asymmetries of the Z^0 into light quarks. *Zeitschrift für Physik C Particles and Fields*, 76(3):387–400.

[Adam et al., 2005] Adam, I. et al. (2005). The DIRC particle identification system for the BaBar experiment. *Nucl. Instrum. Meth.*, A538:281–357.

[Anderson, 2006] Anderson, M. (2006). Results from the 1st and 2nd prototype low gain bases (qweak document 604-v1). Technical report, JLab.

[Anthony et al., 2004] Anthony, P. L. et al. (2004). Observation of parity nonconservation in Møller scattering. *Physical review letters*, 92(18):181602.

[Anthony et al., 2005] Anthony, P. L. et al. (2005). Precision measurement of the weak mixing angle in Møller scattering. *Phys. Rev. Lett.*, 95(8):081601.

[Armstrong et al., 2005] Armstrong, D., Arvieux, J., Asaturyan, R., Averett, T., Bailey, S., Batigne, G., Beck, D., Beise, E., Benesch, J., Bimbot, L., et al. (2005). Strange-quark contributions to parity-violating asymmetries in the forward $G0$ electron-proton scattering experiment. *Physical review letters*, 95(9):92001.

[Armstrong et al., 2007] Armstrong, D., Arvieux, J., Asaturyan, R., Averett, T., Bailey, S., Batigne, G., Beck, D., Beise, E., Benesch, J., Bimbot, L., et al. (2007). Transverse beam spin asymmetries in forward-angle elastic electron-proton scattering. *Physical review letters*, 99(9):92301.

[Armstrong et al., 2003] Armstrong, D., Moffit, B., and Suleiman, R. (2003). Target density fluctuations and bulk boiling in the Hall A cryotarget. Technical Report JLAB-TN-03-017.

[Arnaudon et al., 1993] Arnaudon, L., Assmann, R., Billan, J., Birr, W., Blondel, A., Bobbink, G., Bordry, F., Burkhardt, H., Crozon, M., Dehning, B., et al. (1993). Measurement of the mass of the Z boson and the energy calibration of LEP. *Physics Letters B*, 307:187–193.

[Barry, 1991] Barry, W. (1991). A general analysis of thin wire pickups for high frequency beam position monitors. *Nuclear Instruments and Methods in Physics Research Section A: Accelerators, Spectrometers, Detectors and Associated Equipment*, 301(3):407–416.

[Benesch, 2009] Benesch, J. (2009). Beamline drawings and element names for Qweak (qweak document 1070-v2). Technical report, JLab.

[Bennett and Wieman, 1999] Bennett, S. C. and Wieman, C. E. (1999). Measurement of the $6s \rightarrow 7s$ transition polarizability in atomic cesium and an improved test of the standard model. *Phys. Rev. Lett.*, 82(12):2484–2487.

[Birchall, 1988] Birchall, J. (1988). Reduction of the effects of transverse polarization in a measurement of parity violation in proton-proton scattering at 230 MeV. *Canadian Journal of Physics*, 66:530.

[Bjorken and Drell, 1998] Bjorken, J. D. and Drell, S. D. (1998). *Relativistic Quantum Mechanics*. McGraw-Hill Science/Engineering/Math, 1st edition.

[Blunden et al., 2005] Blunden, P. G., Melnitchouk, W., and Tjon, J. A. (2005). Two-photon exchange in elastic electron-nucleon scattering. *Phys. Rev. C*, 72(3):034612.

[Cohen-Tanugi et al., 2003] Cohen-Tanugi, J., Convery, M., Ratcliff, B., Sarazin, X., Schwiening, J., and Va'vra, J. (2003). Optical properties of the DIRC fused silica Cherenkov radiator. *Nuclear Instruments and Methods in Physics Research Section A: Accelerators, Spectrometers, Detectors and Associated Equipment*, 515(3):680–700.

[Commins and Bucksbaum, 1983] Commins, E. D. and Bucksbaum, P. (1983). *Weak Interactions of Leptons and Quarks*. Cambridge University Press, Cambridge.

[Czarnecki and Marciano, 2000] Czarnecki, A. and Marciano, W. J. (2000). Polarized Møller scattering asymmetries. *International Journal of Modern Physics A*, 15:2365.

[Deconinck, 2009] Deconinck, W. (2009). Q-weak tracking software (qweak document 1094-v2). Technical report.

[Ecklund et al., 2001] Ecklund, S., Field, C., and Mazaheri, G. (2001). A fast luminosity monitor system for PEP II. *Nuclear Instruments and Methods in Physics Research Section A: Accelerators, Spectrometers, Detectors and Associated Equipment*, 463(1-2):68–76.

[Erler et al., 2003] Erler, J., Kurylov, A., and Ramsey-Musolf, M. J. (2003). Weak charge of the proton and new physics. *Phys. Rev. D*, 68(1):016006.

[Erler and Ramsey-Musolf, 2005a] Erler, J. and Ramsey-Musolf, M. (2005a). Low energy tests of the weak interaction, prog. *Part. Nucl. Phys*, 54:351.

[Erler and Ramsey-Musolf, 2005b] Erler, J. and Ramsey-Musolf, M. J. (2005b). Weak mixing angle at low energies. *Phys. Rev. D*, 72(7):073003.

[Forest, 2003] Forest, T. (2003). Region 1 vertex tracker (qweak document 54-v1). Technical report, JLab.

[Frank and Tamm, 1937] Frank, M. and Tamm, I. (1937). Coherent radiation of fast electrons. In *Dokl. AN SSSR*, volume 14, pages 109–112.

[Gaskell et al., 2007] Gaskell, D., Meekins, D., and Yan, C. (2007). New methods for precision Møller polarimetry. *The European Physical Journal A - Hadrons and Nuclei*, 32:561–564. 10.1140/epja/i2006-10438-4.

[Gericke, 2005] Gericke, M. (2005). Excess noise as a function of detector thickness (qweak document 231-v1). Technical report, JLab.

[Gericke, 2006a] Gericke, M. (2006a). Diode mode saturation and linearity tests of the Qweak main Cherenkov detector PMTs (qweak document 534-v1). Technical report, JLab.

[Gericke, 2006b] Gericke, M. (2006b). Selection of light guide geometry for the Q-weak main detectors (q-weak document 533-v1)). Technical report, JLab.

[Gericke, 2009] Gericke, M. (2009). Manitoba radiator box drawings v3 (qweak document 981-v1). Technical report, JLab.

[Glesener, 2005] Glesener, L. (2005). Target density fluctuation monitoring in the HAPPEX helium parity violation experiment. Technical report, JLab.

[Gorchtein et al., 2011] Gorchtein, M., Horowitz, C., and Ramsey-Musolf, M. (2011). Model-dependence of the γz dispersion correction to the parity-violating asymmetry in elastic ep scattering. *Arxiv preprint arXiv:1102.3910*.

[Gorchtein and Horowitz, 2009] Gorchtein, M. and Horowitz, C. J. (2009). Dispersion γz-box correction to the weak charge of the proton. *Phys. Rev. Lett.*, 102(9):091806.

[Greiner and Müller, 2001] Greiner, W. and Müller, B. (2001). *Quantum mechanics: symmetries*. Springer-Verlag, Berlin Heidelberg, fourth edition.

[Griffiths, 2008] Griffiths, D. (2008). *Introduction to Elementary Particles*. Textbook physics. Wiley-VCH, Weinheim, 2nd edition.

[Gross and Wilczek, 1973] Gross, D. J. and Wilczek, F. (1973). Ultraviolet behavior of non-abelian gauge theories. *Phys. Rev. Lett.*, 30(26):1343–1346.

[Halzen and Martin, 1984] Halzen, F. and Martin, A. D. (1984). *Quarks and Leptons: Introductory Course in Modern Particle Physics*. John Wiley & Sons, international edition.

[Hanneke et al., 2008] Hanneke, D., Fogwell, S., and Gabrielse, G. (2008). New measurement of the electron magnetic moment and the fine structure constant. *Phys. Rev. Lett.*, 100(12):120801.

[Hauger et al., 2001] Hauger, M. et al. (2001). A high-precision polarimeter. *Nuclear Instruments and Methods in Physics Research Section A: Accelerators, Spectrometers, Detectors and Associated Equipment*, 462(3):382–392.

[Hecht, 2002] Hecht, E. (2002). *Optics*. Addison Wesley, 4th edition.

[Kaufman, 2007] Kaufman, L. J. (2007). Transverse beam asymmetries measured from 4He and hydrogen targets. *The European Physical Journal A - Hadrons and Nuclei*, 32:501–503. 10.1140/epja/i2006-10423-y.

[Kazimi et al., 1995] Kazimi, R. et al. (1995). Precision intercomparison of beam current monitors at CEBAF. In *Particle Accelerator Conference, 1995., Proceedings of the 1995*, volume vol.4, pages 2610–2612.

[Langacker, 2009] Langacker, P. (2009). *The Standard Model and Beyond*. High Energy Physics, Cosmology and Gravitation. Taylor & Francis.

[Lee and Yang, 1956] Lee, T. and Yang, C. (1956). Question of parity conservation in weak interactions. *Physical Review*, 104(1):254.

[Leo, 1994] Leo, W. R. (1994). *Techniques for Nuclear and Particle Physics Experiments*. Springer-Verlag, 2nd edition.

[Londergan and Thomas, 2005] Londergan, J. and Thomas, A. (2005). Implications of current constraints on parton charge symmetry. *Journal of Physics G: Nuclear and Particle Physics*, 31:1151.

[Maas et al., 2004] Maas, F., Achenbach, P., Aulenbacher, K., Baunack, S., Capozza, L., Diefenbach, J., Grimm, K., Imai, Y., Hammel, T., Von Harrach, D., et al. (2004). Measurement of strange-quark contributions to the nucleon's form factors at $Q^2 = 0.230$ (GeV/c)^2. *Physical review letters*, 93(2):22002.

[Maas et al., 2005a] Maas, F., Aulenbacher, K., Baunack, S., Capozza, L., Diefenbach, J., Gläser, B., Hammel, T., Von Harrach, D., Imai, Y., Kabuß, E., et al. (2005a). Evidence for strange-quark contributions to the nucleon's form factors at $Q^2 = 0.108$ (GeV/c)^2. *Physical review letters*, 94(15):152001.

[Maas et al., 2005b] Maas, F. E., Aulenbacher, K., Baunack, S., Capozza, L., Diefenbach, J., Gläser, B., Imai, Y., Hammel, T., von Harrach, D., Kabuß, E.-M., Kothe, R., Lee, J. H., Sanchez-Lorente, A., Schilling, E., Schwaab, D., Stephan, G., Weber, G., Weinrich, C., Altarev, I., Arvieux, J., Elyakoubi, M., Frascaria, R., Kunne, R., Morlet, M., Ong, S., Vandewiele, J., Kowalski, S., Suleiman, R., and Taylor, S. (2005b). Measurement of the transverse beam spin asymmetry in elastic electron-proton scattering and the inelastic contribution to the imaginary part of the two-photon exchange amplitude. *Phys. Rev. Lett.*, 94(8):082001.

[MacEwan, 2010] MacEwan, S. (2010). Gain tests for current mode PMT bases (qweak document 1154-v2). Technical report, JLab.

[Mack, 2002] Mack, D. (2002). A quartz Cerenkov detector (qweak document 6-v1). Technical report, JLab.

[Mack, 2004] Mack, D. (2004). Non-linearity specification for the Qweak detector chain (qweak document 172-v1). Technical report, JLab.

[Mack, 2005] Mack, D. (2005). PMT selection and prototype voltage dividers for the Qweak Cerenkov detector (qweak document 221-v1). Technical report, JLab.

[Mack, 2006] Mack, D. (2006). Irradiation test of the TRIUMF preamplifier (qweak document 529-v1). Technical report, JLab.

[Mack, 2007] Mack, D. (2007). Status of the Qweak main detector (qweak document 649-v1). Technical report, JLab.

[Mandl and Shaw, 1984] Mandl, F. and Shaw, G. (1984). *Quantum Field Theory*. John Wiley & Sons Inc.

[Marciano and Sirlin, 1983] Marciano, W. J. and Sirlin, A. (1983). Radiative corrections to atomic parity violation. *Phys. Rev. D*, 27(3):552–556.

[Marciano and Sirlin, 1984] Marciano, W. J. and Sirlin, A. (1984). Some general properties of the $O(\alpha)$ corrections to parity violation in atoms. *Phys. Rev. D*, 29(1):75–88.

[Martin and Shaw, 2008] Martin, B. and Shaw, G. (2008). *Particle physics*. John Wiley & Sons Inc.

[Martin et al., 2009] Martin, J. W., Dutta, D., Narayan, A., and Wang, P. (2009). Diamond detectors for Compton polarimetry. *AIP Conference Proceedings*, 1182(1):623–626.

[Maruyama et al., 1992] Maruyama, T., Garwin, E. L., Prepost, R., and Zapalac, G. H. (1992). Electron-spin polarization in photoemission from strained GaAs grown on $GaAs1 - x\,Px$. *Phys. Rev. B*, 46(7):4261–4264.

[Miller, 1998] Miller, G. A. (1998). Nucleon charge symmetry breaking and parity violating electron proton scattering. *Phys. Rev.*, C57:1492–1505.

[Müller, 1972] Müller, D. (1972). Electron showers of high primary energy in lead. *Phys. Rev. D*, 5(11):2677–2683.

[Musolf et al., 1994] Musolf, M., Donnelly, T., Dubach, J., Pollock, S., Kowalski, S., and Beise, E. (1994). Intermediate-energy semileptonic probes of the hadronic neutral current. *Physics Reports*, 239(1-2):1–178.

[Nakamura et al., 2010] Nakamura, K. et al. (2010). Review of particle physics. *Journal of Physics G: Nuclear and Particle Physics*, 37:075021.

[Page et al., 2006] Page, S. A. et al. (2006). The Qweak experiment at Jefferson Laboratory. In de Jager, K. et al., editors, *From parity violation to hadronic structure and more*, Berlin. Springer.

[Pan, 2010] Pan, J. (2010). Momentum determination in QTR (qweak document 1171-v1). Technical report, JLab.

[Pierce et al., 1980] Pierce, D., Celotta, R., Wang, G., Unertl, W., Galejs, A., Kuyatt, C., and Mielczarek, S. (1980). The GaAs spin polarized electron source. *Review of Scientific Instruments*, 51(4):478–499.

[Porsev et al., 2009] Porsev, S., Beloy, K., and Derevianko, A. (2009). Precision determination of electroweak coupling from atomic parity violation and implications for particle physics. *Physical review letters*, 102(18):181601.

[Powers, 1998] Powers, T. (1998). Improvement of the noise figure of the CEBAF switched electrode electronics BPM system. *AIP Conference Proceedings*, 451(1):256–265.

[Prepost and Maruyama, 1995] Prepost, R. and Maruyama, T. (1995). Advances in polarized electron sources. *Annual Review of Nuclear and Particle Science*, 45(1):41–88.

[Prescott et al., 1979] Prescott, C., Atwood, W., Cottrell, R., Destaebler, H., Garwin, E., Gonidec, A., Miller, R., Rochester, L., Sato, T., Sherden, D., et al. (1979). Further measurements of parity non-conservation in inelastic electron scattering. *Physics Letters B*, 84(4):524–528.

[Qattan et al., 2005] Qattan, I. A. et al. (2005). Precision Rosenbluth measurement of the proton elastic form factors. *Phys. Rev. Lett.*, 94(14):142301.

[Qweak-Collaboration, 2004] Qweak-Collaboration (2004). The Q-Weak experiment: A search for new physics at the TeV scale via a measurement of the proton's weak charge. http://www.jlab.org/qweak/. Proposal JLab E02-020.

[Qweak-Collaboration, 2007] Qweak-Collaboration (2007). The Q-Weak experiment: A search for new physics at the TeV scale via a measurement of the proton's weak charge. http://www.jlab.org/qweak/. Proposal JLab E02-020.

[Rajotte, 2011] Rajotte, J.-F. (2011). Helicity-correlated beam properties (qweak document 1419-v2). Technical report, JLab.

[Ramsay, 2006] Ramsay, D. (2006). Current mode electronics for the Qweak experiment (qweak document 552-v1). Technical report, JLab.

[Ramsey-Musolf, 1999] Ramsey-Musolf, M. J. (1999). Low-energy parity-violation and new physics. *Phys. Rev. C*, 60(1):015501.

[Rislow and Carlson, 2010] Rislow, B. and Carlson, C. (2010). Gamma-z box contributions to parity violating elastic ep scattering. *Arxiv preprint arXiv:1011.2397*.

[Rubbia, 1985] Rubbia, C. (1985). Experimental observation of the intermediate vector bosons W^+, W^-, and Z^0. *Reviews of Modern Physics*, 57(3):699.

[Sachs, 1964] Sachs, R. G. (1964). Nucleon electromagnetic form factors at high momentum transfer. *Phys. Rev. Lett.*, 12(9):231–233.

[Schubert, 2006] Schubert, E. F. (2006). *Light-emitting Diodes*. Cambridge University Press, 2nd edition.

[Sibirtsev et al., 2010] Sibirtsev, A., Blunden, P. G., Melnitchouk, W., and Thomas, A. W. (2010). $\gamma - Z$ corrections to forward-angle parity-violating ep scattering. *Phys. Rev. D*, 82(1):013011.

[Smith, 2009] Smith, G. (2009). Quarterly report for FY09 quarter 3 (qweak document 989-v2). Technical report, JLab.

[Smith, 2011] Smith, G. (2011). Qweak status (qweak document 1410-v3). Technical report, JLab.

[Souder et al., 1990] Souder, P. A. et al. (1990). Measurement of parity violation in the elastic scattering of polarized electrons from $C12$. *Phys. Rev. Lett.*, 65(6):694–697.

[Steiner et al., 2007] Steiner, B., Ackermann, W., Muller, W., and Weiland, T. (2007). Wien filter as a spin rotator at low energy. In *Particle Accelerator Conference, 2007. PAC. IEEE*, pages 170–172. IEEE.

[Tjon et al., 2009] Tjon, J., Blunden, P., and Melnitchouk, W. (2009). Detailed analysis of two-boson exchange in parity-violating ep scattering. *Physical Review C*, 79(5):055201.

[Vincenzi et al., 1984] Vincenzi, M. D., Penso, G., Sciubba, A., and Sposito, A. (1984). Experimental study of non-linear effects of photomultiplier gain. *Nuclear Instruments and Methods in Physics Research*, 225(1):104–112.

[Wang, 2007] Wang, P. (2007). Magnetic field simulation and mapping for the Qweak experiment. Master's thesis, University of Manitoba, Winnipeg, Canada.

[Wang, 2010] Wang, P. (2010). Distribution of diagnostic LED power (qweak document 1204-v1). Technical report, JLab.

[Wang et al., 2008] Wang, P. et al. (2008). Diamond detector for Compton polarimetry (qweak document 769-v1). Technical report, JLab.

[Weinberg, 1967] Weinberg, S. (1967). A model of leptons. *Physical Review Letters*, 19(21):1264.

[Weinberg, 1971] Weinberg, S. (1971). Physical processes in a convergent theory of the weak and electromagnetic interactions. *Physical Review Letters*, 27(24):1688–1691.

[Weinberg, 1974] Weinberg, S. (1974). Recent progress in gauge theories of the weak, electromagnetic and strong interactions. *Reviews of Modern Physics*, 46:255–277.

[Wu et al., 1957] Wu, C., Ambler, E., Hayward, R., Hoppes, D., and Hudson, R. (1957). Experimental test of parity conservation in beta decay. *Physical review*, 105(4):1413.

[Yamashita, 1977] Yamashita, M. (1977). Observation of a hysteresis effect in rate-dependent photomultiplier gain variations. *Nuclear Instruments and Methods*, 142(3):435–437.

[Yamashita, 1978] Yamashita, M. (1978). Mechanism of the hysteresis effect in rate-dependent photomultiplier gain variations. *Review of Scientific Instruments*, 49(9):1336–1342.

[Yan et al., 1995] Yan, C., Adderley, P., Barker, D., Beaufait, J., Capek, K., Carlini, R., Dahlberg, J., Feldl, E., Jordan, K., Kross, B., Oren, W., Wojcik, R., and VanDyke, J. (1995). Superharp – a wire scanner with absolute position readout for beam energy measurement at CEBAF. *Nuclear Instruments and Methods in Physics Research Section A: Accelerators, Spectrometers, Detectors and Associated Equipment*, 365(2-3):261–267.

[Young et al., 2006] Young, R., Roche, J., Carlini, R., and Thomas, A. (2006). Extracting nucleon strange and anapole form factors from world data. *Physical review letters*, 97(10):102002.

[Young et al., 2007] Young, R. D., Carlini, R. D., Thomas, A. W., and Roche, J. (2007). Testing the standard model by precision measurement of the weak charges of quarks. *Phys. Rev. Lett.*, 99(12):122003.

[Zeller et al., 2002] Zeller, G. P. et al. (2002). Precise determination of electroweak parameters in neutrino-nucleon scattering. *Phys. Rev. Lett.*, 88(9):091802.

Index

$SU(2)$, 10

$SU(2) \times U(1)$, 6

$U(1)$, 10

γZ-box, 39

$\langle Q^2 \rangle$ bias, 115

Čerenkov angle, 91

Čerenkov radiation, 91

Čerenkov threshold, 91

“running” of the weak mixing angle, 6

4-momentum transfer, 25

Aliasing, 144

ANSYS, 68

APV, 40

axial form factor, 26

baryon, 7

BCM, 57

beam modulation, 180

bi-alkali, 123

blind analysis, 179

Born approximation, 25

box diagram, 36

BPMs, 58

cable capacitance, 146

CAEN, 149

calibration mode, 49

CEBAF, 54

CERN, 40

charge, 8

Charge symmetry, 28

charge-normalized yield, 175

CHL, 69

CMM, 208

CODA, 151

collimator, 71

Compton polarimeter, 62, 65

counting statistics, 100

coupling constant, 11, 19

critical angle, 94

cross-section, 29

cut value, 108

Dirac equation, 10

Dirac form factor, 26

effective Hamiltonian density, 21
effective weak Lagrangian, 22
elastomer, 133
electro-weak interactions, 6
electro-weak mixing matrix, 13
electromagnetic form factor, 28
equivalent noise bandwidth, 143
ESR, 68
ESTAR, 154
excess noise, 101
exoskeleton, 131

Fermi theory, 20
fermion, 7
flavor decomposition, 23
flavor mixing angle, 44
flavors, 7
four-fermion contact interaction, 21
FPGA, 147
fundamental interactions, 5
FWHM, 163

gauge boson, 6, 11
gauge field, 10
gauge transformation, 10
Geant4, 107
GEM, 51, 76
generations of matter, 6

hadron, 7
hadronic form factor, 34
halo, 59
HDCs, 51, 78
helicity, 31
helicity correlated beam properties, 179
Higgs mechanism, 11
Higgs vacuum expectation, 13
hypercharge, 17
hyperon, 8

IA, 60
IHWP, 56
in-situ mounting scheme, 135
insertable half wave plate, 56
integration scheme, 147
Intensity Attenuator, 60
isospin symmetry, 12

JLab, 1

Klein-Gordon Lagrangian, 11

left-handed, 17
LEP, 40
light yield, 94
linear regression, 180
LUMIs, 85

macropulse, 56

main detectors, 2

mass term, 11

mass/coupling ratio, 42

matter fields, 10

meson, 7

Mexican hat potential, 12

MPS, 56

mu-metal, 127

multialkali, 123

Møller, 72

Møller polarimeter, 62

neutral current, 16

null-asymmetry, 85

NuTeV, 40

one-loop, 36

parity transformation, 5

parity violation, 17

parity-violating asymmetry, 31

pattern asymmetry, 176

Pauli form factor, 26

physics asymmetry, 185

Poron, 132

power line phase monitor, 150

pre-radiator, 120

production mode, 49

PVES, 24

PZT, 61

Q-weak collaboration, 1

Q-weak experiment, 2

QED, 34

QTOR, 73

quark sea, 7

quartet, 56

quasi-differential, 147

radiative corrections, 35

rastering, 64

rate effect, 125

raw asymmetry, 176

registration point (edge, surface), 208

right-handed, 17

ROCs, 151

S20, 123

Sachs Form Factors, 26

SbCs dynodes, 125

scanner, 51

scattering angle, 25

screening effect, 35

SEE, 58

settling time, 102

SFR, 54

sheet resistance, 123

shot noise, 101, 141, 143, 144

SLAC E-158, 40

SLC, 40

slug, 174

SPA, 157

Spectrosil, 117

spontaneous symmetry breaking, 11

stopping power, 154

strange quark current, 23

superharp, 59

Switched Electrode Electronics, 58

synthetic fused silica, 117

TBE, 39

the proton's weak charge, 2

the Standard Model, 1

thermal noise, 101

TIR, 94

TJNAF, 1, 54

toroidal magnet, 73

total internal reflection, 94

trans-impedance, 142

tree level, 18

two-LED technique, 156

Unser monitor, 58

vacuum polarization, 35

VDCs, 51, 79

vector boson, 5, 16

VME, 153

weak (or Weinberg) mixing angle, 6

weak hypercharge, 10

weak isospin, 11, 20

weak mixing angle, 15

Wien filter, 56

Yang-Mills field, 35

Z-pole, 6